Rotating planes, fluctuating shapes

Anisotropic flow and magnetic fields in heavy-ion collisions

Jacopo Margutti

A catalogue record is available from the Utrecht University Library.

ISBN: 978-90-393-7053-7

Cover design by Bastiaan Schravendeel (Polder Animation), based on a simulation of a heavy-ion collision with T$_{\mathrm{R}}$ENTo 3D (Duke University QCD Group)
Typset using LaTeX
Printed by ProefschriftMaken

Rotating planes, fluctuating shapes

Anisotropic flow and magnetic fields in heavy-ion collisions

Roterende vlakken, fluctuerende vormen

Anisotrope flow en magnetische velden in zware-ionenbotsingen

(met een samenvatting in het Nederlands)

ter verkrijging van de graad van doctor aan de Universiteit Utrecht op gezag van de rector magnificus, prof.dr. H.R.B.M. Kummeling, ingevolge het besluit van het college voor promoties in het openbaar te verdedigen op woensdag 26 november 2018 des middags te 12.45 uur

door

Jacopo Margutti

geboren op 21 april 1990
te Milaan, Italië

Promotor: Prof.dr. R.J.M. Snellings

Contents

Chapter 1

Theory

1.1 Quantum Chromodynamics

Four forces are known to determine interactions between elementary particles[1]: gravitational, electromagnetic, weak and strong. The last three can be described within a common relativistic quantum field theory, the Standard Model (SM). Each force acts on one or more specific *charges*, unevenly shared between elementary particles, through the exchange of other particles called *gauge bosons*, which are said to "carry" the interaction. Photons (γ) carry electromagnetic interactions between particles with electric charge; $W^{\pm}$ and Z^0 bosons carry weak interactions, which affect particles with *flavour* charge; gluons (g) carry strong interactions between particles with *colour* charge. A full description of the SM is beyond the scope of this dissertation and can be found in [1]. Here, we will focus on the strong force, which in the SM is described by *Quantum Chromodynamics* (QCD).

QCD is a non-abelian gauge theory with symmetry group SU(3) and describes the dynamics of quarks and gluons, which together are called *partons*. Colour charge, contrary to the electric one, can assume three values, conventionally called red, green and blue (with the prefix anti- for anti-particles). Each quark has a single colour charge, while gluons have two, a colour and an anti-colour one. This is connected to the most distinct feature of QCD with respect to the other fundamental forces: gluons can self-interact [2], which in turn determines what is called *anti-screening*.

In quantum field theory, interactions between particles are effectively determined by the contributions of all possible processes that can occur. In particular, if we take the simple case of the interaction between two quarks in the vacuum, on top of the simple one-gluon exchange we will have to consider processes in which the exchanged gluon can undergo further interactions with short-lived particles. One possibility is that the gluon produces a quark anti-quark ($q\bar{q}$) pair (Fig. 1.1, left): this decreases the interaction strength, as the pair is oppositely charged and effectively "masks" the charge of the interacting quarks[2], therefore called *screening*. In QCD other processes can occur: a pair of gluons can be formed (Fig. 1.1, right), which attract each other, effectively increasing the interaction strength. This mechanism is called *anti-screening* and is the dominant one

[1] Particles thought to be not composed of other particles.

[2] This is analogous to the polarisation of a dielectric medium in the presence of an electric charge.

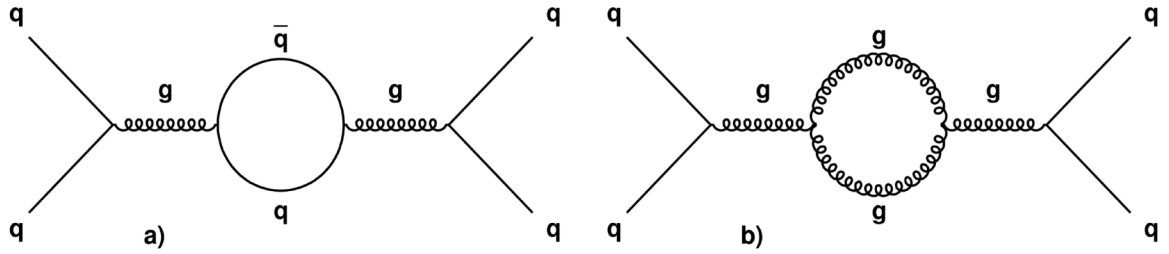

Figure 1.1: Feynman diagrams at first order of QCD interactions determining screening (left) and anti-screening (right). In the case of quantum electrodynamics (QED), anti-screening does not take place since photons do not self-interact. Figure from [3].

in QCD.

The strength of these processes depends on the momentum exchanged between the two quarks (Q^2), which is inversely proportional to the spatial distance within which the interaction itself takes place, according to the uncertainty principle. Thus, the total interaction strength between two quarks - quantified in terms of strong *coupling constant* α_s - behaves as follows (see Fig. 1.2). For large momentum transfer, i.e. small distances, anti-screening becomes progressively less important and α_s decreases, to the point that partons can exist as quasi-free particles, from which the name *asymptotic freedom*. Conversely, for low momentum transfer, i.e. large distances between the interacting quarks, anti-screening dominates and α_s diverges. The result can be effectively described as follows: if we pull a $q\bar{q}$ pair apart, as the distance between the quarks increases so does the binding energy, to the point that it is energetically favourable to produce another $q\bar{q}$ pair from the vacuum and split the original pair in two. This behaviour is usually referred to as *colour confinement*: quarks are confined to colourless bound states called *hadrons*. These two properties (asymptotic freedom and colour confinement) are unique to QCD and define its dynamics.

While high-energy QCD interactions are well understood and can be computed analytically through perturbation theory, low-energy ones, where $\alpha_s \gtrsim 1$, cannot. Effective theories and/or numerical methods need to be used, e.g. using non-perturbative calculations in a discretised spacetime (lattice QCD [5]). This latter approach, in particular, has been extremely useful for studying static, equilibrated QCD systems, as we will see later, but has fundamental problems in predicting properties of dynamical ones [6], which are far more relevant when describing natural phenomena.

1.2 High-energy nuclear physics

The goal of high-energy nuclear physics[3] is, despite the name, to study the low-energy regime of QCD, where the limits of validity of our theory stand.

How can we do it, experimentally? We have to start from what we have available, i.e. long-lived bound states of quarks: *nucleons* (protons and neutrons) and nuclei. We want to obtain an interacting system whose fundamental degrees of freedom are partonic, so we first need to overcome confinement. This can be achieved on one hand with individual,

[3]Often called "heavy-ion physics" within the tribe of physicists, for reasons that will be clear soon.

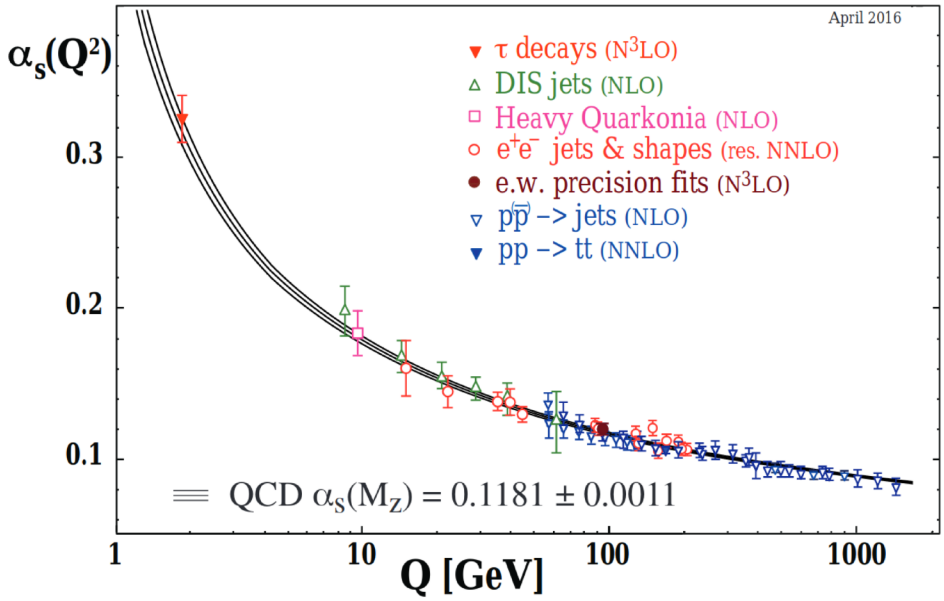

Figure 1.2: Summary of measurements of α_s (points), together with predictions from QCD (bands), as a function of the energy scale Q. Figure from [4].

high-energy collisions, in which at least two partons of the hadrons interact with high Q^2. On the other hand, we can change the properties of the strong interaction in a hadronic system by increasing the colour charge density, which results in individual quarks being screened from one another (analogously to Debye screening in electromagnetism). This latter approach, in particular, has the advantage of giving access to non-perturbative dynamics at smaller energy scales and is therefore our tool of choice. Colour charge density can in turn be increased either by heating up the system, which results in thermal production of partons, or by compressing it. Therefore, the task at hand can be equivalently formulated as studying the QCD phase diagram, sketched in Fig. 1.3, i.e. characterising the proprieties of QCD matter at high temperatures T and/or baryon chemical potential μ_B. In particular, the phase composed of deconfined partons is conventionally called *Quark-Gluon Plasma* (QGP). Two notable natural phenomena fall, within this diagram, in areas of high T and/or high μ_B: neutron stars, whose inner cores might exhibit colour superconducting properties [7], and the early universe, which we think has been in the QGP phase between electroweak symmetry breaking and hadronisation, at about 10^{-12} s and 10^{-6} s, respectively, after the Big Bang.

Which temperatures must the system reach to be deconfined and how can we achieve it? Estimates from lattice QCD calculations predict the transition from hadrons to QGP at vanishing μ_B to happen at a critical temperature $T_c \sim 155$ MeV, or equivalently at an energy density $\varepsilon \sim 0.7$ GeV/fm^3 [8]. This currently can be achieved only in high-energy hadron collisions, especially with heavy ions. In a typical proton-proton collision, in fact, most energy-momentum is exchanged within few, (semi-)hard parton-parton scatterings. The scattered partons travel outwards, radiating softer gluons, until hadronisation, called *fragmentation* in vacuum, takes place. The mean free path of these partons is large compared to the proton size, i.e. they typically do not interact with other scattered partons[4].

[4]Possible collective effects in such collision system concern a tiny fraction of the hadronic cross-section,

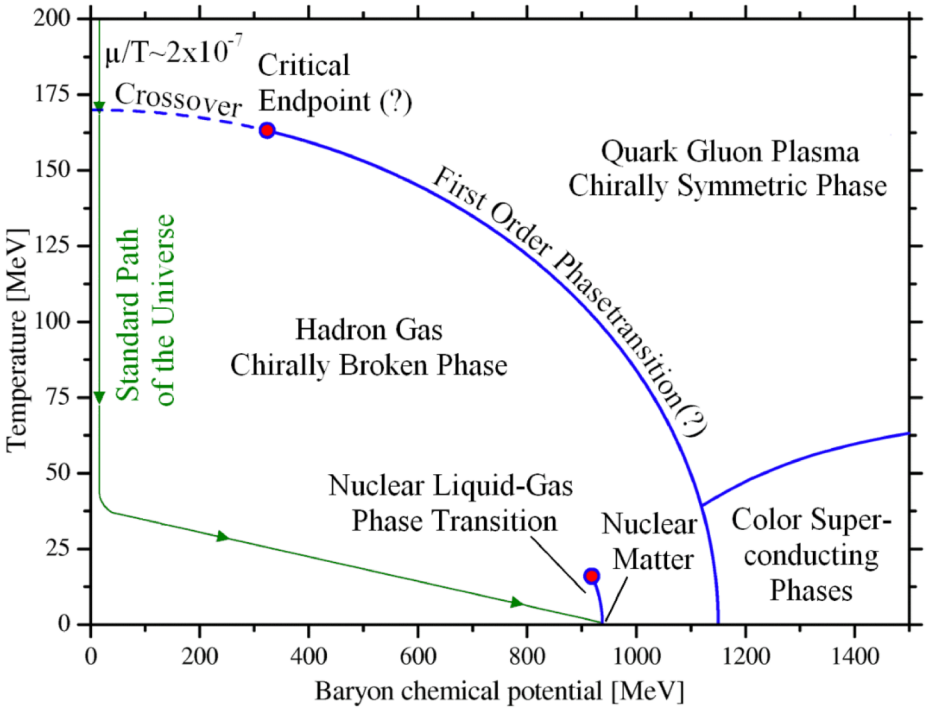

Figure 1.3: Illustration of the QCD phase diagram. Relativistic heavy-ion collisions cover the upper-left corner, with increasing maximum temperature and decreasing baryon chemical potential as the collision energy is increased. Figure from [4].

Therefore, despite these few, (semi-)hard processes, the effective energy density is still low. In a heavy-ion collision, on the contrary, scattered partons interact with each other, since the nuclear system is large (compared to the mean free path) and dense, redistributing energy-momentum among all partons[5]. The energy density quickly increases and a transition to the QGP phase takes place. From this moment to hadronisation, the evolution and properties of this system will then be determined by the type of non-perturbative QCD dynamics that we are interested in; this is why, in a nutshell, we collide heavy ions.

Given the general arguments behind deconfinement in QGP, it is expected that at very high temperatures ($T \gg T_c$) partons would be quasi-free, even for low Q^2 [9]. Practically, the range of maximum temperatures that we can achieve with current accelerators, such as the *Relativistic Heavy-Ion Collider* (RHIC) and the *Large Hadron Collider* (LHC), is of about 2-4 T_c, i.e. right above the transition temperature. It may then not come as a surprise that within this temperature range partons are effectively *strongly coupled*, despite being deconfined, as lattice QCD and experimental results indicate [10], presumably because of the same processes that determine confinement, i.e. gluon self-interactions.

corresponding to high-multiplicity events.

[5]The (quasi-)particle representation that we use here might not be suited for a strongly coupled system, but it has the advantage of being intuitively accessible; apologies to a possible punctilious reader.

1.3 Heavy-ion collisions

It is already clear at this stage that a heavy-ion collision is composed of different heterogeneous and consecutive phases, sketched in Fig. 1.4, which all take place within 10 fm/c (about 10^{-23} s). The only observables at our disposal are the particle that free-stream to our detectors and are detected long after the the collision took place. The properties of these particles are determined by the cumulative effect of the whole system evolution, or at least parts of it. To understand how much each phase contributes to the measured particle yields and kinematic properties - and especially how much the QGP phase contributes - is the challenge before us; unfortunately, it is not an easy one.

We will now summarise the current understanding of these different phases, devoting special attention to what will be discussed later in this dissertation. For a complete and recent review, see [12].

- **Initial state**
  The description of the initial state (IS) of the collision, i.e. the properties the colliding partons and the system that they form after the very first interactions, involves mostly gluons. In fact, the Lorentz-contracted nuclei can be described mostly as sheets of low-x gluons, where x is the longitudinal momentum fraction carried by the gluon, and moderate transverse momenta, $k_\perp \lesssim 1$ GeV. These gluons constitute a large fraction of colliding partons and thus determine how energy is spatially distributed in the initial system. An open question remains if, how and at which scale of Q the number of low-x gluons saturates, a phenomenon called *gluon saturation* [13], since perturbative QCD naïvely predicts that it would diverge for $x \to 0$. Yet, despite the lack of direct evidence supporting gluon saturation, models based on this prescription, such as EKRT [14] and IP-Glasma [15], have been so far favored by observations [16, 17, 18], although uncertainty in some details remain. At the same time, much simpler, non-dynamical models, such as MC-Glauber [19], that compute the geometry of the initial state from the position of colliding nucleons without assuming any sub-structure, also qualitatively (and in several cases quantitatively) describe the same observables [20]. This suggests that parton density, as expected, correlates very much with the position of colliding nucleons.

- **Pre-equilibrium**[6]
  At this stage, gluons from the initial state interact with each other and radiate softer gluons. In this processes, almost all of the entropy is being produced, thus determining the final-state multiplicity [12]. The more the gluons (self-)interact, the higher the parton density and temperature gets. Although this mechanism has been realised very early [25], only recently we were able to prove it numerically [26, 27, 28] via simulations with QCD effective kinetic theory [29]. The pre-equilibrium dynamics, from initial state to QGP, is thought to last for about 1 fm/c, but direct constraints from data are not yet available.

[6]The term "pre-equilibrium" can be misleading: nowhere, we currently think, in a heavy-ion collision we reach a system in global thermal, hadrochemical or mechanical equilibrium; equilibration can be reached only locally and partially, and whether it is reached or not is not relevant for what is being discussed.

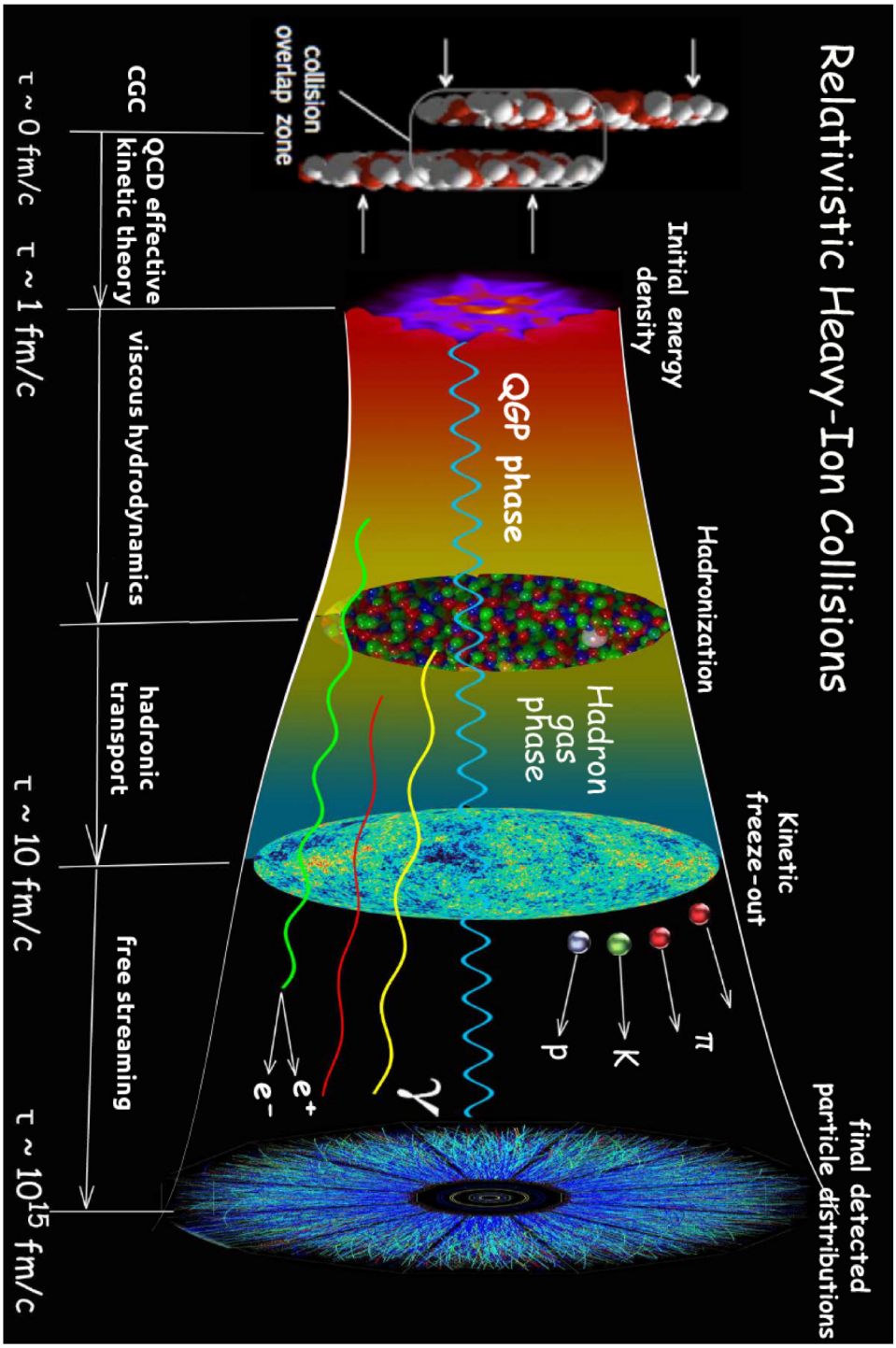

Figure 1.4: Illustration of the dynamical evolution of relativistic heavy-ion collisions. Top: the different phases that the QCD system undergoes. Bottom: the models with which we describe each of these phases. Figure adapted from [11].

- **QGP**
  The QGP phase, being strongly-coupled, can effectively be described as a relativistic fluid with very low specific shear viscosity [30], which progressively expands and cools down, lasting for about 10 fm/c. During this phase, partons within the expanding medium acquire similar velocities, while being pushed outwards in the transverse plane; more about the collective dynamics underlying the QGP expansion will be explained in Sec. 1.4. On top of that, we know that the QGP is opaque to strongly interacting probes, such as partons with high transverse momenta [31], which loose energy via collisional and radiative processes [32]. We also know that it is transparent to electromagnetic probes, such as photons and electrons, i.e. they have a long mean-free-path compared to the size of the system [33].

- **Hadronisation and rescatterings**
  When the system temperature locally falls below $T_c \sim 155$ MeV, partons progressively hadronise, in a process called *chemical freeze-out*. It is still unclear to which extent hadronisation happens via coalescence of quarks from the medium or via fragmentation, as in the vacuum, although studies are ongoing [34]. These hadrons continue to scatter with each other, while expanding, until eventually the system dilutes and they stream outwards freely. Similarly, this is called *kinetic* or *thermal freeze-out*.

The knowledge that we gained about heavy-ion collisions came essentially from two classes of measurements: yields and correlations. Yields, like distributions of particles with respect to their kinematic variables (transverse momentum, pseudorapidity), provide information on cross sections of the corresponding production processes. Ratios of yields in different collision systems - most notably, between nucleus-nucleus and proton-proton collisions[7], known as *nuclear modification factor* R_{AA} [36, 37] - indicate whether the nuclear environment modifies particle production, e.g. through final-state effects such as energy loss. Correlations of kinematic variables, on the other hand, contain information on interactions between specific sets of (or all) particles. Momentum correlations at low transverse momenta due to quantum interference, measured with techniques known as *Hanbury-Brown-Twiss* (HBT) interferometry [38] or *femtoscopy*, are sensitive to the spatial evolution of the system [39]. Finally, correlations in azimuthal angle provide information on *anisotropic flow*, among other effects, as we will discuss extensively in the following.

1.4 Anisotropic flow

Within the varied phenomenology of heavy-ion collisions, anisotropic flow is the main subject of this dissertation. It is experimentally defined as azimuthal anisotropy in momentum space, i.e. the distribution of momenta of produced particle not being uniform in azimuthal angle φ. In heavy-ion collisions, and for particles with low transverse momenta ($p_{\mathrm{T}} \lesssim 3$ GeV/c), this is mostly determined by (1) the spatial distribution of the energy density after the collision, i.e. the shape of the initial state, being not uniform and (2) the

[7] Properly normalised for the number of individual nucleon-nucleon collisions.

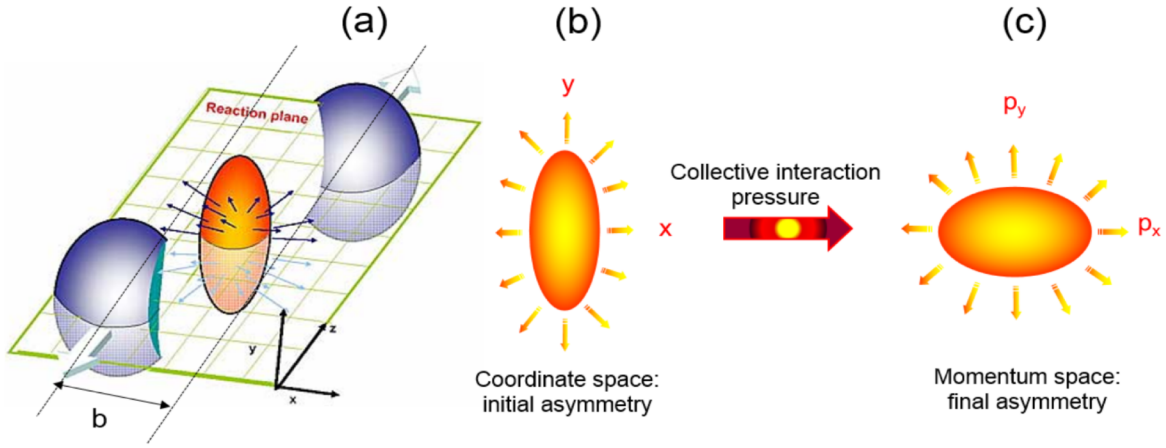

Figure 1.5: (a) A non-central collision of two nuclei leads to an almond-shaped initial state; (b) the initial spatial anisotropy translates into (c) momentum anisotropy of the produced particles, via the collective expansion of the system. Figure from [40].

collective expansion that the system undergoes[8] [41]. This can be intuitively understood as follows (Fig. 1.5). For a QCD system with non-spherical shape in the transverse plane, the pressure gradients are larger along particular azimuthal angles, where the change in energy density is steeper, and smaller elsewhere. If the system can be described by (non-relativistic, ideal) hydrodynamics[9], the momentum conservation equation simply reads

$$\rho \frac{\mathrm{d}\vec{v}}{\mathrm{d}t} = -\vec{\nabla} P, \tag{1.1}$$

where $\vec{v}$ is the fluid cell velocity, P the pressure and ρ the density. It is then straightforward to see that, if the system expands hydrodynamically, partons will be accelerated proportionally to the pressure gradients and therefore anisotropically in azimuthal angle. In other words, spatial anisotropies of the initial state will be converted into final-state momentum anisotropies by the collective, hydrodynamic-like expansion of the system.

Conventionally, the way we quantify these momentum anisotropies is through the Fourier coefficients v_n, called *flow coefficients*, of the harmonic expansion of the particle azimuthal distribution relative to certain *global planes* Φ_n [42]

$$\frac{\mathrm{d}N}{\mathrm{d}[\varphi - \Phi_n]} \propto 1 + \sum_n 2\, v_n \cos(n[\varphi - \Phi_n]), \tag{1.2}$$

where n is referred to as the *harmonic number* of the flow coefficients, which are then defined as

$$v_n = \frac{1}{2\pi} \int_0^{2\pi} \frac{\mathrm{d}N}{\mathrm{d}[\varphi - \Phi_n]} \cos(n[\varphi - \Phi_n])\, \mathrm{d}\varphi \approx \langle \cos(n[\varphi - \Phi_n]) \rangle, \tag{1.3}$$

where the brackets denote an average over all particles produced in a collision. According

[8] Naturally, other phenomena determine momentum anisotropies; a proper distinction will be drawn in Sec. 3.1.

[9] Once more, the punctilious reader will forgive us preferring clarity over precision.

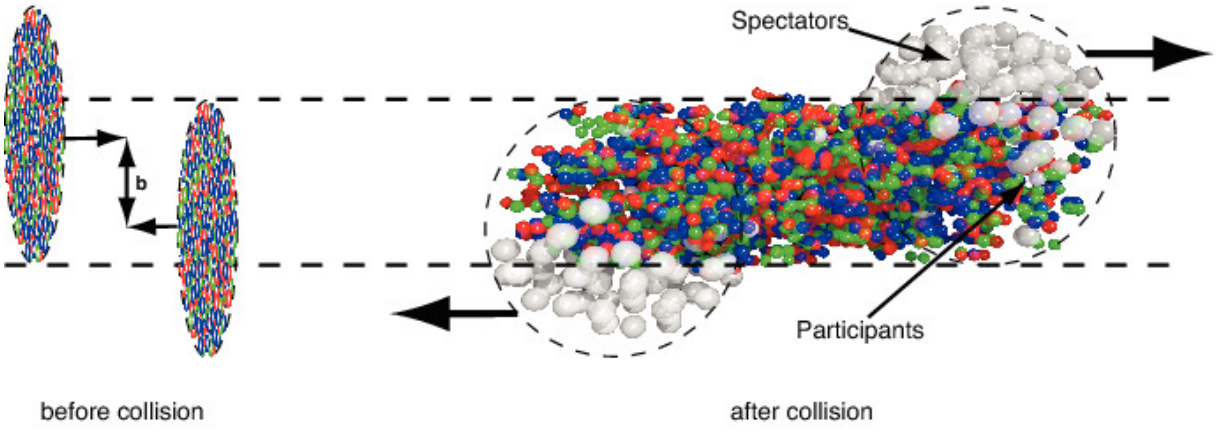

Figure 1.6: Longitudinal view of a heavy-ion collision, showing the distinction between participant and spectator nucleons. Figure from [44].

to the harmonic, they are called *directed* flow (v_1), *elliptic* flow (v_2), *triangular* flow (v_3), etc. The global planes Φ_n are related to the geometry of the system and can be defined in several ways. The most common ones - together with their preferred notation - are

- **Reaction plane $\Psi_{\mathbf{RP}}$**
  It is defined as the azimuthal angle of the plane spanned by the impact parameter between the two colliding nuclei and the beam axis.

- **Symmetry planes (or participant planes) Ψ_n**
  They are defined by the symmetry axes of the initial-state spatial configuration, more precisely of its energy density distribution (see Eq. 1.4 later). Such configuration varies in each collision, even at a fixed impact parameter, because of fluctuations in the nucleus wave-function and of differences in the parton-parton collision processes, a phenomenon referred to as *initial-state fluctuations*. Each harmonic has then a different symmetry plane and different symmetry planes are not necessarily correlated with each other or with the reaction plane [43].

- **Spectator plane $\Psi_{\mathbf{SP}}$**
  The nucleons that do not collide, and that therefore continue moving at beam rapidity after the nuclei fragment, are called *spectators* (Fig. 1.6) and the transverse direction in which they move after the collision defines the spectator plane.

A sketch of these different planes is given in Fig. 1.7, where we use the position of colliding nucleons to approximate the initial-state energy density distribution. It should be noted that, unless otherwise stated, measurements of flow coefficients are conventionally performed with respect to the corresponding symmetry planes, $v_n = \langle\cos(n[\varphi - \Psi_n])\rangle$; the reason comes from the experimental techniques employed, as we will see in Sec. 3.1.

Since anisotropic flow and initial state are so closely related, it is a convention to decompose also the latter in terms of a harmonic expansion and define *eccentricities* ε_n and symmetry planes Ψ_n as [45, 46]

$$\varepsilon_n \, e^{in\Psi_n} = -\frac{\int \rho(r,\varphi)\, r^n \, e^{in\varphi} \, r \, \mathrm{d}r \, \mathrm{d}\varphi}{\int \rho(r,\varphi)\, r^n \, r \, \mathrm{d}r \, \mathrm{d}\varphi}, \tag{1.4}$$

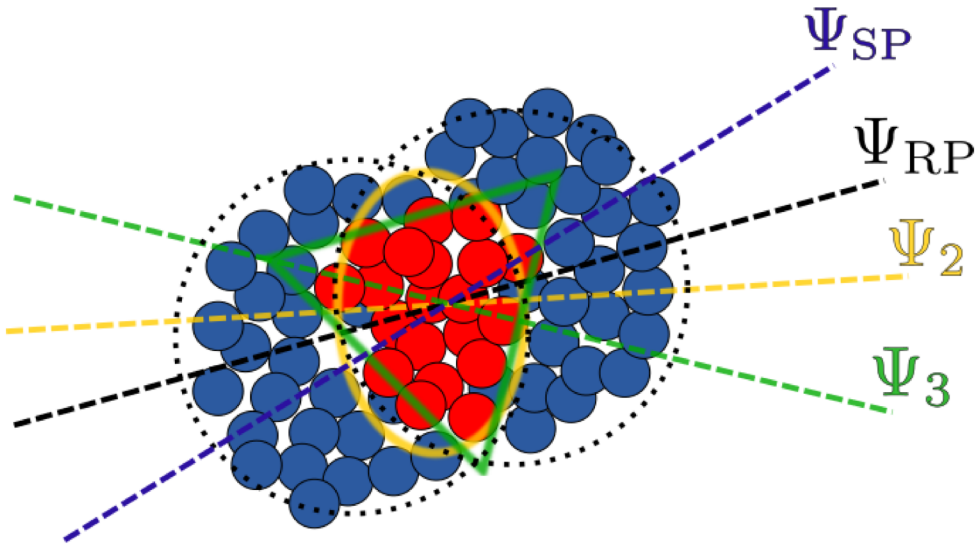

Figure 1.7: Transverse view of a heavy-ion collision, with various global planes sketched. Participant nucleons are shown in red, spectator ones in blue. The yellow ellipse (green triangle) follows the approximate distribution of participant nucleons and define the direction of Ψ_2 (Ψ_3).

where $\rho(r, \varphi)$ is the energy density distribution in polar coordinates. The precise relation between ε_n and v_n will be discussed in detail in Sec. 5.1; suffice it to say that it is roughly linear. The initial state is expected to first approximation to be boost-invariant at LHC energies, i.e. eccentricities and symmetry planes do not depend on rapidity. Indeed, this has been measured to hold within a few % per unit of pseudorapidity [47, 48]. A separate discussion is required for the first harmonic, the directed flow v_1, as we will see in Sec. 7.1.

The dominant flow coefficient in non-central heavy-ion collisions is elliptic flow v_2, which is mostly a result of the average ellipsoidal shape of the overlapping area between the colliding nuclei, whereas higher harmonics (v_3, v_4, ...) originate only from initial-state fluctuations[10]. Anisotropic flow at low transverse momenta is thought to be quantitatively determined by the whole evolution of the system, including the phase of hadronic rescatterings that takes place after chemical freeze-out [49, 50]. Flow coefficients have been shown to be sensitive not only to initial-state anisotropies, but also to the transport parameters (such as specific shear and bulk viscosity [51, 52]) and the equation of state of the system, and they have therefore been used to constrain these properties [53, 54]. In particular, smaller specific shear viscosity η/s, where s is the entropy, implies larger anisotropic flow, since there is lower resistance to shear stress determined by anisotropic pressure gradients. However, given the different heterogeneous phases that the system is believed to undergo, it has not been possible so far to simultaneously constrain the large number of model parameters involved, although insightful attempts have been made [18, 55].

All that has been discussed so far concerns particles with low transverse momenta, whose kinematic properties are determined by the collective phenomena in which they

[10] Additional small contributions to all even harmonics come from the approximately almond shape of the initial system.

participate. At high transverse momenta ($p_{\mathrm{T}} \gtrsim 10$ GeV/c), the dominant mechanism that determines azimuthal anisotropies is thought to be path-length dependent energy-loss of highly energetic partons [56, 57, 58]. The energy that the partons loose while transversing the medium, in fact, depends on the length of their trajectory, which in turn depends on azimuthal angle. Several experimental observations, such as jet azimuthal anisotropies [59, 60], are consistent with this hypothesis, but the details of the process are largely unconstrained. Note that, even though the mechanism that determines it is fundamentally different, the origin of anisotropic flow at high p_{T} is presumably common to the one at low p_{T}: initial-state geometry and its fluctuations. Recent measurements [61] and the results presented in this dissertation seem to confirm this interpretation.

It is interesting to look at the connection between the specific shear viscosity and energy loss. This latter is usually quantified in terms of *jet transport coefficient* $\hat{q}$, the average squared transverse momentum transfer between a parton and the medium per unit length [62]. It is clear that both medium properties, viscosity and opaqueness, are due to parton interactions. In a weakly-coupled, quasi-particle picture the two can be related as [63]

$$\frac{\eta}{s} \approx k \frac{T^3}{\hat{q}}. \tag{1.5}$$

In other words, small specific shear viscosity implies large opacity, up to a constant factor k. Estimates of η/s and $\hat{q}$ at RHIC and LHC energies, i.e. at lower and higher average temperature, respectively, are qualitatively consistent with this behaviour [64, 65].

1.5 Magnetic fields and chiral anomaly

Heavy-ion collisions have another interesting feature: they generate extremely intense, although short-lived, magnetic fields. In fact, if the impact is not head-on, not all nucleons participate in the collision. Those which do not, as we explained in the previous section, are called spectators and continue moving at beam rapidity (Fig. 1.6). A bit less than half of these spectators are protons, therefore they generate an electric current. Having two bunches of protons moving in opposite directions, one from the fragmentation of each nucleus, a strong magnetic field B is generated in the area of the collision, directed approximately perpendicularly to the reaction plane (Fig. 1.8). According to the Biot-Savart law, its magnitude can be estimated as

$$B \sim \gamma Z e \frac{b}{R^3}, \tag{1.6}$$

where $\gamma = \sqrt{s_{\mathrm{NN}}}/2m_{\mathrm{N}}$ is the Lorentz factor, Z the atomic number, e the electric charge, b the impact parameter and R the nuclear radius. At LHC energies, such field can reach a maximum intensity of $eB \approx 10\, m_\pi^2$ (or $\sim 10^{19}$ G $= 10^{15}$ T) [66, 67]. To appreciate the scale, we can compare it with the strongest magnetic field estimated to exist in the universe, on the surface of magnetars ($\sim 10^{14}$ - 10^{15} G) [68]. Extensive theoretical work has been done on the possible effects of such magnetic field on QCD matter and its phases; for a complete overview, see [69]. Unfortunately, on the experimental side little and ambigous evidence has been collected that any of these effects are actually observable. One factor casting doubt on the subject is the lifetime of the magnetic field in the vacuum (≤ 1 fm/c), which is short compared to the timescale of QGP formation and evolution. The electromagnetic

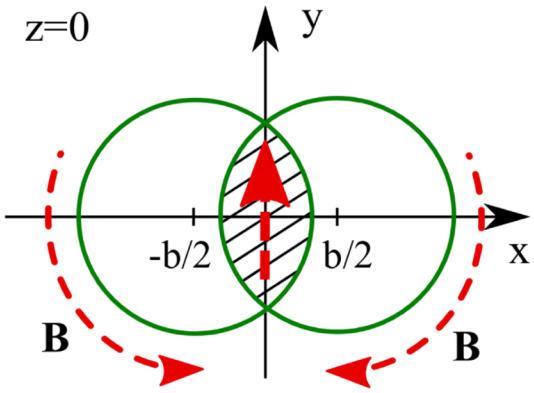

Figure 1.8: Schematic view of the transverse plane of a non-central heavy-ion collision with impact parameter b. The magnetic field is represented with dashed red lines. Figure from [74].

response of the system could extend it significantly, as will be discussed in Sec. 7.1, but no evidence exist so far that such is the case. This is directly connected to the QGP electric conductivity, which is currently known only from lattice QCD calculations [70, 71, 72, 73].

Yet, if such magnetic field coexist in the system, it provides a unique tool to test a broad range of phenomena connected to a fundamental, untested aspect of QCD, namely having topologically nontrivial configurations of the gauge fields. This property is common to all non-Abelian gauge theories, like those constituting the basis of the SM: QCD and electroweak theory. These *topological configurations* can be identified with a quantum number, which we call *topological charge*, *winding number* or *Chern-Simons number*. Transitions between states with different topological charge are possible and go under the name of *instantons* [75] or *sphalerons* [76], which correspond to tunneling and saddle point solutions of the gauge fields, respectively. While in the vacuum these transitions are suppressed by factors of the order of e^{1/α_s}, it was realised very early that sphalerons might occur abundantly in systems at high temperature [77, 76] and not necessarily in equilibrium, such as those produced in a heavy-ion collision. The actual sphaleron rate that one would achieve there is still subject of debate [78, 79]. It has been suggested that topological transitions in QCD are responsible for chiral symmetry breaking [80] and possibly for confinement [81].

If topological transitions occur, how can we detect them? Because of quantum anomalies, they are associated with non-conservation of certain quantum numbers, which are specific to the theory under consideration: for QCD it is chirality [82], for electroweak theory it is baryon and lepton number [83] (a SM candidate for explaining baryogenesis, i.e. the imbalance of matter and antimatter in the observed universe). Therefore, in the context of QCD, topological transitions manifest in the form of chiral imbalance, i.e. the number of left- and right-handed fermions (quarks) is not the same in a given collision [84]. This violates the parity and charge-parity symmetry of QCD. Since the chirally-imbalanced QCD system, in a heavy-ion collision, evolves within a strong magnetic field, a charged current will develop along the magnetic field direction, approximately perpendicularly to the reaction plane, and its sign will change event-by-event [85, 86]. The

explanation is straightforward: semi-classically, the potential energy U of a particle with magnetic moment $\vec{\mu} \propto q\,\vec{S}$ in an external magnetic field $\vec{B}$ is of the form

$$U = -\vec{\mu} \cdot \vec{B} \propto -q\,\vec{S} \cdot \vec{B}, \tag{1.7}$$

i.e. the particle spin tends to be aligned parallel or anti-parallel to $\vec{B}$ according to its charge, analogously to classical magnetisation. If then one considers, for simplicity, a system of only right-handed fermions, i.e. with momentum parallel to the spin, it is clear that particles will move parallel or anti-parallel to $\vec{B}$ according to their charge. This phenomenon is called *Chiral Magnetic Effect* (CME) and is schematically represented in Fig. 1.9. The combination of charge, chirality, magnetic field and local angular momentum - the *vorticity* of the system - has been predicted to determine a rich palette of phenomena analogous to the CME, with similarily sonorous names: *Chiral (Electric) Separation Effect*, *Chiral Vortical Effect*, *Chiral Magnetic Wave*, *Chiral Vortical Wave*, etc. A full description of these goes beyond the scope of this dissertation; we refer the curious reader to the excellent review in [87]. In the following, we will only discuss the theoretical and experimental status of the search for the CME.

While the qualitative picture is clear, the quantitative one is non-existent. This is due to several theoretical uncertainties: local fluctuations of topological density, actual sphaleron rate, theoretical limitations in describing pre-equilibrium dynamics and, as previsouly mentioned, the evolution of the magnetic field [88]. Early estimates of a possible CME signal in heavy-ion collisions differ by orders of magnitude [89, 90]. From an experimental point of view, given the large theoretical uncertainties, it is important to bear in mind the observable, qualitative aspects (and unknowns) of a potential CME signal

- Quarks are separated according to electric charge along the direction of the magnetic field in the early stages of the collision. The collective expansion of the system will then affect those quarks [91], but the separation should partially persist at the hadron level, where it can be measured.

- The number of separated charges equals the chiral imbalance, i.e. the excess of right- or left-handed quarks. The chiral imbalance equals in turn the difference in topological charge of each sphaleron transition. Tentative estimates assign a chiral imbalance of about 1 to 10 for each sphaleron transition [79]. Knowing that in each collision multiple sphaleron transitions can occur with different signs of chiral imbalance [86], the total number of separated charges could vary between 0 and $\mathcal{O}(10)$, based on these general arguments. Note that this is of the order of 10% or less of the final-state multiplicities of a heavy-ion collision at LHC energies [92].

- The correlation between opposite charges due to the CME has a defined structure in azimuthal angle, but is unclear how that depends on rapidity. It is possible that it is of much shorter range than the typical, long-range correlations due to anisotropic flow (see Sec. 3.1). Similarly, the dependence of charge separation on transverse momentum is theoretically unknown.

Given these generic features, we refer to the usual harmonic decomposition of the

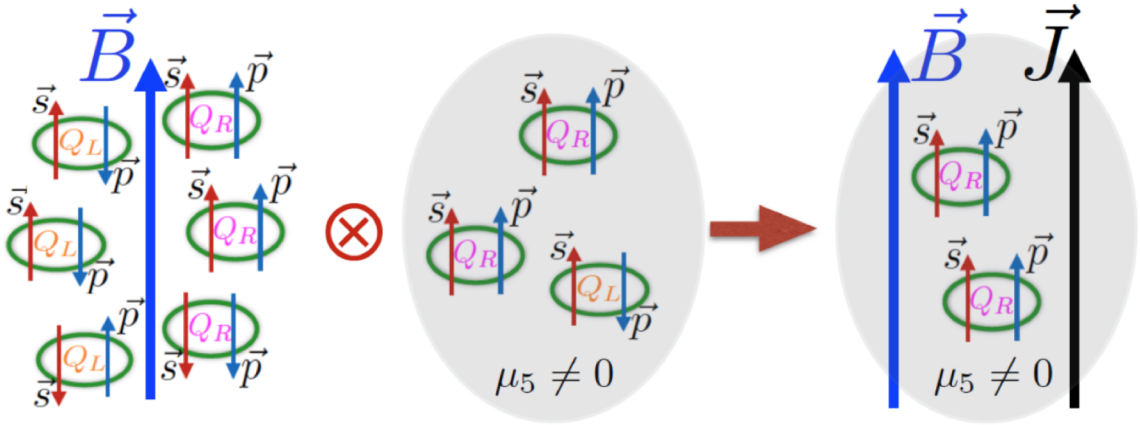

Figure 1.9: Illustration of the Chiral Magnetic Effect, for positive chiral chemical potential μ_5 (more right-handed fermions than left-handed) and for quarks with positive charge. Handedness is represented with (anti-)parallel spins $\vec{s}$ and momenta $\vec{p}$. The charged current $\vec{J}$ flips sign for negative μ_5. Figure from [87].

azimuthal particle distribution to define an observable CME signal a_1 as [93]

$$\frac{\mathrm{d}N}{\mathrm{d}\varphi_\alpha} = 1 + 2\,a_{1,\alpha}\,\sin(\varphi - \Psi_{\mathrm{RP}}) + 2\sum_{n=1}^{+\infty} v_{n,\alpha}\,\cos(n(\varphi - \Psi_n)), \tag{1.8}$$

where $\alpha = \pm$ refers to charge. We now assume the magnetic field to be exactly perpendicular to the reaction plane; in Sec. 6.3 we will see that this is not the case. The simplest observables sensitive to the CME that one can define are the charge-dependent two- and three-particle correlators [93]

$$\delta_{\alpha\beta} = \langle\cos(\varphi_\alpha - \varphi_\beta)\rangle, \tag{1.9}$$
$$\gamma_{\alpha\beta} = \langle\cos(\varphi_\alpha + \varphi_\beta - 2\Psi_{\mathrm{RP}})\rangle, \tag{1.10}$$

where $\alpha, \beta = \pm$ refer again to charge. The potential and limitations of these observables will be extensively discussed in Sec. 6.1. For now, it is sufficient to remark that they unfortunately suffer from a large contribution of background [94, 95, 46, 96, 97] and that we have not been able yet to discriminate such background from a potential signal in a model-independent fashion [87, 88]. The same applies to other observables that have been proposed to study the CME. Therefore, at the time of writing it is still unknown if the CME actually occurs in heavy-ion collisions and there is broad consensus that, if it does, its contribution to known observables is minor. In light of what was discussed before, of the strong connections of the CME with fundamental, unexplored aspects of QCD and, indirectly, with the matter asymmetry problem, we find it a compelling problem to solve for the whole field.

Chapter 2

Experimental Setup

2.1 CERN accelerator complex

The Large Hadron Collider (LHC) is a particle accelerator built at CERN, the European Organization for Nuclear Research, nerby Geneva, Switzerland. It consists of a 27-km-long ring of superconducting magnets, built in an underground tunnel beneath the French-Swiss border. It contains two beam pipes, where particles move in two opposite directions. The LHC is designed to accelerate beams of protons and of lead nuclei Pb^{82+} up to a nominal energy of $\sqrt{s} = 14$ TeV and $\sqrt{s_{NN}} = 5.5$ TeV, respectively. The acceleration of lead ions is achieved in several steps: first, ions are accelerated in the LINAC 3 up to an energy of $\sqrt{s_{NN}} = 50$ MeV, then they are injected in the Low Energy Ion Ring (LEIR), which divides them into bunches of around 2.2×10^8 ions per bunch. The ions then pass in the Proton Synchrotron (PS) and Super Proton Synchrotron (SPS) accelerators, where they reach an energy of about $\sqrt{s_{NN}} = 450$ GeV, and they are finally injected in the LHC, where they reach the nominal energy. Protons start from the LINAC 2, pass through the Proton Synchrotron Booster and the PS, and then follow the same path as the lead ions. A schematic representation of the accelerator complex is shown in Fig. 2.1. The particles collide in four points along the LHC ring, where the beam pipes cross, and at each of these a detector is located: ATLAS [98] and CMS [99], two general purpose detectors, LHCb [100], dedicated to the study of CP violation in B-decays, and ALICE, dedicated to the study of heavy-ion collisions. For a detailed description of the LHC see [101].

2.2 ALICE

ALICE (A Large Ion Collider Experiment) consists of 18 detectors (see Fig. 2.2), designed to measure trajectory, mass, velocity, charge and energy of the particles that transverse them. A detailed overview of the ALICE experiment and its performance can be found in [102, 103, 104, 105]; this section will only describe the detectors directly employed in this dissertation: the Inner Tracking System (ITS), Time Projection Chamber (TPC), V0 system and Zero-Degree Calorimeters (ZDC). What is common to all of these is the coordinate system used: it is right-handed Cartesian, with the x-axis pointing towards the center of the LHC and the z-axis aligned along the beam axis. The particle kinematics are expressed in terms of *transverse momentum* p_{T}, i.e. the magnitude of the

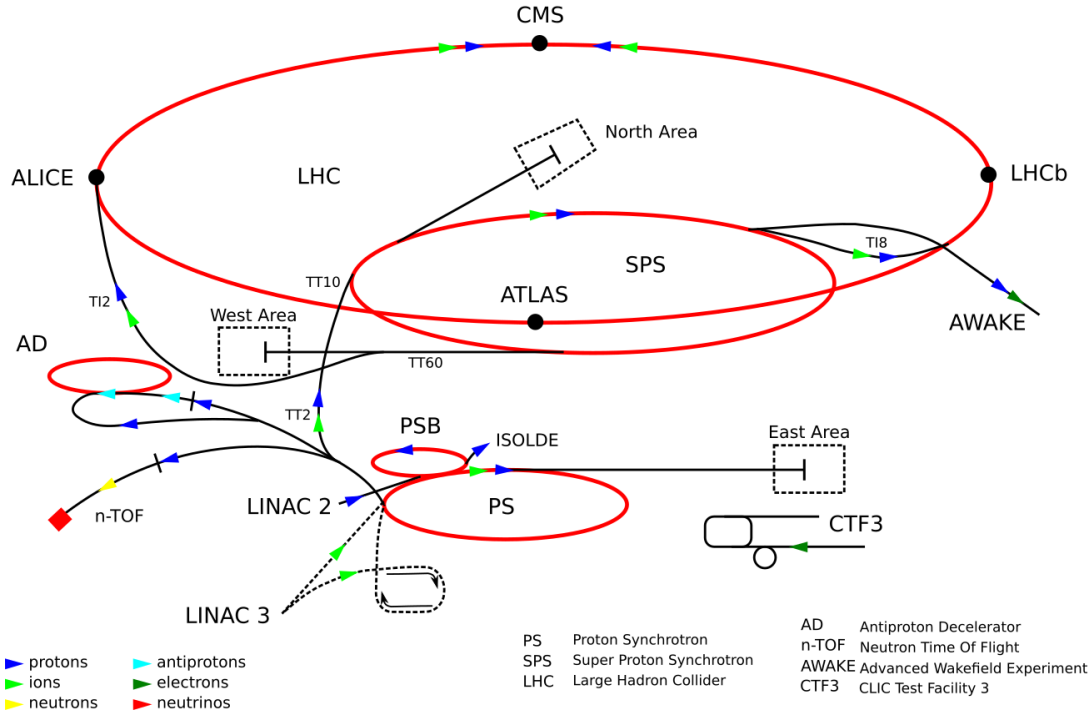

Figure 2.1: Schematic view of the accelerator complex at CERN.

projection of the three-momentum $\vec{p}$ on the x-y plane, *azimuthal angle* φ, in the x-y plane, and *pseudorapidity* η, defined as

$$\eta = -\ln\left(\tan\frac{\theta}{2}\right) = \frac{1}{2}\ln\left(\frac{|\vec{p}| + p_{\mathrm{L}}}{|\vec{p}| - p_{\mathrm{L}}}\right) \tag{2.1}$$

where p_{L} is the z-component of the three-momentum $\vec{p}$ and θ is the *polar angle*, in the y-z plane.

2.2.1 ITS

The ITS [106] (Fig. 2.3, left panel) is the detector located most closely to the beam pipe and in this dissertation is used primarily to reconstruct the primary collision point (*primary vertex*) and the trajectories of charged particles (*tracks*). It constitutes of six concentric cylindrical layers, with a minimum and maximum diameter of 3.9 and 43 cm, respectively. It is a semiconductor detector: charged particle traversing segments of the detector free charges in the doped silicon, which are detected as small ionization currents. Different technologies are used for the different layers, according to the expected track densities: Silicon Pixel Detectors (SPD) for the two innermost layers, Silicon Drift Detectors (SDD) for the middle ones and Silicon Strip Detectors (SSD) for the two outermost ones. The ITS covers full azimuthal angle φ and pseudorapidity region $|\eta| < 0.9$.

2.2.2 TPC

The TPC [107] (Fig. 2.3, right panel) is a cylindrical gas detector placed symmetrically around the nominal interaction point, which is used to reconstruct tracks and identify the particle species. It spans radially from 84.1 cm to 246.6 cm, with a total length of 5 m,

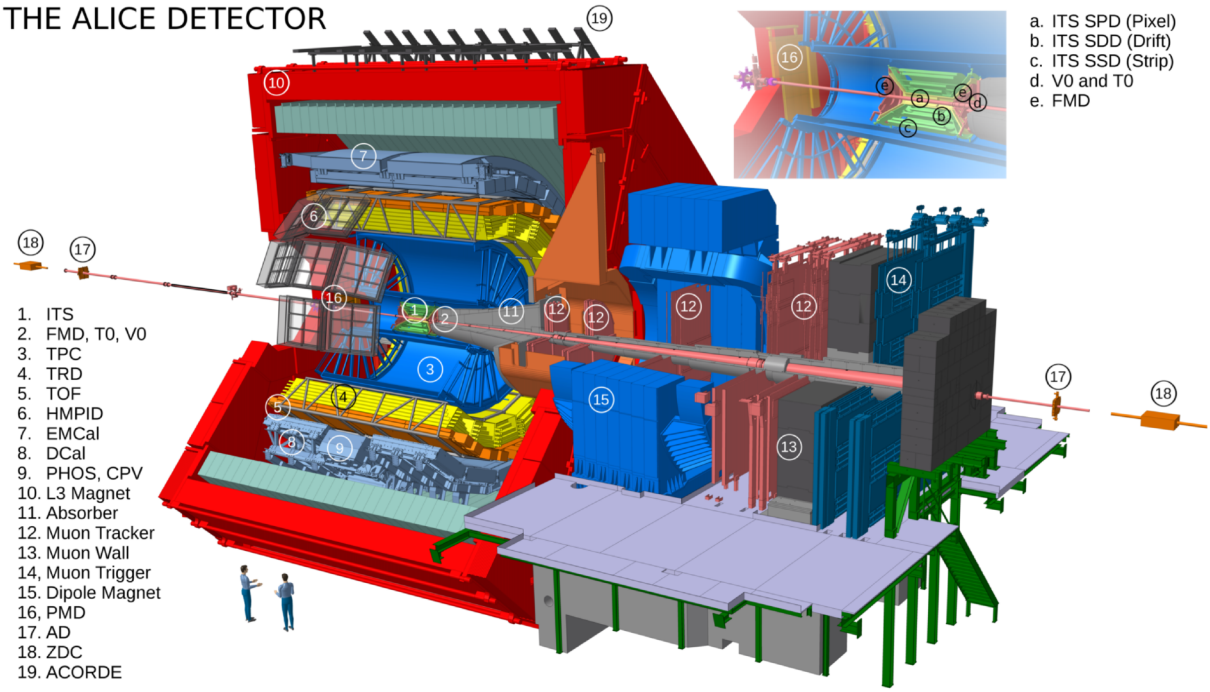

Figure 2.2: Schematic view of the ALICE detector during LHC Run 2 (2015-2018).

covering the full azimuthal angle ϕ and the pseudorapidity region $|\eta| < 0.9$. The gas employed is a mixture of Neon (Argon) and CO_2 (90-10%), for the Run 1 (2) of the LHC. The gas volume is divided in two sections by a central high voltage (100 kV) cathode, which determines an electric field (400 V/cm) aligned with the z-axis and with positive (negative) direction at $\eta > 0$ ($\eta < 0$). When charged particles transverse the gas volume, they ionize the molecules of the gas and the freed electrons drift towards the outer ends of the cylinder, where high-voltage anode wires are located. These determine an avalanche reaction, in which the drifting electrons ionize more gas molecules, before getting absorbed by the wires. The freed ions induce an electric signal, directly proportional to the number of the electrons that triggered the avalanche, on a segmented plane located beneath the wires (*read-out chambers*, ROCs). The radial distance r and azimuthal angle φ of the ionization clusters are therefore measured directly, while the z-direction is calculated from the drift time of the electrons. The number of electrons freed in each ionization process depends on the particle species and momentum, which allow their identification.

2.2.3 V0

The V0 detectors consists of two cylindrical scintillators located at opposite sides of the interaction point, $2.8 < \eta < 5.1$ (V0C) and $-3.7 < \eta < -1.7$ (V0A), see Fig. 2.4, top panel. The scintillating material is BC404 plastic, which emits radiations when charged particles transverse it. This radiation is guided by optical fibres to photo-multipliers tubes, that convert the radiation into a current and amplify it. This current is then read-out as a signal, which is proportional to the number of charged particles traversing the corresponding V0 segment. Each V0 is divide into four concentric rings, with each ring divided in to eight segments (or *cells*), with equal azimuthal width, as shown in Fig. 2.4, bottom panel. The V0 is used for triggering, event centrality determination and event

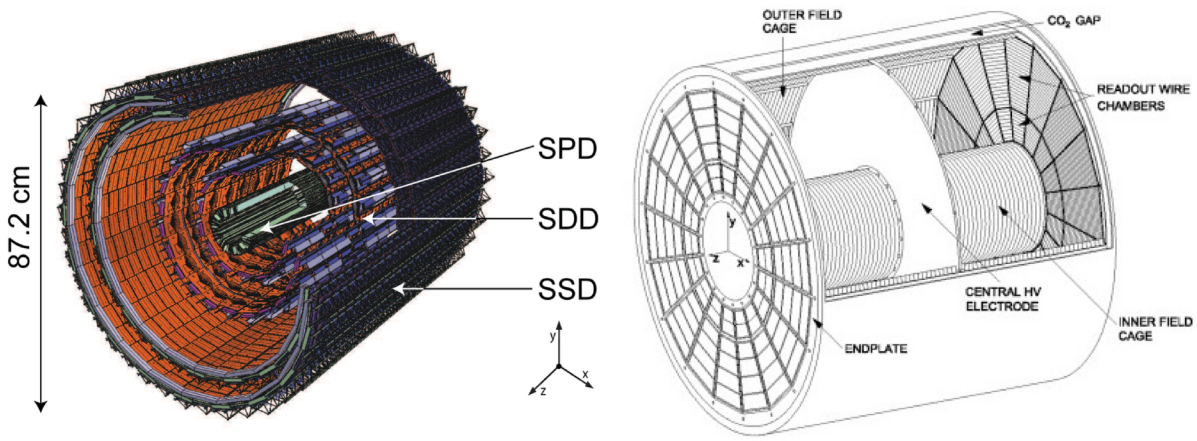

Figure 2.3: Left: design of the ITS detector (figure from [106]). Right: design of the TPC detector (figure from [107]).

plane determination.

2.2.4 ZDC

The ZDC are hadronic calorimiters located at beam rapidities, 116 m from the interaction point, on both sides. They measure the *spectator nucleons*, i.e. the nucleons of the colliding ions that do not take part into the collision and continue moving at beam rapidities, after the ions fragment. It is divided in to a neutron ZDC and a proton ZDC, since the spectator protons are slightly deflected from the beam axis by the magnets near the ALICE experiment (see Fig. 2.5, top panel). In this disseration, only the neutron part of the ZDC is used. The incoming nucleons generate a cascade of particles (*shower*) when colliding with the absorber material of the calorimiters (tantalum). An array of quartz fibres intersects the absorber material - from which the name *spaghetti calorimiter* - and generate Cerenkov light when the shower of particle passes through it. The Cerenkov light is then guided through optical fibres to photomultiplier tubes and read out as signal. The neutron ZDC is a $7 \times 7 \times 100$ cm^3 (in the x- y- and z-directions, respectively) calorimiter and was designed to contain about 80% of the shower [110]. The optical fibres in each neutron ZDC are divided into 5 sets (or *towers*), one covering the entire transverse area (7×7 cm^2) and 4 covering squared transverse segments (3.5×3.5 cm^2 each), see Fig. 2.5, bottom panel. Each set of optical fibres reaches a separate photomultiplier tube, resulting in 5 separate signals. The ZDC are displaced by about ± 1 cm off the beam axis, to account for the 100 μrad/beam crossing angle of the two beams at the interaction point. The ZDC are used for triggering, centrality determination and spectator plane determination.

2.3 Data sample

The data analysed in this dissertation were collected with the ALICE detector during the Run 2 (1) of the LHC in 2015 (2010), at an energy of $\sqrt{s_{\rm NN}} = 5.02$ (2.76) TeV, and consist of a total of 78.4×10^6 (12.6×10^6) minimum-bias collisions, usually referred to as *events*, in the centrality range 0-80%, corresponding to an integrated luminosity of 12.7

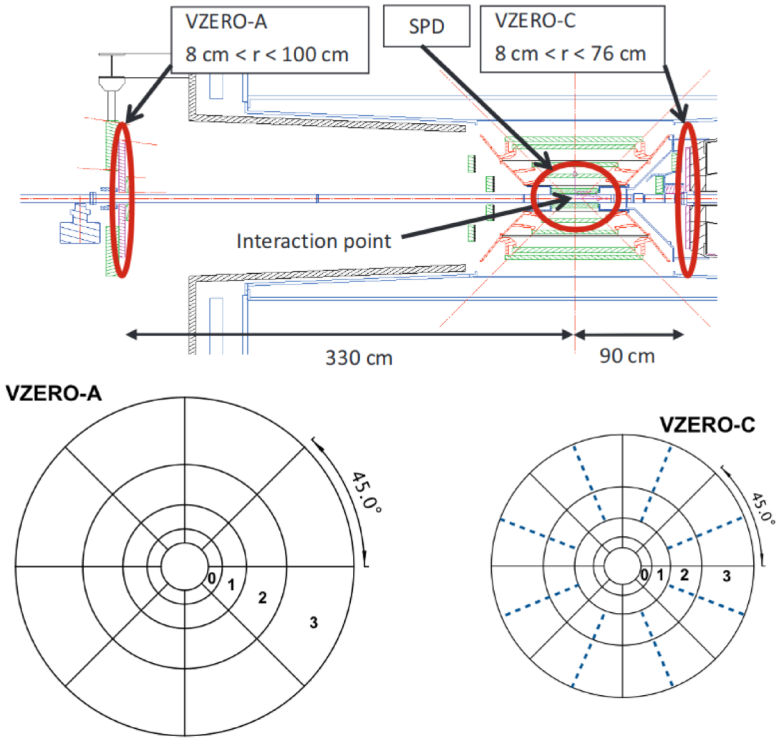

Figure 2.4: Schematic view showing the position (top) and segmentation (bottom) of the VZERO detectors. Figures from [108, 109].

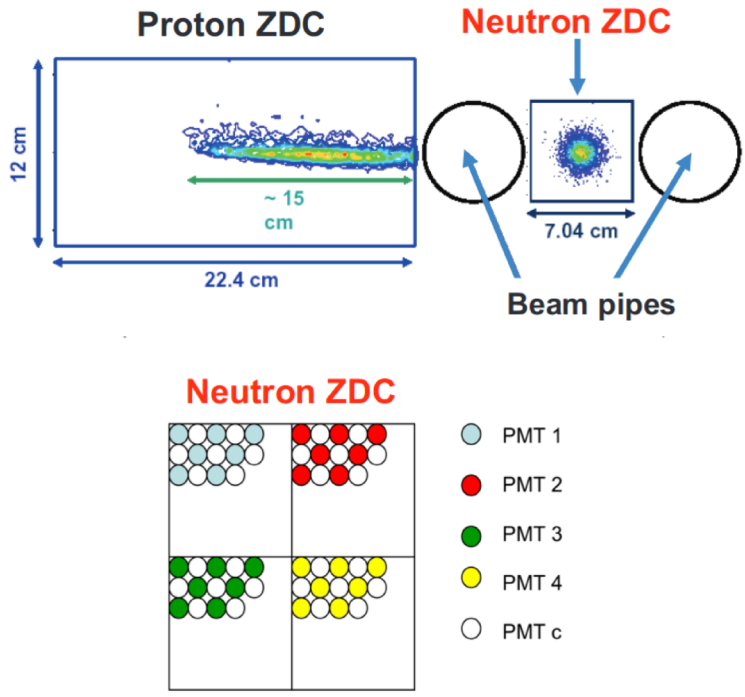

Figure 2.5: Top panel: cross section view (perpendicular to the beam axis) of the ZDC system. Bottom panel: division of the optical fibres in the neutron ZDC (4 segments and 1 common), see text. Figures from [108, 111].

(1.7) μb^{-1}. All events are classified in terms of centrality. Data are divided in *runs*, i.e. periods of continuous data-taking of the ALICE experiment that last up to a few hours[1]. Stops between runs are determined by either dumping of LHC beams, which happens regularly every about 12 hours, or detector requirements (calibration, malfunctioning).

2.3.1 Event selection

A selection of the events recorder in the detectors is needed to disentangle hadronic nucleus-nucleus collisions from, among others, collisions of ions with the beam pipe and electromagnetic processes, which are more frequent. Event selection is usually performed both *online*, discarding non-interesting events while recording them, and *offline*, analysing a recorded data set. Online event selection is based on the simultaneous occurrence (*coincidence*) of determined signals in multiple detectors, which then triggers the recording of the event information from all detectors of interest. This coincidence of signals is therefore called *trigger*. The online trigger conditions used to collect the data sets analysed are

- a minimum signal in the V0C,
- a minimum signal in the V0A,
- two pixel chips hit in the outer layer of the SPD,

with the minimum signal thresholds in both V0 equal to the mean energy deposited by one minimum ionizing particle. The requirements for the run 1 data set ($\sqrt{s_{\rm NN}} = 2.76$ TeV, 2010) were any two out of these three conditions, while for the run 2 data set ($\sqrt{s_{\rm NN}} = 5.02$ TeV, 2015) only the first two, i.e. a minimum signal on both V0. These conditions define the *Minimum Bias* (MB) events, which are thought to comprise the full hadronic cross section. Yet, the recorded minimum-bias data set contains spurious events that need to be removed offline with adequate selection criteria. These spurious events include again a fraction of electromagnetic processes, plus collisions between ions outside of the colliding bunches (*out-of-time pile-up*) and collisions between ions and residual gas molecules in the beam pipe (*beam-gas events*). Moreover, when bunch crosses multiple collisions can take place almost simultaneously (*in-time pile-up*), which are experimentally challenging to reconstruct individually and therefore need to be removed. In order to discriminate against these effects, several selection criteria are applied

- constraints on the time difference between the two V0 detectors,
- primary vertex reconstructed within $|z| < 10$ cm from the nominal interaction point,
- consistency between different centrality estimators (see Sec. 2.3.2),
- consistency between number of charged tracks in $|\eta| < 0.8$ with different track selection criteria (see Sec. 2.3.3).

[1]Not to be confused with "Run" (with capital R), which indicates long operational periods of the LHC spanning 2-3 years

2.3.2 Centrality determination

Centrality quantifies the overlap between the colliding nuclei, in a scale from 0% (head-on collision, full overlap) to 100% (no overlap), where the percentage expresses the fraction of the total nuclear interaction cross section $\sigma_{\rm tot}$. The centrality percentile c of an A-A collision with an impact parameter b is defined theoretically by integrating the impact parameter distribution $\mathrm{d}\sigma/\mathrm{d}b$ as

$$c_{\rm th} = \frac{1}{\sigma_{\rm tot}} \int_0^b \frac{\mathrm{d}\sigma}{\mathrm{d}b'} db'. \tag{2.2}$$

Experimentally, impact parameter is not a measurable quantity and we have to resort to other means. The widespread convention is to define centrality as percentiles of the charged particle multiplicity $N_{\rm ch}$ in a given phase space

$$c_{\rm exp} = \frac{1}{\sigma_{\rm tot}} \int_{N_{\rm ch}^{\rm thr}}^{\infty} \frac{\mathrm{d}\sigma}{\mathrm{d}N_{\rm ch}} dN_{\rm ch} \tag{2.3}$$

and to estimate $\sigma_{\rm tot}$ from the total number of observed events, corrected for the trigger efficiency and determined in a region where the contribution of electromagnetic processes is negligible. The absolute scale is set by the *anchor point*, i.e. the measured $N_{\rm ch}$ equivalent to 90% of the hadronic cross section, which can be derived from a simulated $N_{\rm ch}$ distribution[2] fit to the experimental one. In ALICE we use as default centrality estimator the total signal measured by the V0 detectors, which is a proxy for $N_{\rm ch}$. Alternative estimators include, among others: number of clusters in the SPD (CL1), total signal in the two ZDC. For a detailed description see [112]. Overall, $c_{\rm exp}$ can be reconstructed with a precision of about 0.5% for central and mid-central collisions [112], although its agreement with $c_{\rm th}$ (and therefore b) was estimated to be worse than a few % for central collisions (0-10%) [113].

2.3.3 Track selection

Charged tracks in ALICE are reconstructed from the energy deposition in the various detectors. First, the primary vertex is reconstructed from charged clusters in the two SPD layers of the ITS. The tracks are then constructed via the Kalman filtering algorithm [114], using as a initial seed charged clusters in the outermost part of the TPC, where the spatial separation between trajectories is maximal, and then proceeding inward until the inner radius the TPC. Tracks are then matched to clusters in the outermost layer of the SSD and propagated through the ITS. A second fitting procedure starts from the SPD clusters and proceed outward towards the end of the TPC and further to outer detectors, e.g. TRD or TOF. Tracks can share clusters in both TPC and ITS. For a complete overview see [103, 104, 105]. In this dissertation we use inclusive charged tracks in the kinematic range $|\eta| < 0.8$ and $0.2 < p_{\rm T} < 50$ GeV/c. Two classes of tracks are used: the first one requires one hit per track in the SPD and three hits in total in the ITS, the second one requires no hits in the SPD but uses the primary vertex position as an additional constrain in the fitting procedure, to improve momentum resolution. All tracks are required to have

[2] typically, from Glauber Monte Carlo, in which $N_{\rm ch}$ is a linear function of the number of participant nucleons and number of binary collisions, convoluted with a negative binomial distribution.

at least 70 TPC clusters (out of a maximum of 159) and a χ^2 per TPC cluster χ^2_{TPC} (from the Kalman fit) within $0.1 < \chi^2_{\mathrm{TPC}} < 4$. At the same time, the χ^2 per ITS cluster $\chi^2_{\mathrm{ITS}}$is required to be within $0.1 < \chi^2_{\mathrm{ITS}} < 36$. *Secondary tracks*, i.e. tracks originating from weak decays or from interactions of particles with detector material, are partially rejected requiring a *distance of closest approach* (DCA) to the primary vertex position less than 3.2 cm in the beam direction and 2.4 cm transverse to it. An exact definition of what in the ALICE experiment a *primary track* is can be found in [115]. Overall, these selection criteria ensures a p_{T} resolution better than 5% for the kinematic range used in this dissertation [105]. Reconstruction efficiency and residual secondary contamination will be discussed in Sec. 3.2.

Chapter 3

Analysis Methods

3.1 Flow methods

In Sec. 1.4 we saw that anisotropic flow coefficients quantify correlations in azimuthal angles of final-state particles with *global planes* of interests, which define the geometry of the system. Unfortunately, these global planes are either not measurable (e.g. the reaction plane Ψ_{RP}) or can be measured only with limited precision. Various experimental methods to measure flow were constructed to overcome this issue. They all share one basic idea: if the only observables are final-state particle momenta, we need to use correlations between those to extract information on flow. In fact, if we assume that azimuthal correlations between particle momenta are solely due to correlations between each particle and the event planes Ψ_n, it is easy to see that they provide a direct measurement of flow coefficients

$$\langle\cos(n(\varphi_1-\varphi_2))\rangle = \langle\cos(n(\varphi_1-\Psi_n))\rangle\,\langle\cos(n(\varphi_2-\Psi_n))\rangle = \langle v_n^2\rangle. \tag{3.1}$$

In reality, additional sources of azimuthal correlations need to be taken into account, which are mostly (mini-)jets and resonance decays. Their contribution to 2- or multi-particle azimuthal correlations is usually referred to as *non-flow*. More precisely, non-flow is defined as any few-body short-range correlation which is unrelated to the global planes; "few" is with respect to the total event multiplicity and "short-range" is with respect to the typical separation in $\Delta\eta = |\eta_1 - \eta_2|$ of tracks originating from (mini-)jet fragmentation and resonance decays, which is of about 2 units in Pb–Pb collisions at LHC energies[1] [116]. Note that correlations with the global planes are long-range in nature, i.e. they span over more than 2 units in $\Delta\eta$, since the system itself is highly boosted along the beam direction. Variations of event planes within $2 < |\Delta\eta| < 5$ have been observed to be less than a few % at LHC energies [47].

In this dissertation, we measure anisotropic flow coefficients using the *Q-vector* (also called *flow vector*) formalism [117, 118]. The definition of Q-vector changes according to the type of detector employed. When measuring fully reconstructed tracks, e.g. from ITS

[1] This is estimated from the width in $\Delta\eta$ of the near-side jet-like peak of the $\Delta\eta$-$\Delta\varphi$ correlation function, see reference.

and TPC, with azimuthal angle φ the Q-vector is defined as

$$Q_{n,m} = \sum_{j=1}^{M} w_j^m e^{in\varphi_j}, \tag{3.2}$$

where M is the track multiplicity, n refers to the harmonic and m is the power of the particle weight w_j, which is used to correct for detector effects (see Sec. 3.2). When using detectors with finite granularity, such as the V0 or the ZDC, the Q-vector is constructed by means of a center-of-gravity algorithm, where the azimuthal positions of the different detector segments φ are weighted with the segment signal E [119]:

$$Q_n = \sum_{j=1}^{M} E_j e^{in\varphi_j}. \tag{3.3}$$

We use two methods to compute flow coefficients from Q-vectors: the Q-cumulant method [120], explained in Sec. 3.1.1, and the scalar product method [121], esplained in Sec. 3.1.2. They have three main advantages with respect to other flow methods (for an overview, see [119]):

- they are computationally efficient, permitting to compute correlations on an event-by-event basis with a single pass over the set of tracks [120];
- the correlations have well-defined biases related to detector effects (non-uniform acceptance, finite resolution), which can be corrected for [120, 122];
- the correlations have well-defined sensitivity on flow fluctuations [120, 123].

3.1.1 Multi-particle Q-cumulants

The multi-particle cumulant method [124] allows to measure the different cumulants of the flow p.d.f., while analytically suppressing non-flow contributions order by order: m-particle cumulants are free from any (m-2)-particle non-flow correlations. The sensitivity of each m-particle cumulant $c_n\{m\}$ to different moments of the flow p.d.f. can be seen in the definitions:

$$\begin{aligned}
c_n\{2\} =& \langle\langle 2\rangle\rangle = \langle v_n^2\rangle, && (3.4)\\
c_n\{4\} =& \langle\langle 4\rangle\rangle - 2\langle\langle 2\rangle\rangle^2 = \langle v_n^4\rangle - 2\langle v_n^2\rangle^2, && (3.5)\\
c_n\{6\} =& \langle\langle 6\rangle\rangle - 9\langle\langle 2\rangle\rangle\langle\langle 4\rangle\rangle + 12\langle\langle 2\rangle\rangle^3 \\
=& \langle v_n^6\rangle - 9\langle v_n^2\rangle\langle v_n^4\rangle + 12\langle v_n^2\rangle^3 && (3.6)\\
c_n\{8\} =& \langle\langle 8\rangle\rangle - 16\langle\langle 2\rangle\rangle\langle\langle 6\rangle\rangle - 18\langle\langle 4\rangle\rangle^2 + 144\langle\langle 2\rangle\rangle^2\langle\langle 4\rangle\rangle - 144\langle\langle 2\rangle\rangle^4 \\
=& \langle v_n^8\rangle - 16\langle v_n^2\rangle\langle v_n^6\rangle - 18\langle v_n^4\rangle^2 + 144\langle v_n^2\rangle^2\langle v_n^4\rangle - 144\langle v_n^2\rangle^4, && (3.7)
\end{aligned}$$

where $\langle\langle N\rangle\rangle$ refers to the N-particle correlator

$$\langle N\rangle = \frac{M!}{(M-N)!} \sum_{i_1 \ldots i_N=1}^{M\,\prime} e^{in(\varphi_{i_1} + \ldots \varphi_{i_{N/2}} - \varphi_{i_{N/2+1}} - \ldots \varphi_{i_N})}. \tag{3.8}$$

The prime in the sum ($\sum'$) indicates that all indices must be taken different. Double brackets denote an average first over all M particles in a given event and then over all events. Different order cumulants provide independent estimates for the flow harmonics v_n. In particular we define

$$v_n\{2\} = \sqrt[2]{c_n\{2\}}, \tag{3.9}$$

$$v_n\{4\} = \sqrt[4]{-c_n\{4\}}, \tag{3.10}$$

$$v_n\{6\} = \sqrt[6]{\frac{1}{4}c_n\{6\}}, \tag{3.11}$$

$$v_n\{8\} = \sqrt[8]{-\frac{1}{33}c_n\{8\}}. \tag{3.12}$$

Correlators can be constructed directly from Q-vectors following the prescriptions of [120], from which the name *Q-cumulants*. Here, we report for conciseness only the equations for $\langle\langle 2\rangle\rangle$ and $\langle\langle 4\rangle\rangle$

$$\langle 2\rangle = \frac{1}{M_{11}}\sum_{i,j=1}^{M}{}' w_i\, w_j\, e^{in(\varphi_i-\varphi_j)} = \frac{|Q_{n,1}|^2 - S_{1,2}}{S_{2,1} - S_{1,2}} \tag{3.13}$$

$$\langle\langle 2\rangle\rangle = \frac{\sum_{k=1}^{N}(M_{11})_k\,\langle 2\rangle_k}{\sum_{k=1}^{N}(M_{11})_k}, \tag{3.14}$$

$$\begin{aligned}\langle 4\rangle &= \frac{1}{M_{1111}}\sum_{i,j,k,l=1}^{M}{}' w_i\, w_j\, w_k\, w_l\, e^{in(\varphi_i+\varphi_j-\varphi_k-\varphi_l)} \\ &= \left(|Q_{n,1}|^4 + |Q_{2n,2}|^2 - 2\,\mathrm{Re}\left[Q_{2n,2}\,Q^*_{n,1}\,Q^*_{n,1}\right]\right. \\ &\quad + 8\,\mathrm{Re}\left[Q_{n,3}\,Q^*_{n,1}\right] - 4\,S_{1,2}\,|Q_{n,1}|^2 - 6\,S_{1,4} - 2\,S_{2,2}\Big) \\ &\quad / \left(S_{4,1} - 6\,S_{1,2}\,S_{2,1} + 8\,S_{1,3}\,S_{1,1} + 3\,S_{2,2} - 6\,S_{1,4}\right),\end{aligned} \tag{3.15}$$

$$\langle\langle 4\rangle\rangle = \frac{\sum_{k=1}^{N}(M_{1111})_k\,\langle 4\rangle_k}{\sum_{k=1}^{N}(M_{1111})_k}. \tag{3.16}$$

where

$$M_{abcd\ldots} = \sum_{i,j,k,l,\ldots=1}^{M}{}' w_i^a\, w_j^b\, w_k^c\, w_l^d \ldots \tag{3.17}$$

$$S_{p,k} = \left[\sum_{i=1}^{M} w_i^k\right]^p. \tag{3.18}$$

The event weights $M_{abcd\ldots}$ are used to minimize the effect of multiplicity variations in the event sample and quantify the number of different m-particle combinations in an event with multiplicity M. Equations for higher order correlators ($\langle\langle\langle 6\rangle\rangle\rangle$, $\langle\langle 8\rangle\rangle, \ldots$) can be analytically derived, but this is unpractical because of the large number of terms involved. It is more convenient to compute them with the Generic Framework algorithms [122], which permit to automatize the process without any loss of precision or generality. This is what we used in this dissertation.

It is also possible to define so-called *differential* or *reduced* m-particle Q-cumulants, in which one correlates 1 particle of interest, denoted with a prime ($'$), with m-1 other particles. The 2- and 4-particle differential Q-cumulant read

$$d_n\{2\} = \langle\langle 2' \rangle\rangle = \langle v'_n v_n \rangle, \tag{3.19}$$

$$d_n\{4\} = \langle\langle 4' \rangle\rangle - 2\langle\langle 2' \rangle\rangle\langle\langle 2 \rangle\rangle = \langle v'_n v_n^3 \rangle - 2\langle v'_n v_n \rangle \langle v_n^2 \rangle \tag{3.20}$$

and the corresponding differential flow estimates

$$v'_n\{2\} = \frac{d_n\{2\}}{\sqrt{c_n\{2\}}}, \tag{3.21}$$

$$v'_n\{4\} = -\frac{d_n\{4\}}{\sqrt[4]{-c_n\{4\}^3}}. \tag{3.22}$$

The equations to compute the differential 2- and 4-particle correlator ($\langle\langle 2' \rangle\rangle$, $\langle\langle 4' \rangle\rangle$) from Q-vectors can be found in [120]. In this dissertation, we use differential Q-cumulants to measure the p_{T} dependence of v_n, correlating one particle at a given p_{T} with all other measured particles, which are in the range $0.2 < p_{\mathrm{T}} < 50$ GeV/c. In the context of differential cumulants, the names *Particles Of Interest* (POIs) and *Reference Particles* (RPs) are typically used to denote the former and the latter set, respectively.

3.1.2 Scalar product method

The scalar product method [121] is used to compute 2-particle correlators between fully reconstructed tracks and event planes estimated with detectors at forward rapidities (V0, ZDC). In terms of sensitivity to moments of the flow p.d.f., it is analogous to the 2-particle cumulant defined in Eq. 3.4. In this case, non-flow is suppressed by the large interval in η that separates tracks at mid-rapidity ($|\eta| < 0.8$) and the forward detectors. Given Q_n^{V0A} and Q_n^{V0C} (see Sec. 3.3) we measure anisotropic flow coefficients v_n as [125]

$$v_n\{2, |\Delta\eta| > 2\} = \frac{\langle u_{n,0} Q_n^{\mathrm{V0A}*} \rangle}{\sqrt{\frac{\langle Q_n^{\mathrm{V0A}} Q_{n,1}^* \rangle \langle Q_n^{\mathrm{V0A}} Q_n^{\mathrm{V0C}*} \rangle}{\langle Q_{n,1} Q_n^{\mathrm{V0C}*} \rangle}}}, \tag{3.23}$$

where $u_{n,0} = e^{in\varphi}$ is the unit Q-vector from charged particle tracks at mid-rapidity and $Q_{n,1}$ is computed from the same type of tracks according to Eq. 3.2. The term at the denominator quantifies the finite resolution on Q_n^{V0A}. Because of the finite segmentation of the V0 (eight segments in φ), it is possible to reliably measure only up to the fourth harmonic with this method; for a general discussion of this problem see [122].

The scalar product method is also used to measure directed flow v_1 with respect to the neutron spectator plane Ψ_{SP}, as reconstructed by the ZDC. The corresponding equations are very similar and will be discussed in more detail in Sec. 7.1.

3.2 Efficiency and acceptance corrections

Corrections for non-uniformities in efficiency and acceptance of charged tracks are performed via track weights w_j in the Q-vector construction, as defined in Eq. 3.2. In particular, weights can be factorized in a p_{T}-dependent efficiency and contamination part

(w_j^{eff}), which is computed by means of Monte Carlo simulations, and an acceptance part (w_j^{acc}), which is derived in a data-driven fashion

$$w_j = w_j^{\text{eff}}(p_{\text{T}}, \text{cen})\, w_j^{\text{acc}}(\eta, \varphi, v_z, \text{cen}, \text{run}) \tag{3.24}$$

where v_z is the z-position of the reconstructed primary vertex, while "cen" and "run" indicate centrality percentile and run number, respectively. p_{T}-dependent non-uniform efficiency is in general due to the tracking procedure itself: very low-p_{T} tracks, for instance, are strongly bended by the magnetic field and do not cross the TPC in its full length, resulting in a smaller number of TPC clusters and therefore lower momentum resolution (see Sec. 2.3.3). Absorption in the detector material and secondary interactions contribute as well. These effects can be studied via a Monte Carlo simulation. First, a collision is simulated with random sampling of relevant physical variables (e.g. impact parameter), together with possible particle interactions and decays: this is performed by so-called *event generators*, that encode specific microscopic physics. In this dissertation, we use HIJING [126] (*Heavy-Ion Jet Interaction Generator*), which does not simulate final-state collective effects but has a pQCD-based jet production description and uses the Lund string model [127] for hadronization. Tracks generated by HIJING are then propagated through the detectors and their interaction with the material is simulated with GEANT3 [128]. The full detector geometry and conditions are included at this stage. We can then compute the efficiency ε as

$$\varepsilon(p_{\text{T}}) = \frac{N_{\text{rec}}(p_{\text{T}})}{N_{\text{gen}}(p_{\text{T}})}, \tag{3.25}$$

where N_{gen} and N_{rec} are the number of particles at the event generator level and after reconstruction, respectively. The contamination λ quantifies the fraction of secondary particles, i.e. particles from weak decays or from interactions with the detectors, and is defined as

$$\lambda(p_{\text{T}}) = \frac{N_{\text{sec}}(p_{\text{T}})}{N_{\text{tot}}(p_{\text{T}})}, \tag{3.26}$$

where N_{sec} and N_{tot} are the number of secondary particles and total particles (secondaries and primaries), respectively, after reconstruction. Efficiency and contamination as a function of p_{T} in several centrality intervals are shown in Fig. 3.1 for the default choice of track selection criteria used in this dissertation and collision energy $\sqrt{s_{\text{NN}}} = 5.02$ TeV. Results at $\sqrt{s_{\text{NN}}} = 2.76$ TeV change by less than a few %. For $p_{\text{T}} > 20$ GeV/c, where Monte Carlo data suffer from large statistical uncertainties, the values of ε and λ at $p_{\text{T}} = 20$ GeV/c are used. The total efficiency and contamination correction $w_j^{\text{eff}}(p_{\text{T}})$ is computed according to

$$w_j^{\text{eff}}(p_{\text{T}}) = \frac{1 - \lambda(p_{\text{T}})}{\varepsilon(p_{\text{T}})}, \tag{3.27}$$

separately in the centrality classes shown in Fig. 3.1: 0-5%, 5-10%, 10-20%, ... 70-80%. The factorization used in Eq. 3.24 is tested looking at the (η, φ)-dependence of $\varepsilon(p_{\text{T}})$. Overall, differences are observed to be within 2%.

The acceptance correction w_j^{acc} is computed from real data as a function of η and φ, separately for each run number, centrality interval and v_z (with 10 intervals in the range

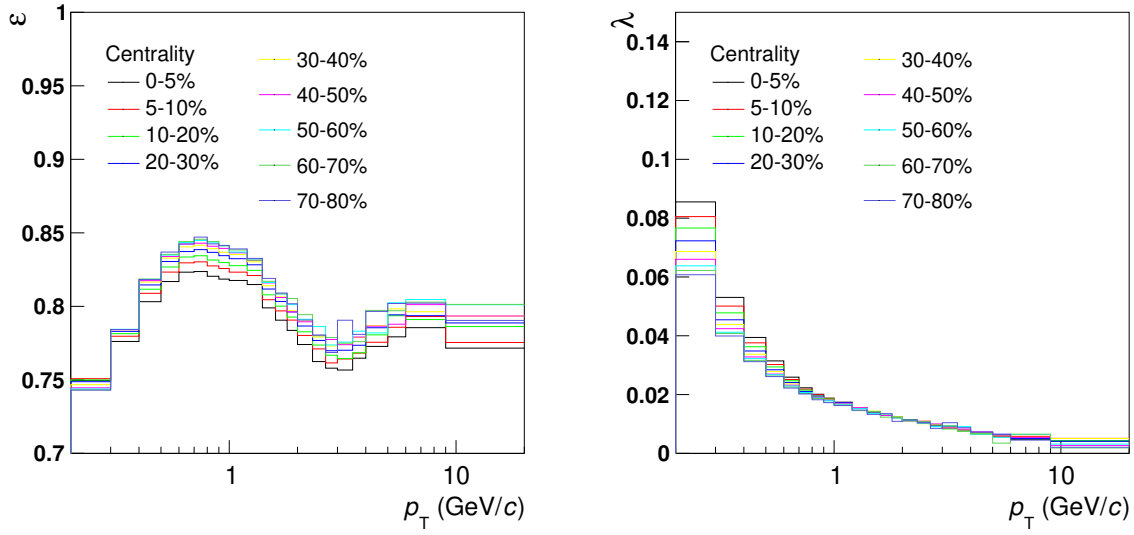

Figure 3.1: Efficiency (left) and contamination (right), as defined in Eq. 3.25 and 3.26 respectively, in several centrality bins, for Pb–Pb collisions at $\sqrt{s_{\mathrm{NN}}} = 5.02$ TeV.

employed, $|v_z| < 10$ cm). It is defined as

$$w_j^{\mathrm{acc}}(\eta, \varphi) = \frac{\langle \mathrm{d}N(\eta, \varphi)/\mathrm{d}\eta\mathrm{d}\varphi \rangle_\varphi}{\mathrm{d}N(\eta, \varphi)/\mathrm{d}\eta\mathrm{d}\varphi}, \tag{3.28}$$

where the average track density $\langle \mathrm{d}N(\eta, \varphi)/\mathrm{d}\eta\mathrm{d}\varphi \rangle_\varphi$ is computed over $0 < \varphi < 2\pi$ in each interval of η. The variations in $w_j^{\mathrm{acc}}(\eta, \varphi)$ between runs and centrality intervals are observed to be generally small ($< 5\%$), while those in v_z can be important, especially at the edges of the detector acceptance: $-0.8 < \eta < -0.6$ and $0.6 < \eta < 0.8$. An example of $\mathrm{d}N(\eta, \varphi)/\mathrm{d}\eta\mathrm{d}\varphi$, normalized by the number of events, with and without the correction factors $w_j^{\mathrm{acc}}(\eta, \varphi)$, is shown in Fig. 3.2, respectively, in different intervals of v_z.

3.3 V0 calibration

The Q-vector from the V0 system, described in Sec. 2.2.3, is defined as

$$Q_n^{\mathrm{V0C,\ V0A}} = \sum_{j=1}^{32} E_j e^{in\varphi_j}, \tag{3.29}$$

where E_j is the signal amplitude in each V0 cell. The cell azimuthal positions φ_j are given by

$$\varphi_j = \frac{\pi}{4}\left(\frac{1}{2} + j\%8\right), \tag{3.30}$$

where $j\%8$ is the remainder of the Euclidean division of j by 8. In order to ensure a uniform azimuthal response of the detector, the V0 system needs to be calibrated. This is performed in two sequential steps: gain equalization and re-centring.

Gain equalization consists in ensuring that all cells within one V0 have equal average signal. In fact, the average track multiplicity in each cell is expected to be roughly the

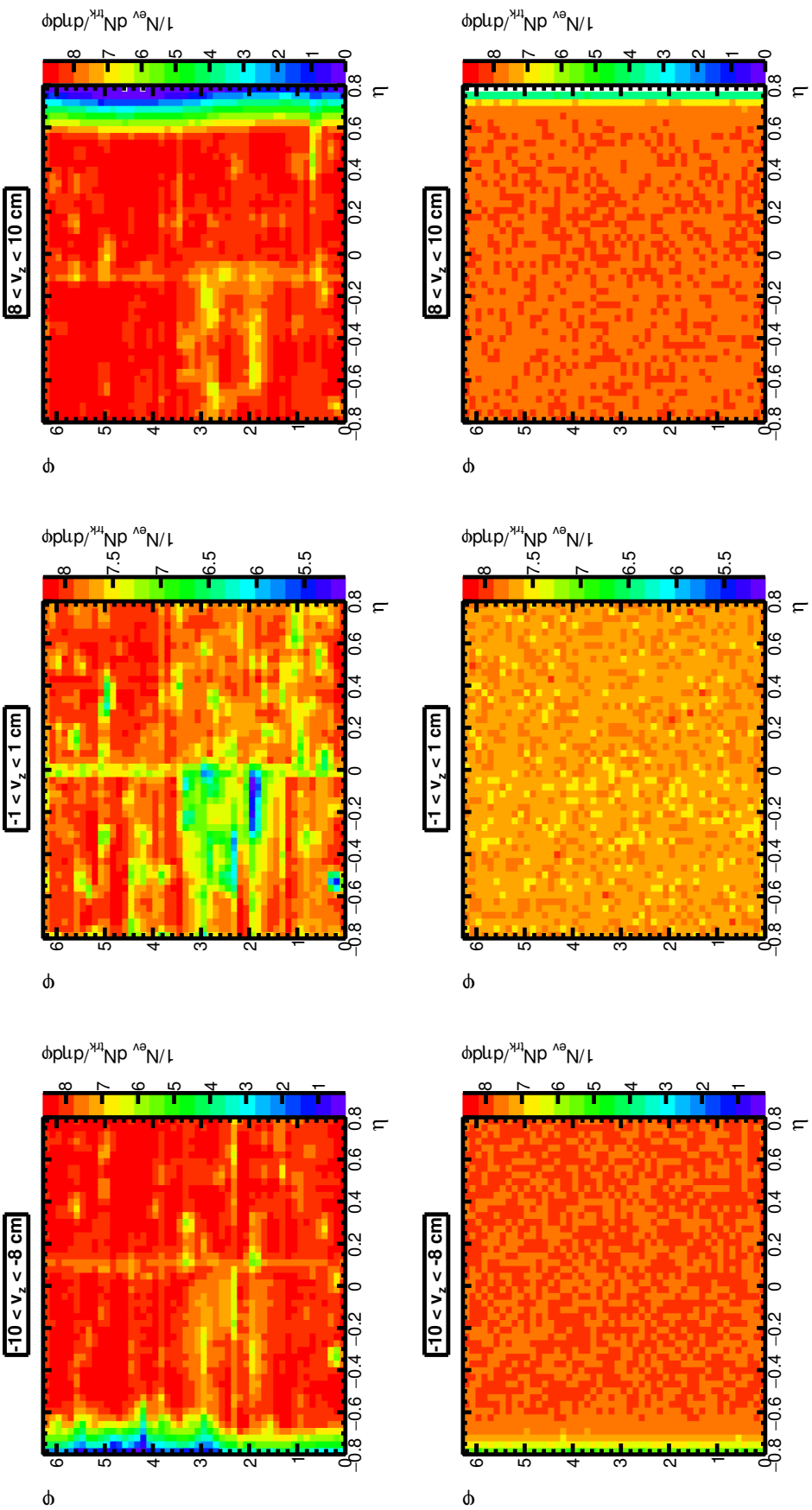

Figure 3.2: Charged track density distributions $\mathrm{d}N(\eta,\varphi)/\mathrm{d}\eta\mathrm{d}\varphi$, normalized by the number of events, without (top panels) and with (bottom) the correction factors $w_j^{\mathrm{acc}}(\eta,\varphi)$, in different intervals of v_z.

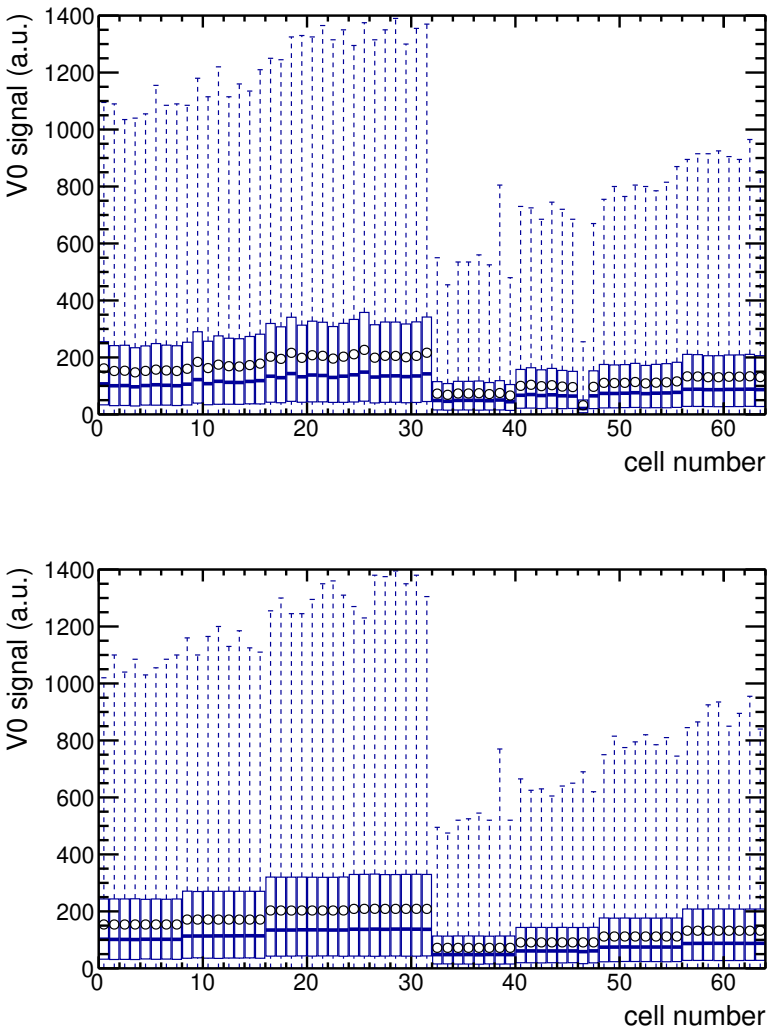

Figure 3.3: Boxplots of the distributions of the signal amplitudes from the V0 cells, before (top) and after (bottom) gain equalization. Run number 246087, centrality range 0-80%.

same and differences in the response are expected to arise only from detector inefficiencies or mis-calibration. First, we store the signal distribution for each cell j and we compute its average $\langle E_j \rangle$. Then, in a second pass over the data, we correct the cell signal as

$$E'_j = E_j \, \frac{\xi}{\langle E_j \rangle}, \tag{3.31}$$

where ξ is the average signal across each ring of each V0. This is performed separately for each run, to compensate for time-dependent variations of the detector response. Figure 3.3 shows the signal distributions in each V0 cell before (top panel) and after (bottom panel) gain equalization. The cell numbering is 1 to 32 for V0C and 33 to 64 for V0A. A uniform average response across all cells of each ring is achieved at this stage.

The second step is re-centring, which ensures that the distribution of Q_n^{V0C} and Q_n^{V0A} is isotropic in azimuthal angle. We first store separately the distributions of the real and

imaginary component of the two Q-vectors, also referred to x- and y-component, and we compute their mean $\langle Q_{n,x}^{\mathrm{V0k}} \rangle$, $\langle Q_{n,y}^{\mathrm{V0k}} \rangle$ and standard deviation $\sigma_{n,x}^{\mathrm{V0k}}$, $\sigma_{n,y}^{\mathrm{V0k}}$, where k=A,C. Then, in a second pass over the data, we correct the Q-vectors as

$$Q_{n,j}^{\mathrm{V0k'}} = \frac{Q_{n,j}^{\mathrm{V0k}} - \langle Q_{n,j}^{\mathrm{V0k}} \rangle}{\sigma_{n,j}^{\mathrm{V0k}}}. \tag{3.32}$$

The re-centring procedure is applied separately for each run, each 1 cm interval of reconstructed primary vertex z-position (v_z) and each centrality interval of 1% width (0-1%, 1-2%, ...), where centrality is measured by means of a non-V0 based estimator (CL1, see Sec. 2.3.2) to avoid any correlation between Q-vector calibration, centrality determination and trigger. Figure 3.4 shows an example of the Q-vector distributions before (top panels) and after (bottom panels) re-centring, as a function of centrality, for the second and third harmonic.

3.4 ZDC calibration

For the ZDC detectors, described in Sec. 2.2.4, the Q-vector is defined as

$$Q^{\mathrm{ZNA,\ ZNC}} = \frac{\sum_{j=1}^{4} E_j^{\alpha}\, r_j\, e^{i\varphi_j}}{\sum_{j=1}^{4} E_j^{\alpha}}, \tag{3.33}$$

where E_j is the total energy deposited in the j-th tower of the calorimiters, r_j and φ_j the position and azimuthal angle of its center with respect to the beam axis ($x = \pm 1.75$ cm, $y = \pm 1.75$ cm, $\varphi_j = \pi/4,\ 3\pi/4,\ 5\pi/4,\ 7\pi/4$), respectively. The parameter α compensates for saturation effects in case of high energy depositions in the towers and is set to $\alpha = 0.395$, according to previous Monte Carlo studies [111]. Note that in this case we drop the subscript n in the Q-vector notation, since we only measure the first harmonic ($n = 1$).

The calibration of the ZDC Q-vectors, which is needed to correct for detector misalignment and non-uniform azimuthal response, is similar to the VZERO ones and is performed in two sequential steps: gain equalization and re-centring.

Gain equalization is first applied on the 4 towers of each ZN, storing the signal distribution for each tower j, computing its average $\langle E_j \rangle$ and then, in a second pass over the data, correcting the tower signal as

$$E_j' = E_j\, \frac{\xi}{\langle E_j \rangle}. \tag{3.34}$$

in this case, the correction factor ξ is chosen equal to 1/4 of the average signal in the common tower $\langle E_{\mathrm{com}} \rangle$, separately for ZNA and ZNC. The averages are computed in intervals of centrality and run number, to compensate for time-dependent variations of the detector response. A further correction procedure is required at the level of E_j for a large fraction of the 2015 data set (Pb–Pb collisions at $\sqrt{s_{\mathrm{NN}}} = 5.02$ TeV), since one tower (#2) of the ZNA was malfunctioning (the photomultiplier tube stopped working). We use the signal in the common channel to reconstruct the missing information. After gain equalization, the signal in the second tower is measured as

$$E_2 = E_{\mathrm{com}} - E_1 - E_3 - E_4. \tag{3.35}$$

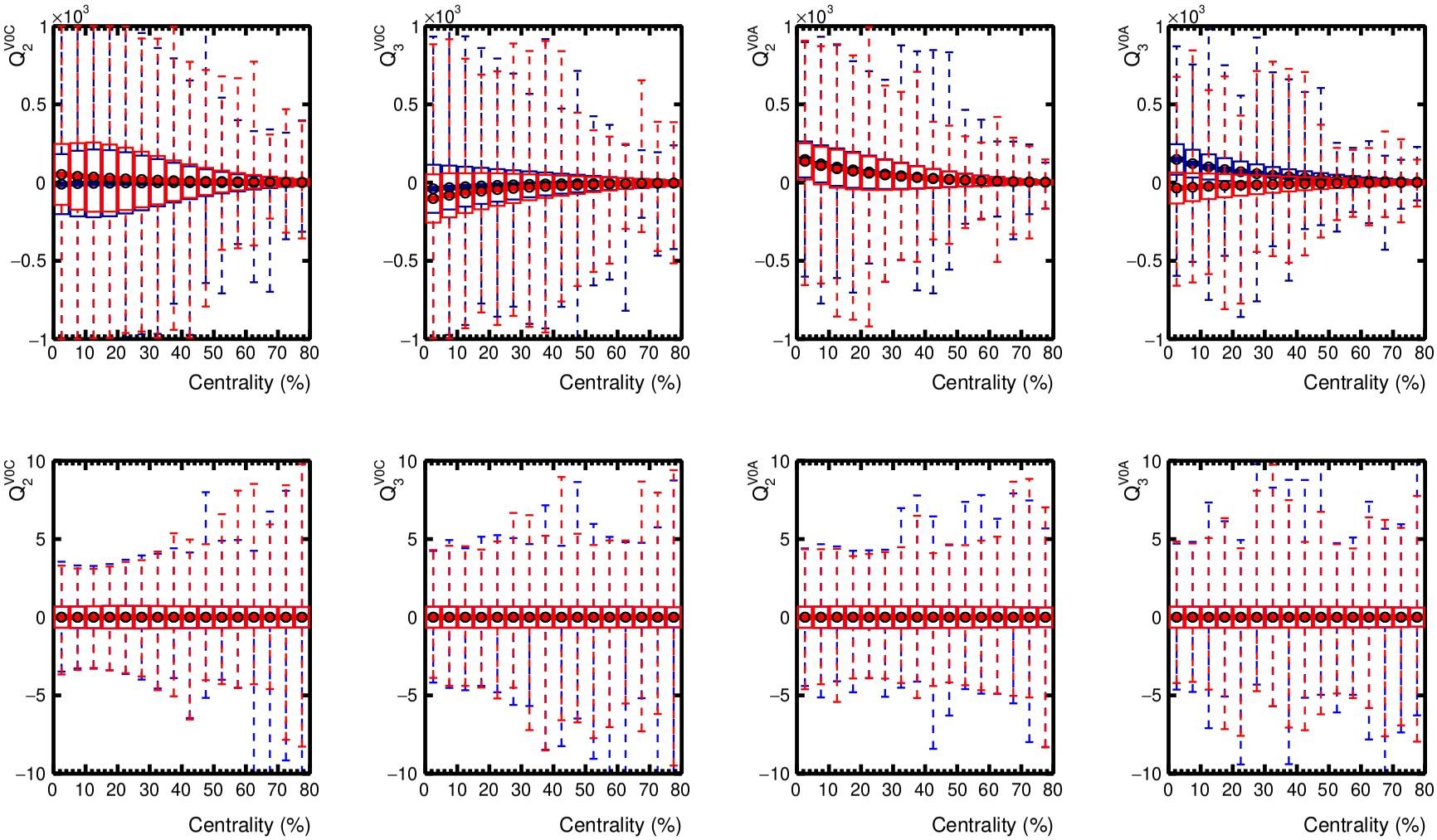

Figure 3.4: Boxplots of the $Q_{n,x}$ (red) and $Q_{n,y}$ (blue) distributions from V0A and V0C as a function of centrality, before (top) and after (bottom) the calibration procedure. Run number 246087.

An example of the signal distributions from the various ZDC towers are reported in fig.3.5, before (top) and after (bottom) gain equalization. The tower numbering is 1 to 5 for ZNC and 6 to 10 for ZNA, with the first one of each (1 and 6, respectively) being the common tower.

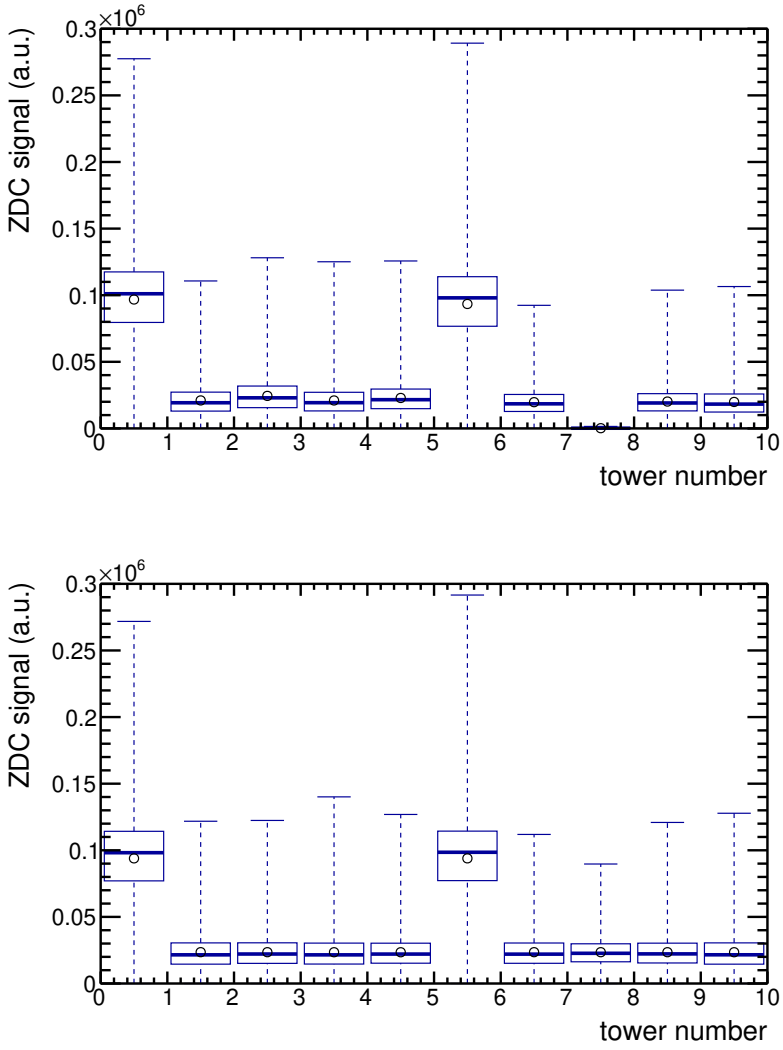

Figure 3.5: Boxplots of the distributions of the signal amplitudes from the ZDC towers, before (top) and after (bottom) gain equalization. Run number 246087, centrality range 0-80%.

The ZDC Q-vector re-centring is then performed, similarly to what is done with the VZERO, subtracting the average components $\langle Q_x^{\mathrm{ZNk}} \rangle$, $\langle Q_y^{\mathrm{ZNk}} \rangle$ (k=A,C) of the different Q-vectors:

$$Q_j^{\mathrm{ZNk}'} = Q_j^{\mathrm{ZNk}} - \langle Q_j^{\mathrm{ZNk}} \rangle. \tag{3.36}$$

In the case of the ZDC, a strong dependence of all components Q_j^{ZNk} on centrality, run number and all primary vertex coordinates (v_x, v_y, v_z) is observed, with some degree of correlation between all of these. This is due to the peculiar position of the ZDC:

a deviation in the polar beam crossing angle of ± 1 μrad results in a displacement of the centroid position of about 7 mm at the ZDC surface, which is sizeable compared to both the tower transverse size (3.5 cm) and the physical deflection of the spectator neutrons between the A- and C-side. While it is necessary to correct for all event variables simultaneously, the limited amount of data at our disposal requires to do approximations. In fact, it is impossible to compute statistically meaningful averages of Q_j^{ZNk} dividing the data set in a 5-dimensional event variable space.

The chosen solution consists in decomposing the correction procedure in 3 consecutive steps:

1. re-center as a function of centrality (1% intervals) and run number.
2. re-center as a function of centrality (10% intervals) and v_x, v_y, v_z.
3. re-center as a function of run number and v_x, v_y, v_z.

Given the run-dependent variations of $\langle v_x \rangle$, $\langle v_y \rangle$, $\langle v_z \rangle$, the primary vertex position is centred around 0 in each run before step 2:

$$v_i \rightarrow v_i - \langle v_i \rangle_{\mathrm{run}}.$$

The resulting average Q-vector components, after the re-centring procedure, are indeed consistent with 0 as a function of centrality, run number and primary vertex position, as shown in Fig.3.6. Correlations with respect to multiple event variables are also observed to be corrected for; an example of $Q_j^{\mathrm{ZNk}}(v_x, v_y)$ before and after the re-centring procedure is shown in Fig.3.7.

Once detectors effects are properly corrected for, the azimuthal position of the ZDC centroids is expected to be determined only by the deflection of the spectator neutrons, which is opposite between the A- and C-side. This would result in the centroid positions to be anti-correlated in azimuthal angle: $\langle \cos(\Psi_{\mathrm{SP}}^{\mathrm{A}} - \Psi_{\mathrm{SP}}^{\mathrm{C}}) \rangle < 0$, i.e. in terms of Q-vector cross-terms $\langle Q_y^{\mathrm{ZNC}} Q_y^{\mathrm{ZNA}} \rangle = \langle Q_x^{\mathrm{ZNC}} Q_x^{\mathrm{ZNA}} \rangle < 0$ and $\langle Q_y^{\mathrm{ZNC}} Q_x^{\mathrm{ZNA}} \rangle = \langle Q_x^{\mathrm{ZNC}} Q_y^{\mathrm{ZNA}} \rangle = 0$. Deviations from the expected behaviour are still observed in the average Q-vector cross-terms after the calibration procedure has been applied, which become important for more peripheral collisions. These deviations provide a quantification of spurious azimuthal correlations due to detector effects. We attribute them to space-momentum correlations between the Pb ions in the two colliding bunches, which can arise from correlated fluctuations in the beam crossing angle. We are not able to neither prove this interpretation nor correct for the expected bias, as neither the spectator deflection nor the beam correlations can be precisely simulated via Monte Carlo simulations, which cannot therefore be used to deconvolute the two effects. However, we also note that within a limited centrality range (5-40%), which is used for the results presented in this dissertation, the residual detector effects are small: $\langle Q_y^{\mathrm{ZNC}} Q_y^{\mathrm{ZNA}} \rangle \approx \langle Q_x^{\mathrm{ZNC}} Q_x^{\mathrm{ZNA}} \rangle$ up to a few % and $\langle Q_y^{\mathrm{ZNC}} Q_x^{\mathrm{ZNA}} \rangle, \langle Q_x^{\mathrm{ZNC}} Q_y^{\mathrm{ZNA}} \rangle \ll \langle Q_y^{\mathrm{ZNC}} Q_y^{\mathrm{ZNA}} \rangle = \langle Q_x^{\mathrm{ZNC}} Q_x^{\mathrm{ZNA}} \rangle$.

3.5 Systematic uncertainties

The systematic uncertainties on the measurements presented in this dissertation are evaluated as following, unless otherwise stated. For each possible source of systematic

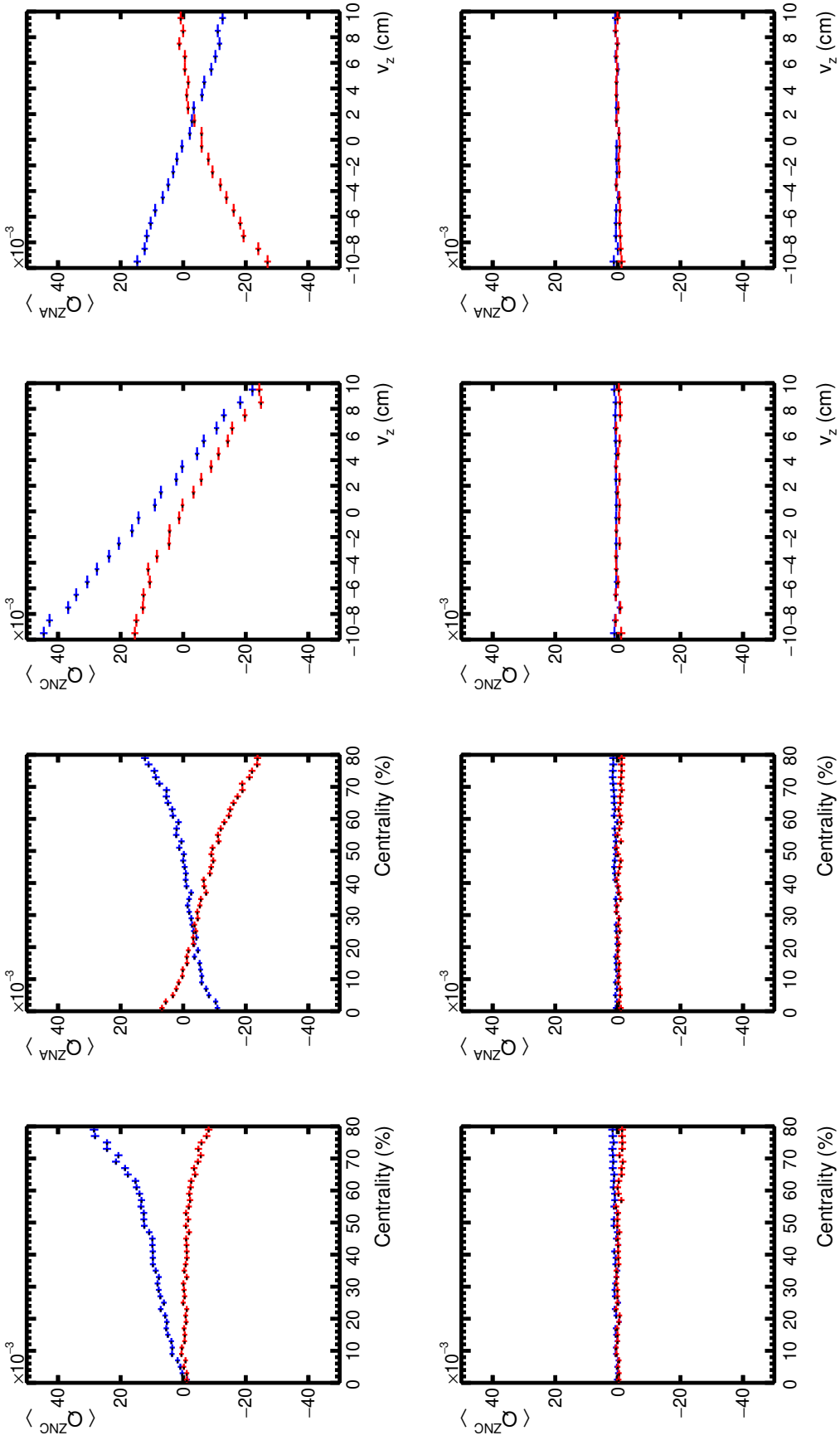

Figure 3.6: $\langle Q_{n,x} \rangle$ (red) and $\langle Q_{n,y} \rangle$ (blue) from ZNA and ZNC as a function of centrality (left) and v_z (right), before (top) and after (bottom) the calibration procedure. Run number 246087.

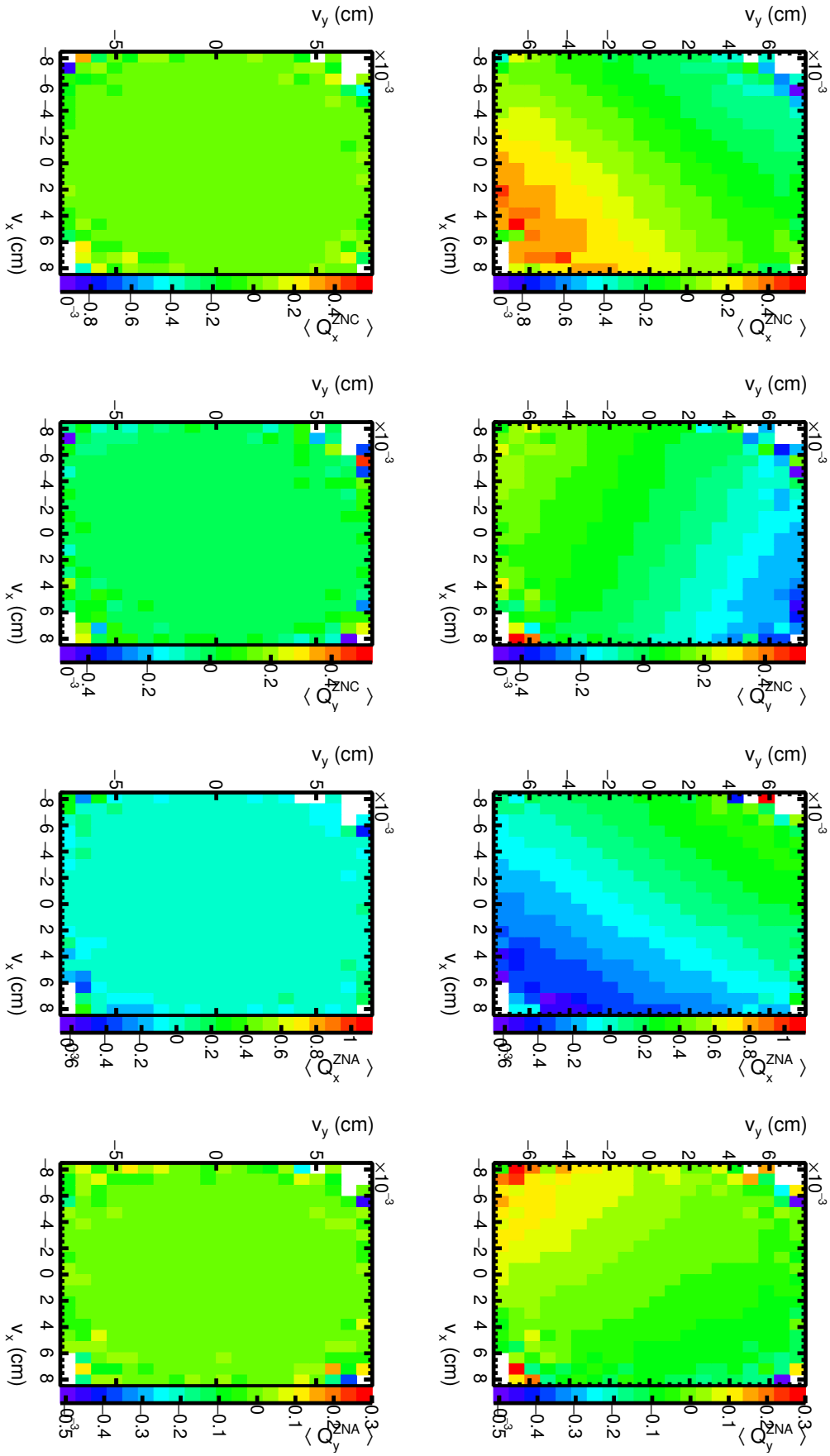

Figure 3.7: $\langle Q_{n,x} \rangle$ and $\langle Q_{n,y} \rangle$ from ZNA and ZNC as a function of v_x and v_y, before (top) and after (bottom) the calibration procedure. Run number 246087, centrality 0-80%.

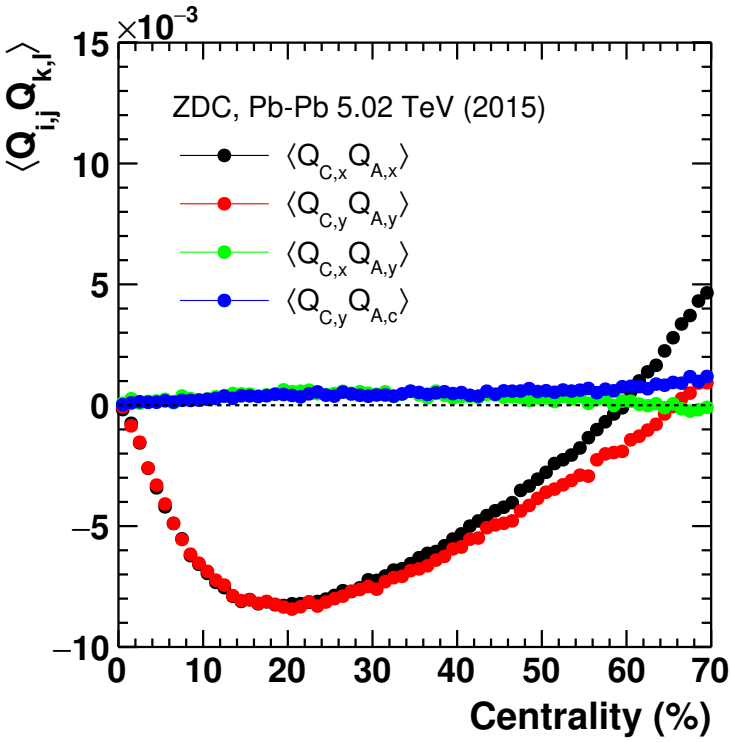

Figure 3.8: Correlations between ZDC Q-vector components, after calibration.

uncertainty, the corresponding parameters (track selection criteria, detector calibration parameters, etc.) are varied within a reasonable range, as discussed case-by-case, and the measurement is repeated. The default measurement x_{def} and the measurement obtained with varied parameters x_{var} are then compared, to see if a systematic difference is present or not. To see if such differences are statistically significant, the Barlow test [129] is employed

$$\mathrm{B} = \frac{x_{\mathrm{def}} - x_{\mathrm{var}}}{\sqrt{|\sigma^2_{\mathrm{def}} \pm \sigma^2_{\mathrm{var}}|}}, \tag{3.37}$$

where σ is the statistical uncertainty and the sign at the denominator is determined by the correlation between x_{def} and x_{var}, which depends in turn on the degree of overlap between the default data sample and the data sample with varied parameters. The sign is positive (+) if the two samples are independent (e.g. comparing results from different runs) and negative (−) if one sample is a sub-set of the other (e.g. comparing results obtained with more stringent and looser track selection criteria); intermediate cases are treated conservatively. If B is larger than 1, the corresponding difference is accounted as a systematic uncertainty. The contributions from the different sources are added in quadrature as an estimate of the total systematic uncertainty.

Chapter 4

Energy Dependence of Anisotropic Flow

in collaboration with Alexandru Dobrin, Jürgen Schukraft and Cvetan Cheshkov

4.1 Introduction

The main interest in studying the energy dependence on anisotropic flow is twofold:

- Test the robustness of current models of heavy-ion collisions, with which predictions on the variation of anisotropic flow coefficients between Pb–Pb collisions at $\sqrt{s_{\mathrm{NN}}} =$ 2.76 and 5.02 TeV were obtained [130] [131] [132] [133]. In particular, theoretical uncertainties are expected to partially cancel in the ratios of v_n at different energies, since some details of the models are known not to depend significantly on collision energy [130]. Also on the experimental side, systematic uncertainties are expected to be reduced in such ratios, as they are partially correlated between different datasets. Therefore, this constitutes a high-precision test of our current understanding of anisotropic flow in heavy-ion collisions.

- Provide additional constraints on the variations of the model parameters to which anistropic flow is most sensitive with respect to collision energy and, therefore, average system temperature. In particular, the relative increase of flow coefficients has been shown [131] to be sensitive to the temperature dependence of η/s close to and during the QGP fase (Fig. 4.3), which is currently poorly constrained by data [18].

The main differences that were expected between Pb–Pb collisions at $\sqrt{s_{\mathrm{NN}}} = 2.76$ and 5.02 TeV, based on our current understanding of heavy-ion collisions, are

- a relative increase of 4-5% of the average system temperature [131],

- an increase of $\langle p_{\mathrm{T}} \rangle$ of about 3-4%, due to an increase of radial flow [130],

- an increase in charged hadron multiplicity at midrapidity of about 20% [131] [130],

- possibly a small variation (about 1% or less) of average initial-state spatial anisotropies [130].

Therefore, concerning anisotropic flow, the general expectations were that $p_{\rm T}$-integrated flow coefficients would increase by a few percent due to the increase of $\langle p_{\rm T}\rangle$, while the $p_{\rm T}$ dependence of v_n would be mostly unchanged. $v_n(p_{\rm T})$ would in principle vary because of the increase of radial flow, but such a variation was expected to be of $\mathcal{O}(1\%)$ at most, given the striking similarity already observed between measurements of $v_n(p_{\rm T})$ at LHC energies ($\sqrt{s_{\rm NN}}$ = 2.76 TeV) [134] and RHIC ones ($\sqrt{s_{\rm NN}}$ = 200 GeV) [135]. The changes in initial-state spatial anisotropies (ε_n) were also expected to play a role, since to first approximation $v_n \propto \varepsilon_n$ (see the discussion in Sec. 5.1), although numerically their contribution was estimated to be around 1% (2%) or less for v_2 (v_3), as shown in Fig. 4.1. The residual sensitivity on other model parameters was estimated to be of a few percent at most, as shown in Fig. 4.2. Overall, the strongest sensitivity seemed to be indeed on the temperature dependence of η/s (Fig. 4.3, bottom panel). However, the relatively broad range of temperature probed by the system introduces some ambiguity: as we see in Fig. 4.3, top left panel, the two parametrizations η/s = 0.2 and *param*3 are dramatically different, while resulting in a similar increase of v_n, suggesting that the temperature-averaged values of η/s, i.e. integrating over the full evolution of the system, for these two parametrizations are quite similar. In particular, the system temperature at which transverse flow builds up at these energies is in the range 200-250 MeV [136]. At the same time, when compared to a broader set of observables at $\sqrt{s_{\rm NN}}$ = 2.76 TeV and 200 GeV, *param*3 fails to describe several of them [137], making thus possible to exclude it from the comparison. We conclude that measurements of anisotropic flow coefficients in Pb–Pb collisions at $\sqrt{s_{\rm NN}}$ = 2.76 and 5.02 TeV probably have little discriminating power on model parameters by themselves, but are likely to have it in combination with other bulk observables, most importantly the charged particle pseudorapidity ($\mathrm{d}N_{\rm ch}/\mathrm{d}\eta$) and $p_{\rm T}$ distributions ($\mathrm{d}N_{\rm ch}/\mathrm{d}p_{\rm T}$).

As a final remark, it is worth to note that the variations of temperature, multiplicity and $\langle p_{\rm T}\rangle$ (this latter driven by radial flow) across collision energies are related in ideal hydrodynamics via the QCD equation of state. In fact, in terms of thermodynamic quantities, the multiplicity at midrapidity ($N_{\rm ch}$) is proportional to the total entropy density (s), while the $\langle p_{\rm T}\rangle$ scales as the mean energy per particle, therefore as $\epsilon/N_{\rm ch} = \epsilon/s$, where ϵ is the total energy [138]. Therefore it follows [130]

$$\frac{d\langle p_{\rm T}\rangle}{\langle p_{\rm T}\rangle} = \frac{d\epsilon}{\epsilon} - \frac{ds}{s} = \frac{P}{\epsilon}\frac{dN_{\rm ch}}{N_{\rm ch}}. \tag{4.1}$$

The QCD equation of state is encoded in the ratio P/ϵ.

4.2 Event and track selection

The full data sample of Pb–Pb collisions at $\sqrt{s_{\rm NN}}$ = 5.02 (2.76) TeV collected by the ALICE detector in 2015 (2010), corresponding to an integrated luminosity of 12.7 (1.7) $\mu\mathrm{b}^{-1}$ in the centrality range 0-80%, is analysed. The event and track selection follows the procedure explained in Sec. 2.3.1 and 2.3.3, respectively. Unidentified charged particles in the pseudorapidity range $|\eta| < 0.8$ and transverse momentum $0.2 < p_{\rm T} < 50$ GeV/c are

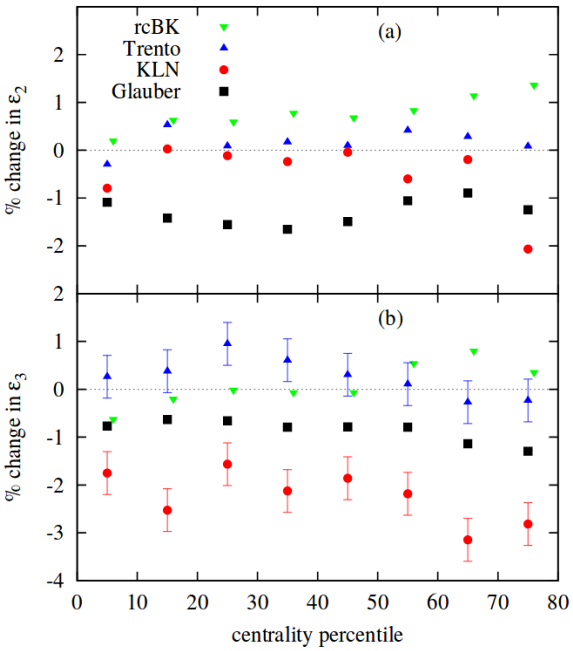

Figure 4.1: Percent change in rms eccentricity ε_2 (a) and triangularity ε_3 (b) between $\sqrt{s_{\rm NN}} = 2.76$ and 5.02 TeV, for several initial state models: MC-Glauber [19], Trento [139], MC-KLN [140] and MCrcBK [141].

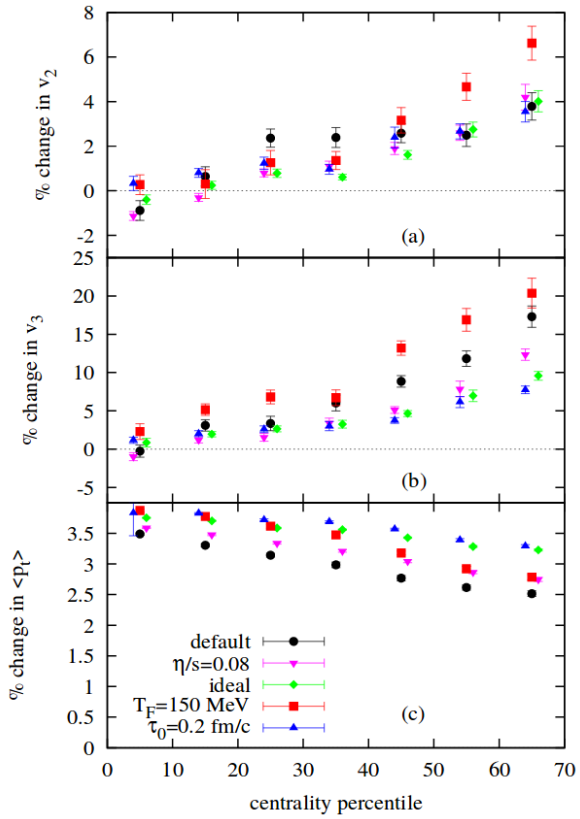

Figure 4.2: Percentage change in hydrodynamic response v_2/ε_2 (a), v_3/ε_3 (b) and $\langle p_{\rm T}\rangle$ (c) between $\sqrt{s_{\rm NN}} = 2.76$ and 5.02 TeV varying several model parameters: $\eta/s(T) = 0.08$, 0 (default *param*1 from [137]), freeze-out temperature $T_{FO} = 150$ MeV (default 130 MeV), initial time of hydrodynamic phase $\tau_0 = 0.2$ fm/c (default 0.6 fm/c).

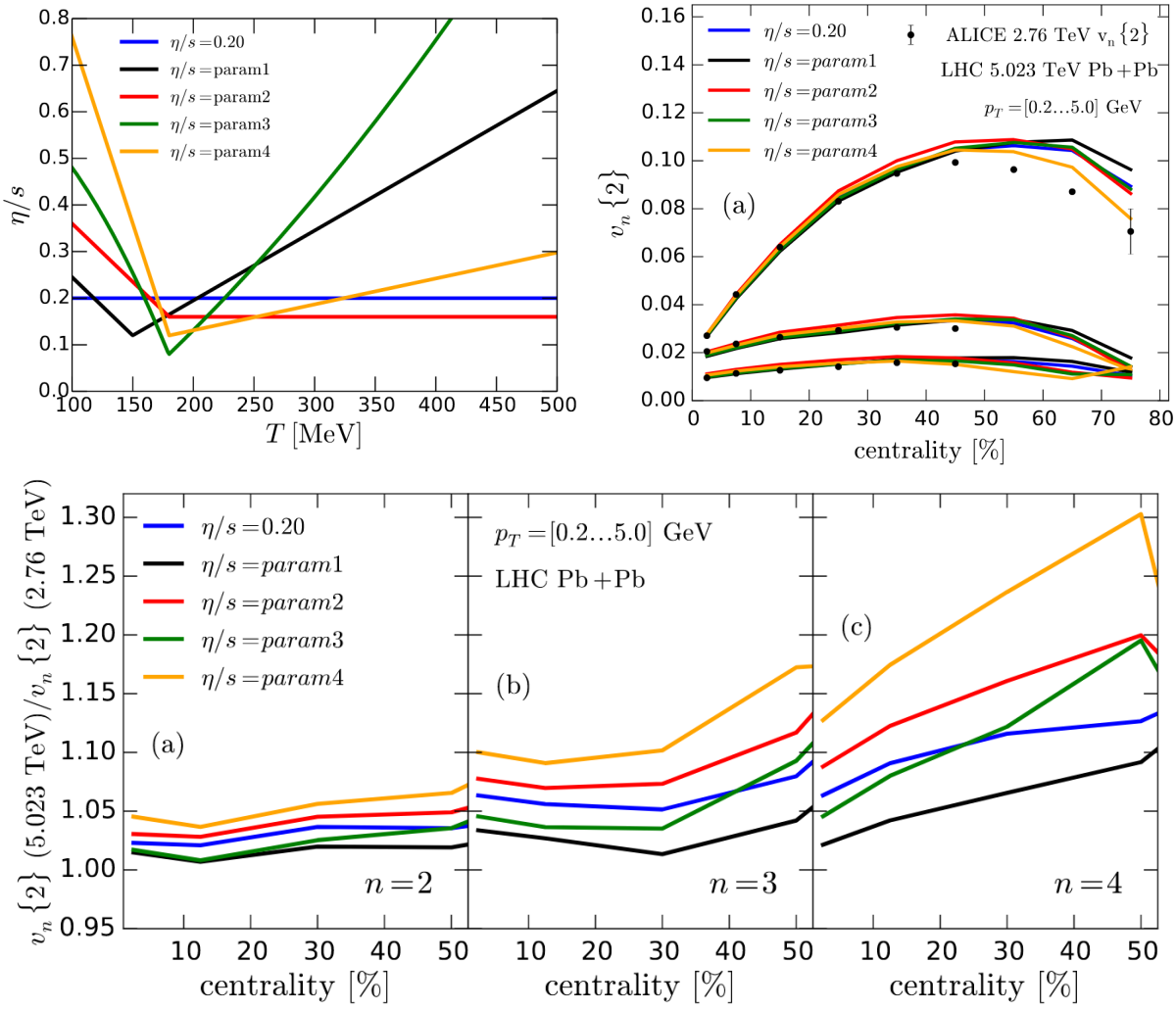

Figure 4.3: Collision energy dependence of flow coefficients for different parametrizations of the temperature dependence of η/s [131]. Top left: the different parametrizations of $\eta/s(T)$ employed in this study. Top right: the relative increase of p_{T}-integrated flow coefficients $v_2 - v_4$ between Pb-Pb collisions at $\sqrt{s_{\mathrm{NN}}} = 2.76$ and 5.02 TeV for the different parametrizations. Bottom: ratios of flow coefficients at the different collision energies for the different parametrizations.

selected. Centrality is determined via the total energy deposited in the two V0 detectors, as explained in Sec. 2.3.2.

4.3 Systematic uncertainties

The systematic uncertainties are evaluated following the procedure explained in Sec. 3.5. Possible sources of systematic uncertainties that are investigated are:

- track quality variables:
  - number of TPC space points
  - χ^2_{TPC}
  - χ^2_{ITS}
  - fraction of shared TPC space points
  - ITS layers in which hits are required
- particle charge
- event selection criteria:
  - pile-up cuts
  - centrality determination
  - ALICE dipole magnet polarity
- pseudorapidity-dependent detector effects: POIs and RPs (defined in Sec. 3.1.1) from different η regions (but fixed $|\Delta\eta|$, if relevant).

Additional sources of systematic uncertainties that are investigated and are found to be negligible include:

- reconstructed primary vertex position
- contamination from secondary particles
- uncertainties in estimating the efficiency

In addition to these and only for results at $\sqrt{s_{\mathrm{NN}}} = 5.02$ TeV, the following sources of uncertainties are investigated and are found to be negligible:

- variations in TPC and TOF calibration (different strategies were adopted for different parts of the dataset)
- space-charge distortions in the TPC
- variations in instantaneous luminosity

Source	v_2			v_3			v_4		
	0.2-1	1-4	4-10	0.2-1	1-4	4-10	0.2-1	1-4	4-10
tracking	2%	0.5%	0.5%	2%	1%	2%	6%	2%	1%
particle charge	0.2%	0.2%	n.s.	1%	n.s.	n.s.	1%	1%	1%
pile-up	0.4%	n.s.	n.s.	n.s.	n.s.	n.s.	n.s.	n.s.	n.s.
centrality determination	1%	1%	1%	n.s.	n.s.	n.s.	n.s.	n.s.	n.s.
magnet polarity	0.2%	0.5%	0.5%	0.5%	0.5%	1%	2%	2%	1%
η-range POIs and RPs	0.3%	0.4%	0.5%	0.5%	0.5%	1%	2%	n.s.	1%

Table 4.1: Maximum value of the systematic uncertainties from each source for v_2, v_3 and v_4 in 3 p_{T} ranges (0.2-1, 1-4 and 4-10 GeV/c) in Pb–Pb collisions at $\sqrt{s_{\mathrm{NN}}} = 5.02$ TeV and centrality 20-30%.

The variations in track quality variables are chosen in order to reject around 10% less or more tracks, with respect to the default choice, for each variable. The number of variations tested is between 1 and 4 for each of the sources and are performed independently, i.e. possible correlations are ignored. Pile-up rejection criteria (described in Sec.2.3.1) are varied in order to require a better agreement between different multiplicity estimators from the central barrel and result in rejecting around 20% of the total data sample, with respect to the default choice.

The contributions of the aforementioned sources to the total systematic uncertainty of anisotropic flow coefficients v_2, v_3 and v_4 at $\sqrt{s_{\mathrm{NN}}} = 5.02$ and 2.76 TeV are reported in Tab. 4.1 and 4.2, respectively. Three p_{T} ranges are shown: $0.2 < p_{\mathrm{T}} < 2$ GeV/c, $2 < p_{\mathrm{T}} < 4$ GeV/c and $4 < p_{\mathrm{T}} < 50$ GeV/c, for the centrality range 20-30%. Little centrality dependence is observed in the systematic uncertainties. Higher harmonics (v_5, v_6), not reported here, closely follow v_4.

For $p_{\mathrm{T}} > 10$ GeV/c (4 GeV/c) large statistical uncertainties on v_2-v_4 (v_5-v_6) prevent to reliably estimate the systematic ones. Systematic uncertainties in this p_{T} range are therefore extrapolated from those at lower p_{T}, assuming a linear dependence of the uncertainties on p_{T}. Different assumptions on the functional dependency of the systematic uncertainties on p_{T} result in similar extrapolated systematic uncertainties and the procedure is therefore judged to be robust enough. Overall, systematic uncertainties on v_n are similar between $\sqrt{s_{\mathrm{NN}}} = 5.02$ and 2.76 TeV and mostly arise from the track selection criteria. A notable exception is observed to be the uncertainty on centrality determination, which is sizeable only for v_2 in Pb–Pb collisions at $\sqrt{s_{\mathrm{NN}}} = 5.02$ TeV. This is estimated to arise from a small deterioration of the energy resolution of the V0 detectors across the years. Higher harmonics, having a much weaker centrality dependence, are not expected to be affected by this uncertainty, as observed.

The systematic uncertainties of the ratios $v_n[5.02\ \mathrm{TeV}]/v_n[2.76\ \mathrm{TeV}]$ are evaluated independently, in order to estimate and remove the sources of uncertainty that are correlated between datasets. Practically, this means to vary event and track selection criteria by the same amount in the analyses of both datasets and estimate the systematic uncertainties from the variations of the ratios. The contributions from the different sources are reported in Tab. 4.3 for the same p_{T} ranges previously described. We note that a good fraction of the uncertainties arising from tracking are indeed correlated between the two datasets

Source	v_2			v_3			v_4		
	0.2-1	1-4	4-10	0.2-1	1-4	4-10	0.2-1	1-4	4-10
tracking	1.5%	1%	1%	4%	1%	1%	5%	2%	2%
particle charge	n.s.	n.s.	n.s.	0.2%	1%	n.s.	1%	1%	2%
pile-up	n.s.	n.s.	n.s.	n.s.	n.s.	n.s.	n.s.	n.s.	n.s.
centrality determination	n.s.	n.s.	n.s.	n.s.	n.s.	n.s.	n.s.	n.s.	n.s.
magnet polarity	n.s.	0.2%	n.s.	1%	n.s.	1%	2%	n.s.	1%
η-range POIs and RPs	0.4%	0.2%	0.5%	1%	1%	2%	2%	n.s.	1%

Table 4.2: Maximum value of the systematic uncertainties from each source for v_2, v_3 and v_4 in 3 p_{T} ranges (0.2-1, 1-4 and 4-10 GeV/c) in Pb–Pb collisions at $\sqrt{s_{\mathrm{NN}}} = 2.76$ TeV and centrality 20-30%.

Source	v_2			v_3			v_4		
	0.2-1	1-4	4-50	0.2-1	1-4	4-50	0.2-1	1-4	4-50
tracking	1.2%	0.6%	0.8%	2%	1%	1%	5%	2%	2%
particle charge	0.2%	0.2%	0.5%	0.5%	0.4%	0.5%	1%	1%	n.s.
pile-up	n.s.	n.s.	n.s.	n.s.	n.s.	n.s.	n.s.	n.s.	n.s.
centrality determination	0.9%	1%	1%	n.s.	n.s.	n.s.	n.s.	n.s.	n.s.
magnet polarity	n.s.	n.s.	n.s.	0.8%	1.%	0.8%	1%	2%	n.s.
η-range POIs and RPs	n.s.	n.s.	n.s.	n.s.	n.s.	n.s.	n.s.	n.s.	n.s.

Table 4.3: Maximum value of the systematic uncertainties from each source for the ratios of v_2, v_3 and v_4 in 3 p_{T} ranges (0.2-1, 1-4 and 4-10 GeV/c) between Pb–Pb collisions at $\sqrt{s_{\mathrm{NN}}} = 5.02$ and 2.76 TeV and centrality 20-30%.

and cancel out in the ratios, while the one on centrality determination, as expected from what discussed previously, is not.

4.4 Results

Figure 4.4 presents the centrality dependence of the flow coefficients v_n ($n = 2, \ldots 6$) averaged in the p_{T} range $0.2 < p_{\mathrm{T}} < 3.0$ GeV/c, where collective effects are expected to dominate azimuthal anisotropies. Measurements are performed with the two- and four-particle cumulant method, denoted with $v_n\{2, |\Delta\eta| > 1\}$ and $v_n\{4\}$, respectively. Results at both $\sqrt{s_{\mathrm{NN}}} = 5.02$ and 2.76 TeV are shown. A clear hierarchy is observed among flow coefficients, with the second harmonic (elliptic flow) being the dominant one and the higher harmonics progressively smaller. The centrality-averaged (0-50%) values of harmonics v_3-v_6 are decreasing as $v_{n+1}/v_n \sim 0.5$. In contrast to a strong increase in v_2 from central to mid-central collisions and a decrease after about 45% centrality towards peripheral collisions, a weak centrality dependence is observed for the higher harmonics. This holds true at both energies and is consistent with previous observations [134, 142]. The characteristic centrality dependence of the elliptic flow was observed already at RHIC energies [143]. Compared to previous measurements in the p_{T} range $0.2 < p_{\mathrm{T}} < 5$ GeV/c [142], the differences in v_n coefficients arising from the different choice of p_{T} range are of about 1% and 2% for v_2 and v_3-v_6, respectively.

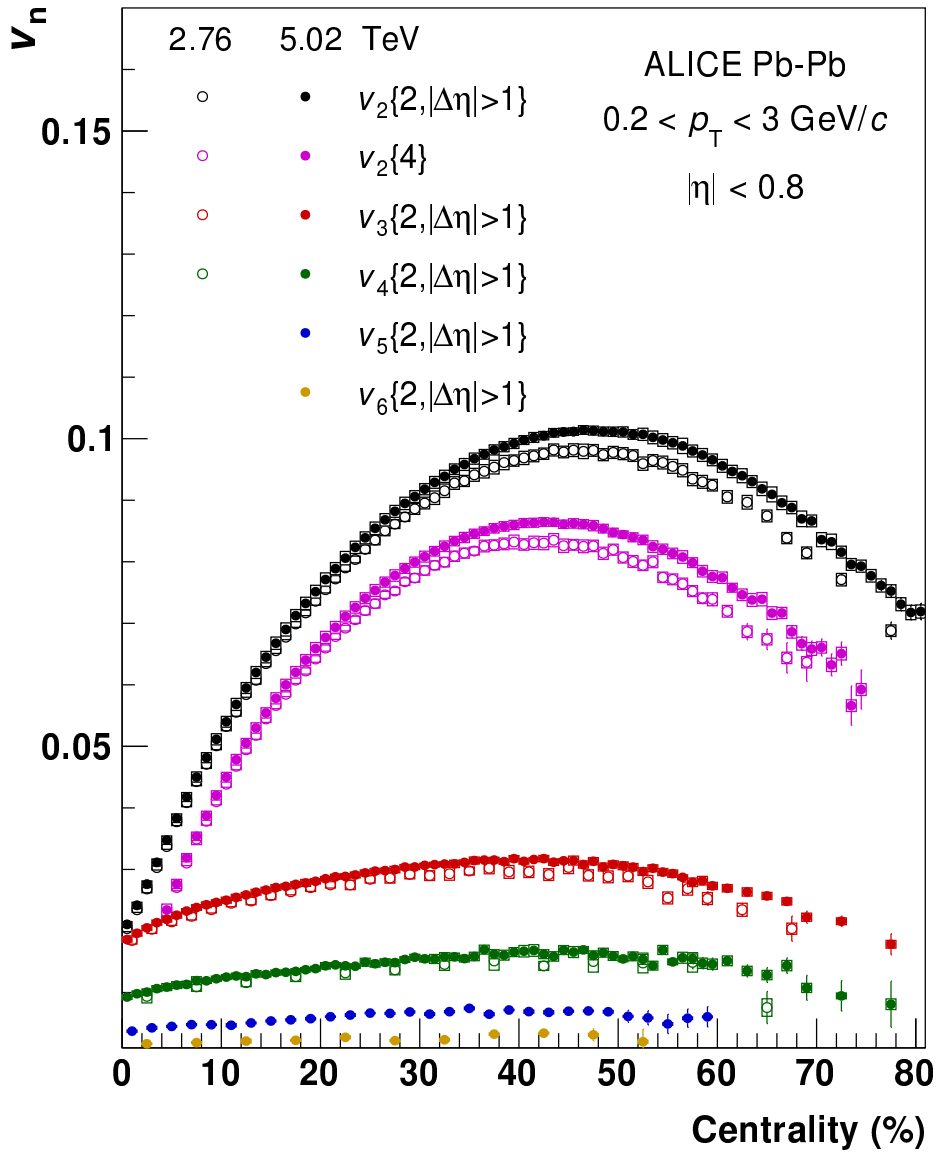

Figure 4.4: Anisotropic flow coefficients v_n of inclusive charged particles as a function of centrality, for the two-particle (denoted with $|\Delta\eta| > 1$) and four-particle cumulant methods. Measurements for Pb–Pb collisions at $\sqrt{s_{\rm NN}} = 5.02$ (2.76) TeV are shown by solid (open) markers.

	$\eta/s = 0.2$	$\eta/s(T)$ param1	1
$v_2\{2, \|\Delta\eta\| > 1\}$	0.712	0.645	0.477
$v_2\{4\}$	0.467	0.357	0.028
$v_3\{2, \|\Delta\eta\| > 1\}$	0.053	0.003	0.001
$v_4\{2, \|\Delta\eta\| > 1\}$	0.484	0.468	0.022

Table 4.4: p-values for the comparison among ratios of $v_n\{2, |\Delta\eta| > 1\}$ ($n = 2, 3, 4$) and $v_2\{4\}$ between $\sqrt{s_{\rm NN}} = 5.02$ and 2.76 TeV and model calculations using different parametrisations of $\eta/s(T)$ [131], shown in Fig. 4.5, and unity, in the centrality range 5-50%.

Figure 4.5 shows the ratio of $v_n\{2, |\Delta\eta| > 1\}$ ($n = 2, 3, 4$) and $v_2\{4\}$ between $\sqrt{s_{\rm NN}} =$ 5.02 and 2.76 TeV, i.e. the relative variation of these flow coefficients between those two energies. Since the systematic uncertainties of the measurements at different energies are partially correlated, the resulting systematic uncertainty on the ratio is reduced. All harmonics are observed to increase with energy, between about 2 and 10%. A hint of a centrality dependence is observed only for v_2, with the increase growing slightly from mid-central towards more peripheral collisions. No significant difference is observed in the increase of v_2 measured with two- or four-particle correlations. Since the difference between $v_2\{2, |\Delta\eta| > 1\}$ and $v_2\{4\}$ is directly related to flow fluctuations, this observation suggests that the fluctuations of elliptic flow do not vary significantly between the two energies, within experimental uncertainties. This will be extensively investigated in Ch. 5. The ratios are compared to hydrodynamical calculations with EKRT initial conditions [14] and different parametrisations of the temperature dependence of η/s [131]. The p-values for the comparison between data and models are also shown in Tab. 4.4. Among the two parametrisations that provide the best description of RHIC and LHC data [137], both are consistent with the measurements, except for $v_3\{2, |\Delta\eta| > 1\}$, albeit the one with constant $\eta/s = 0.2$ agrees slightly better. These comparisons take into account the correlation between systematic uncertainties of data points in different centrality intervals. This observation might indicate little or no temperature dependence of η/s within the temperature range at which anisotropic flow develops at the two center of mass energies. As a reference, the p-values for the comparison between data and unity in the same centrality range (5-50%) are also reported in Tab. 4.4.

Figure 4.6 shows the $p_{\rm T}$-differential measurements of v_n ($n = 2, \ldots 6$), with two- and four-particle cumulants, in the $p_{\rm T}$ range $0.2 < p_{\rm T} < 50$ GeV/c and in wide centrality bins, between 0% and 70%. The $p_{\rm T}$ dependence is qualitatively similar for all harmonics: v_n increases with increasing $p_{\rm T}$ up to about 3–4 GeV/c, after which it starts decreasing. Comparing the different harmonics, they seem to follow the hierarchy observed in the $p_{\rm T}$-integrated results in the whole $p_{\rm T}$ range: $v_2 > v_3 > \ldots v_6$, except for very central collisions (0–5%), where $v_3\{2, |\Delta\eta| > 1\}$ is observed to be greater than $v_2\{2, |\Delta\eta| > 1\}$ for $p_{\rm T} \gtrsim 2$ GeV/c and $v_4\{2, |\Delta\eta| > 1\}$ is observed to be similar to $v_2\{2, |\Delta\eta| > 1\}$ for $p_{\rm T} \gtrsim 3$ GeV/c. In the centrality range 10–40% a significant non-zero value of $v_2\{2, |\Delta\eta| > 1\}$ and $v_2\{4\}$ is observed up to $p_{\rm T} \approx 30$ GeV/c; for the higher harmonics, significant values are only measured for $p_{\rm T} \leq 10$ GeV/c.

Looking at the $p_{\rm T}$ dependence in more detail, the flow harmonics are found to follow

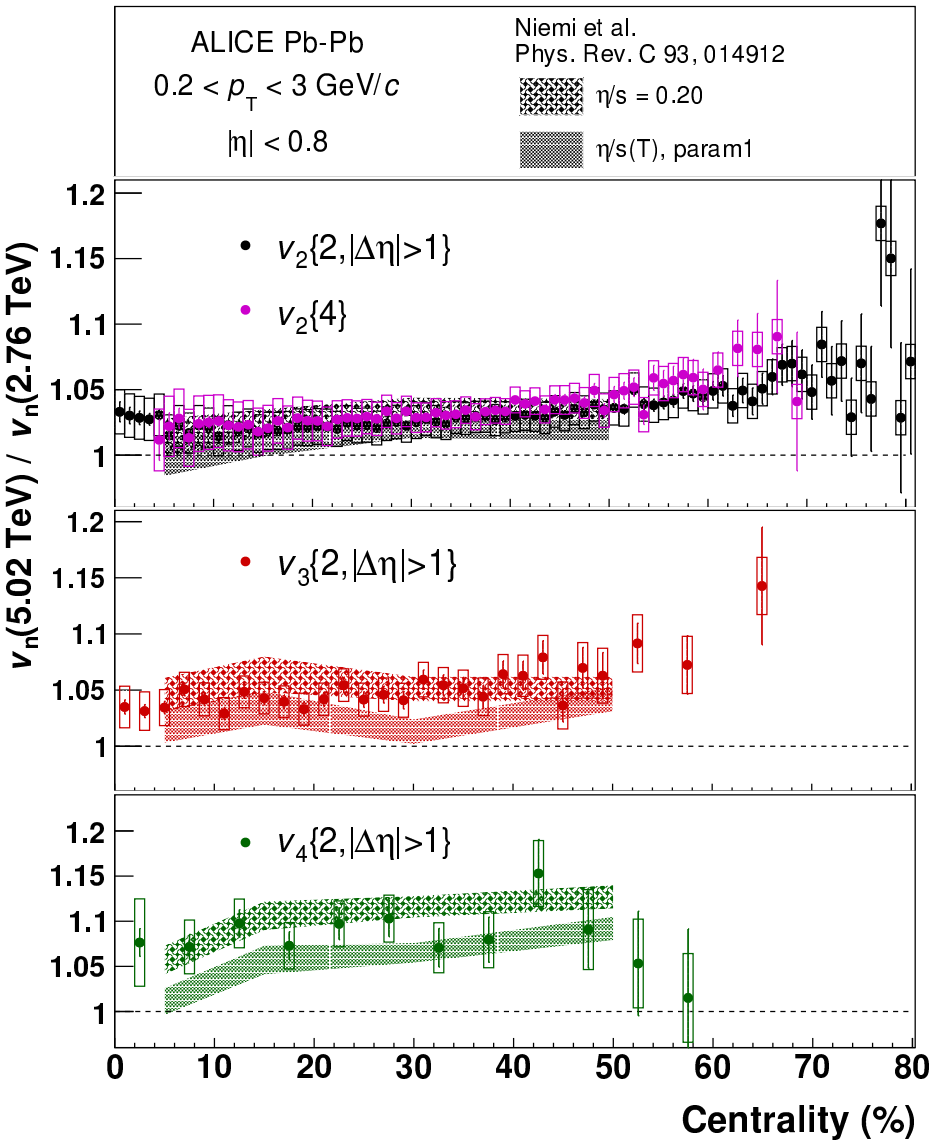

Figure 4.5: Ratios of anisotropic flow coefficients v_n of inclusive charged particles between Pb–Pb collisions at $\sqrt{s_{\mathrm{NN}}} = 5.02$ and 2.76 TeV, as a function of centrality. Hydrodynamic calculations employing different $\eta/s(T)$ parametrizations [131] are shown for comparison.

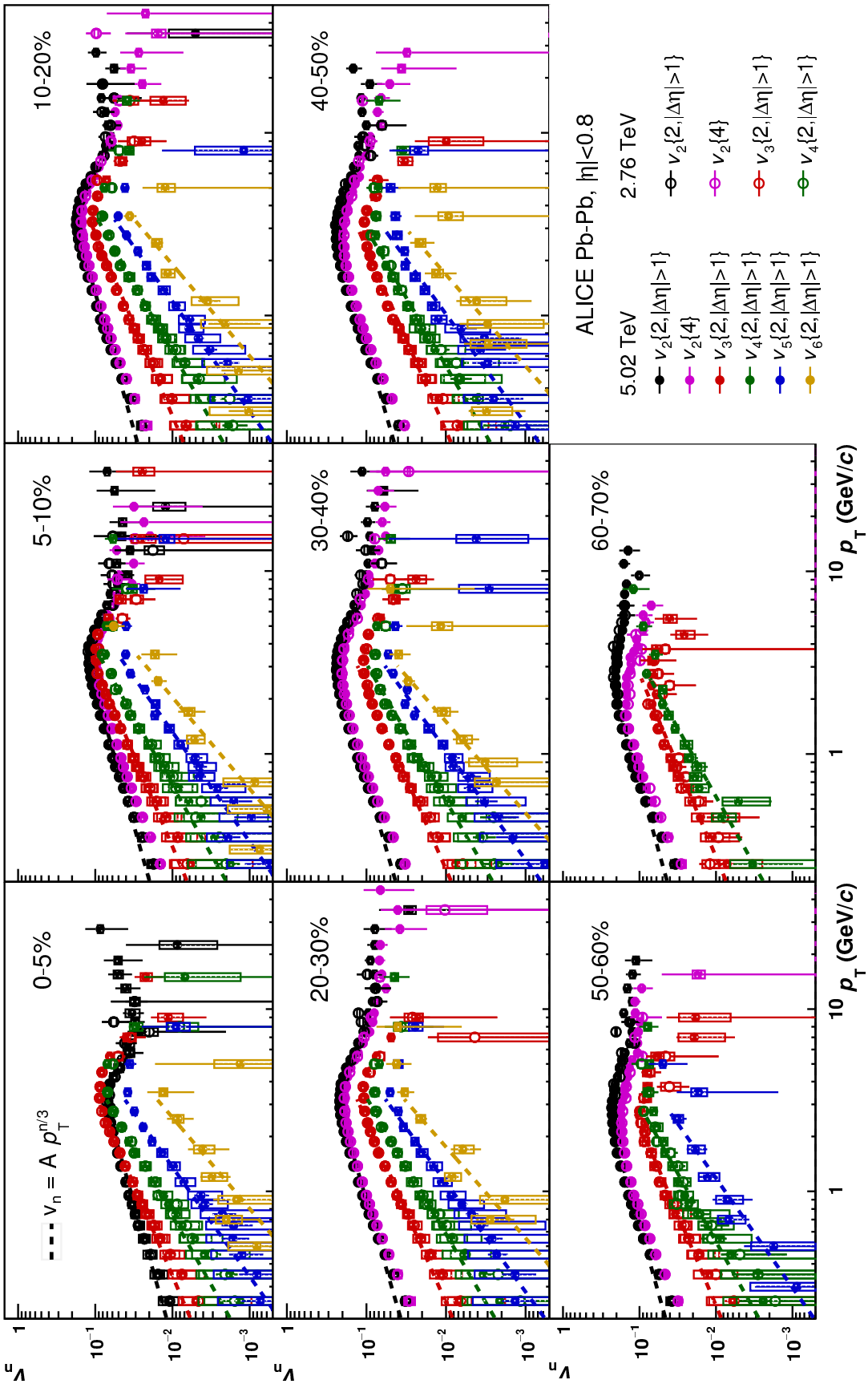

Figure 4.6: Anisotropic flow coefficients $v_n(p_T)$ of inclusive charged particles in different centrality classes, measured with two-particle (denoted with $|\Delta\eta| > 1$) and four-particle cumulant methods. Measurements for Pb–Pb collisions at $\sqrt{s_{NN}} = 5.02$ (2.76) TeV are shown by solid (open) markers. Dashed lines are fits with a power-law function $v_n(p_T) = A\, p_T^{n/3}$, with A as free parameter.

an approximate power-law scaling up to around the maximum, with exponents being proportional to the harmonic number n, $v_n(p_{\mathrm{T}}) \sim p_{\mathrm{T}}^{n/3}$, as shown by the dashed fitted lines in Fig. 4.6. In ideal hydrodynamics, the p_{T} dependence of anisotropic flow for massive particles should follow a power-law function $v_n(p_{\mathrm{T}}) \sim p_{\mathrm{T}}^n$ in the region of p_{T}/M up to order one, where M is the particle's mass, and at higher momenta it has been predicted to be linear in p_{T} for all n, $v_n(p_{\mathrm{T}}) \sim p_{\mathrm{T}}$ [144, 145]. This p_{T} dependence is notably different from the one observed in the data. At very low p_{T} this is presumably because the relevant momentum region for inclusive particles, mostly pions, is below the range of our measurements, and at higher p_{T} ideal hydro is not expected to hold because of momentum dependent viscous corrections at freeze out [146] and/or non-linear mode mixing for $n \geqslant 4$ [147, 148]. The power-law dependence for $n = 2$ was noticed before and it was attributed to a novel energy loss mechanism [149], which however cannot explain the scaling observed for $n > 2$. The emergence of this simple power-law dependence remains unexpected and surprising.

Figure 4.7 shows the p_{T}-differential measurements of v_n ($n = 2, 3, 4$) calculated with the scalar product method with respect to V0A, in different centrality intervals. The same p_{T} and centrality range as in Fig. 4.6 is shown. A significant $v_2\{2, |\Delta\eta| > 2\}$ is observed up to $p_{\mathrm{T}} \approx 40$ GeV/c in the centrality range 10-40%. $v_n\{2, |\Delta\eta| > 2\}$ and $v_n\{2, |\Delta\eta| > 1\}$ ($n = 2, 3, 4$) are found to be compatible within 2% in the p_{T} range $0.2 < p_{\mathrm{T}} < 10$ GeV/c, while a systematic difference (with $v_2\{2, |\Delta\eta| > 1\} > v_2\{2, |\Delta\eta| > 2\}$) is observed for $10 < p_{\mathrm{T}} < 50$ GeV/c, ranging from about 3% in centrality 0-5% to about 10% in centrality 40-50%. This difference is attributed to small residual non-flow contributions which are suppressed by the larger pseudorapidity gap. Such an interpretation is consistent with the observed centrality dependence: the relative contribution of non-flow increases with decreasing multiplicities, therefore from central to peripheral collisions. Possible differences among $v_n\{2, |\Delta\eta| > 1\}$ and $v_n\{2, |\Delta\eta| > 2\}$ ($n = 2, 3, 4$) arising from the decorrelation of event planes at different pseudorapidities have been estimated to be less than 1% and 3% for v_2 and v_{3-4}, respectively, based on η-dependent factorization ratios [150] measured at $\sqrt{s_{\mathrm{NN}}} = 2.76$ TeV [47]. This estimation assumes that such decorrelation only depends on $|\Delta\eta|$ and not η in the pseudorapidity range under consideration ($|\eta| < 5.1$).

Figure 4.8 shows the ratios of p_{T}-differential $v_n\{2, |\Delta\eta| > 1\}$ ($n = 2, 3, 4$) and $v_2\{4\}$ between $\sqrt{s_{\mathrm{NN}}} = 5.02$ and 2.76 TeV, in different centrality intervals. Overall, the ratios are consistent with unity, indicating that p_{T}-differential anisotropic flow does not change significantly across collision energies and that the increase observed in the p_{T}-integrated values can be mostly attributed to an increase of $\langle p_{\mathrm{T}} \rangle$, as previously noted [142]. This observation is also consistent with little or no variation of η/s between the two collision energies, as already shown in Fig. 4.5. The possible variations in p_{T}-integrated values arising from the differences in the p_{T}-differential ones have been estimated to be less than 1%, by integrating $v_n(p_{\mathrm{T}})$ at $\sqrt{s_{\mathrm{NN}}} = 5.02$ (2.76) TeV with charged particle spectra at 2.76 (5.02) TeV.

Figure 4.9 shows the comparison of p_{T}-differential flow measurements with different models, in three centrality intervals: 5–10% (top panel), 20–30% (middle panel) and 40–50% (bottom panel). At low p_{T} ($p_{\mathrm{T}} < 2$ GeV/c), flow coefficients are expected to be mostly determined by the collective expansion of the system, which is commonly described by hydrodynamic models. The measurements are compared to three calculations, one

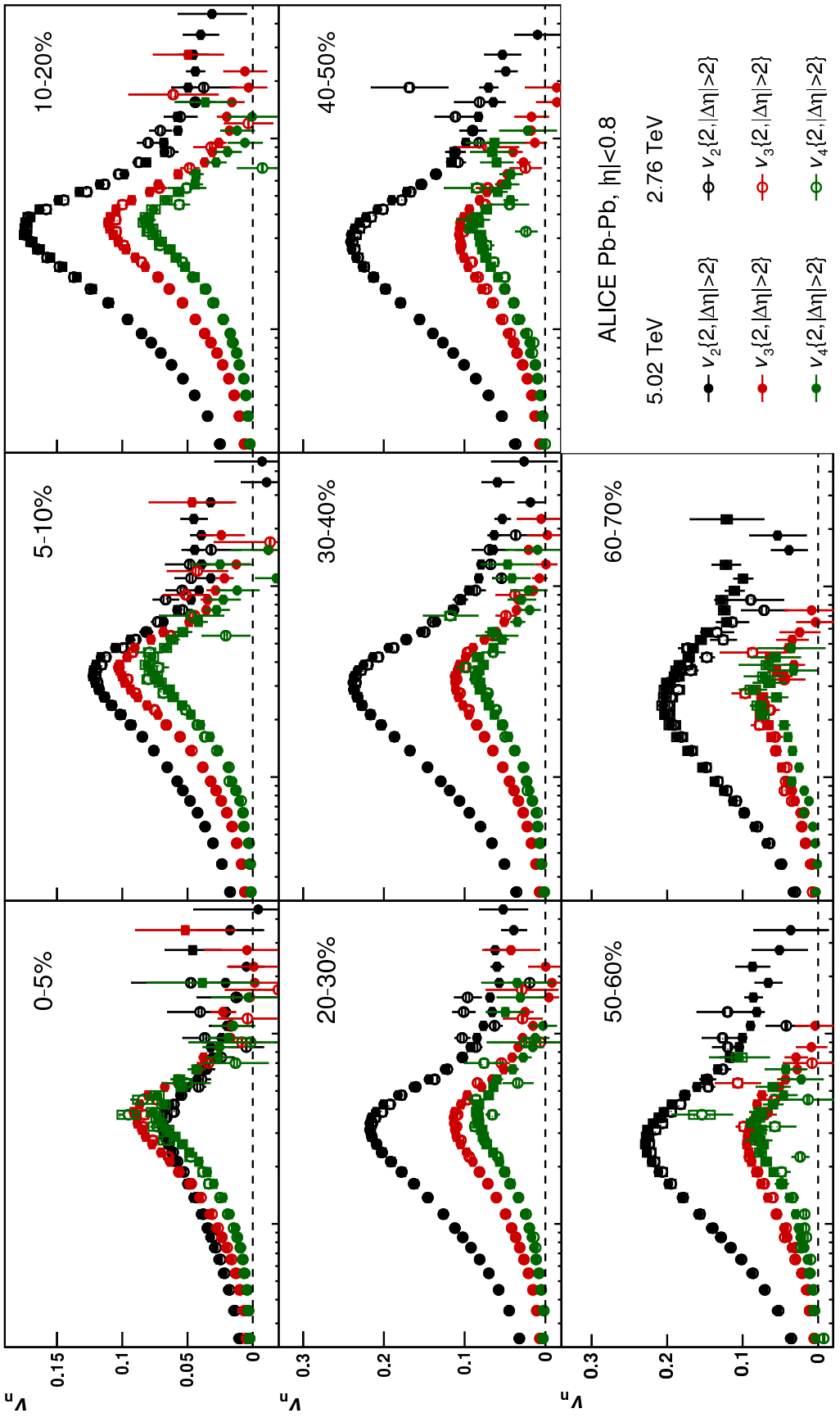

Figure 4.7: Anisotropic flow coefficients $v_n(p_T)$ of inclusive charged particles in different centrality classes, measured with the scalar product method with respect to the V0A Q-vector. Measurements for Pb–Pb collisions at $\sqrt{s_{NN}} = 5.02$ (2.76) TeV are shown by solid (open) markers.

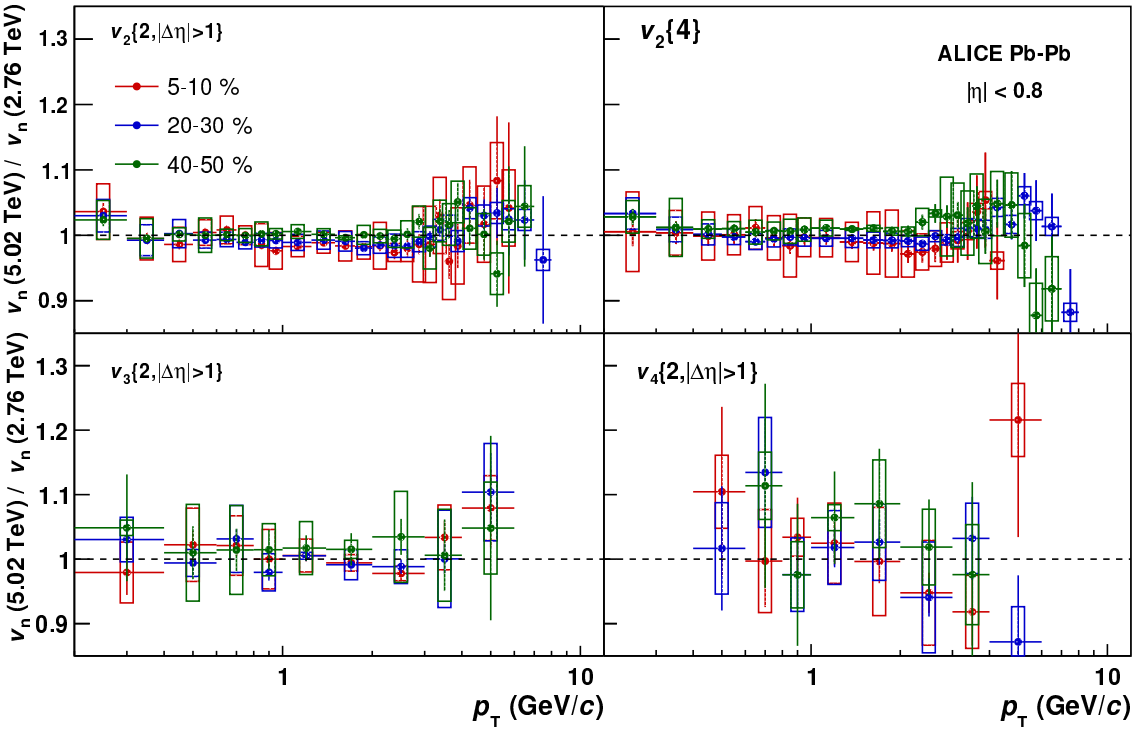

Figure 4.8: Ratios of anisotropic flow coefficients $v_n(p_{\mathrm{T}})$ of inclusive charged particles between Pb–Pb collisions at $\sqrt{s_{\mathrm{NN}}} = 5.02$ and 2.76 TeV, in different centrality classes, measured with two-particle (denoted with $|\Delta\eta| > 1$) and four-particle cumulant methods.

employing IP-Glasma initial conditions [15] matched to the MUSIC viscous hydrodynamic code [132] and two calculations using iEBE-VISHNU viscous hydrodynamic code [133] with AMPT [151] or TRENTo [139] initial conditions. The parameters of TRENTo were tuned to reproduce previous measurements in Pb–Pb collisions at $\sqrt{s_{\rm NN}} = 2.76$ TeV [18]; with such tuning TRENTo has been shown [139] to effectively mimic IP-Glasma initial conditions and therefore the two calculations TRENTo+iEBE-VISHNU and IP-Glasma+MUSIC are expected to be based on similar initial conditions. All models employ a transport cascade model (UrQMD [152]) to describe the hadronic phase after freeze-out. Compared to data, all models are found to underestimate the data for $p_{\rm T} < 0.5$ GeV/c. For $1 < p_{\rm T} < 2$ GeV/c the predictions from IP-Glasma+MUSIC and TRENTo+iEBE-VISHNU overestimate the data, while those from AMPT-IC+iEBE-VISHNU are found to be still in agreement. Overall, all models qualitatively describe the $p_{\rm T}$ dependence of flow coefficients in this low $p_{\rm T}$ range.

At high $p_{\rm T}$ ($p_{\rm T} > 10$ GeV/c), azimuthal anisotropies are on the contrary expected to be determined by path-length dependent parton energy-loss. The measurements are compared to predictions from [153], which combine an event-by-event hydrodynamic description of the medium (v-USPhydro [154]) with a jet quenching model (BBMG [155]). Two sets of predictions for $v_2\{2\}$, $v_2\{4\}$ and $v_3\{2\}$, assuming a linear ($\mathrm{d}E/\mathrm{d}x \sim L$) and a quadratic ($\mathrm{d}E/\mathrm{d}x \sim L^2$) dependence of the energy loss on the path length L, are compared to data. Other parameters of the model, such as η/s, are expected to have a minor contribution within the presented centrality ranges [153]. For $v_2\{2, |\Delta\eta| > 2\}$, the linear case is compatible with the data, while the quadratic one can be excluded within 95% confidence level. For $v_3\{2, |\Delta\eta| > 2\}$, neither of the two sets of predictions can be excluded within uncertainties. Our results are found to be in good agreement with CMS data [61].

The evolution of the shape of $p_{\rm T}$-differential v_n coefficients with respect to centrality is investigated by calculating the ratios of $v_n(p_{\rm T})$ in a given centrality range and $v_n(p_{\rm T})$ in centrality 20–30%, normalised by the corresponding ratio of $p_{\rm T}$-integrated v_n

$$v_n(p_{\rm T})_{\text{ratio to 20-30\%}} = \frac{v_n(p_{\rm T})}{v_n(p_{\rm T})[\text{20-30\%}]} \frac{v_n[\text{20-30\%}]}{v_n}.$$

If the shape of $v_n(p_{\rm T})$ does not change with centrality, but only scales according to $\langle v_n \rangle$, $v_n(p_{\rm T})_{\text{ratio to 20-30\%}}$ is identical to 1 in the full $p_{\rm T}$ range. In order to reduce statistical fluctuations, a parametrisation of $v_n(p_{\rm T})$[20-30%] fitted to data is employed. The results are shown in Fig. 4.10: deviations from unity up to about 10% are observed at low $p_{\rm T}$ ($p_{\rm T} < 3$ GeV/c) and up to about 30% at intermediate $p_{\rm T}$ ($3 < p_{\rm T} < 6$ GeV/c), where $v_n(p_{\rm T})$ reaches its maximum. These variations are observed to be larger for higher harmonics (v_{3-4}), in particular for central collisions. The effects due to a change in particle composition of the inclusive charged particle sample with centrality are estimated to be negligible. These deviations are attributed mostly to the combined effect of radial flow and parton density which, in the coalescence model picture [156], decrease from central to peripheral collision shifting the maximum of $v_n(p_{\rm T})$ from higher to lower $p_{\rm T}$. At high $p_{\rm T}$ ($p_{\rm T} > 10$ GeV/c), results on $v_2\{2, |\Delta\eta| > 2\}$ are consistent with those at low $p_{\rm T}$, suggesting a common origin of the centrality evolution of elliptic flow in the two regimes, presumably initial-state geometry and its fluctuations. This interpretation is consistent

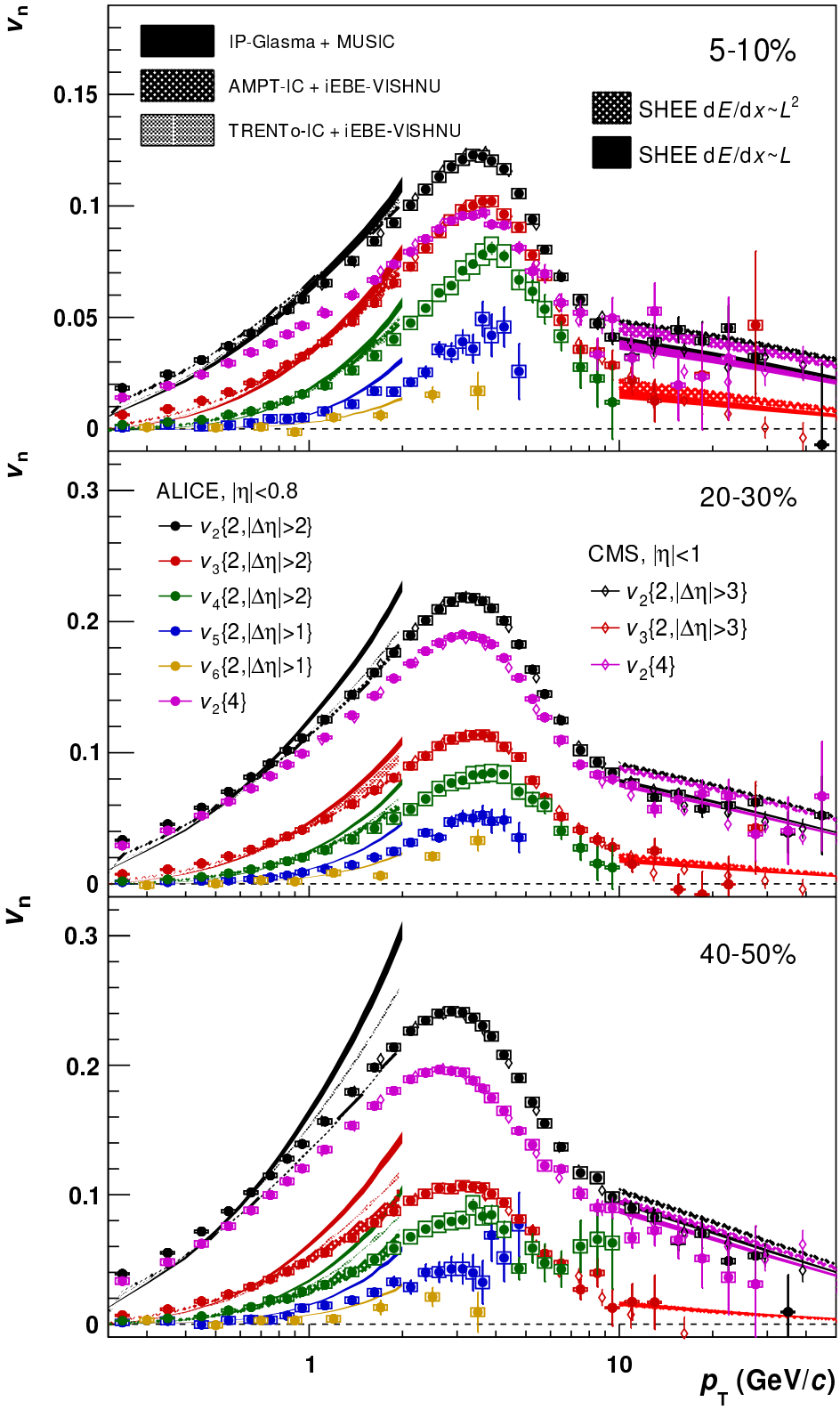

Figure 4.9: Anisotropic flow coefficients $v_n(p_{\mathrm{T}})$ of inclusive charged particles in different centrality classes, measured with two- and four-particle cumulant and scalar product methods with respect to the V0A Q-vector, for Pb–Pb collisions at $\sqrt{s_{\mathrm{NN}}} = 5.02$ TeV. Several hydrodynamic calculations [132, 133, 153] and previous measurements from CMS [61] are shown for comparison.

with the findings of [61]. The attribution of the scaling of $v_n(p_T)$ up to $p_T = 8$ GeV/c to initial-state geometries agrees with studies [157, 158] using the Event Shape Engineering technique [159] and p_T-dependent elliptic flow fluctuations [160]. Finally, the models using hydrodynamic calculations [133] and jet energy loss ones [153] are observed to be in good agreement with the v_2 data at low and high p_T, respectively.

At RHIC [161, 162] and LHC [163] it had been observed that the ratios of harmonics follow a power-law scaling, i.e. $v_n^{1/n} \sim v_m^{1/m}$, for semi-central and peripheral collisions up to about 6 GeV/c and independent of the harmonic n and m. In order to test this scaling, we use the ratios $v_n/v_m^{n/m}$ which in practice are more sensitive than $v_n^{1/n} \sim v_m^{1/m}$. Figure 4.11 shows these ratios for $n = 3, 4$ and $m = 2, 3$, as a function of p_T. These ratios are indeed observed to be independent of p_T, in most of the p_T range and for most centrality ranges, except for centrality 0–5%. Up to about the maximum of $v_n(p_T)$, the scaling is numerically related to, but actually significantly more precise than, the observed approximate power-law dependences $v_n(p_T) \sim p_T^{n/3}$ pointed out in Fig. 4.6. Surprisingly however, the scaling extends much further, in particular $v_3(p_T)/v_2(p_T)^{3/2}$ is constant to better than about 10%, out to the highest measured p_T in excess of 10 GeV/c. The ratio $v_4(p_T)/v_2(p_T)^{4/2}$ shows stronger deviations at high p_T, starting at around the maximum of $v_2(p_T)$. A separation of v_4 into linear and non-linear components would be required to see if the v_4/v_2 scaling at low p_T, and/or its violations at high p_T, is related to the mode mixing, which is particularly strong for the 4th harmonic and at high p_T, or possibly also to quark coalescence [144, 164, 165].

As noted in the context of Fig. 4.6, the observed ratio scaling is not expected in ideal hydrodynamics. While not all viscous hydrodynamical models shown in Fig. 4.9 describe the data up to the highest p_T very well, they all do exhibit the same power-law scaling in the ratio of harmonics over the p_T range $0.5 < p_T < 3$ GeV/c, with a precision comparable to the one seen in the data, while they strongly deviate for $p_T < 0.5$ GeV/c. The scaling may be related to viscosity, as also postulated in [166, 167], in particular to the large and p_T-dependent viscous corrections appearing at hadronisation [146]. However, a harmonic number dependence of these viscous corrections which could reproduce the scaling observed in the data, has so far, to the best of our knowledge, never been quantitatively investigated.

Finally, the charged particle spectra at both energies and the $\langle p_T \rangle$ are shown in Fig. 4.12 and 4.13, respectively. We observe indeed an increase of $\langle p_T \rangle$ of around 4.5%, with no significant centrality dependence within uncertainties, which is consistent with expectations [130]. In Fig. 4.13, values of $\langle p_T \rangle$ derived from previous ALICE measurements [168] [169] are also reported, as a reference, and are observed to be consistent within uncertainties. A somehow worse agreement is observed at $\sqrt{s_{NN}} = 5.02$ TeV. We speculate this discrepancy to be mostly determined by the correction to particle composition in the Monte Carlo generators, which was introduce for the first time in the analysis of data at $\sqrt{s_{NN}} = 5.02$ TeV [169] and its contribution to reconstruction efficiency was estimated to be of around 2% near $\langle p_T \rangle$. The problem lies in the fact that Monte Carlo generators cannot yet correctly describe the yields of hyperons. Therefore, the relative abundances of different particle species within the inclusive charged particle sample are incorrect. Since the detector has different tracking efficiency for all these particle species, the efficiency for inclusive charged particles differ in Monte Carlo simulations and in data. A correction

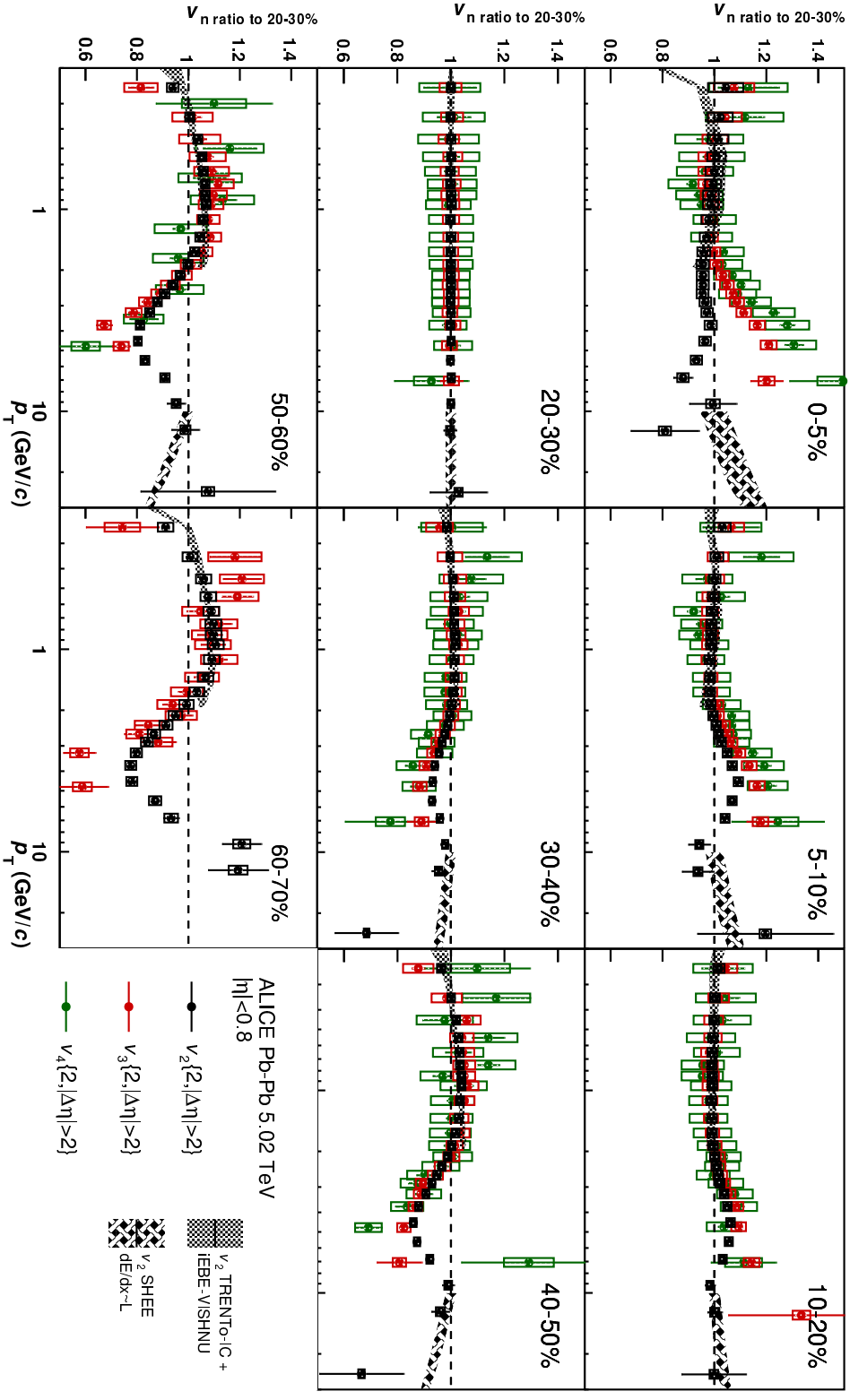

Figure 4.10: Ratios $v_n(p_T)_{\text{ratio to 20-30\%}}$ of inclusive charged particles for Pb–Pb collisions at $\sqrt{s_{NN}} = 5.02$ TeV, in different centrality classes, measured with the scalar product method with respect to the V0A Q-vector. Hydrodynamic calculations [133, 153] are shown for comparison.

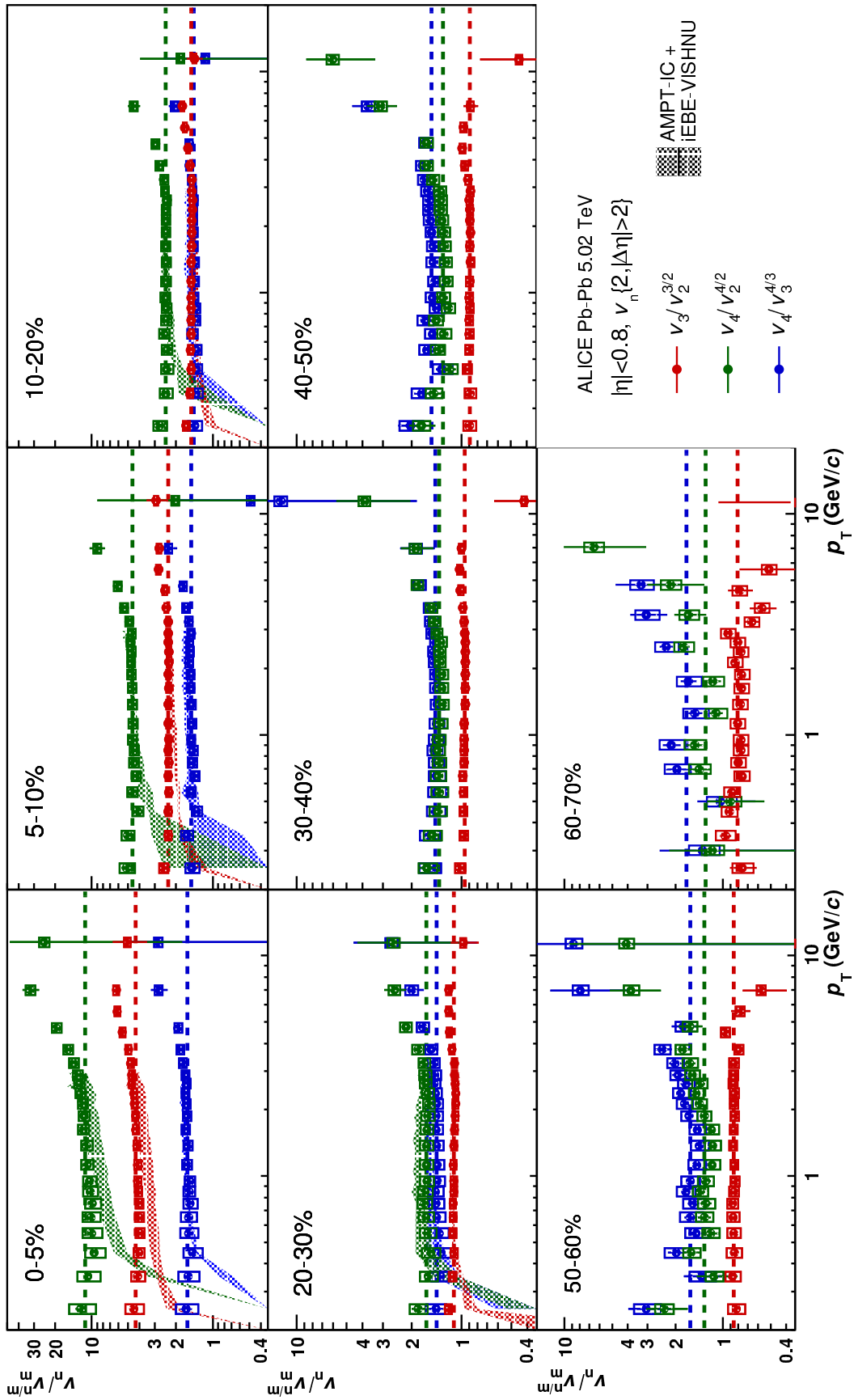

Figure 4.11: Ratios $v_n(p_{\mathrm{T}})/v_m(p_{\mathrm{T}})^{n/m}$, $n = 3, 4$, $m = 2, 3$ of inclusive charged particles for Pb–Pb collisions at $\sqrt{s_{\mathrm{NN}}} = 5.02$, in different centrality classes, measured with the scalar product method with respect to the V0A Q-vector. Dashed lines represent averages in $0.2 < p_{\mathrm{T}} < 3$ GeV/c. The ratios are also shown for one hydrodynamic model [133] in the four most central centrality intervals; it is qualitatively similar in the other centrality intervals and for the other models.

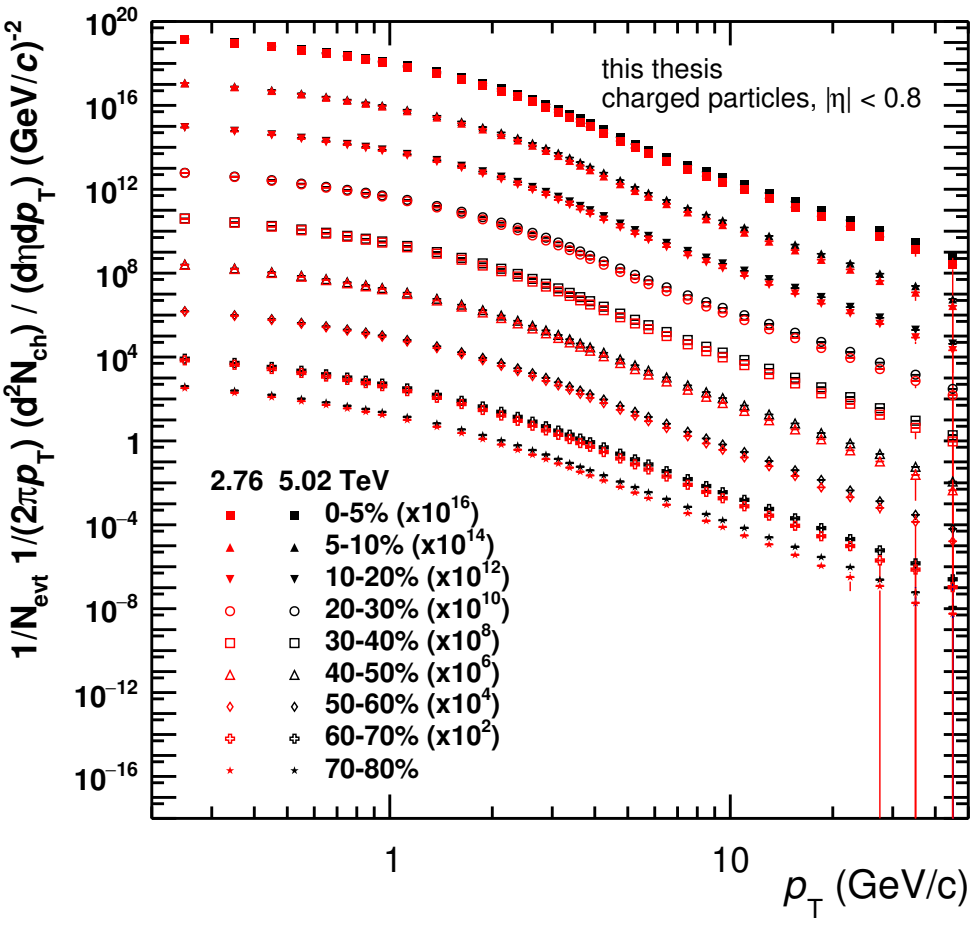

Figure 4.12: p_{T} distribution of inclusive charged particles in different centrality classes for Pb-Pb collisions at $\sqrt{s_{\mathrm{NN}}} = 5.02$ and 2.76 TeV.

based on measured yields of hyperons has therefore been developed, but was not employed for this analysis.

4.5 Discussion

p_{T}-integrated anisotropic flow of inclusive charged particles in Pb–Pb collisions at $\sqrt{s_{\mathrm{NN}}} = 5.02$ TeV is observed to increase with respect to $\sqrt{s_{\mathrm{NN}}} = 2.76$ TeV by 2-9%, according to the flow harmonic, with no or weak centrality dependence. This is attributed mostly to an increase of $\langle p_{\mathrm{T}} \rangle$ of around 4.5%. The p_{T} dependence of anisotropic flow is in fact observed to be unchanged between the two collision energies, within experimental uncertainties.

We hypothesize that the dominant mechanism at play is the increase of average energy density in the initial state, which is converted during the evolution of the system in radial flow, therefore increasing the average transverse momentum. At the same time, a possible variation of other physical quantities (initial state fluctuations, transport parameters) of

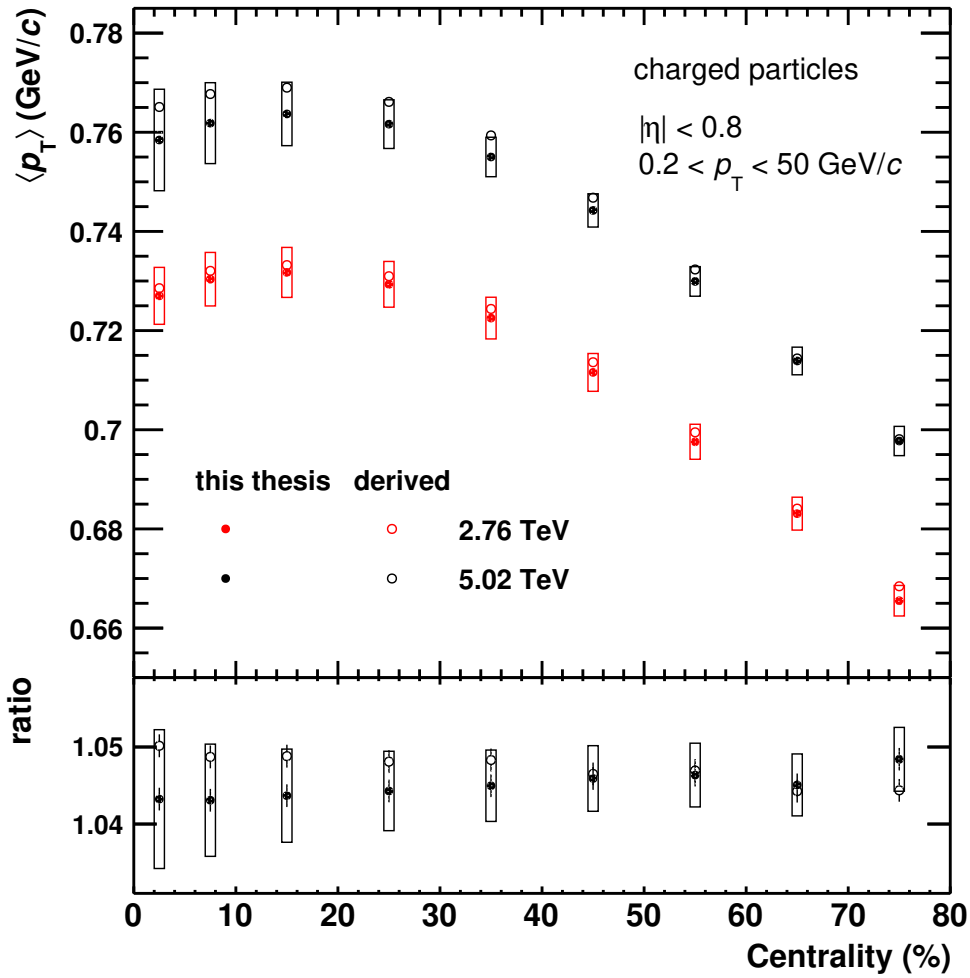

Figure 4.13: Solid markers: $\langle p_{\mathrm{T}} \rangle$ of inclusive charged particles as a function of centrality for Pb-Pb collisions at $\sqrt{s_{\mathrm{NN}}} = 5.02$ and 2.76 TeV (top panel) and ratio of the measurements at the two energies (bottom panel). Open markers: values of $\langle p_{\mathrm{T}} \rangle$ derived from previous ALICE measurements [168] [169].

$\mathcal{O}(1\%)$ cannot be excluded. In particular, concerning the temperature dependence of η/s, it was shown that these measurements alone are not sufficient to provide constraints. However, we argue that they might play an important role once included in a broader analysis of bulk observables, such as what was recently carried out at lower energies [18, 170].

The evolution of $v_n(p_{\mathrm{T}})$ with respect to centrality and harmonic number n is also investigated. Flow coefficient of all harmonics are observed to follow an approximate power-law scaling of the form $v_n(p_{\mathrm{T}}) \sim p_{\mathrm{T}}^{n/3}$ in the p_{T} range $0.2 < p_{\mathrm{T}} < 3$ GeV/c. The ratios $v_n/v_m^{n/m}$ $n = 3, 4$ and $m = 2, 3$ are also observed to be independent of p_{T} within the same p_{T} range and show deviations of about 10% for $3 < p_{\mathrm{T}} < 10$ GeV/c.

One final question that remains concerns the observed consistency of $v_n(p_{\mathrm{T}})$ at the two energies. An increase of radial flow, that we argue being responsible for the increase of $\langle p_{\mathrm{T}} \rangle$, is expected to imply a difference in $v_n(p_{\mathrm{T}})$, although small, and it remains to be proven that such difference is consistent with the measurements. For that, we need to

1. have a functional description of $v_n(p_{\mathrm{T}})$, tuned on data at $\sqrt{s_{\mathrm{NN}}} = 2.76$ TeV,

2. estimate how much radial flow increases between $\sqrt{s_{\mathrm{NN}}} = 2.76$ and 5.02 TeV and compute its effect on $v_n(p_{\mathrm{T}})$.

We will use the Retiere-Lisa Blast-Wave model [171], explained in Sec. 6.2, which provides a simplified description of bulk particle production in heavy-ion collisions consistent with boost invariant ideal hydrodynamics. For simplicity, we will discuss only v_2, being the flow harmonic subject to the smallest experimental uncertainties and, therefore, providing the most stringent limits, in the centrality range 20-30%.

For the first step, data on identified particle ($\pi^{\pm}$, $K^{\pm}$, p) spectra [172] and elliptic flow [173] at $\sqrt{s_{\mathrm{NN}}} = 2.76$ TeV is simultaneously fit with a Blast-Wave model (fig.4.14). The results of the fit are shown in tab.4.5. The inclusive charged particle elliptic flow $v_2(p_{\mathrm{T}})$ can then be computed as

$$v_2(p_{\mathrm{T}}) = \frac{N^{\pi}(p_{\mathrm{T}})v_2^{\pi}(p_{\mathrm{T}}) + N^{K}(p_{\mathrm{T}})v_2^{K}(p_{\mathrm{T}}) + N^{p}(p_{\mathrm{T}})v_2^{p}(p_{\mathrm{T}})}{N^{\pi} + N^{K} + N^{p}},$$

where $N^i(p_{\mathrm{T}})$ is the yield of the particle species i.

For the second step, we will only use inclusive charged particle spectra at both energies[1]. These are again fit with the Retiere-Lisa Blast-Wave model (Fig. 4.15), fixing T_{fo}, ρ_2 and s_2 to results at $\sqrt{s_{\mathrm{NN}}} = 2.76$ TeV (Tab. 4.5) and keeping only ρ_0, which is directly related to radial flow, as a free parameter. The mass is set to the one of the pions, being the dominant species in the p_{T} range under study. ρ_0 is observed to increase by around 2.3% between the two energies, corresponding to an increase in mean radial boost $\langle \beta_T \rangle$ of around 1%. We note that the Blast-Wave model is not suited to describe a sample of different particle species and therefore the results of this fit have to be taken with great care: we only want a reasonable estimate of the increase of radial flow and we leave further considerations aside.

[1]The corresponding data on identified particles at $\sqrt{s_{\mathrm{NN}}} = 5.02$ TeV is not yet available at the time of writing

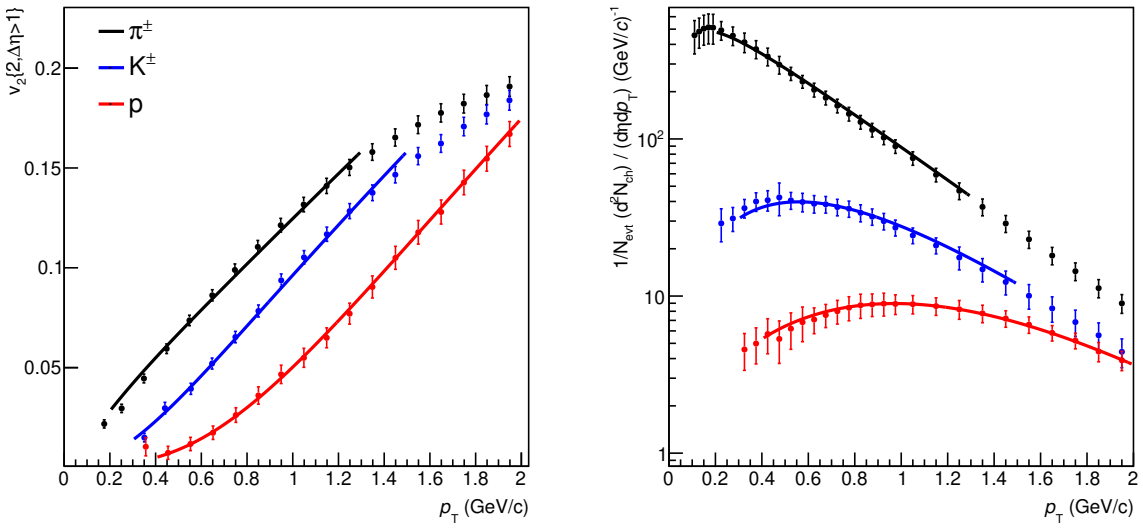

Figure 4.14: Blast-Wave fit to spectra [172] and elliptic flow [173] of $\pi^{\pm}$, $K^{\pm}$ and p at $\sqrt{s_{\rm NN}} = 2.76$ TeV. Only statistical uncertainties are shown. The range in which the lines are shown correspond to the fit range for each of the particle species.

T_{fo} (GeV)	ρ_0	ρ_2	s_2	χ^2/NDF
0.105 ± 0.004	1.11 ± 0.01	0.09 ± 0.01	0.08 ± 0.01	0.31

Table 4.5: Results of the Blast-Wave fit to spectra [172] and elliptic flow [173] of $\pi^{\pm}$, $K^{\pm}$ and p at $\sqrt{s_{\rm NN}} = 2.76$ TeV.

Finally, in order to estimate $v_n(p_{\rm T})$ at $\sqrt{s_{\rm NN}} = 5.02$ TeV, we take the results of the fits at $\sqrt{s_{\rm NN}} = 2.76$ TeV, we change ρ_0 accordingly and we compute $v_n(p_{\rm T})$. Figure 4.16 shows the results of this exercise and compare them to measurements of $v_2\{2, \Delta\eta > 1\}$. The estimates from the Blast-Wave model are found to be in agreement with data within $p_{\rm T} < 1.3$ GeV/c. One can see that the variation of $v_2(p_{\rm T})$ is indeed expected to be of the order of 2% or less, with a clear dependence on $p_{\rm T}$: positive for $p_{\rm T} < 0.2$ GeV/c and negative above. The measurements are consistent with this prediction and are even suggestive of such $p_{\rm T}$-dependence, although the large uncertainties do not allow to draw conclusions.

We conclude that there is no tension between the interpretation of the variations of $p_{\rm T}$-integrated flow coefficients as being mostly due to the increase of radial flow and the observed limits on the variations of $p_{\rm T}$-differential flow coefficients.

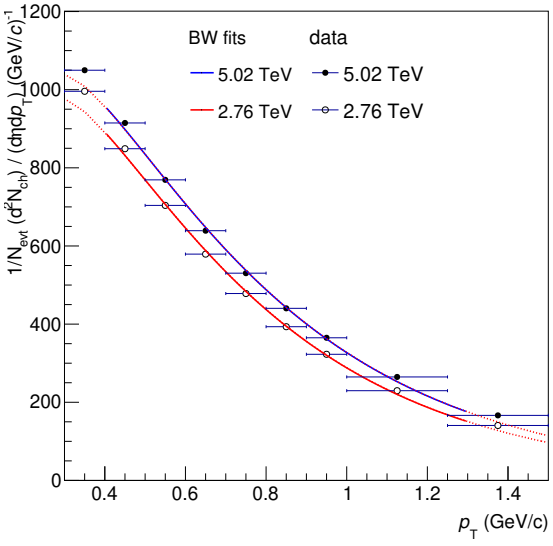

Figure 4.15: Blast-Wave fit to inclusive charged particle spectra at $\sqrt{s_{\rm NN}} = 2.76$ and 5.02 TeV (see text for details).

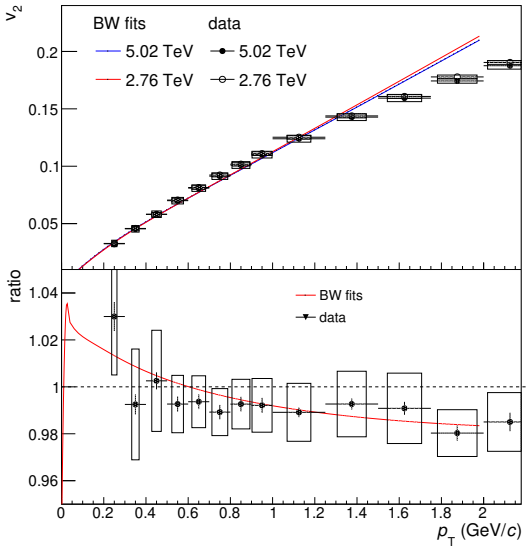

Figure 4.16: Top panel: $v_n(p_{\rm T})$ of inclusive charged particles at $\sqrt{s_{\rm NN}} = 2.76$ and 5.02 TeV (see text for details). Bottom panel: ratios of $v_n(p_{\rm T})$ at the two energies.

Chapter 5

Elliptic Flow Fluctuations

in collaboration with Alexandru Dobrin

5.1 Introduction

It is known that the magnitude of anisotropic flow fluctuates from collision to collision even for fixed centrality [174, 175, 176, 177, 134, 43]. This can be mostly attributed to fluctuations of initial-state spatial anisotropies, usually referred to concisely as *initial-state fluctuations* and quantified in terms of eccentricities ε_n, defined in Eq.1.4. For elliptic flow, the relation between ε_2 and v_2 is in fact linear, to first approximation [148]

$$v_2 = k_2 \, \varepsilon_2, \tag{5.1}$$

where the proportionality coefficient k_2 parametrises mostly the hydrodynamic response of the system. This holds true in the regime where collective effects dominate, $0 < p_{\mathrm{T}} < 3$ GeV/c. Therefore, the study of elliptic flow fluctuations can be related directly to the study of initial-state ones, up to a certain precision, and can give insights into the non-perturbative QCD dynamics that determine them.

Concerning the functional description of initial-state fluctuations, several parametrisation of the underlying p.d.f. $P(\varepsilon_2)$ have been proposed. To first approximation, fluctuations are expected to be Bessel-Gaussian [178], i.e. the product of a modified Bessel function and a Gaussian function

$$P(\varepsilon_2) = \frac{\varepsilon_2}{\sigma_{2x}^2} \exp\left(\frac{-\varepsilon_2^2 + \langle\varepsilon_{2x}\rangle^2}{2\sigma_{2x}^2}\right) I_0\left(\frac{\varepsilon_2\langle\varepsilon_{2x}\rangle}{\sigma_{2x}^2}\right), \tag{5.2}$$

where I_0 is the modified Bessel function and $\langle\varepsilon_{2x}\rangle$ (σ_{2x}) refers to the average (standard deviation of the) eccentricity with respect to the reaction plane Ψ_{RP} (see Sec. 1.4). Here and in the following, brackets $\langle\cdots\rangle$ indicate an average over a set of collisions. It has been pointed out that small deviations from a Bessel-Gaussian shape are to be expected independently from the details of initial-state fluctuations or, once considering v_2, of the hydro response [179, 180, 181, 182]. Evidences of such small deviations at the level of v_2 have indeed been previously reported [183]. These observations led to the proposal of a

different parametrisation of $P(\varepsilon_2)$, namely the Elliptic-Power distribution [179, 180]

$$P(\varepsilon_2) = 2\alpha\varepsilon_2(1-\varepsilon_2^2)^{\alpha-1}(1-\langle\varepsilon_{2x}\rangle^2)^{\alpha+1/2}\frac{1}{\pi}\int_0^\pi(1-\varepsilon_2\langle\varepsilon_{2x}\rangle\cos\varphi)^{-2\alpha-1}\,d\varphi, \tag{5.3}$$

which allows for non-zero higher order central moments, e.g. skewness. Note that in the limit $\alpha \gg 1$ and $\langle\varepsilon_{2x}\rangle \ll 1$, Eq. 5.3 reduces to Eq. 5.2 and we can identify $\alpha = 1/\sqrt{2\sigma_{2x}}$. The Elliptic-Power distribution provides a good description of the fluctuations of ε_n in several initial-state models [180], as shown in Fig. 5.1, and naturally satisfies the geometrical constraint $0 < \varepsilon_2 < 1$. It was also shown to correctly describe of $P(v_2)$ in a wide centrality range [184]. It is interesting to look at the assumptions under which the Elliptic Power distribution can be analytically derived [180]:

1. the energy density profile of the initial-state is a superposition of a number of point-like sources,
2. the positions of the sources are independent,
3. the distribution of the positions of the sources is a 2-dimensional Gaussian in the transverse plane.

While none of these apply exactly to the initial-state, we believe to correctly take it into account in initial-state models: sources have a finite size, they are correlated according to the geometry of the collision and their distribution is set by the details of the model itself. Still, the Elliptic Power distribution well describes $P(\varepsilon_n)$, irrespectively of the model, up to a centrality of about 70%. This suggests that the above set of assumptions effectively holds in describing initial-state spatial anisotropies in central and mid-central heavy-ion collisions.

Once considering elliptic flow fluctuations, two caveats are of order. First, it has been argued that in more peripheral collisions small deviations from the linear relation between v_2 and ε_2 (Eq. 5.1) are to be expected from the hydrodynamic evolution of the medium [184], whose contribution to the total v_2 can arrive up to about 10% at centrality 50% [185]. Such deviations can be parametrised with a cubic response coefficients k_2', defined as

$$v_2 = k_2\varepsilon_2 + k_2'\varepsilon_2^3, \tag{5.4}$$

The estimation of k_2' as a function of centrality in hydrodynamic models is shown in Fig. 5.2. The existence of a non-zero cubic response implies that the distribution of v_2 is not exactly homothetic to the distribution of ε_2. Secondly, it has been proposed that nonlinear hydrodynamic effects also invalidate Eq. 5.1, although their contribution was estimated to be of the order of 1% [184] in mid-central collisions. It remains to be studied if and how much other processes that take place during the system evolution, such as hadronic re-scatterings, have a sizeable effect on flow fluctuations.

A robust experimental method to quantify elliptic flow fluctuations is to measure v_2 with multi-particle cumulants, defined in Sec. 3.1.1, which have different sensitivities to the central moments of the underlying flow p.d.f.

$$v_2\{2\} = \sqrt{\langle v_{2x}\rangle + \sigma_{2x}^2 + \sigma_{2y}^2}, \tag{5.5}$$

$$v_2\{4\} \simeq \langle v_{2x}\rangle + \frac{\sigma_{2y}^2 - \sigma_{2x}^2}{2\langle v_{2x}\rangle} - \frac{s_1 + s_2}{\langle v_{2x}\rangle^2}, \tag{5.6}$$

$$v_2\{6\} \simeq \langle v_{2x}\rangle + \frac{\sigma_{2y}^2 - \sigma_{2x}^2}{2\langle v_{2x}\rangle} - \frac{\frac{2}{3}s_1 + s_2}{\langle v_{2x}\rangle^2}, \tag{5.7}$$

$$v_2\{8\} \simeq \langle v_{2x}\rangle + \frac{\sigma_{2y}^2 - \sigma_{2x}^2}{2\langle v_{2x}\rangle} - \frac{\frac{7}{11}s_1 + s_2}{\langle v_{2x}\rangle^2}. \tag{5.8}$$

Here, v_{2x} refers to elliptic flow with respect to the reaction plane. Similarly, σ_{2x} and σ_{2y} are the standard deviation of elliptic flow with respect to the reaction plane and the one perpendicular to it, respectively, while s_1, s_2 are defined as

$$s_1 = \langle (v_{2x} - \langle v_{2x}\rangle)^3\rangle, \tag{5.9}$$

$$s_2 = \langle (v_{2x} - \langle v_{2x}\rangle)\, v_{2y}^2\rangle. \tag{5.10}$$

A large difference between $v_2\{2\}$ and $v_2\{4\}$ and approximately equal values of the higher order cumulants ($v_2\{4\}$, $v_2\{6\}$, $v_2\{8\}$) have been previously observed [186, 183], which is indeed consistent with an approximately Bessel-Gaussian flow p.d.f.. However, a fine-splitting of a few percent between the higher orders cumulants ($v_2\{4\}$, $v_2\{6\}$, $v_2\{8\}$) has also been reported [183], which is thought to be determined by the residual deviations from Bessel-Gaussian shape and is also observed in hydrodynamic model calculations, see Fig. 5.3.

Deviations from a Bessel-Gaussian distribution are to first order described by a finite skewness. Its quantitative determination would therefore improve the characterization of these deviations. For dimensional reasons, it is convenient to use a standardized skewness (γ_1), defined as [182]

$$\gamma_1 = \frac{\langle (v_{2x} - \langle v_{2x}\rangle)^3\rangle}{\langle (v_{2x} - \langle v_{2x}\rangle)^2\rangle^{3/2}} = \frac{s_1}{\sigma_{2x}^3}, \tag{5.11}$$

A negative value of γ_1, which corresponds to $P(v_2)$ being left skewed, is expected from the necessary condition $\varepsilon_2 < 1$, which acts as a right cutoff on $P(\varepsilon_2)$ [180]. This can be easily seen in Fig. 5.1, top right panel: since $\langle\varepsilon_2\rangle > 0$, because of the average ellipsoidal shape of the overlapping area between the colliding nuclei, and $0 < \varepsilon_2 < 1$, $P(v_2)$ cannot be symmetric around its mean and in particular will be left skewed. Moreover, γ_1 has been predicted to increase in absolute value from central to peripheral collisions [182], being roughly proportional to $\langle v_{2x}\rangle$ and being inversely proportional to the square root of the system size [181]. Different initial-state models agree at least qualitatively with this expectation. The non-linear dependence between v_2 and ε_2, which becomes important in peripheral collisions, is expected to qualitatively enhance this trend, as previously shown in 5.3. γ_1 can be estimated from the fine-splitting between two- and multi-particle cumulants [182]:

$$\gamma_1^{\text{exp}} = -6\sqrt{2}v_2\{4\}^2 \frac{v_2\{4\} - v_2\{6\}}{(v_2\{2\}^2 - v_2\{4\}^2)^{3/2}}. \tag{5.12}$$

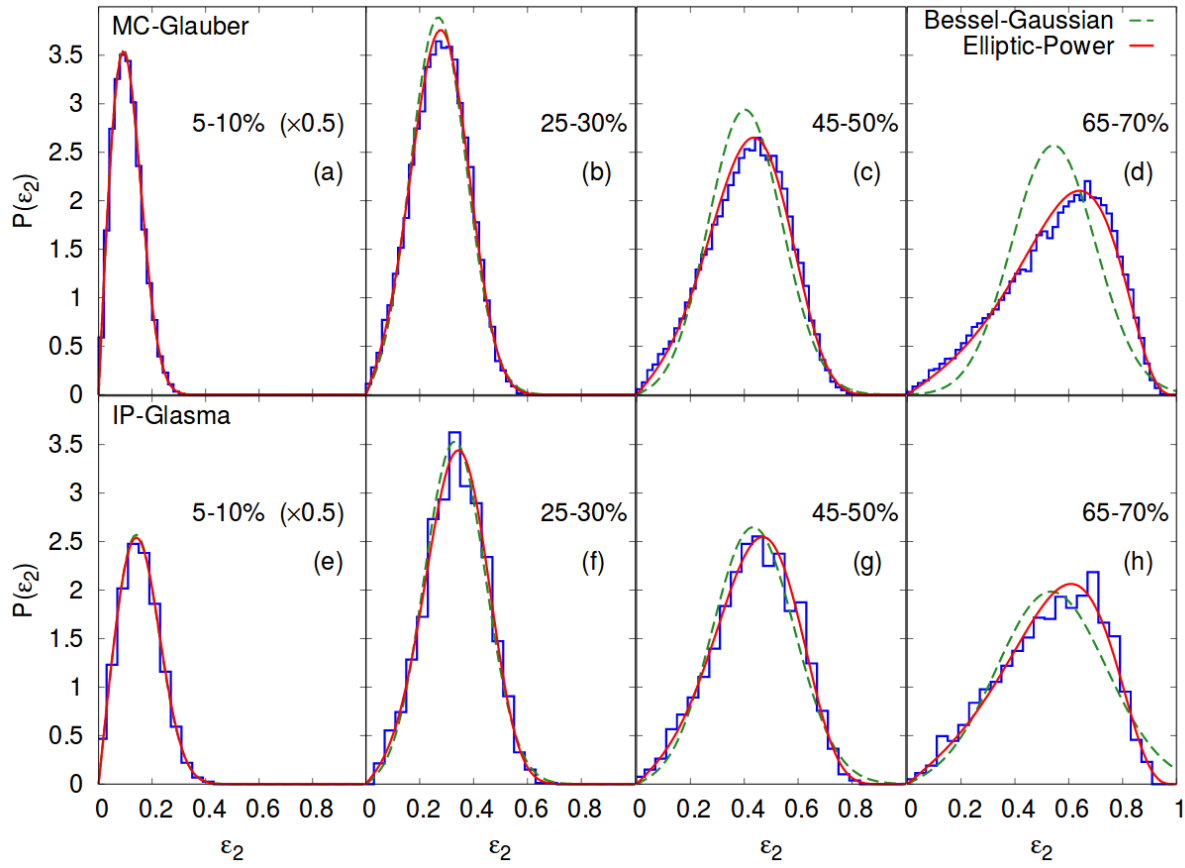

Figure 5.1: (Color online) Distribution of ε_2 in Pb–Pb collisions at 2.76 TeV using the PHOBOS Monte Carlo Glauber [19] (panels (a) to (d)) and the IP-Glasma [15] (panels (e) to (h)) for four centrality bins (with decreasing centrality or increasing centrality percentile from left to right). Solid curves are fits using the Elliptic Power distribution, eq.5.3, dashed curves are fits using the Bessel-Gaussian distribution, eq. 5.2. Figure taken from [180].

It is noted as γ_1^{exp} to underline that it does not exactly match the definition of γ_1 given in Eq. 5.11, although the two have been estimated to coincide within a few percents [182]. The derivation of Eq. 5.12 relies on a Taylor expansion of the generating function in powers of the moments, truncated at the order of the skewness. It is experimentally possible to test the validity of such approximation through the universal equality that implies [182]:

$$v_2\{6\} - v_2\{8\} = \frac{1}{11}(v_2\{4\} - v_2\{6\}). \tag{5.13}$$

The precision up to which this equality holds depends on the residual contribution of higher central moments of the flow p.d.f., e.g. the kurtosis, to the multi-particle cumulants.

Recent CMS results on non-Gaussian elliptic flow fluctuations [187] appeared during the writing of this dissertation. Numerical data are not yet available, but seem to be essentially compatible with our measurements.

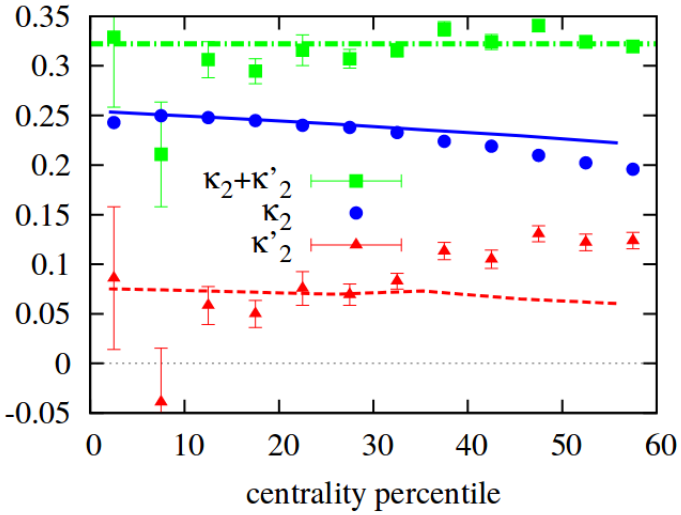

Figure 5.2: Response coefficients k_2 and k_2', defined in Eq. 5.4, for Pb-Pb collisions at $\sqrt{s_{\mathrm{NN}}} = 2.76$ TeV, as a function of centrality. Markers: with fluctuating initial conditions, lines: with smooth initial conditions. Figure taken from [185].

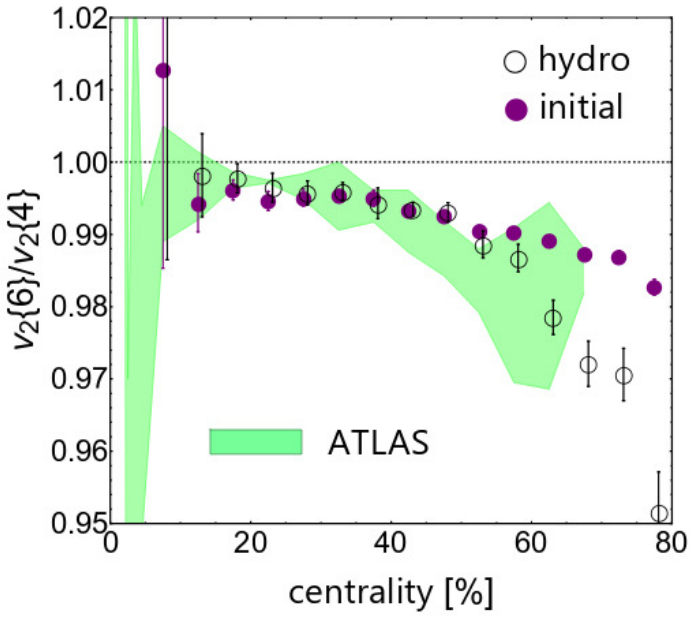

Figure 5.3: Shaded band: ATLAS data for $v_2\{6\}/v_2\{4\}$ versus centrality [183]. Open symbols: hydrodynamic calculations. Full symbols: $\varepsilon_2\{6\}/\varepsilon_2\{4\}$. Figure taken from [182].

Source	$v_2\{2\}$	$v_2\{4\}$	$v_2\{6\}$	$v_2\{8\}$
tracking	1.2%	1%	1%	1%
particle charge	n.s.	n.s.	n.s.	n.s.
primary vertex position	n.s.	n.s.	n.s.	n.s.
centrality determination	0.8%	0.8%	0.8%	0.8%
magnet polarity	n.s.	n.s.	n.s.	n.s.

Table 5.1: Relative systematic uncertainties for $v_2\{m\}$, $c_2\{m\}$ ($m = 2, 4, 6, 8$), their ratios and γ_1^{exp} in Pb–Pb collisions at $\sqrt{s_{\text{NN}}} = 5.02$ TeV and centrality 20-30%.

Source	$v_2\{6\}/v_2\{4\}$	$v_2\{8\}/v_2\{4\}$	$v_2\{8\}/v_2\{6\}$	γ_1^{exp}
tracking	0.04%	0.03%	0.003%	11%
particle charge	n.s.	n.s.	0.002%	7%
primary vertex position	n.s.	n.s.	n.s.	4%
centrality determination	0.03%	0.03%	0.001%	6%
magnet polarity	n.s.	n.s.	n.s.	2%

Table 5.2: Relative systematic uncertainties for $v_2\{m\}$, $c_2\{m\}$ ($m = 2, 4, 6, 8$), their ratios and γ_1^{exp} in Pb–Pb collisions at $\sqrt{s_{\text{NN}}} = 5.02$ TeV and centrality 20-30%.

5.2 Event and track selection

The full data sample of Pb–Pb collisions at $\sqrt{s_{\text{NN}}} = 5.02$ (2.76) TeV collected by the ALICE detector in 2015 (2010), corresponding to an integrated luminosity of 12.7 (1.7) μb^{-1} in the centrality range 0-80%, is analysed. The event and track selection follows the procedure explained in Sec. 2.3.1 and 2.3.3, respectively. Unidentified charged particles in the pseudorapidity range $|\eta| < 0.8$ and transverse momentum $0.2 < p_{\text{T}} < 50$ GeV/c are selected. Centrality is determined via the total energy deposited in the two V0 detectors, as explained in Sec. 2.3.2.

5.3 Systematic uncertainties

The systematic uncertainties are evaluated following the procedure explained in Sec. 3.5. The same sources of systematic uncertainties presented in Sec. 4.3 are investigated, varying track and event quality variables with the same procedure.

The contributions of the sources of systematic uncertainty to the total systematic uncertainty for the different multi-particle cumulants $c_2\{m\}$ and the corresponding flow coefficients $v_2\{m\}$ is very similar. For results at $\sqrt{s_{\text{NN}}} = 5.02$ TeV, the dominant ones are track quality variables and centrality determination. The same applies for results at $\sqrt{s_{\text{NN}}} = 2.76$ TeV, with slightly larger uncertainties from track quality variables and smaller ones from centrality determination. As discussed in Sec. 4.3, the larger uncertainties in centrality determination for results at $\sqrt{s_{\text{NN}}} = 5.02$ TeV are attributed to a deterioration of the energy resolution of the V0 detectors across the years. Little or no centrality dependence of the absolute value of systematic uncertainties is observed for results at both energies. Concerning the ratios $v_2\{n\}/v_2\{m\}$, the systematic uncertainties are greatly reduced, since they are strongly correlated between any given $v_2\{n\}$ and $v_2\{m\}$. The same applies for γ_1^{exp}, which is a combination of different $v_2\{m\}$. As a refer-

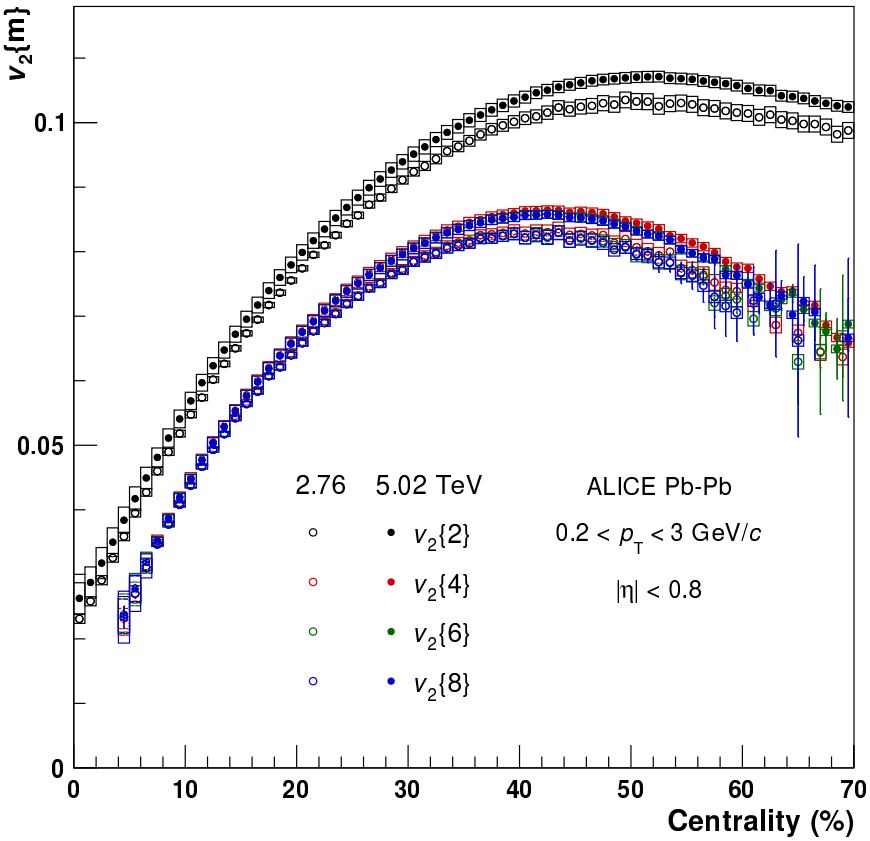

Figure 5.4: Elliptic flow coefficient v_2 of inclusive charged particles as a function of centrality, measured with the two- and multi-particle cumulant methods. Measurements for Pb–Pb collisions at $\sqrt{s_{\rm NN}} = 5.02$ (2.76) TeV are shown by solid (open) markers.

ence, the contribution of the different sources of systematic uncertainty to the observables hereby presented is summarised in Tab. 5.1, for results at $\sqrt{s_{\rm NN}} = 5.02$ TeV and centrality 20-30%.

5.4 Results

Figure 5.4 shows the integrated v_2 in the $p_{\rm T}$ range $0.2 < p_{\rm T} < 3$ GeV/c as a function of centrality, measured with two-, four-, six- and eight-particle cumulants at $\sqrt{s_{\rm NN}} = 2.76$ and 5.02 TeV. The corresponding cumulants ($c_2\{2, 4, 6, 8\}$) are reported in Fig. 5.5. The centrality dependence is similar for all multi-particle cumulants and similar to what is shown in Fig. 4.4. The differences between $v_2\{2\}$ (shown in Fig. 5.4) and $v_2\{2, |\Delta\eta| > 1\}$ (shown in Fig. 4.4) are mostly attributed to non-flow contributions, which are suppressed in the case of results with a pseudorapidity gap. The possible differences arising from the decorrelation of event planes at different pseudorapidities are expected to be less than 1%, as explained in Sec. 4.4. Non-flow contributions in $v_2\{m\}$ ($m > 2$) have been previously found to be negligible [134, 186]. This is tested explicitly for $v_2\{4\}$ by correlating 2 tracks at $\eta < 1$ with 2 tracks at $\eta > 1$, i.e. by measuring a two-subevent four-particle cumulant [188] with a pseudorapidity gap of 0 ($|\Delta\eta| > 0$). No significant differences are observed.

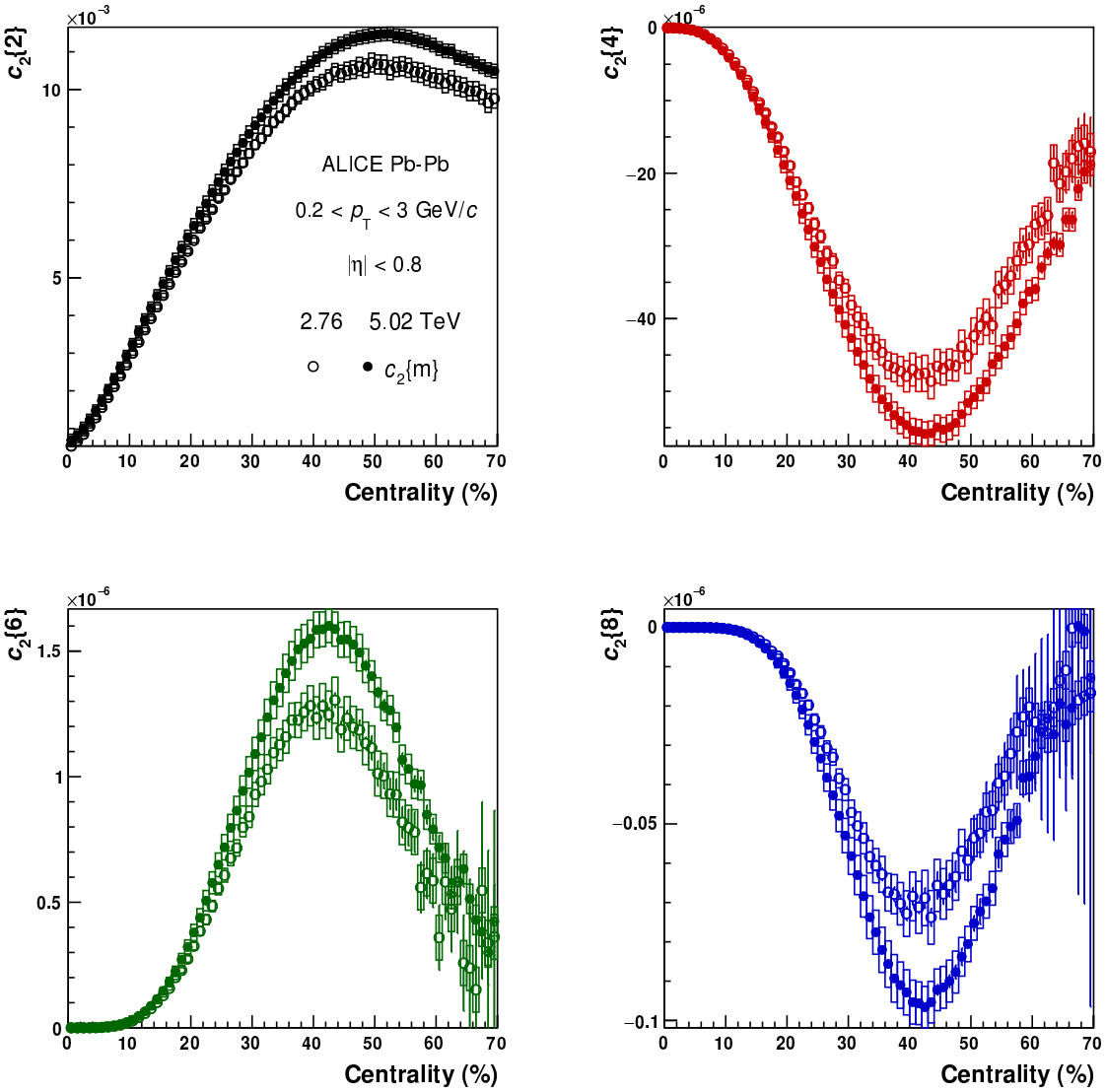

Figure 5.5: Cumulants c_2 of elliptic flow of inclusive charged particles as a function of centrality, for the two-particle and multi-particle cumulant methods. Measurements for Pb–Pb collisions at $\sqrt{s_{\mathrm{NN}}} = 5.02$ (2.76) TeV are shown by solid (open) markers.

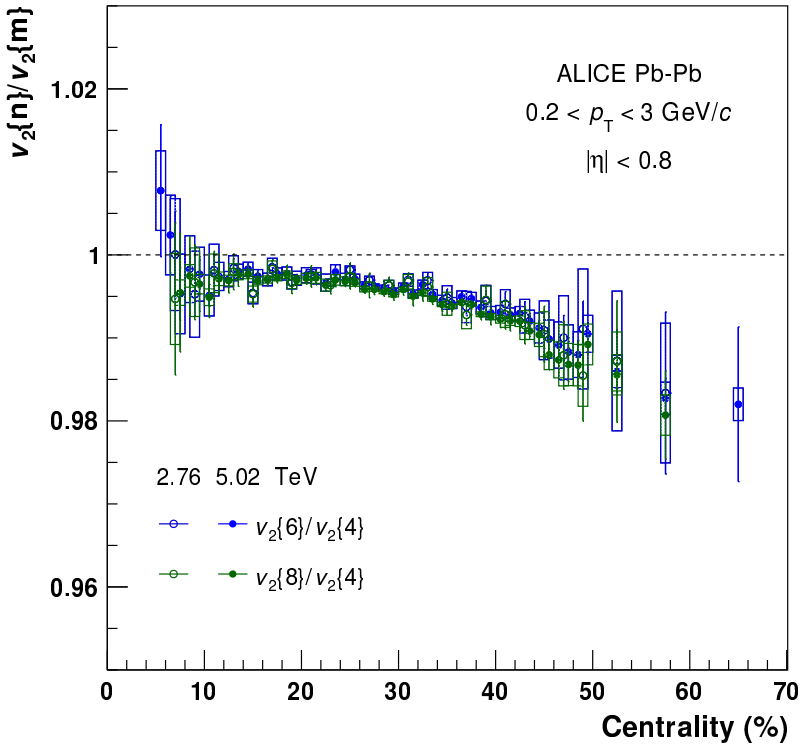

Figure 5.6: Ratios of elliptic flow coefficients $v_2\{4\}$, $v_2\{6\}$ and $v_2\{8\}$ as a function of centrality. Measurements at $\sqrt{s_{\rm NN}} = 5.02$ (2.76) TeV are shown by solid (open) markers.

A fine-splitting of less than 1% is observed among $v_2\{4\}$, $v_2\{6\}$ and $v_2\{8\}$, as it can be seen from their ratios, shown in Fig. 5.6 for both collision energies. The ratios $v_2\{6\}/v_2\{4\}$ and $v_2\{8\}/v_2\{4\}$ at $\sqrt{s_{\rm NN}} = 5.02$ TeV show a significant centrality dependence: the deviations of the ratios from unity is about 0.2% in central and increases up to about 1% for midcentral collisions. A further increase seems to be observed for more peripheral collisions, up to about 2% for centralities above 50%. This fine-splitting is consistent with non-Bessel-Gaussian behaviour of event-by-event flow fluctuations, as previously explained. These ratios are found to be independent from the choice of $p_{\rm T}$ range within $0.2 < p_{\rm T} < 3$ GeV/c, indicating that the characterization of flow fluctuations at low $p_{\rm T}$ does not depend on $p_{\rm T}$. Results at $\sqrt{s_{\rm NN}} = 2.76$ TeV are found to be compatible, indicating that these ratios do not change significantly across collision energies. Compared to calculations [182] employing MC-Glauber initial conditions [19] and viscous hydrodynamics (v-USPhydro [154]) for Pb–Pb collisions at $\sqrt{s_{\rm NN}} = 2.76$ TeV, the ratios $v_2\{6\}/v_2\{4\}$ and $v_2\{8\}/v_2\{4\}$ are found to be compatible. A good agreement is found between the results at $\sqrt{s_{\rm NN}} = 2.76$ TeV and ATLAS results on flow p.d.f. via a data-driven unfolding technique [183], as shown in Fig. 5.7.

Figure 5.8 shows the ratio between $v_2\{8\}$ and $v_2\{6\}$ at $\sqrt{s_{\rm NN}} = 5.02$ TeV. A hint of a further fine-splitting between these two, of the order of 0.05%, is observed. The results suggest little or no centrality dependence within centrality 10-50%. This difference is

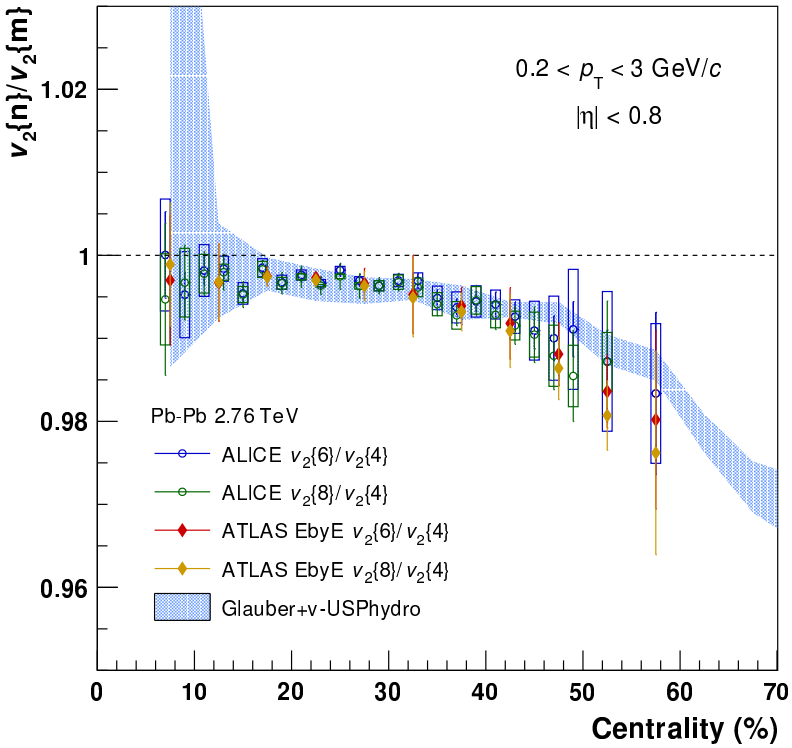

Figure 5.7: Ratios of elliptic flow coefficients $v_2\{4\}$, $v_2\{6\}$ and $v_2\{8\}$ as a function of centrality, at $\sqrt{s_{\mathrm{NN}}} = 2.76$ TeV. Hydrodynamic calculations [182] and ATLAS measurements [183] are shown for comparison.

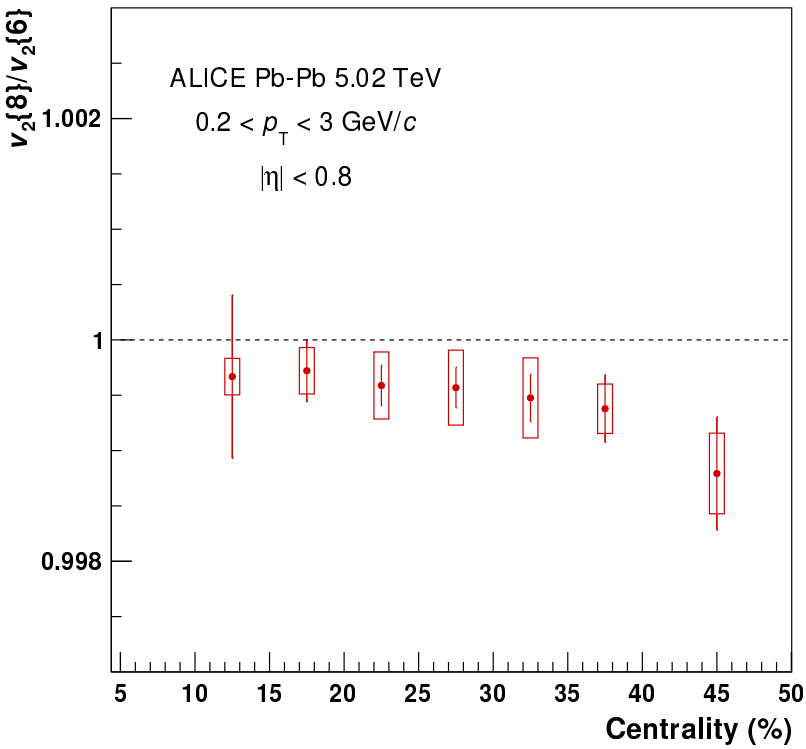

Figure 5.8: Ratio of elliptic flow coefficients $v_2\{8\}/v_2\{6\}$ of inclusive charged particles as a function of centrality.

also consistent with non-Bessel-Gaussian elliptic flow fluctuations, and can be attributed to different contributions of the skewness to these higher-order cumulants [182], see Eq. 5.7-5.8. Corresponding results at $\sqrt{s_{\rm NN}} = 2.76$ TeV, here and in the following, are not shown because of the large statistical uncertainties. Figure 5.9 shows $v_2\{6\} - v_2\{8\}$ and $(v_2\{4\} - v_2\{6\})/11$ at $\sqrt{s_{\rm NN}} = 5.02$ TeV: these two are observed to be in agreement, which demonstrates the validity of Eq. 5.13. This observation sets an upper limit of 4×10^{-4} at 95% confidence level for possible contributions to multi-particle cumulants from higher moments of the flow p.d.f. (kurtosis and beyond) in the centrality range 10-50%. This estimate is obtained assuming Gaussian systematic uncertainties and summing them in quadrature with the statistical ones.

Figure 5.10 shows the measurement of the standardised skewness ($\gamma_1^{\rm exp}$) at $\sqrt{s_{\rm NN}} = 5.02$ TeV as a function of centrality. To suppress non-flow contributions, the values of $v_2\{2, |\Delta\eta| > 1\}$ from Fig. 4.4 are used for $v_2\{2\}$ in Eq. 5.12. A negative value of the skewness, with a strong centrality dependence, is observed: $\gamma_1^{\rm exp}$ decreases from zero in central to about -0.4 in peripheral collisions. Compared to model calculations [182] for Pb–Pb collisions at $\sqrt{s_{\rm NN}} = 2.76$ TeV, the results are found to be compatible for the entire centrality range. This observation is consistent with the elliptic flow p.d.f. being progressively more left-skewed going from central to peripheral collisions. We attribute this feature to the combination of an increase in $\langle\varepsilon_2\rangle$ and the geometrical constraint

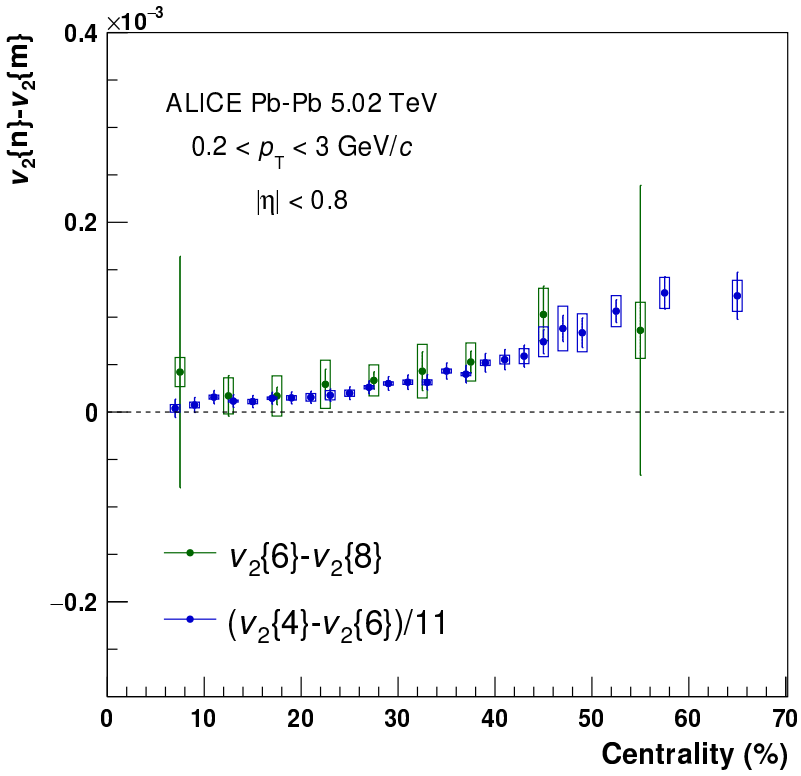

Figure 5.9: Differences of elliptic flow coefficients v_2 of inclusive charged particles between measurements with different multi-particle cumulant methods, as a function of centrality.

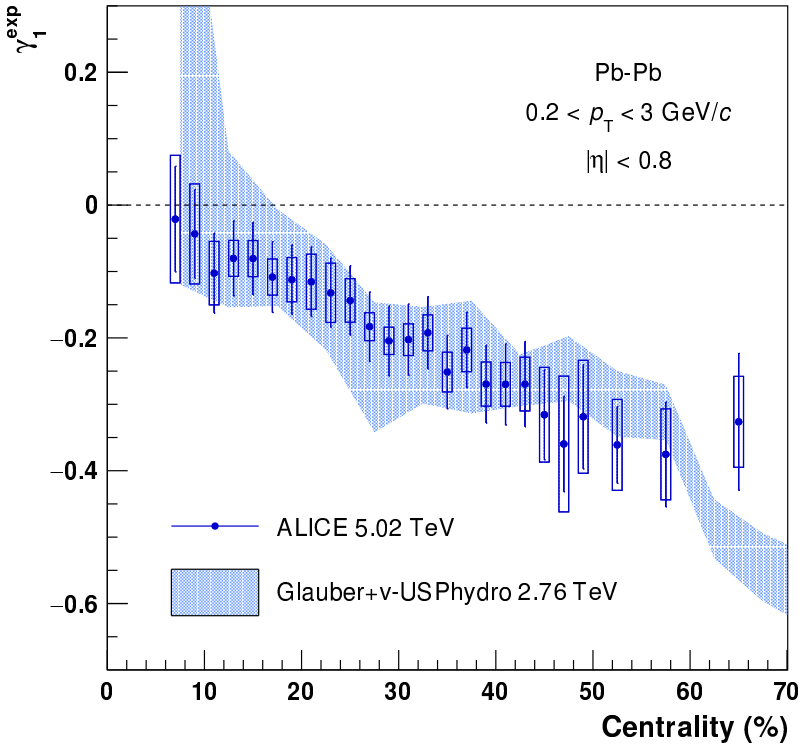

Figure 5.10: Skewness of elliptic flow γ_1^{exp} of inclusive charged particles as a function of centrality, for Pb–Pb collisions at $\sqrt{s_{\text{NN}}} = 5.02$ TeV. Hydrodynamic calculations [182] for Pb–Pb collisions at $\sqrt{s_{\text{NN}}} = 2.76$ TeV are shown for comparison.

$0 < \varepsilon_2 < 1$, as previously argued.

In order to report the full p.d.f. of elliptic flow $P(v_2)$, which can be compared to previous experimental results and theoretical predictions, it is parametrised with the Elliptic Power distribution [179, 180]

$$P(v_2) = \frac{\mathrm{d}\varepsilon_2}{\mathrm{d}v_2} P(\varepsilon_2) = \frac{1}{k_2} P\left(\frac{v_2}{k_2}\right) = \frac{2\alpha v_2}{\pi k_2^2} (1-\varepsilon_0^2)^{\alpha+1/2} \int_0^\pi \frac{(1 - v_2^2/k_2^2)^{\alpha-1}}{(1 - v_2\varepsilon_0 \cos\varphi/k_2)^{2\alpha+1}} \mathrm{d}\varphi, \tag{5.14}$$

and its three free parameters (α, ε_0 and k_2) are extracted from fits to the elliptic flow cumulants $c_2\{2, |\Delta\eta| > 1\}$ and $c_2\{m\}$ ($m = 4, 6, 8$) at $\sqrt{s_{\text{NN}}} = 5.02$ TeV. The parameter α quantifies the magnitude of elliptic flow fluctuations, ε_0 the mean eccentricity in the reaction plane and k_2 is the proportionality coefficient between initial-state eccentricity and v_2 coefficient: $v_2 = k_2\varepsilon_2$. The relation between cumulants and Elliptic Power parameters is given by [180]

$$c_2\{2\} = k_2^2 \, (1 - f_1) \,, \tag{5.15}$$

$$c_2\{4\} = -\, k_2^4 \, \left(1 - 2\, f_1 + 2\, f_1^2 - f_2\right) , \tag{5.16}$$

$$c_2\{6\} = k_2^6 \, \left(4 + 18\, f_1^2 - 12\, f_1^3 + 12 f_1 \, (3 f_2 - 1) - 6\, f_2 - \, f_3\right) , \tag{5.17}$$

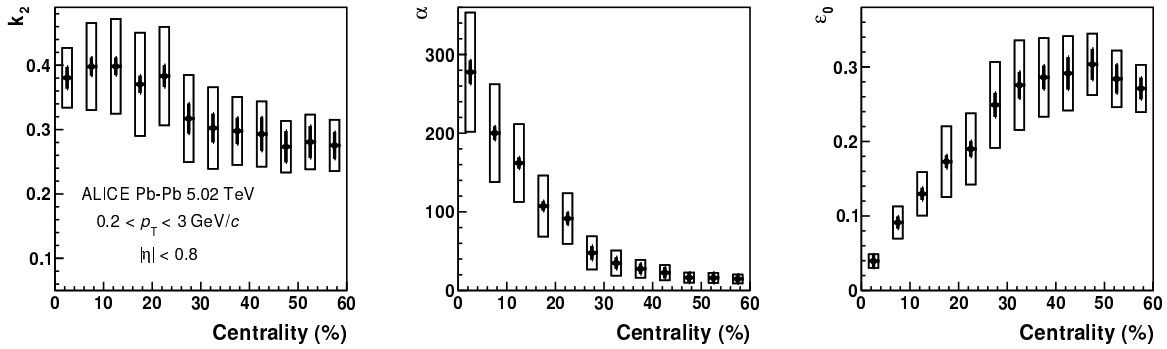

Figure 5.11: Elliptic power parameters k_2, α and ε_0 as a function of centrality, for Pb–Pb collisions at $\sqrt{s_{\rm NN}} = 5.02$ TeV, extracted from measurements of v_2 of inclusive charged particles with two-particle and multi-particle cumulant methods.

$$\begin{aligned} c_2\{8\} = &- k_2^8\,(33 - 288\,f_1^3 + 144\,f_1^4 - 66\,f_2 + 18\,f_2^2 - 24\,f_1^2(-11 + 6\,f_2) \\ &- 12\,f_3 + 4\,f_1(-33 + 42\,f_2 + 4\,f_3) - f_4) \end{aligned} \tag{5.18}$$

where

$$f_k \equiv \langle (1 - \varepsilon_n^2)^k \rangle = \frac{\alpha}{\alpha + k}\,(1 - \varepsilon_0^2)^k\,{}_2F_1\left(k + \frac{1}{2}, k; \alpha + k + 1, \varepsilon_0^2\right) \tag{5.19}$$

and ${}_2F_1$ is the hypergeometric function. The goodness of the fits is evaluated analysing the normalised residual distributions, which were found to be compatible with Gaussian distributions in most centrality bins according to a Kolmogorov-Smirnov test [189, 190]. The parameters extracted from the fits are shown in Fig. 5.11, as a function of centrality. The systematic uncertainties are assigned varying the fit ranges and initial values of the parameters and shifting the data points according to the corresponding systematic uncertainties. An additional source of uncertainty, which is investigated, is a possible cubic response coefficient k_2', defined as $v_2 = k_2\varepsilon_2 + k_2'\varepsilon_2^3$. This coefficient is introduced to quantify the possible increase of flow fluctuations that the hydrodynamic expansion of the medium introduces with respect to geometrical fluctuations in the initial state and was argued to be non-zero in mid-central and peripheral collisions due to general properties of the hydrodynamic phase [185]. In particular, k_2' is expected to be ≤ 0.15 in the centrality range 0-60% (Fig. 5.2). The residual differences in α, ε_0 and k_2 when including k_2' as an additional free parameter are considered in the systematic uncertainties. The statistical uncertainties are evaluated using the subsampling method: the analysed dataset is divided into 10 sub-samples and $c_2\{m\}$ is measured in each of them. The Elliptic Power parameters are then extracted in each subsample and their dispersion is used to estimate the statistical uncertainties.

The resulting p.d.f., scaled by the mean of $P(v_2)$ ($\langle v_2 \rangle$), is reported in Fig. 5.12, for the centrality intervals 5-10%, 25-30% and 45-50%. Other centralities intervals are shown in Fig. 5.13-5.15. Scaling by $\langle v_2 \rangle$ allows a comparison of our data with results by the ATLAS collaboration [157] obtained in different $p_{\rm T}$ ranges via a data-driven unfolding technique. The observed agreement is also consistent, as previously noted, with elliptic flow fluctuations at low $p_{\rm T}$ not depending on $p_{\rm T}$ and not changing significantly between collision energies, except for the trivial increase in $p_{\rm T}$-integrated v_2 due to the change in

$\langle p_{\rm T} \rangle$. Comparison with iEBE-VISHNU model calculations with AMPT and Trento initial conditions [133] indicates that Trento initial conditions are best at describing the data. The data are found to be in agreement also with predictions from the IP-Glasma+MUSIC model [132], although the uncertainties on the theoretical predictions do not allow to draw firm conclusions.

5.5 Discussion

A fine-splitting is observed among the flow coefficients estimated with different multi-particle cumulants $v_2\{m\}$ $(m = 2, 4, 6, 8)$ of inclusive charged particles in Pb–Pb collisions at $\sqrt{s_{\rm NN}} = 5.02$ and 2.76 TeV. Its origin is attributed to the non-Gaussian nature of elliptic flow fluctuations, that is expected to arise mostly from geometrical constraints to initial-state fluctuations. We observe no significant energy or $p_{\rm T}$ dependence of this fine-splitting within the $p_{\rm T}$ range under consideration ($0.2 < p_{\rm T} < 3$ GeV/c) and we find the data to be in good agreement with previous measurements at 2.76 TeV.

From a combination of $v_2\{m\}$ $(m = 2, 4, 6, 8)$, we extract a measurement of the skewness $\gamma_1^{\rm exp}$ of elliptic flow fluctuations and we find it to be in agreement with the general expectations: it is negative and decreasing from central to peripheral collisions. Compared with predictions from hydrodynamical models, it is found to be in good agreement.

In order to report the full elliptic flow p.d.f. $P(v_2)$, we choose to parametrise it with the Elliptic Power distribution, Eq. 5.14, and we extract its free parameters (α, ε_0 and k_2) from fits to elliptic flow coefficients $v_2\{m\}$ $(m = 2, 4, 6, 8)$, according to Eq. 5.15-5.18. Also for these results, the data show no significant $p_{\rm T}$ dependence, if not for a trivial increase in $\langle v_2 \rangle$, at low $p_{\rm T}$ and are found to be in good agreement with previous measurements at 2.76 TeV. It is worth to note that these latter were obtained with a different method, namely a data-driven unfolding technique, and with a different detector. The observed agreement with the present results therefore constitutes an important experimental validation of both measurements of $P(v_2)$.

Concerning the comparison with hydrodynamic model calculations, those employing IP-Glasma initial conditions, either fully modelled or with effective descriptions, such as Trento, favor the data as far as statistical uncertainties allow to tell. This might suggest that such model provides the best description of initial-state fluctuations. However, we also know that the hydrodynamic evolution has a small but sizable effect on elliptic flow fluctuations, and estimates will depend on the details of the hydrodynamic model itself (numerical implementation, input parameters such as η/s). In model calculations, e.g. those in [133], the hydrodynamic response is tuned to match the measured $\langle v_2 \rangle$ differently for each initial-state model and therefore its relative contribution to flow fluctuations differs. In other words, the contributions of initial-state fluctuations and hydrodynamic evolution are convoluted and we find it hard to decouple them from an analysis of $P(v_2)$ distributions alone, making it difficult to discriminate among initial-state models. However, we argue that these results might play an important role in this regard once included in a broader analysis of bulk observables, as discussed in the context of the results of Ch. 4.

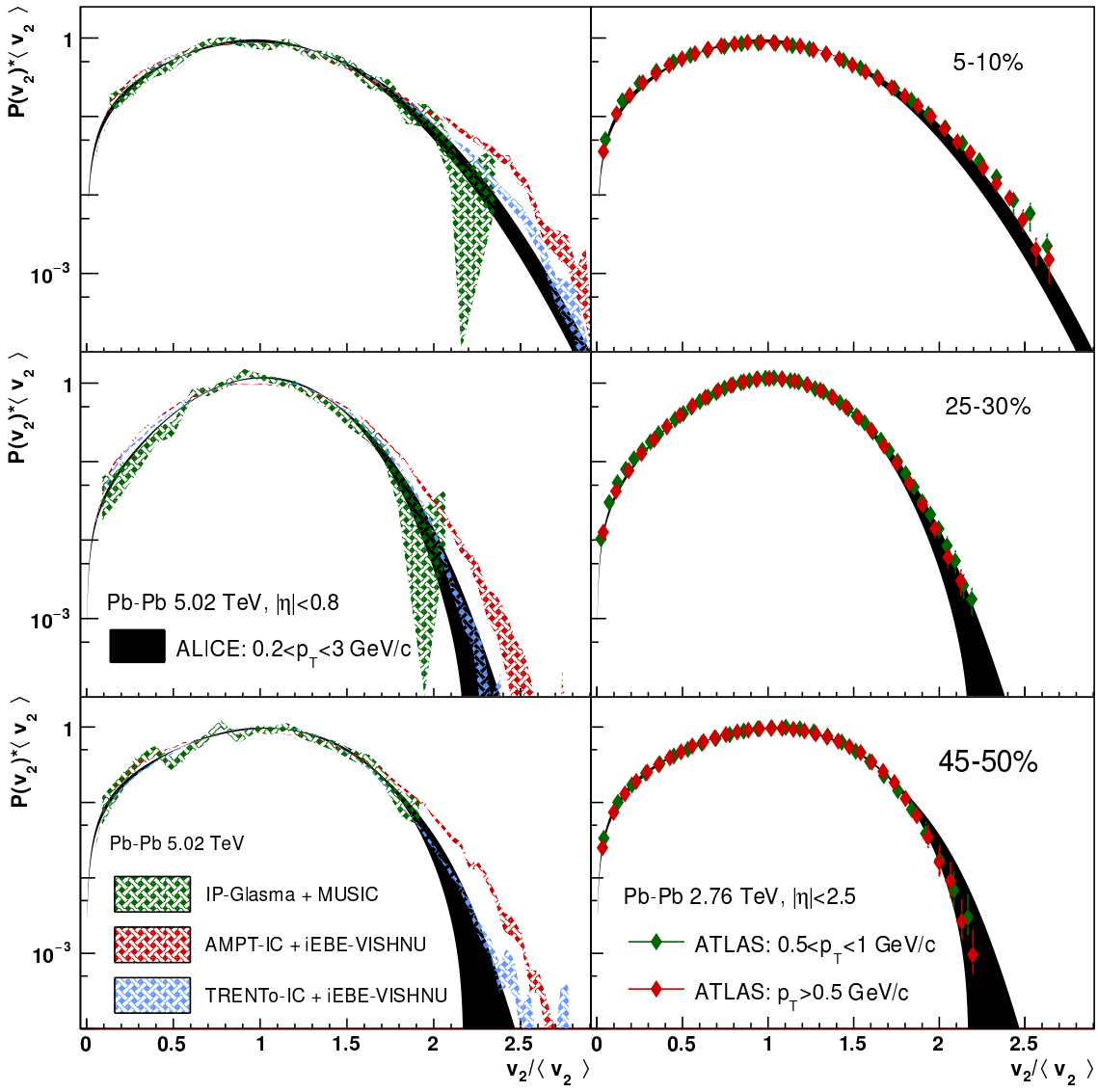

Figure 5.12: Elliptic flow p.d.f. $P(v_2)$ rescaled by the mean v_2 ($\langle v_2 \rangle$) of inclusive charged particles for Pb–Pb collisions at $\sqrt{s_{\rm NN}} = 5.02$ TeV, in different centrality classes. Several hydrodynamic calculations [132, 133] and previous measurements from ATLAS [157] at lower energies are shown for comparison.

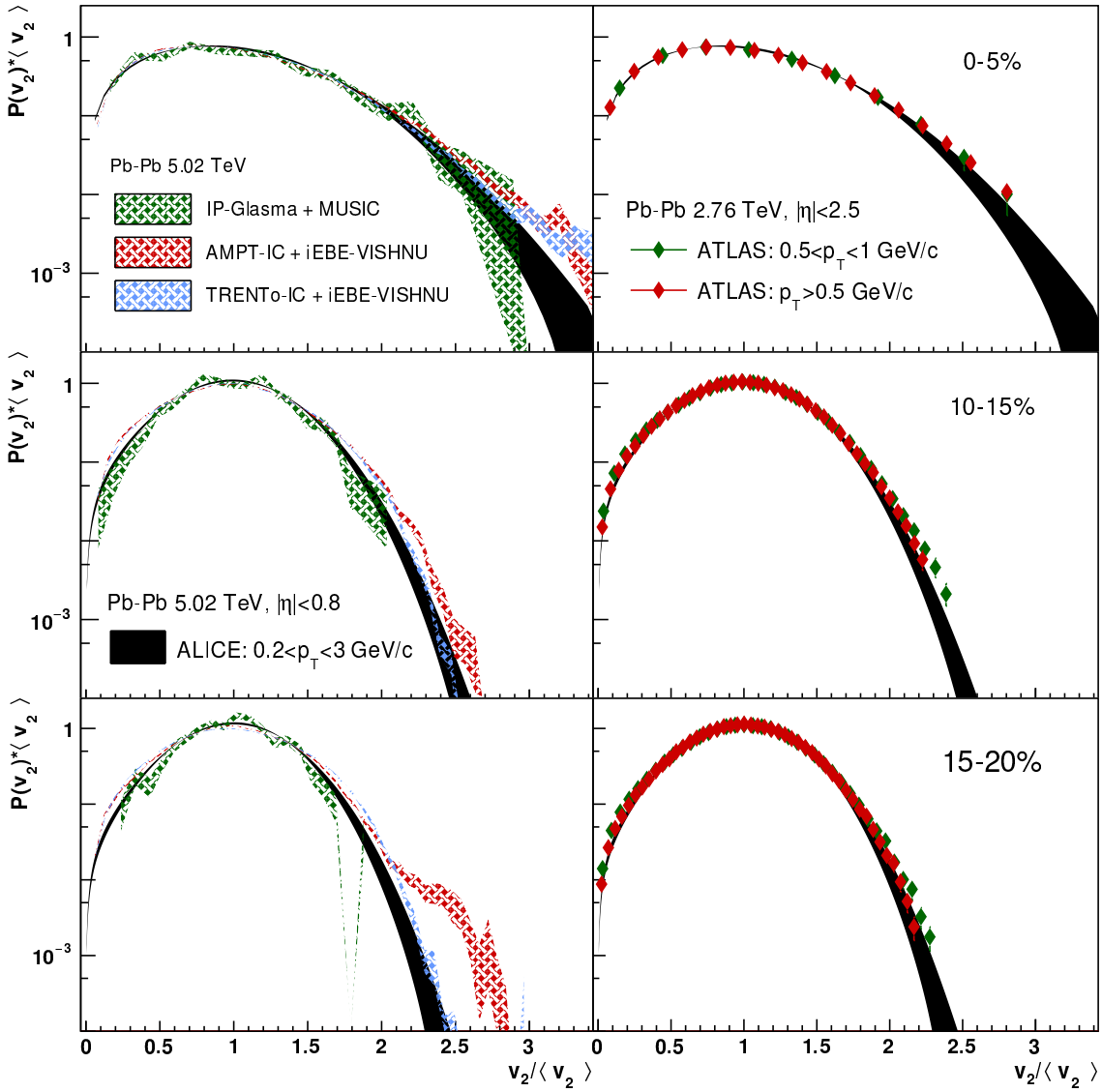

Figure 5.13: Elliptic flow p.d.f. $P(v_2)$ rescaled by $\langle v_2 \rangle$ in the centralities intervals 0-5%, 10-15% and 15-20% for Pb–Pb collisions at $\sqrt{s_{\mathrm{NN}}} = 5.02$ TeV.

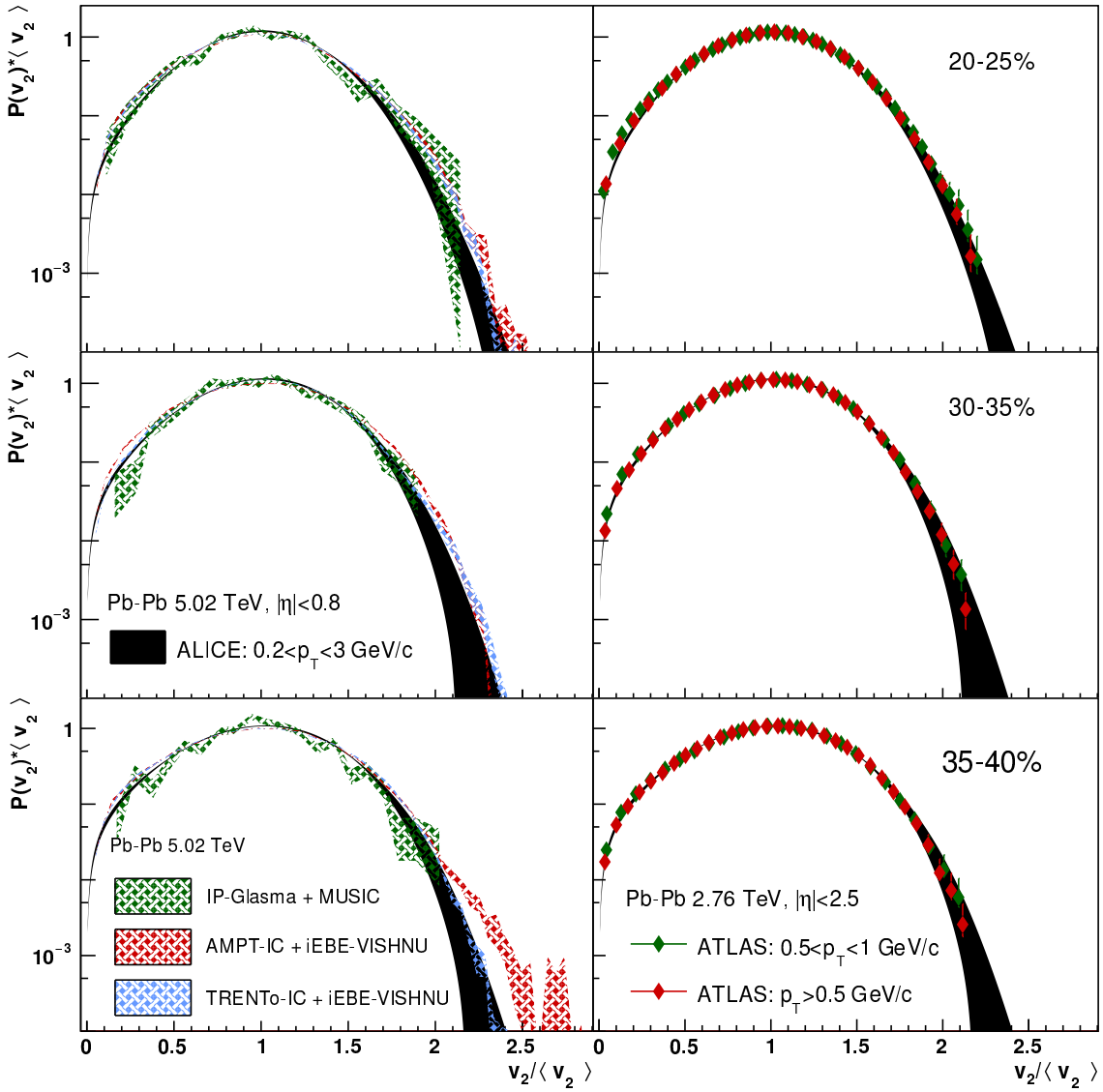

Figure 5.14: Elliptic flow p.d.f. $P(v_2)$ rescaled by $\langle v_2 \rangle$ in the centralities intervals 20-25%, 30-35% and 35-40% for Pb–Pb collisions at $\sqrt{s_{\mathrm{NN}}} = 5.02$ TeV.

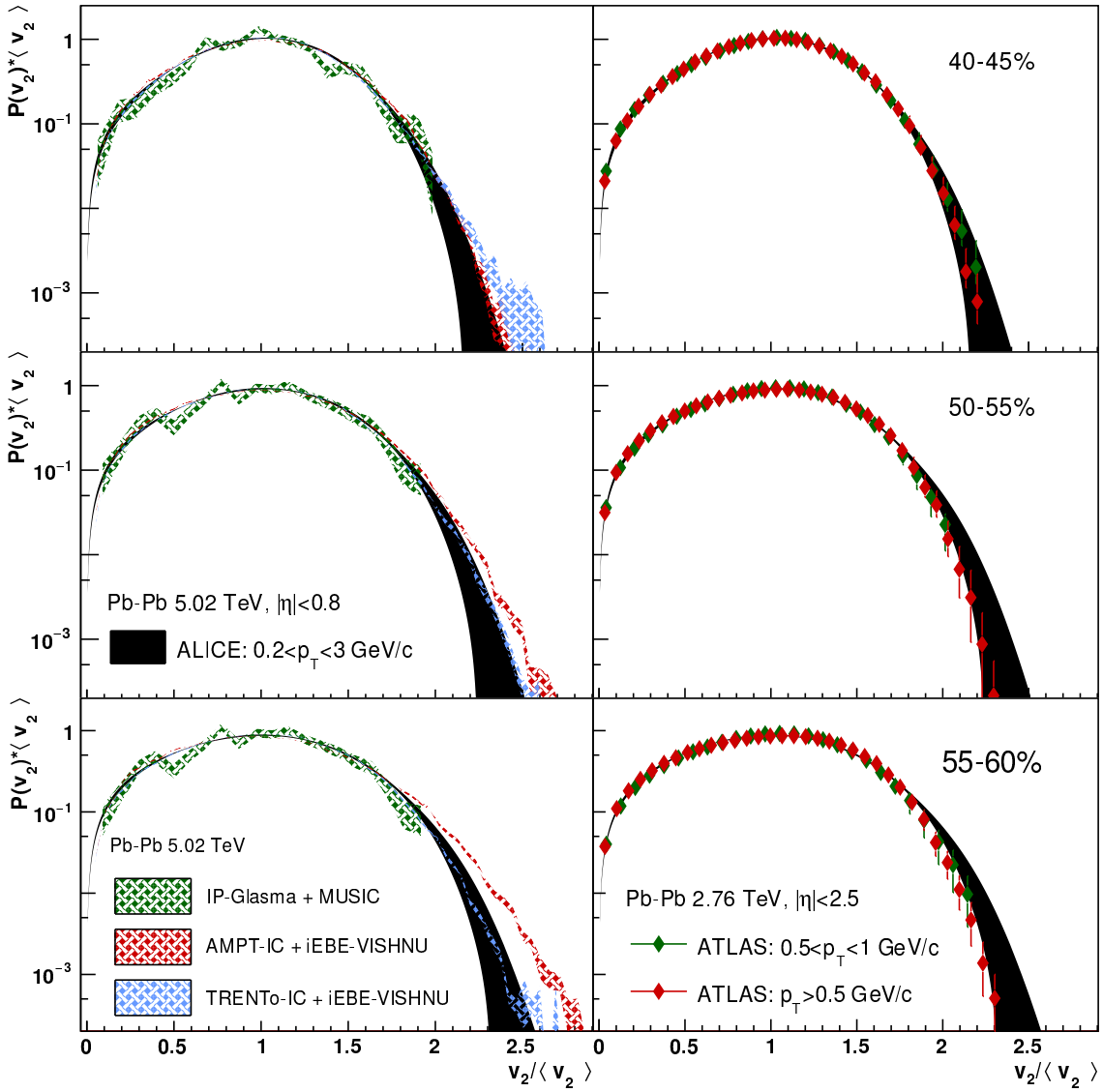

Figure 5.15: Elliptic flow p.d.f. $P(v_2)$ rescaled by $\langle v_2 \rangle$ in the centralities intervals 40-45%, 50-55% and 55-60% for Pb–Pb collisions at $\sqrt{s_{\mathrm{NN}}} = 5.02$ TeV.

Chapter 6

Charge Correlations and Flow Fluctuations

from an idea of Sergei Voloshin,
in collaboration with Alexandru Dobrin

6.1 Introduction

In this chapter, we investigate the dependence of some observables sensitive to the Chiral Magnetic Effect (CME) on the fluctuations of elliptic flow. In particular, we study how the background and the signal in such observables are expected to change as a function of the strength of the elliptic flow, on an event-by-event basis, and we use the differences to estimate their relative contribution.

As introduced in sec.1.5, the searches for the Chiral Magnetic Effect (CME) in Heavy–Ion collisions have mostly been based on the charge-dependent 2- and 3-particle correlators $\delta_{\alpha\beta}$ and $\gamma_{\alpha\beta}$ [93]

$$\delta_{\alpha\beta} = \langle \cos(\varphi_\alpha - \varphi_\beta) \rangle, \tag{6.1}$$
$$\gamma_{\alpha\beta} = \langle \cos(\varphi_\alpha + \varphi_\beta - 2\Psi_{\mathrm{RP}}) \rangle, \tag{6.2}$$

where $\alpha, \beta = \pm$ refer to charge. The reaction plane Ψ_{RP} is not experimentally accessible and is approximated with the second-order event plane Ψ_2, which can be reconstructed from the azimuthal particle distribution

$$\Psi_n = \frac{1}{n} \operatorname{atan2}\left(\frac{\operatorname{Im} Q_n}{\operatorname{Re} Q_n}\right), \tag{6.3}$$

where the Q-vector is defined in Eq. 3.2-3.3. This is why $\gamma_{\alpha\beta}$ is effectively a 3-particle correlator. If one defines a CME signal a_1 in the azimuthal distribution of particles as in Eq. 1.8, it is clear that such correlators, in the absence of background, are proportional to

$$\delta_{\alpha\beta} = \langle v_{1,\alpha} v_{1,\beta} \rangle + \langle a_{1,\alpha} a_{1,\beta} \rangle, \tag{6.4}$$
$$\gamma_{\alpha\beta} = \langle v_{1,\alpha} v_{1,\beta} \rangle - \langle a_{1,\alpha} a_{1,\beta} \rangle. \tag{6.5}$$

Assuming $a_{1,+} = -a_{1,-}$ and the directed flow v_1 to be charge-independent, one would expect the difference between same- and opposite-charge pair correlators $\Delta\gamma$ and $\Delta\delta$ to be exactly equal to the CME signal, with the two correlators having same magnitude and opposite sign

$$\Delta\delta = \delta_{\pm\mp} - \delta_{\pm\pm} = -2\langle a_1^2 \rangle, \tag{6.6}$$

$$\Delta\gamma = \gamma_{\pm\mp} - \gamma_{\pm\pm} = 2\langle a_1^2 \rangle. \tag{6.7}$$

The presence of a CME signal would have a clear signature in terms of the differences between these correlators: $\delta_{\pm\mp} = \gamma_{\pm\pm} < 0$, $\delta_{\pm\mp} = \gamma_{\pm\mp} > 0$. Previous measurements at RHIC [191, 192, 193, 194] and LHC [195] showed to be only partially in agreement with the expectations, proving that sources of background are undoubtedly present and raising the question of how much they actually contribute to these observables. Recent studies [196] that compared $\delta_{\alpha\beta}$ and $\gamma_{\alpha\beta}$ in peripheral Pb–Pb collisions and central p–Pb ones, where no or small CME signal is expected [197, 198], suggest that the background contribution is indeed dominant. The possible sources of background are believed to be both charge-independent, such as momentum conservation [94, 95] and directed flow fluctuations [46], and charge-dependent, such as Local Charge Conservation (LCC) [96, 94]. This latter, in particular, does not cancel in the difference between same- and opposite-charge pair correlators and is therefore expected to be the dominant source of background in $\Delta\gamma$ and $\Delta\delta$ [97]. Because of this, here and in the following, we focus on the study of LCC.

In a heavy-ion collision, electric charge is conserved; this is true both globally, which is trivial, and, up to a certain extent, locally in phase-space (φ, η, p_{T}). In fact, the majority of quarks are produced during the evolution of the system through multiple parton-parton interactions, each of which preserves electric charge. Therefore, correlations in phase-space between n-tuples of oppositely-charged quarks (with $n = 2, 4, 6 \ldots$) are to be expected simply from the common origin of such n-tuples, irrespectively of the details of the production mechanism. Such correlations are modified by the collective evolution of the system and by hadronization, but essentialy propagate to final-state particles. One would then expect the azimuthal correlations due to LCC to be stronger for opposite-charge pairs than for same-charge pairs. In terms of correlators, this translate into a positive contribution to both $\Delta\delta$ and $\Delta\gamma$, which, contrary to the CME hypothesis, is qualitatively consistent with measurements (in particular with the positive sign of both $\Delta\delta$ and $\Delta\gamma$). The LCC background cannot be estimated and subtracted by means of Monte Carlo (MC) event generators, as it is usually done in high-energy particle physics, since the precision to which they are able to reproduce this mechanism is inadequate for practical purposes. This can be seen, for instance, in the studies of balance functions, both at RHIC [199, 200] and LHC [201, 202], which are sensitive to the strength of LCC-induced correlations and were shown to be poorly reproduced by common MC generators, such as HIJING [126] and AMPT [151]. Therefore, alternative methods were proposed to decouple background and signal contributions to $\delta_{\alpha\beta}$ and $\gamma_{\alpha\beta}$, one of which exploits the differences in the dependence on elliptic flow v_2 of these two.

Event-Shape-Engineering (ESE) [159] is an experimental technique that allows to select events with higher or lower average values of v_2 in a given centrality class [158, 203], or, in other words, to classify events according to the strength of v_2. This corresponds to selecting events with higher or lower initial-state eccentricity ε_2 for a given impact param-

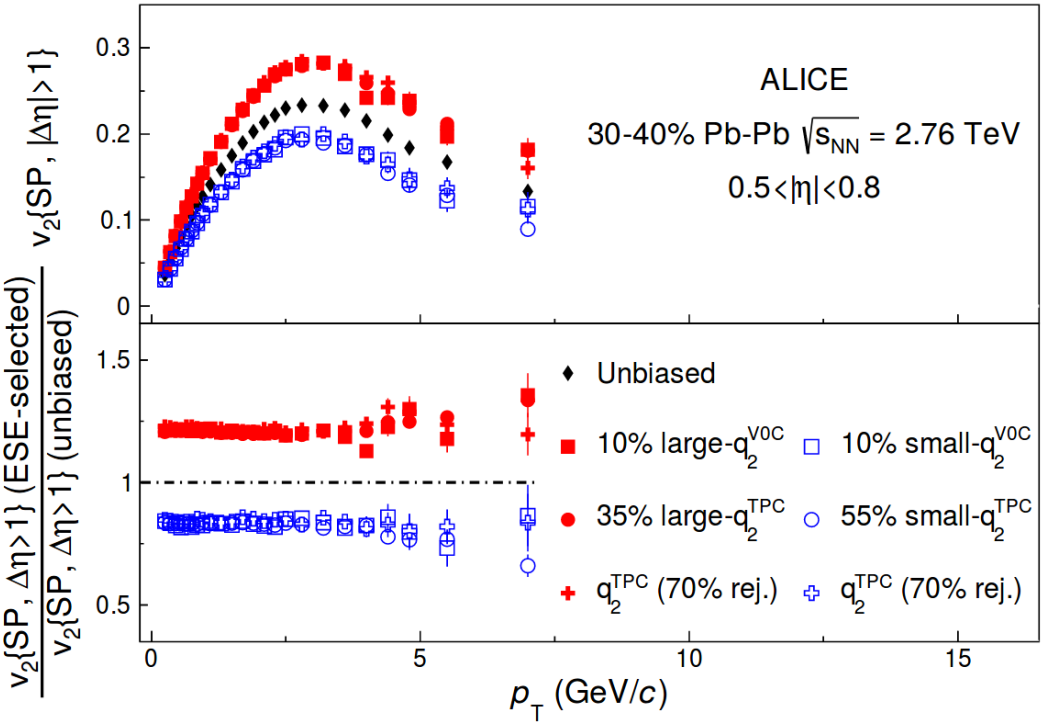

Figure 6.1: Comparison between the effect of the event-shape selection obtained with different detectors, for Pb–Pb collisions at $\sqrt{s_{\rm NN}} = 2.76$ TeV in the centrality class 30–40%. Figure taken from [158].

eter, since to first approximation v_2 is proportional to ε_2 (see Sec. 5.1). The classification is based on the magnitude of the second-order reduced flow vector q_2 [121], defined as

$$q_2 = \frac{|Q_2|}{\sqrt{M}}, \tag{6.8}$$

where Q_2 is the flow vector of the second harmonic and M is the multiplicity of the particles with which Q_2 is constructed. q_2 is used as a proxy for the magnitude of v_2 in a given event. In order to avoid trivial auto-correlations and the effects of non-flow, it is sufficient to impose a pseudorapidity gap of 1 unit or more between the tracks used to compute q_2 and those used to measure v_2 itself (or the observable of choice in a given ESE class) [158]. The discriminating power of q_2 depends mostly on the resolution of the detectors with which it is estimated. The effects of ESE classification can be seen in Fig. 6.1: changes on $\langle v_2 \rangle$ up to about 20% with respect to the unbiased sample can be obtained, with the effect being mostly independent of $p_{\rm T}$.

The application of ESE on the CME correlators allows to study their dependence on the magnitude of v_2, for a fixed centrality. The interest lies mostly on $\gamma_{\alpha\beta}$, which quantifies the correlation of charges with respect to the second order event plane Ψ_2 and is experimentally defined as

$$\gamma_{\alpha\beta} = \frac{\langle \cos(\varphi_\alpha + \varphi_\beta - 2\Psi_2) \rangle}{\mathrm{Res}(\Psi_2)}. \tag{6.9}$$

The event-plane resolution Res(Ψ_2) can be calculated from the correlations between Ψ_2 determined with different detectors [117]. It is expected that the correlation between the charge azimuthal distribution due to LCC and Ψ_2, which determines the background contribution in $\gamma_{\alpha\beta}$, is modulated by elliptic flow. This comes from two combined mechanisms. Firstly, charged tracks parallel to Ψ_2 (i.e. in-plane) are more correlated in $\Delta\varphi$ than those perpendicular to it (i.e. out-of-plane), because of the stronger collective expansion experienced by the former (Fig. 6.2, left). Secondly, for a given charged track it is more likely to find a balancing partner, i.e. another charged track with opposite charge, in-plane than out-of-plane (Fig. 6.2, right) [97]. The degree to which these mechanisms affect charge-dependent correlators depends on the magnitude of v_2. Therefore, the background contribution in $\gamma_{\alpha\beta}$ can be effectively changed with the use of ESE.

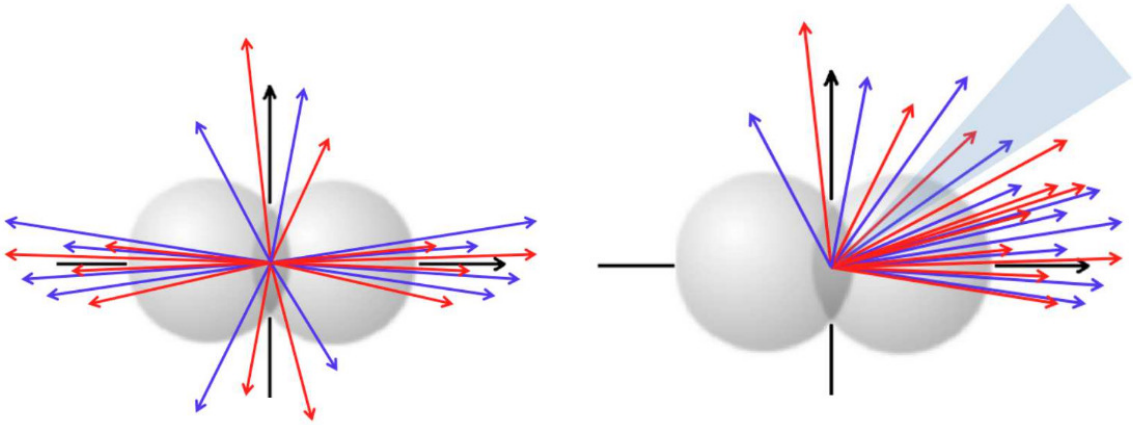

Figure 6.2: Charge-dependent azimuthal correlations due to LCC (see text). Figure adapted from [97].

The ALICE and CMS collaborations were the first to perform such measurements [204, 206] and reported, consistently with each other, a linear dependence of the form $\Delta\gamma \approx a \langle v_2 \rangle$, while $\Delta\delta$ was observed to be approximately independent of $\langle v_2 \rangle$ (Fig. 6.3 and 6.4). The proportionality coefficient a was also observed to increase from central to peripheral collisions. Given the experimental results, the questions that follow are:

1. how do the background and, possibly, the signal in $\gamma_{\alpha\beta}$ depend on the magnitude of v_2?

2. can we use this information to decouple the two?

The dependence of background in $\gamma_{\alpha\beta}$ and $\Delta\gamma$ on the magnitude of v_2 is investigated in Sec. 6.2. We assume LCC as being the dominant source, we parametrise it with a toy MC and we estimate its contribution to the CME correlators. While quantitatively we do not expect these estimates to be realistic, since the actual strength of LCC-induced correlations is presumably determined by the convolution of a number of effects, as discussed earlier, we do consider the model realistic enough to discuss the dependence of the background contribution to v_2.

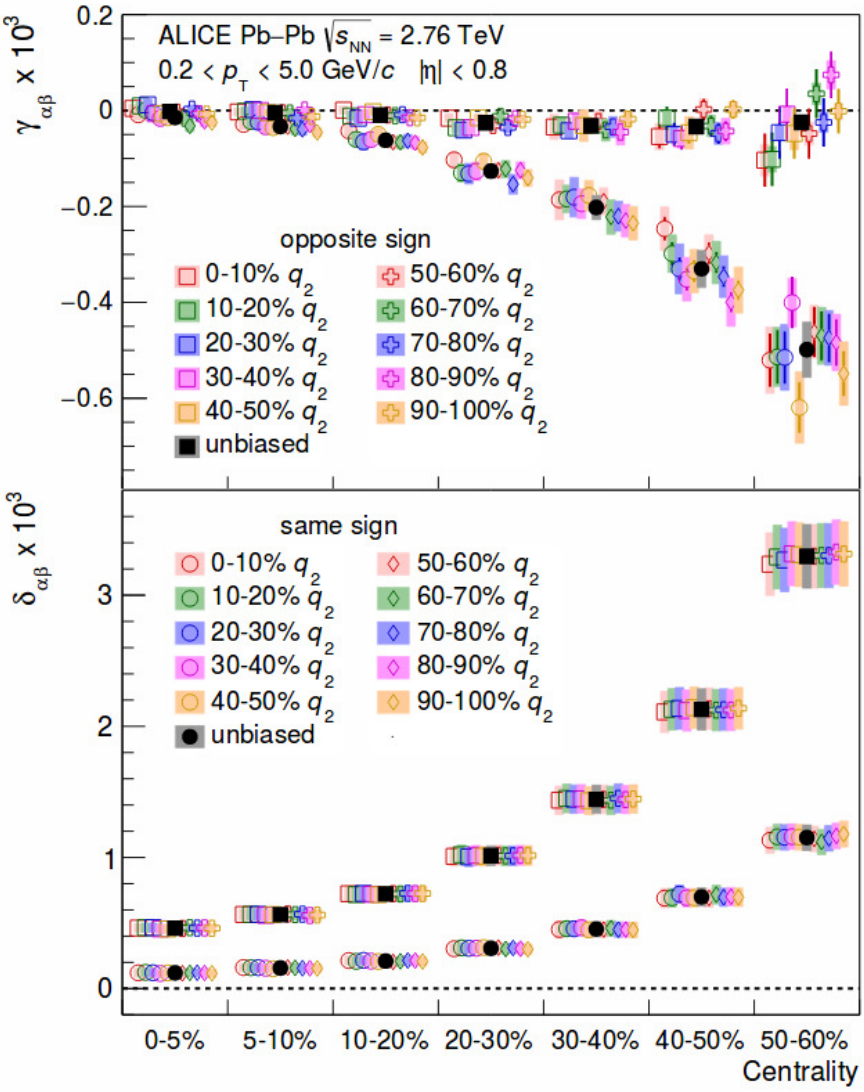

Figure 6.3: Centrality dependence of $\gamma_{\alpha\beta}$ (top) and $\delta_{\alpha\beta}$ (bottom) for pairs of particles with same and opposite charge for event-shape selected and unbiased events. Figure taken from [204].

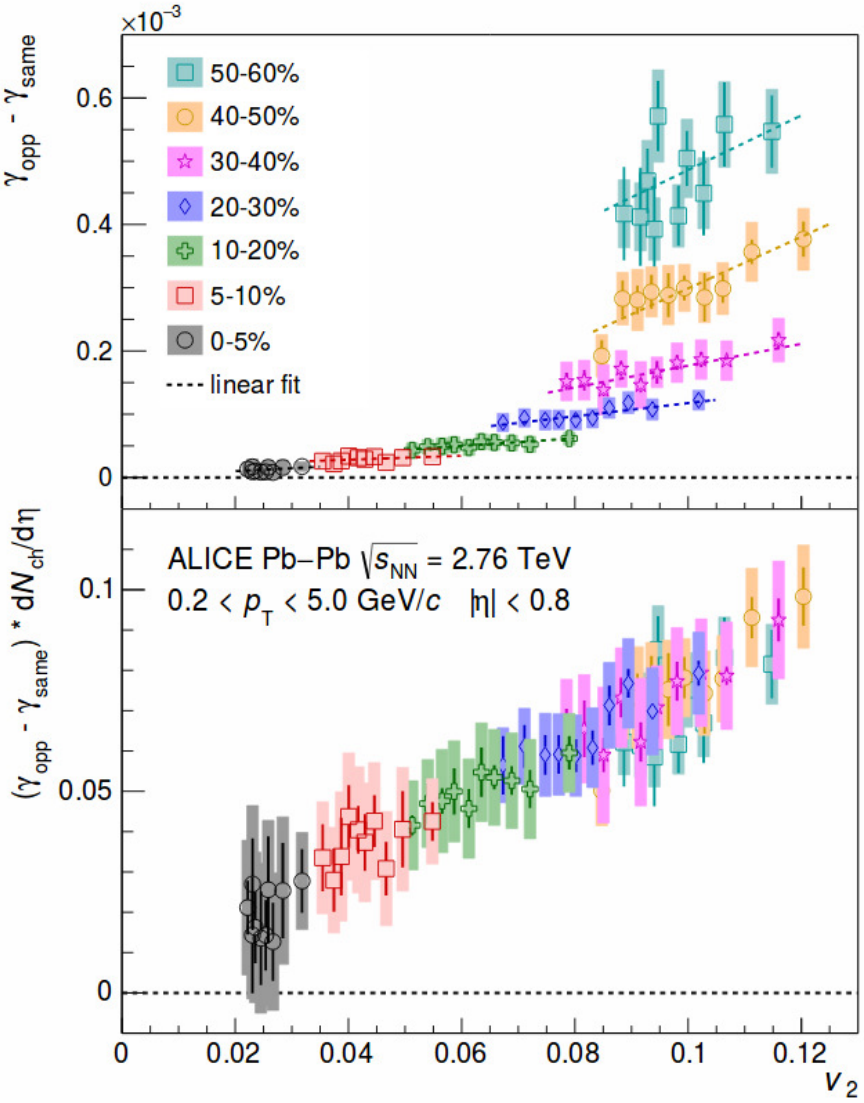

Figure 6.4: Top: $\Delta\gamma$ as a function of v_2 for event-shape selected events together with a linear fit (dashed lines) for various centrality classes. Bottom: $\Delta\gamma$ multiplied by the charged-particle density [92] as a function of for shape selected events for various centrality classes. Figure taken from [204].

In Sec. 6.3 we investigate the dependence of the CME signal in $\gamma_{\alpha\beta}$ and $\Delta\gamma$ on v_2. We hypothesize the (de-)correlation between the magnetic field and the event planes to be the main source of this dependence. We then use several initial-state models to estimate this effect. Finally, we use these results to estimate the relative contribution of signal and background in the measured $\Delta\gamma$ and discuss its implications.

6.2 Background

We use a Monte Carlo Blast-Wave (BW) model based on a simplified version of the Retiere and Lisa (RL) model [171]. In constructing this model, we follow to a large extent the prescriptions of a previous study on LCC [97]. The BW model parametrises the coordinate and momentum configuration of the produced particles at the kinetic freeze-out. The shape of the system at the freeze-out is described by an ellipse, in the transverse direction, with the major axis aligned with the reaction plane, while boost-invariance is assumed along the beam direction. The shape of the ellipse is set by the length of its axes ($R_{x,y}$), which are related to its eccentricity ε_2 (or, equivalently, its azimuthal density variation s_2 [205]) via:

$$\varepsilon_2 \equiv \frac{R_y^2 - R_x^2}{R_y^2 + R_x^2}, \qquad s_2 \equiv \frac{1}{2}\frac{(R_y/R_x)^2 - 1}{(R_y/R_x) + 1}. \tag{6.10}$$

Particles' initial positions in the transverse plane (called *sources* in the following) are uniformly distributed within the system. The particles' momenta are first sampled from a Maxwell-Boltzmann distribution, according to the system temperature at the freeze-out (T), with isotropic directions. The particles are then boosted along the direction normal to the surface of the system (Fig. 6.5). The azimuthal angle of the boost direction (ϕ_b) is related to the source one (ϕ_s) by

$$\tan(\phi_s) = \frac{R_y^2}{R_x^2}\tan(\phi_b). \tag{6.11}$$

The magnitude of the boost (β_b) depends on the source azimuthal angle and radius

$$\beta_b = \tilde{r}_s(r_s, \phi_s)^\alpha \cdot (\rho_0 + \rho_2\cos(2\phi_b) + \rho_4\cos(4\phi_b)), \tag{6.12}$$

where the reduced system radius ($\tilde{r}_s$) is defined as

$$\tilde{r}_s(r_s, \phi_s) = \sqrt{\left(\frac{r_s\cos(\phi_s)}{R_x}\right)^2 + \left(\frac{r_s\sin(\phi_s)}{R_y}\right)^2}. \tag{6.13}$$

The coefficients ρ_0, ρ_2 and ρ_4 parametrise, respectively, radial, elliptic and quadrangular flow. The exponent α relates the strength of the boost to the reduced system radius, i.e. it parametrises the dependency of the radial flow on the position of the source in the system volume. The total number of particles generated in one event is constant and it is set by the charged particle multiplicity M.

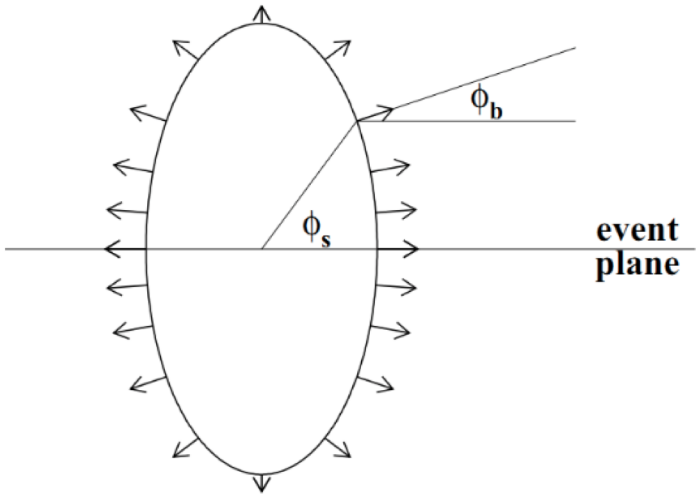

Figure 6.5: Schematic illustration of the source in a BW model, with $R_y > R_x$. Arrows represent the direction and magnitude of the flow boost. Figure from [171].

The kinematic range of charged tracks is set as the one of ALICE experiment ($|\eta| < 1$, $p_{\mathrm{T}} > 0.2$ GeV/c); we verified that this choice has little effect on the results, if not for a trivial variation of $\langle v_2 \rangle$ due to $\langle p_{\mathrm{T}} \rangle$. The parameters T, γ, ρ_0, ρ_2, ρ_4, and ε_2 are first tuned to give a reasonable estimate of p_{T}-differential elliptic flow $v_2(p_{\mathrm{T}})$ and charged particle spectra $\mathrm{dN/d}p_{\mathrm{T}}$, in different centrality classes, up to centrality 50% (Fig. 6.6). The track multiplicity M corresponds to the measured charged particle multipliticity at midrapidity $\langle N_{ch} \rangle_{|\eta|<1}$ [92]. We estimate that for the purposes of this study the agreement with experimental results is reasonable enough.

LCC is implemented assuming that n particles of opposite charge are generated for each source. Tracks are isotropically distributed in the reference frame of the source and they are all boosted in the laboratory frame according to the source position. The common boost determines their correlation in phase-space and thus the strength of LCC background. The contribution of LCC background in charge-dependent correlators grows with increasing number of balancing charges per source (n) and with the strength of the boost, which parametrises the effect of the collective expansion; on the contrary, it decreases with increasing multiplicities (M), as this acts as a dilution factor. While M and the collective expansion can be constrained with experimental data, n is *a priori* undetermined. In the following, we choose $n = 8$, as we observe it results in reasonable values of $\Delta\delta$ and $\Delta\gamma$. We observe that while all charge-dependent correlators scale with n, their dependence on v_2, which is the aim of this study, is not affected.

centrality	T	α	ρ_0	ρ_2	ρ_4	ε_2	M
5-10%	0.112	0.36	0.930	0.008	0.0016	0.096	1294
10-20%	0.100	0.38	0.935	0.013	0.0011	0.130	966
20-30%	0.099	0.42	0.938	0.015	0.0009	0.172	649
30-40%	0.098	0.45	0.940	0.016	0.0007	0.204	426
40-50%	0.095	0.45	0.942	0.016	0.0006	0.224	261

Table 6.1: Parameters of the BW model in several centrality ranges.

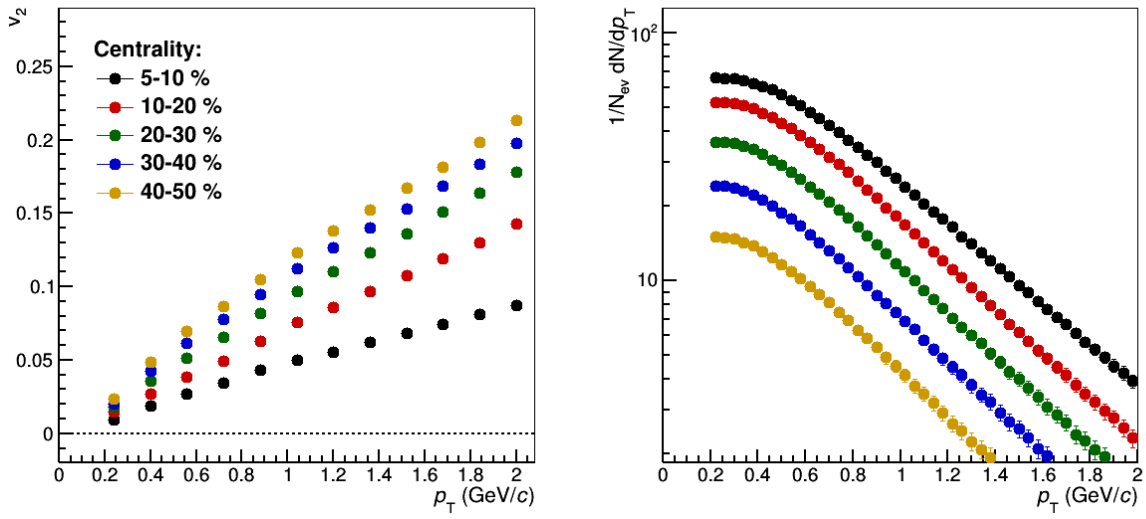

Figure 6.6: Elliptic flow (left) and charged particle spectra (right) in several centrality classes from the Blast-Wave model.

The second-order event plane Ψ_2 is calculated in the same kinematic range of the charged particles, i.e. the effects of short-range (in $\Delta\eta$) LCC-induced correlations are included. The charge-dependent correlators are then corrected for the corresponding event plane resolution. In order to distinguish between the two possible definitions of $\gamma_{\alpha\beta}$, in the following we will note them as

$$\gamma_{\alpha\beta}\{\Psi_{\rm RP}\} = \langle\cos(\phi_a + \phi_b - 2\Psi_{\rm RP})\rangle, \tag{6.14}$$

$$\gamma_{\alpha\beta}\{\Psi_2\} = \langle\cos(\phi_a + \phi_b - 2\Psi_2)\rangle. \tag{6.15}$$

Measurements of these correlators as a function of centrality are reported in Fig.6.7-6.9. Model parameters in the different centrality classes are reported in Tab. 6.1. We observe both $\delta_{\alpha\beta}$ and $\gamma_{\alpha\beta}\{\Psi_{\rm RP}\}$ to increase going from central to peripheral collisions, due to the combined effect of decreasing multiplicities and increasing $\langle v_2\rangle$ (Fig. 6.7 and 6.8, left panels). At the same time, the values of opposite-charge pair correlators are systematically larger than those of same-charge pair correlators, as expected, and their difference ($\Delta\delta$, $\Delta\gamma\{\Psi_{\rm RP}\}$) increases going from central to peripheral collisions (Fig. 6.7 and 6.8, right panels). These observations are qualitatively consistent with experimental measurements. The same conclusions apply for $\gamma_{\alpha\beta}\{\Psi_2\}$ (Fig. 6.9). However, we also note that $\gamma_{\alpha\beta}\{\Psi_2\}$ is about one order of magnitude bigger than $\gamma_{\alpha\beta}\{\Psi_{\rm RP}\}$ in every centrality

ESE class	ρ_2	ε_2	$\langle v_2 \rangle$
1	0.012	0.12	0.047
2	0.015	0.15	0.059
3	0.018	0.18	0.071
4	0.021	0.21	0.083
5	0.024	0.24	0.095

Table 6.2: Values of BW parameters ρ_2 and ε_2, and resulting $\langle v_2 \rangle$, for different ESE classes, in the centrality range 20-30%.

range, while the difference between same- and opposite-charge pair correlators is almost unchanged $\Delta\gamma\{\Psi_2\} \approx \Delta\gamma\{\Psi_{\rm RP}\}$. We conclude that LCC constitutes a background in all charge-dependent correlators, as previously noted, and that for $\gamma_{\alpha\beta}$ such background is largely dependent on how the event plane is estimated, being minimal for correlations with the reaction plane $\Psi_{\rm RP}$. We speculate that experimental non-flow-suppression techniques, such as applying pseudorapidity gap(s) between tracks that are correlated, can partially suppress this background, but never remove it exactly to the level of $\gamma_{\alpha\beta}\{\Psi_{\rm RP}\}$. At the same time, we conclude that for $\Delta\gamma_{\alpha\beta}$ the opposite applies: the LCC background contribution depends little on how the event plane is estimated. Note that in this model we assume no de-correlation between Ψ_2 and $\Psi_{\rm RP}$, which is known to occur due to initial-state fluctuations and would imply additional differences between $\gamma_{\alpha\beta}\{\Psi_{\rm RP}\}$ ($\Delta\gamma\{\Psi_{\rm RP}\}$) and $\gamma_{\alpha\beta}\{\Psi_2\}$ ($\Delta\gamma\{\Psi_2\}$).

The dependence of these correlators on v_2 is then investigated varying the relevant parameters in the BW model (ρ_2, ε_2), while keeping the others (T, γ, ρ_0, ρ_4, and M) fixed. For simplicity, only the centrality class 20-30% is shown; results in other centrality classes are qualitatively similar. The values of ρ_2 and ε_2 parameters in the different ESE classes are reported in Tab. 6.2. The variations on the parameters are chosen such as to vary v_2 by more than 20%, in order to cover the full range experimentally achievable with ESE.

The 2- and 3-particle correlators as a function of v_2 are reported in Fig. 6.10-6.12. We observe that while $\delta_{\alpha\beta}$ does not significantly depend on v_2, $\gamma_{\alpha\beta}\{\Psi_{\rm RP}\}$ and $\gamma_{\alpha\beta}\{\Psi_2\}$ show a linear dependence over the entire range. The increase as a function of v_2 is larger for opposite-charge pair correlators than for same-charge ones; their difference $\Delta\gamma\{\Psi_{\rm RP}\}$ increases linearly as well. This applies to $\Delta\gamma\{\Psi_2\}$ as well. We fit the data with a function of the form

$$f(v_2) = p_0 \left(1 + p_1 \left(\frac{v_2 - \langle v_2 \rangle}{\langle v_2 \rangle}\right)\right). \tag{6.16}$$

The parameters p_0 and p_1 obtained from the fits are reported in Tab. 6.3. We conclude that the LCC background in $\Delta\gamma$ is proportional to the relative variations of v_2 and that the proportionality coefficient (p_1) is equal to unity. Since this holds both for $\Delta\gamma\{\Psi_{\rm RP}\}$ and $\Delta\gamma\{\Psi_2\}$, it is independent of possible LCC contributions to the event plane estimation. We verified that repeating the same exercise in other centrality bins (not shown here), p_1 is equally consistent with unity, although the values of $\Delta\gamma$ differ.

Correlator	p_0 ($\times 10^3$)	p_1	χ^2/DoF
$\Delta\delta$	1.04 ± 0.05	0.02 ± 0.06	0.37
$\Delta\gamma\{\Psi_{\mathrm{RP}}\}$	0.60 ± 0.05	1.00 ± 0.02	0.79
$\Delta\gamma\{\Psi_2\}$	0.91 ± 0.09	1.02 ± 0.02	0.63

Table 6.3: Parameters extracted from fits to charge-dependent correlators, according to Eq. 6.16.

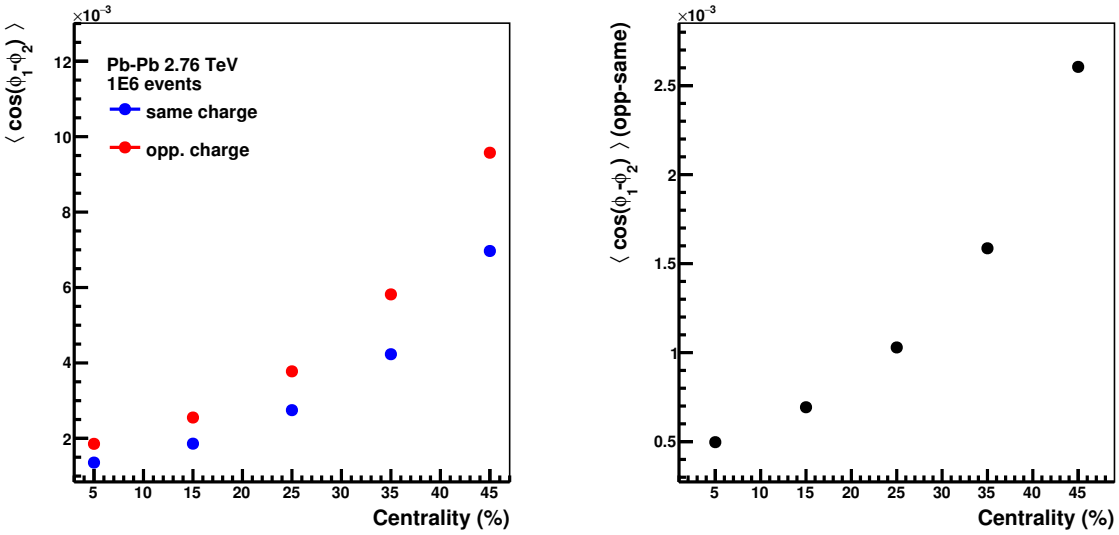

Figure 6.7: $\delta_{\alpha,\beta}$ and $\Delta\delta$ as a function of centrality.

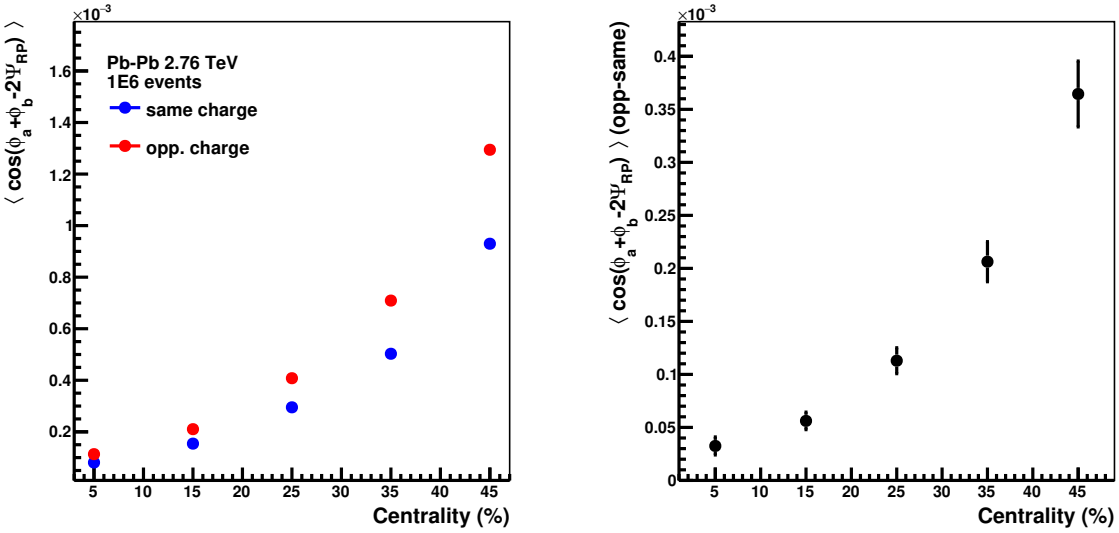

Figure 6.8: $\gamma_{\alpha,\beta}\{\Psi_{\mathrm{RP}}\}$ and $\Delta\gamma\{\Psi_{\mathrm{RP}}\}$ as a function of centrality.

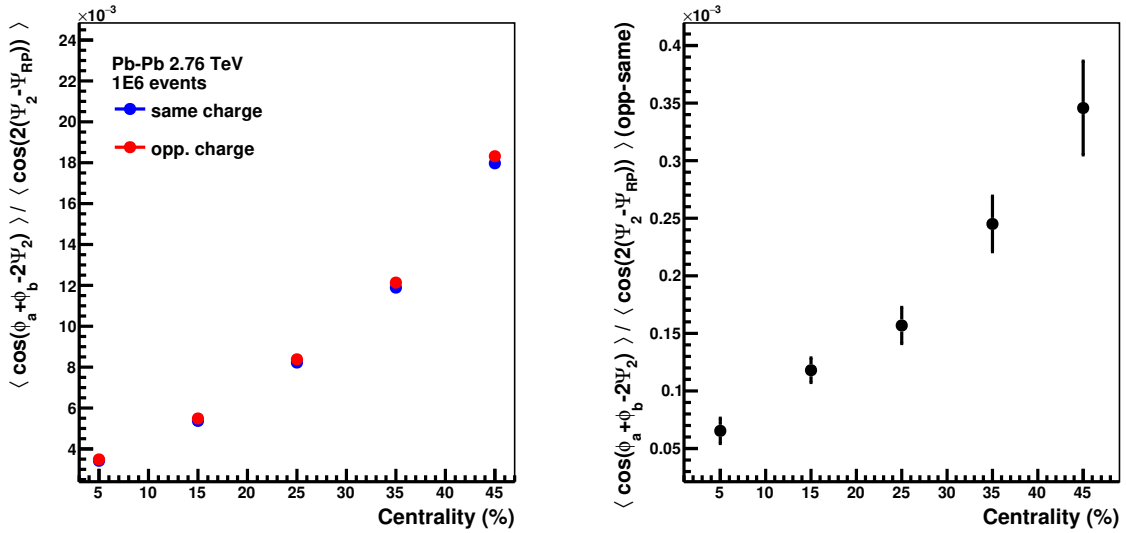

Figure 6.9: $\gamma_{\alpha,\beta}\{\Psi_2\}$ and $\Delta\gamma\{\Psi_2\}$ as a function of centrality.

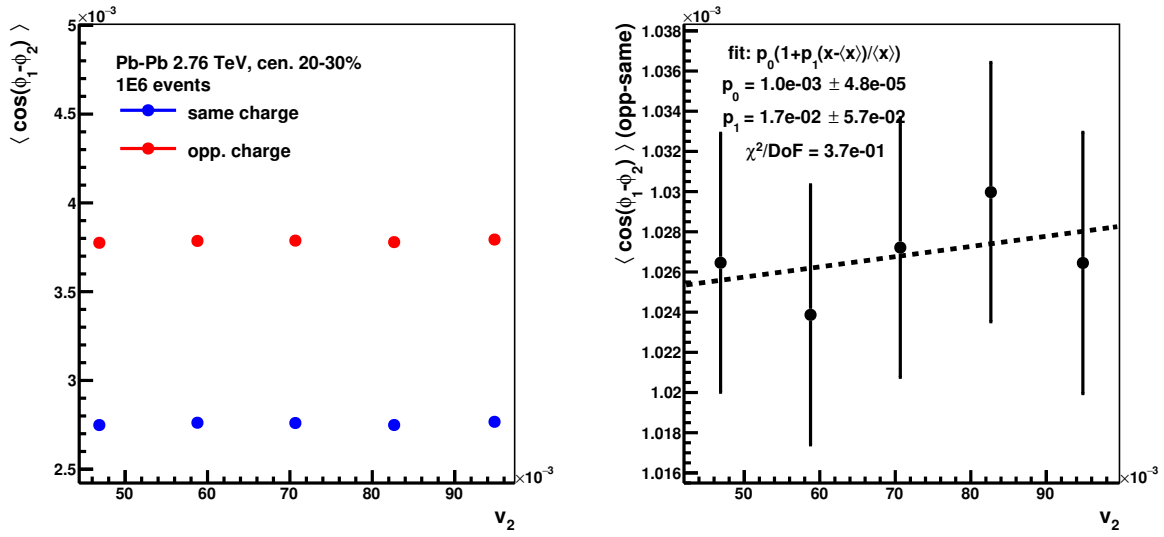

Figure 6.10: $\delta_{\alpha,\beta}$ and $\Delta\delta$ as a function of v_2, for centrality 20-30% and several ESE classes.

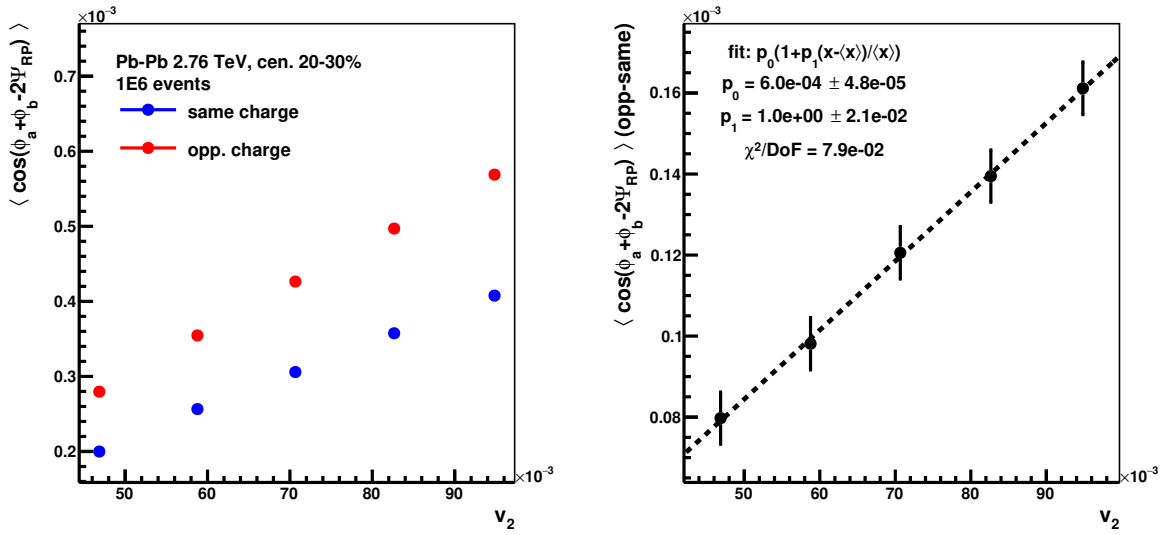

Figure 6.11: $\gamma_{\alpha,\beta}\{\Psi_{\mathrm{RP}}\}$ and $\Delta\gamma\{\Psi_{\mathrm{RP}}\}$ as a function of v_2, for centrality 20-30% and several ESE classes.

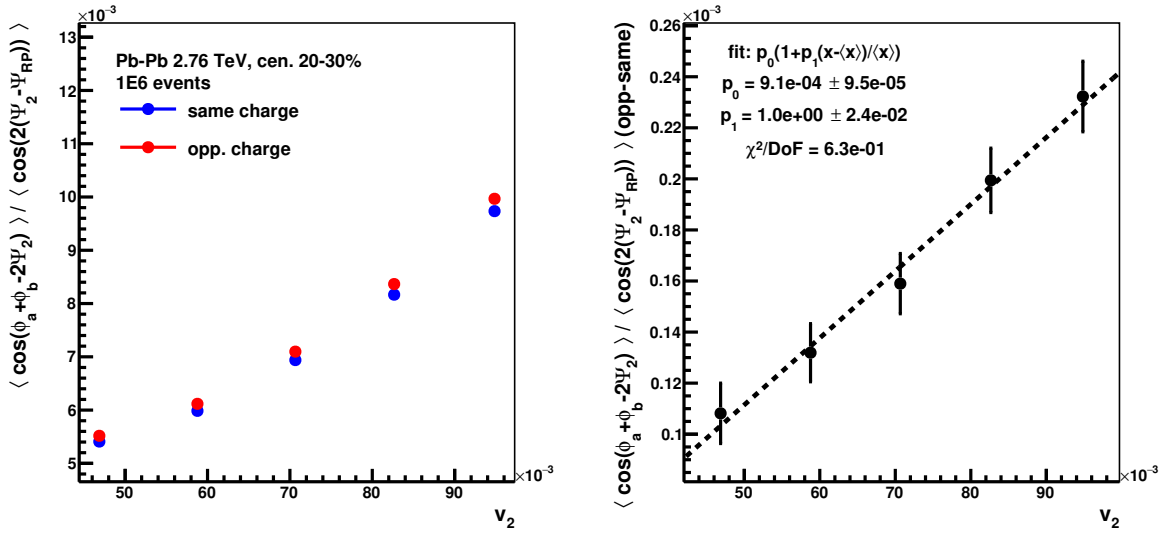

Figure 6.12: $\gamma_{\alpha,\beta}\{\Psi_2\}$ and $\Delta\gamma\{\Psi_2\}$ as a function of v_2, for centrality 20-30% and several ESE classes.

6.3 Signal

As previously introduced, we hypothesize that the de-correlation between the reaction plane, the event planes and the direction of the magnetic field, due to initial-state fluctuations, affects the CME signal contribution to $\gamma_{\alpha,\beta}$. In fact, assuming that these planes do not necessarily correspond with each other, we can re-write Eq. 6.3 as

$$\frac{\mathrm{d}N}{\mathrm{d}\varphi_{\alpha\,\pm}} = 1 + 2\,a_{1,\alpha}\,\sin(\varphi - \Psi_{\mathrm{B}}) + 2\sum_{n=1}^{+\infty} v_{n,\alpha}\,\cos(n(\varphi - \Psi_{\mathrm{n}})), \tag{6.17}$$

where we now see that the CME-induced charge separation develops along the magnetic field angle Ψ_B and the azimuthal anisotropies due to the collective expansion of the system (quantified by the flow coefficients v_n) along to the corresponding symmetry planes Ψ_n. Initial-state fluctuations imply that event-by-event $\Psi_B \pm \pi/2 \neq \Psi_n \neq \Psi_{\mathrm{RP}}$. We assume that a_1 is exactly proportional to the magnitude of the magnetic field ($a_1 \propto |\vec{B}|$), as early calculations showed [85]. It follows that the signal component in $\Delta\gamma$ is proportional to[1]

$$\Delta\gamma \propto \langle |\vec{B}|^2 \cos(2(\Psi_B - \Psi_2))\rangle. \tag{6.18}$$

For a fixed impact parameter, the alignment between Ψ_B and Ψ_2 will only depend on the geometry of the collision. Qualitatively, the higher the eccentricity ε_2 in the initial state, the more perpendicular Ψ_B and Ψ_2 are expected to be, as illustrated in Fig. 6.13. In order to quantify this effect, we measure the correlations between these angles and ε_2 using different initial-state models.

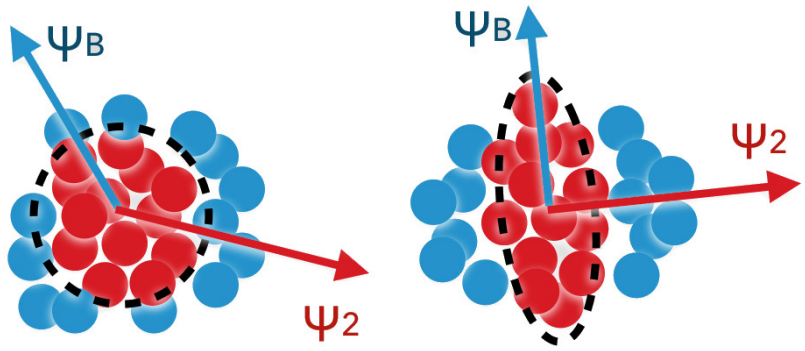

Figure 6.13: Schematic representation of the dependence of the relative alignment between Ψ_B and Ψ_2 to initial-state geometry. In a spherical system (left) they are more misaligned than in a highly elliptical one (right). Participant nucleons are depicted in red, spectator ones in blue.

The magnetic field $\vec{B}$ generated by spectator protons is calculated by means of Liénard-Wiechert potentials. A point-like charged particle moving along $\vec{x}_p(t)$ with constant ve-

[1] strictly speaking, the argument of the cosine is $2(\Psi_B - \Psi_2) + \pi$; here and in the following, we will omit the π for conciseness and implicitly multiply by -1.

locity $\vec{\beta}$ generates EM fields $\vec{B}(\vec{x},t)$, $\vec{E}(\vec{x},t)$ as

$$\vec{E} = e\left[\frac{(\vec{n}-\vec{\beta})\,(1-|\vec{\beta}|^2)}{k^3\,|\vec{R}|^2}\right]_{t=t_{\rm ret}}, \tag{6.19}$$

$$\vec{B} = \vec{n}(t_{\rm ret}) \times \vec{E}, \tag{6.20}$$

where $\vec{R}$ is the vector connecting $\vec{x}$ and $\vec{x}_p(t)$, $\vec{n}$ the unitary vector along the direction of $\vec{R}$ and k quantifies the alignment between $\vec{n}$ and $\vec{\beta}$. They are defined as

$$\vec{R}(t) = \vec{x} - \vec{x}_p(t), \tag{6.21}$$

$$\vec{n}(t) = \vec{R}(t)/|\vec{R}(t)|, \tag{6.22}$$

$$k(t) = 1 - \vec{n}(t)\cdot\vec{\beta}. \tag{6.23}$$

$$\tag{6.24}$$

We use Lorentz-Heaviside natural units, where the electric charge $e = \sqrt{4\pi\alpha_{\rm em}}$, with $\alpha_{\rm em}$ being the fine-structure constant. The retarded time $t_{\rm ret}$ is defined as

$$t_{\rm ret} - t + |\vec{x} - \vec{x}_p(t_{\rm ret})| = 0. \tag{6.25}$$

Assuming the spectators to move along the beam direction (z) according to $\vec{x}_p(t) = (x_s, y_s, \beta\, t)$ ($\beta = |\vec{\beta}|$) and the point at which the magnetic field is probed to lie on the transverse plane $\vec{x} = (x, y, 0)$, $t_{\rm ret}$ is simply

$$t_{\rm ret} = \gamma^2\left(t - \sqrt{\frac{(x-x_s)^2 + (y-y_s)^2}{\gamma^2} + \beta^2 t^2}\right), \tag{6.26}$$

where γ is the Lorentz factor: $\gamma = 1/\sqrt{1-\beta^2}$. In the case of Pb–Pb collisions at $\sqrt{s_{\rm NN}} = 2.76$ TeV, we have $\beta^2 = 1 - (2\,m_{\rm P}/\sqrt{s_{\rm NN}})^2$, where $m_{\rm P}$ is the proton mass, and therefore $\gamma \approx 1470$. For simplicity, we ignore the contribution of participant nucleons to the magnetic field, which has been estimated to be much smaller than the spectators' one in the early times of the collision ($\tau \leq 0.1$ fm) [85].

Two Monte Carlo initial-state models are employed to calculate the distribution of nucleons and the corresponding spatial anisotropies: MC-Glauber [19] and TRENTo [139], this latter tuned to reproduce IP-Glasma [15] initial conditions. In both models, nucleon positions in each nucleus are first sampled from a Wood-Saxon distribution

$$\rho(r) = \rho_0\,\frac{1}{1+e^{(r-R)/a}}, \tag{6.27}$$

where R is the nuclear radius, ρ_0 the average nucleon density and a the skin depth. For ^{208}Pb, $R = 6.62$ fm and $a = 0.546$ fm [207]. Here and in the following, no neutron skin R_n is assumed, i.e. neutrons and protons are equally distributed in the nucleus, since available measurements anyhow indicate $R_n \approx 0.3$ fm $\ll R$ [208]. The impact parameter b is then chosen randomly within $b < 2R$ and the nuclei are sumperimposed. Two nucleons from different nuclei collide if their relative distance is less than $\sqrt{\sigma_{\rm NN}/\pi}$, with $\sigma_{\rm NN}$ being the inelastic nucleon-nucleon cross section, extracted from p–p collisions. At $\sqrt{s_{\rm NN}} = 2.76$

TeV, $\sigma_{\mathrm{NN}} = 64$ mb [4].

The resulting magnetic field perpendicular to the reaction plane (B_y) is shown in Fig. 6.14, as a function of proper time (left) and distance in the transverse plane (right), for a non-central collision ($b = 7$ fm, corresponding to a centrality of about 20%). Consistently with previous studies [67, 74, 209, 66, 210, 211], we observe a strong magnetic field, with a maximum magnitude of about 10 fm^{-2} $\approx 20\, m_\pi^2 \sim 10^{19}$ G at $\tau \approx 0$, which changes little across the transverse area of the system and quickly vanishes, decreasing by about 6 orders of magnitude within $\tau = 3$ fm. In the following, we will compute the magnetic field at fixed proper time $\tau = 0.1$ fm and position $(x, y) = (0, 0)$ fm.

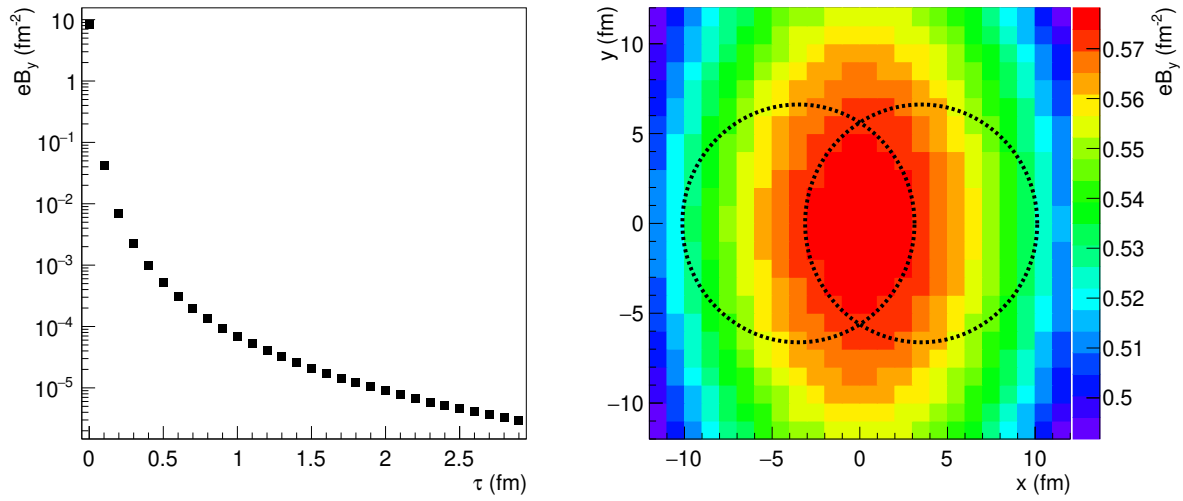

Figure 6.14: Time and spatial dependence of the magnetic field in Pb–Pb collisions at $\sqrt{s_{\mathrm{NN}}} = 2.76$ TeV, for $b = 7$ fm, computed with the MC-Glauber model. Left: $eB_y(\tau)$ at $(x, y) = (0, 0)$ fm. Right: $eB_y(x, y)$ at $\tau = 0.1$ fm.

In Fig. 6.15 we show the centrality dependence of the magnetic field and its alignment with the second-order event plane Ψ_2, defined analogously to Eq. 6.3 as

$$\Psi_2 = \frac{1}{2}\,\mathrm{atan2}\left(\frac{\mathrm{Im}\, Q_n}{\mathrm{Re}\, Q_n}\right), \qquad Q_n = \frac{1}{N}\sum_{j=1}^{N} r^2 e^{i2\varphi}, \tag{6.28}$$

where φ is the azimuthal angle of the N participant nucleons and r their radial position with respect to the center of the system. The centrality of the collision is defined here as percentile of the impact parameter distribution. We see that while the magnitude of the magnetic field $e|\vec{B}|^2$ monotonously increase from central to peripheral collisions, because of the increasing number of spectator protons, the de-correlation factor $\cos(2(\Psi_B - \Psi_2))$ increases from central to mid-central, reaches a maximum $\cos(2(\Psi_B - \Psi_2)) \approx 0.8$ at centrality 20-40 % and then decreases for more peripheral collisions. This can be understood in terms of the relative contribution of the average ellipsoidal shape of the overlapping area between the colliding nuclei and initial-state fluctuations to Ψ_2 and Ψ_B.

The initial-state azimuthal eccentricity is quantified via ε_2. In case of point-like

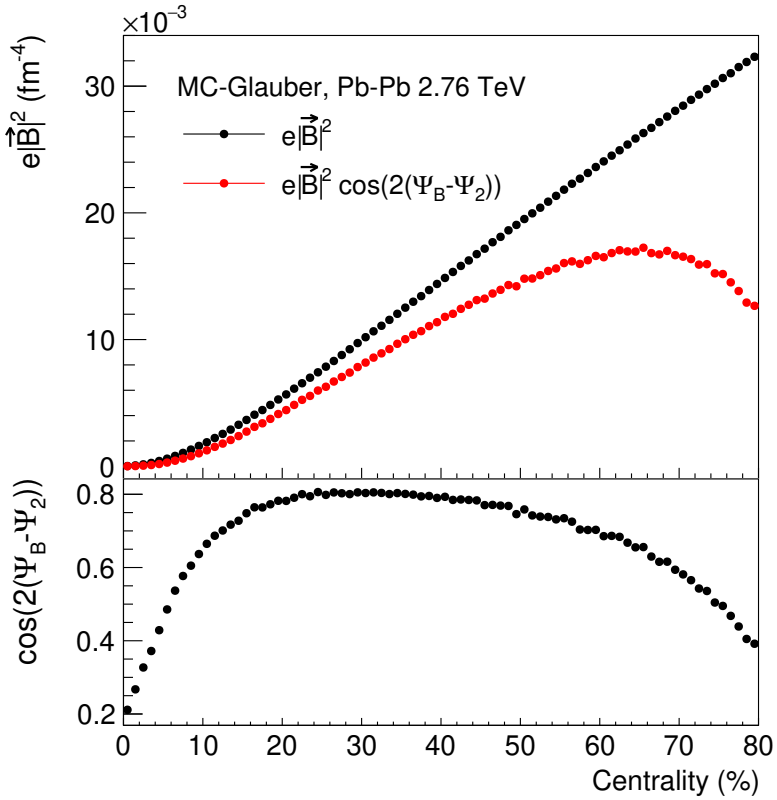

Figure 6.15: Centrality dependence of the magnetic field and its alignment with the second-order event plane in Pb–Pb collisions at $\sqrt{s_{\mathrm{NN}}} = 2.76$ TeV, with the MC-Glauber model.

sources, like the participant nucleons in MC-Glauber, it can be defined as

$$\varepsilon_2 = \frac{\sum_{i=1}^{N}(\vec{x}_i - \vec{x}_0)^2}{\sum_{i=1}^{N}|\vec{x}_i - \vec{x}_0|^2}, \tag{6.29}$$

where $\vec{x}_i$ are the positions of the N sources in the transverse plane and $\vec{x}_0 = (1/N)\sum_{i=1}^{N}\vec{x}_i$ is the center of the distribution. In case of a continuous energy density distribution $\rho(x, y)$, such as the one generated by TRENTo, ε_2 is defined as

$$\varepsilon_2 = \frac{\iint_{x,y}(x^2 - y^2)\,\rho(x, y)\,\mathrm{d}x\mathrm{d}y}{\iint_{x,y}(x^2 + y^2)\rho(x, y)\,\mathrm{d}x\mathrm{d}y}, \tag{6.30}$$

where the coordinates x, y have been shifted so that the mean of $\rho(x, y)$ is at the origin, $(x, y) = (0, 0)$ fm. The dependence of $e|\vec{B}|^2$ and $\cos(2(\Psi_B - \Psi_2))$ on ε_2, for several centrality classes, is shown in Fig. 6.16 and 6.17, from the MC-Glauber and TRENTo models, respectively. In order to avoid possible biases coming from the large centrality intervals, the results are first obtained in 1% centrality intervals and then averaged. Concerning the magnitude of the magnetic field, we observe a positive correlation with ε_2, whose strength decreases from central to peripheral collisions. Such correlation is enhanced once the decorrelation term $\cos(2(\Psi_B - \Psi_2))$ is included. In order to quantify it and compare with experimental results on $\Delta\gamma$, we fit $e|\vec{B}|^2\cos(2(\Psi_B - \Psi_2))$ with Eq. 6.16, where we use as independent variable ε_2 instead of v_2. The fit ranges in the different centrality classes are chosen accordingly to the relative variations of v_2 experimentally observed with ESE (Fig. 1 from [204]) with respect to the unbiased values $\langle v_2\rangle$, reported in Tab. 6.4. Taking the values of v_2 in the minimum (maximum) ESE class 0-10% (90-100%) of q_2, the fit range is defined as

$$\left[\frac{v_2[0\text{-}10\%]}{\langle v_2\rangle}\langle\varepsilon_2\rangle,\ \frac{v_2[90\text{-}100\%]}{\langle v_2\rangle}\langle\varepsilon_2\rangle\right]. \tag{6.31}$$

We observe the dependence of $e|\vec{B}|^2\cos(2(\Psi_B - \Psi_2))$ on ε_2 to be well described by Eq. 6.16 around $\langle\varepsilon_2\rangle$, which implies a linear relationship between the two, and the proportionality coefficient (p_1) to be between 0 and 1. Concerning the centrality dependence, p_1 seems to follow the inverse of what discussed in the context Fig. 6.15, i.e. p_1 decreases from central to mid-central, reaches a minimum at centrality 20-40 % and then increases for more peripheral collisions. This is attributed, as before, to the variation in the relative contribution of the average ellipsoidal shape of the overlapping area between the colliding nuclei and initial-state fluctuations.

Little but significant differences are observed between MC-Glauber and TRENTo, indicating some sensitivity of the results on the details of the model employed. On the contrary, the results do not change significantly when the proper time and the transverse position at which the magnetic field are computed are varied within a reasonable range. In order to investigate a possible sensitivity on the centrality definition, we use as alternative estimator percentiles of the charged particle multiplicity distribution $P(M)$, which can be derived from the number of participant nucleons (N_{part}) and of binary collisions (N_{coll}) via the empirical formula [112]

$$M = P_{\mu,k}\,[f\,N_{\mathrm{part}} + (1 - f)\,N_{\mathrm{coll}}], \tag{6.32}$$

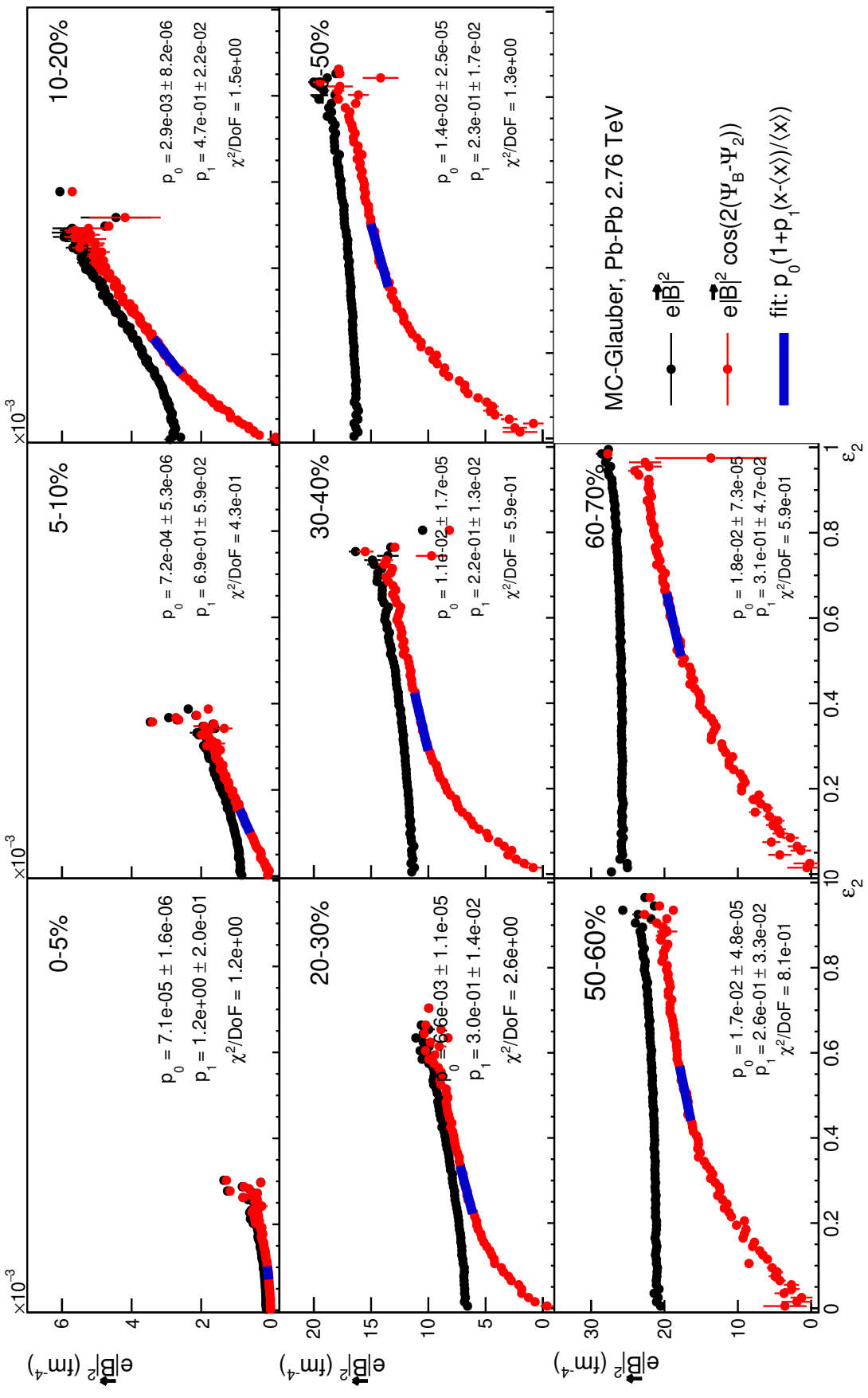

Figure 6.16: Dependence of the magnetic field magnitude and orientation w.r.t. Ψ_2 on initial-state eccentricity ε_2 in the MC-Glauber model, together with linear fits around $\langle\varepsilon_2\rangle$. See text for details.

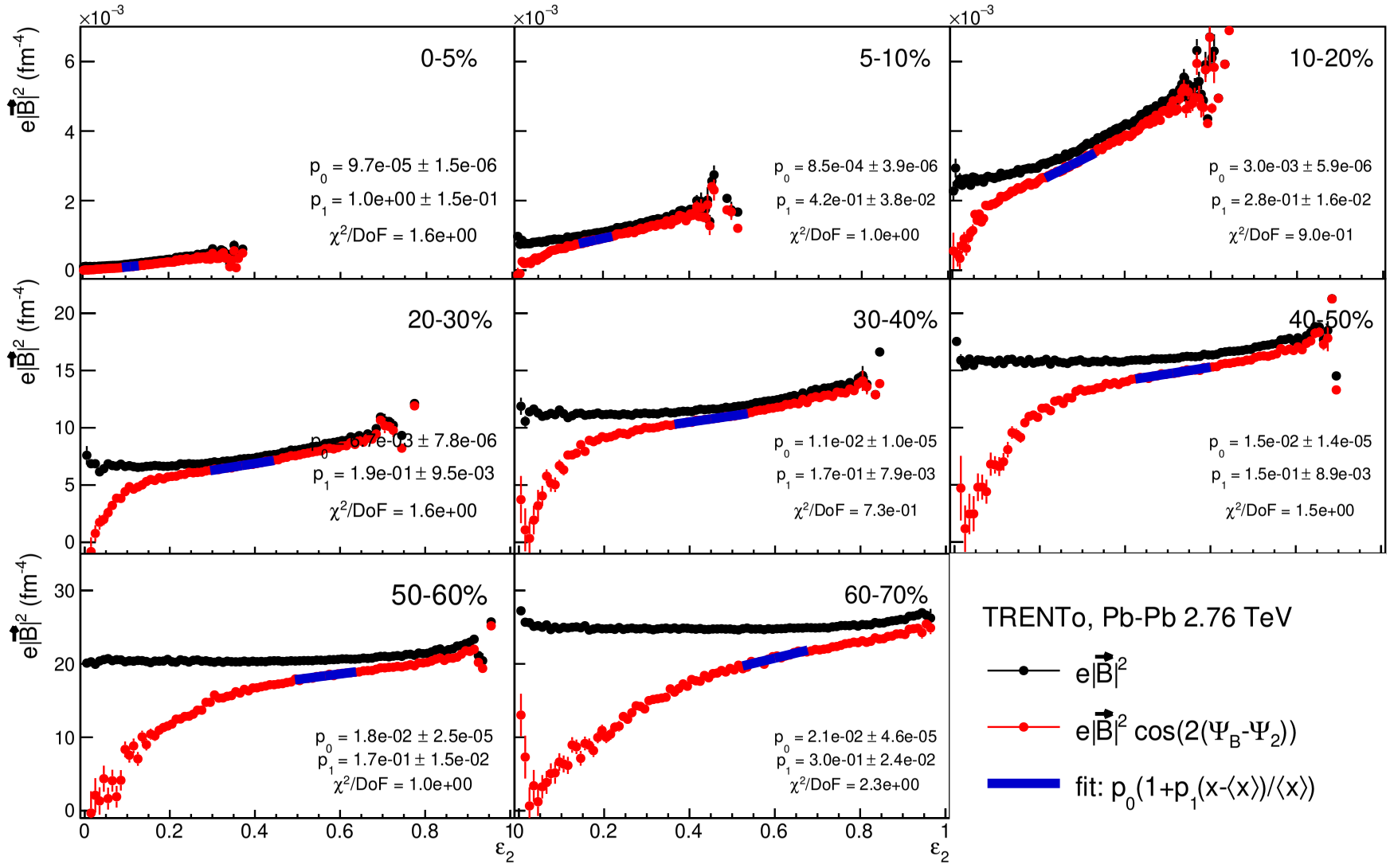

Figure 6.17: Dependence of the magnetic field magnitude and orientation w.r.t. Ψ_2 on initial-state eccentricity ε_2 in the TRENTo model, together with linear fits around $\langle\varepsilon_2\rangle$. See text for details.

centrality	v_2 (unbiased)	v_2 (0-10% q_2)	v_2 (90-100% q_2)
0-5%	0.02552	0.02220	0.03181
5-10%	0.04343	0.03545	0.05482
10-20%	0.06340	0.05127	0.07901
20-30%	0.08281	0.06730	0.10186
30-40%	0.09461	0.07852	0.11598
40-50%	0.09969	0.08474	0.12037
50-60%	0.09840	0.08867	0.11479

Table 6.4: Variations of v_2 with ESE in Pb–Pb collisions at $\sqrt{s_{\rm NN}} = 2.76$ TeV, from ALICE measurements [204].

where $P_{\mu,k}$ is a negative binomial distribution. The parameters k, μ and f are taken from fits to ALICE measurements [112]. In the case of TRENTo, multiplicity can be directly estimated from the total produced entropy, which is allowed to fluctuate nucleon-by-nucleon collision. Percentiles of the entropy distribution are then used as alternative centrality estimator. When using both these alternative centrality estimators, small differences of the order of a few % are observed at the level of p_0 and p_1, suggesting that this introduces an additional model uncertainty. Noting that such effect is anyhow much smaller than the observed differences between the two initial-state models, it was not included as a systematic uncertainty. The study of the contribution of participant protons (more generally, of the charges in the participant system) to the magnetic field, which can become important for $\tau > 0.1$ fm, is left for future studies.

6.4 Discussion

We observe that in the models employed both the CME signal and the LCC background in $\Delta\gamma$ are proportional to the relative variations of v_2: the former, because of the (de-)correlation between the angle of the magnetic field and the second-order event plane; the latter, because the collective expansion determines the degree of correlation between balancing charges. In particular, the proportionality coefficient p_1 for the LCC background is precisely equal to 1, irrespectively of the centrality of the collision, while for the signal it depends on centrality and the details of initial-state fluctuations. Knowing the experimental value of p_1, we can use this information to estimate the relative contribution of the two (signal and background) to $\Delta\gamma$. The total measured proportionality coefficient $p_{1,\,\rm data}$ relates to the signal one $p_{1,\,\rm CME}$ and the background one $p_{1,\,\rm LCC} = 1$ as

$$f_{\rm CME} \cdot p_{1,\,\rm CME} + (1 - f_{\rm CME}) \cdot p_{1,\,\rm LCC} = p_{1,\,\rm data}, \tag{6.33}$$

where $f_{\rm CME}$ is the signal fraction in $\Delta\gamma$

$$f_{\rm CME} = \frac{\Delta\gamma_{\rm CME}}{\Delta\gamma_{\rm CME} + \Delta\gamma_{\rm LCC}}, \qquad \Delta\gamma = \Delta\gamma_{\rm CME} + \Delta\gamma_{\rm LCC}. \tag{6.34}$$

The centrality dependence of $p_{1,\,\rm data}$ and $p_{1,\,\rm CME}$ from three different initial-state models (MC-Glauber, TRENTo and MC-KLN [141]) is shown in Fig. 6.18. For these results from MC models, centrality is estimated from multiplicity (via Eq. 6.32) and ε_2 is mapped to v_2 before the fit, in order to mimic as much as possible experimental results. We

observe a clear centrality dependence for $p_{1,\,\mathrm{CME}}$, as discussed before, which decreases from central to mid-central collision. This trend appears in all initial-state models employed, although large differences between the three are also observed. Regarding $p_{1,\,\mathrm{data}}$, given the uncertainties, conclusions are less straightforward: we can neither exclude all data points to be consistent with unity, nor that there is a centrality dependence, apparently increasing from central to mid-central collisions.

The resulting signal fraction f_{CME}, derived according to Eq. 6.33, is shown in Fig. 6.19. While nothing can be concluded for the most central (0-10%) and peripheral (50-60%) collisions, since uncertainties are larger than the physical parameter space of f_{CME}, we can use results in the intermediate centrality ranges to extract an upper limit on the CME signal. Averaging over the centrality range 10-50%, assuming Gaussian statistical and systematic uncertainties, and taking into account the boundary condition $0 < f_{\mathrm{CME}} < 1$, we can extract an upper limit on the CME contribution to $\Delta\gamma$ of 26% to 33%, according to the initial-state model, at 95% confidence level. The treatement of the boundary condition follows the Feldman-Cousins approach [212].

It is interesting to speculate on the possible centrality dependence of f_{CME}, which, let us stress, is currently not significant and needs to be confirmed by future measurements. The decreasing trend from central to peripheral collisions might indicate that the CME probability is not only proportional to the magnitude of $\vec{B}$, which would naively result in the opposite (see Fig. 6.15), but possibly also on system size, entropy density and/or temperature, which all decrease with centrality and which might effectively be dominant factors. This is qualitatively consistent, for instance, with the idea that the QCD medium, being electrically conductive, could delay the decay of $\vec{B}$. An extensive explanation of the phenomenon is given in Sec.7.1.

It is also important to remark the assumptions under which these conclusions were obtained, which certainly are approximations.

- The background contribution to $\Delta\gamma$ is directly proportional to v_2; this is observed to be the case for LCC.
- The contribution of signal and background to $\Delta\gamma$ is additive, i.e. CME-separated charges are not correlated with LCC ones, if not by the global correlation with event planes (Ψ_{RP}, Ψ_B, Ψ_2).
- The correlation between Ψ_B and Ψ_2 is only determined by initial-state geometry, i.e. there is no interplay between $\vec{B}$ and v_2.

Finally, we note that this constitutes the first upper limit on CME signal ever reported for Pb–Pb collisions at LHC energies, together with the one by the CMS Collaboration [206], published approximately at the same time. The CMS upper limit, although more stringent (3.8% at 95% confidence level), is qualitatively much different than what discussed here. The CME signal contribution to $\Delta\gamma$ is defined in [206] as the intercept p_0 in the fit

$$\frac{\Delta\gamma}{\Delta\delta}(v_2) = p_0 + p_1 v_2. \tag{6.35}$$

The rationale is that the v_2 dependence is entirely determined by background and that a CME signal would imply a non-zero value of p_0. While the first assumption was shown

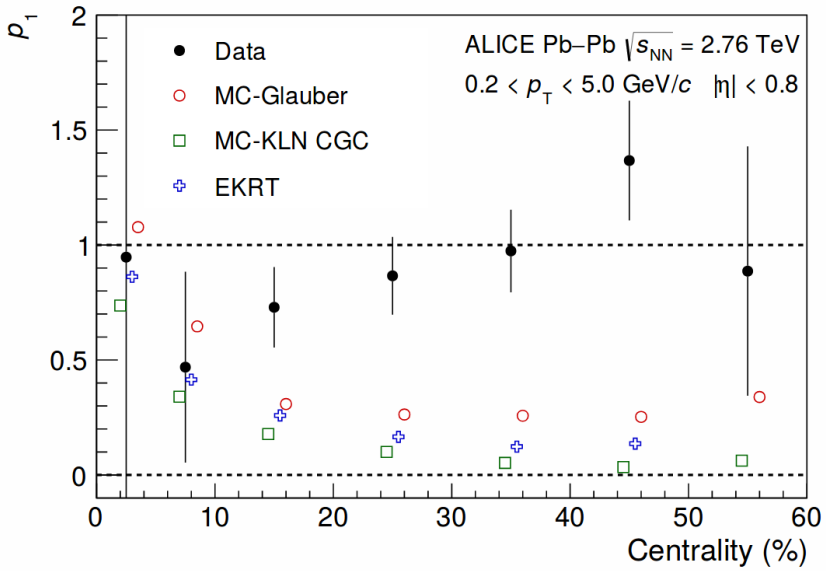

Figure 6.18: Centrality dependence of the proportionality coefficient p_1 from a linear fit to $\Delta\gamma$ (data) and $e|\vec{B}|^2 \cos(2(\Psi_B - \Psi_2))$ (MC) with Eq. 6.16. Points from MC simulations are slightly shifted along the horizontal axis for better visibility. Only statistical uncertainties are shown.

not to be correct, the second one is expected to hold, but only approximately. If we extrapolate the fit lines in Fig. 6.16 down to $\varepsilon_2 = 0$, we see that a non-zero, positive intercept is indeed expected, but that intercept corresponds only to a fraction of the average signal strength, which is proportional to $e|\vec{B}|^2 \cos(2(\Psi_B - \Psi_2))$ at around $\langle\varepsilon_2\rangle$. Therefore, we conclude that both ALICE and CMS results leave room for a CME signal fraction of the order of several percent in $\Delta\gamma$ in Pb–Pb collisions at LHC energies.

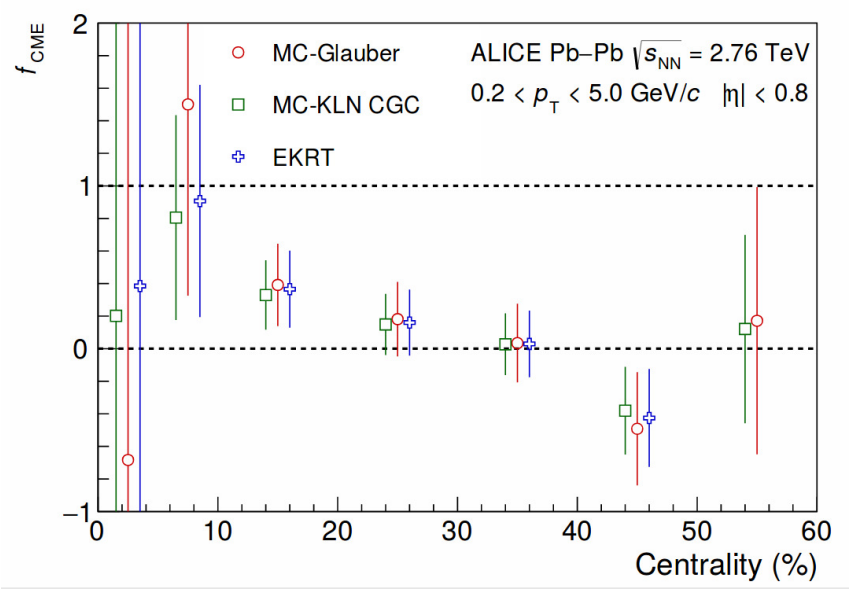

Figure 6.19: Centrality dependence of the CME fraction f_{CME}, defined in Eq. 6.33. The dashed lines indicate the physical parameter space of the CME fraction. Points are slightly shifted along the horizontal axis for better visibility. Only statistical uncertainties are shown.

Chapter 7

Charge-Dependent Directed Flow

7.1 Introduction

In this chapter, we present measurements of charge-dependent directed flow in Pb–Pb collisions, which is expected to be a simple observable - theoretically, since it is connected to a purely classical phenomenon, and experimentally, since it is well defined - that can constrain the strength and lifetime of magnetic fields in heavy-ion collisions. The interest in this measurement concerns not only the characterisation of the properties of the QCD system, but also the search for the CME. As explained in Sec. 6.1, observables connected to chiral imbalance are, up to a certain extent, affected by background, which is mostly due to charge production mechanisms, collective expansion of the system and, possibly, hadronization. So far, it has been impossible to unambigously discriminate a signal from such background, mostly because of the uncertainties in the modelling of the latter. This makes it imperative to establish that the early-time magnetic field has observable consequences on final-state charged particles. Also, as introduced in Sec. 1.5, a major source of uncertainty in theoretical modeling of the CME is the time evolution of electro-magnetic fields, which depends strongly on the electric conductivity of the system [87, 66]. Experimental measurements not related to chiral imbalance but sensitive to the magnetic field can provide important constraints in this regard.

One way to address the issue is to look at the electromagnetic response that such fields would induce in the system. The idea has first been proposed in [211] and consists in the appeareance of charged currents, due to the combination of two phenomena. On one hand, assuming the QCD system to be electrically conductive, as lattice calculations suggest [70, 71, 72, 73], an electric current will be generated inside of it, counteracting the decrease of $\vec{B}$, according to Faraday's law. This would delay the decay of the magnetic field, which is otherwise expected to be fast with respect to the timescale of the evolution of the system (Fig. 6.14), as first suggested in [66]. On the other hand, since the system is rapidly expanding in the longitudinal direction, charge carriers in the system would experience a force in the transverse direction, which is simply the Lorentz force. Both phenomena thus result in oppositely charged particles being accelerated in opposite directions, with the effect having opposite sign at opposite rapidities, as illustrated in Fig. 7.1. In terms

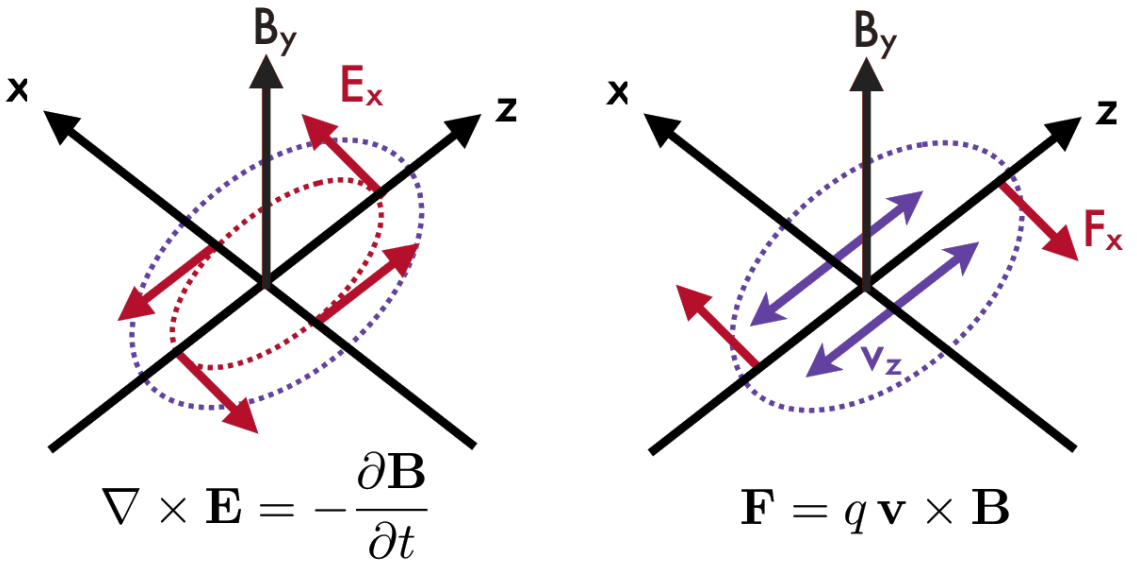

Figure 7.1: Charged currents in heavy-ion collisions, due to Faraday's law (left) and Lorentz force (right). Purple lines represent the QCD system (dashed: contours in the x-z plane, continuous: velocity), red ones its EM response.

of anisotropic flow, this corresponds to charge- and rapidity-odd directed flow

$$v_1(+,\eta) = -v_1(+,-\eta) = v_1(-,-\eta) = -v_1(-,\eta), \tag{7.1}$$

where $\pm$ refers to electric charge. This directed flow would develop perpendicularily to the magnetic field plane Ψ_B. Such observable is, in principle, experimentally accessible and has the important advantage of having clear qualitative features that distinguish it from known background. An order-of-magnitude estimate of the phenomenon was also given in [211]: for Pb–Pb collisions at $\sqrt{s_{\mathrm{NN}}} = 2.76$ TeV a charge difference $\Delta v_1(\eta) = v_1(+,\eta) - v_1(-,\eta)$ of $\mathcal{O}(10^{-5})$ is expected for a p_{T}-integrated measurement and $\langle p_{\mathrm{T}} \rangle \sim 0.73$ GeV/c (Fig. 4.13). The signal was predicted to strongly depend on p_{T} (Fig. 7.2, left), because of variations in the relative strength of the two effects, Faraday's law and Lorentz force, which have opposite sign (Fig. 7.2, right), and on particle species, not only in terms of magnitude but also of sign.

This charge-dependent directed flow will manifest itself on top of the known, charge-independent one, whose origin and characteristics will be discussed in the following. Directed flow in heavy-ion collisions is thought to be driven by several mechanisms, whose relative importance strongly depend on the collision energy and rapidity range [213, 119]. We will limit the discussion to what is relevant at LHC and top RHIC energies, in the mid-rapidity range ($|\eta| \leq 1$). Here, the origin of directed flow is thought to be twofold. The first one is connected to the geometry of the collision and can be ascribed to a *tilt* of the initial state in the x-z plane [215], combined with the collective radial expansion of the system. Hydrodynamical calculations employing this prescription [215] have been shown to quantitatively describe RHIC measurements in Au–Au and Cu–Cu collisions at $\sqrt{s_{\mathrm{NN}}} = 62.4$ and 200 GeV [216, 217] and to correctly predict the decrease of v_1^{odd} at LHC energies [218], contrary to other calculations [219, 220]. The second source of directed

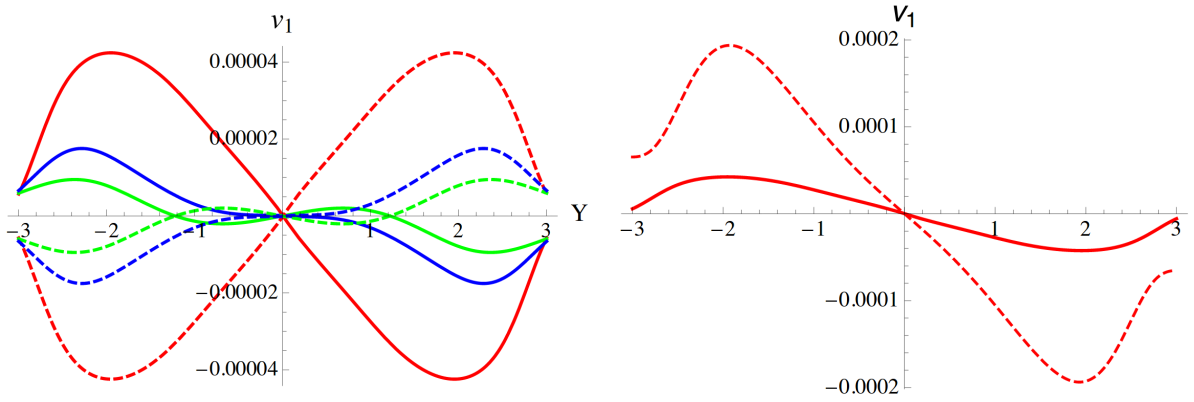

Figure 7.2: Left: $v_1(+)$ (solid lines) and $v_1(-)$ (dashed lines) of charged pions as a function of rapidity Y for Pb–Pb collisions at $\sqrt{s_{\rm NN}} = 2.76$ TeV and centrality 20-30%. Results for $p_{\rm T} = 0.25$ (green), 0.5 (blue) and 1 (red) GeV are shown. Right: comparison of Faraday and Lorentz effects, for charged pions at $p_{\rm T} = 1$ GeV and same collision parameters. Dashed line: Faraday only, continuous line: Faraday and Lorentz.

flow is believed to be the same one of higher harmonics: initial-state fluctuations, in this case *dipole-like* [46, 221]. However, differently than for the higher harmonics, the sign of v_1 changes with $p_{\rm T}$, due to the fact that the net transverse momentum of the system is zero by construction, i.e. $\langle p_x \rangle = \langle p_{\rm T} \cos(\varphi - \Psi_{\rm RP}) \rangle = 0$. This implies that low-$p_{\rm T}$ particles flow in the direction opposite to high-$p_{\rm T}$ ones [221, 222]. We can discriminate between the contribution of these two mechanisms (tilt and dipole fluctuations) looking at the η dependence of directed flow. It is convention to decompose v_1 into a rapidity-even and a rapidity-odd component

$$v_1 = v_1^{\rm even} + v_1^{\rm odd}, \tag{7.2}$$
$$v_1^{\rm even}(\eta) = v_1^{\rm even}(-\eta), \tag{7.3}$$
$$v_1^{\rm odd}(\eta) = -v_1^{\rm odd}(-\eta). \tag{7.4}$$

While dipole-like initial-state fluctuations, not having a defined symmetry with respect to η, contribute to both $v_1^{\rm even}$ and $v_1^{\rm odd}$, the tilt is precisely anti-symmetric and therefore contributes to $v_1^{\rm odd}$ only. This was first proposed by ALICE in [218] and is consistent with what observed both at RHIC [216, 217, 223] and LHC [218, 222, 224].

In order to separate the rapidity-even and rapidity-odd component, v_1 is usually measured with respect to two separate event planes, measured at positive and negative rapidities. For this study, we will use the spectator plane $\Psi_{\rm SP}$, defined by the azimuthal angle at which the spectator neutrons are deflected and measured by means of hadronic calorimeters placed near beam rapidity, such as the Zero Degree Calorimeters (ZDC) [110, 103] of the ALICE detector. This choice has two advantages with respect to using the first-order event plane Ψ_1, measured by means of charged particles produced in the collision, as more commonly done for anisotropic flow measurements.

1. It is free from biases coming from non-flow and transverse momentum conservation, which are important in the case of v_1 [222].

2. It is, in principle, maximally correlated with the angle of the magnetic field Ψ_B, since this is determined by the spectator themselves, while Ψ_1, being mostly due to initial-state fluctuations, is expected to be weakly correlated.

It also has two disadvantages.

1. The deflection that the spectators experience is theoretically not well understood. At LHC energies, it has been estimated that such nucleons have $\langle p_{\mathrm{T}} \rangle \approx 20$ MeV/c [218]. Concerning the direction of the deflection, data on asymmetric Cu–Au collisions [225, 226] strongly favor the hypothesis that they move outward, i.e. opposite to the collision point, but no definitive proof exist [227].

2. Some of the spectator neutrons are clustered in composite nuclear fragments, which are deflected by the expermients' dipole magnetic field and therefore are not measurable [228] (see Sec. 8.2). This constitutes a potential source of decorrelation between Ψ_{SP} and Ψ_B, whose importance grows from central to peripheral collisions.

Directed flow can then be measured with the scalar product method [121] with respect to the two Q-vectors separately

$$v_1\{\Psi_{\mathrm{SP}}^{\mathrm{A,C}}\} = \frac{\langle q_1 \, Q_{\mathrm{A,C}}^{*} \rangle}{\sqrt{|\langle Q_{\mathrm{A}} \, Q_{\mathrm{C}}^{*} \rangle|}}, \tag{7.5}$$

where q_1 is the Q-vector built from charged tracks at mid-rapidity

$$q_1 = \frac{\sum_{j=1}^{M} w_j \, e^{i\varphi_j}}{\sum_{j=1}^{M} w_j} \tag{7.6}$$

and w_j are weights used to correct for non-uniform acceptance and efficiency (Sec. 3.2). Conventionally, the even and odd component of v_1 are defined so that the directed flow of the spectator neutrons[1] at positive pseudorapidity has positive sign [223, 218]

$$v_1^{\mathrm{odd}} = \frac{1}{2}(v_1\{\Psi_{\mathrm{SP}}^{\mathrm{A}}\} - v_1\{\Psi_{\mathrm{SP}}^{\mathrm{C}}\}), \tag{7.7}$$

$$v_1^{\mathrm{even}} = \frac{1}{2}(v_1\{\Psi_{\mathrm{SP}}^{\mathrm{A}}\} + v_1\{\Psi_{\mathrm{SP}}^{\mathrm{C}}\}). \tag{7.8}$$

We note that the sign of v_1 is therefore defined by this choice. The signal that we look for is a charge difference in the odd component, which we can quantify as

$$\Delta v_1^{\mathrm{odd}} = v_1^{\mathrm{odd}}(+) - v_1^{\mathrm{odd}}(-), \tag{7.9}$$

$$\Delta v_1^{\mathrm{even}} = v_1^{\mathrm{even}}(+) - v_1^{\mathrm{even}}(-). \tag{7.10}$$

The even component is expected not to be sensitive to the signal, i.e. $\Delta v_1^{\mathrm{even}} = 0$, and can therefore be used as a control measurement. The η and centrality dependence of v_1^{odd} and v_1^{even} in Pb–Pb collisions at $\sqrt{s_{\mathrm{NN}}} = 2.76$ TeV [218] is shown in Fig. 7.3. The even component is observed to be negative and independent on η, while the odd one shows a negative slope, as observed in previous STAR measurements [217]. Both components show

[1] more in general, of the particles that define the event plane

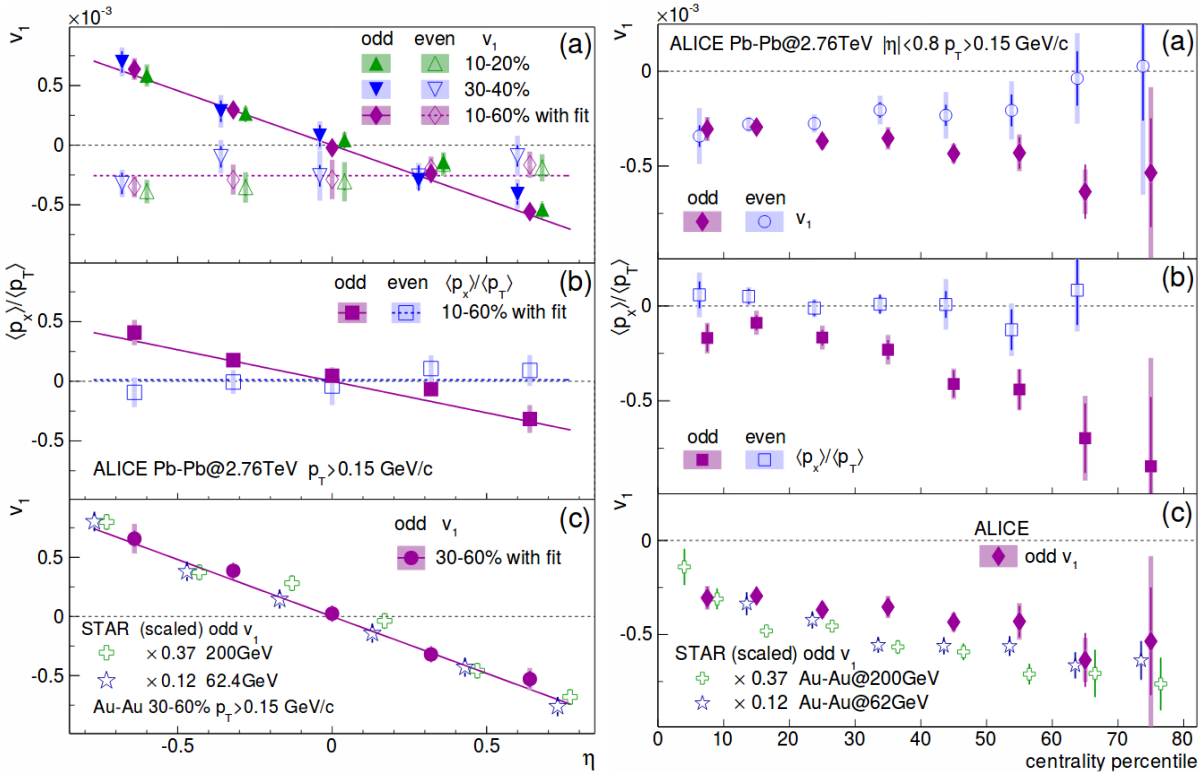

Figure 7.3: Left: (a) v_1 and (b) $\langle p_x \rangle / \langle p_\mathrm{T} \rangle$ as a function of η in Pb–Pb collisions at $\sqrt{s_\mathrm{NN}} = 2.76$ TeV. (c) v_1^odd compared to STAR measurements [217]. Right: same observables as a function of centrality (here, $v_1^\mathrm{odd} = v_1^\mathrm{odd}(\eta) - v_1^\mathrm{odd}(-\eta)$). Figures taken from [218].

a weak centrality dependence. These results are consistent with v_1^odd being determined by dipole-like fluctuations and tilted initial state, with the latter being increasingly important going from central to peripheral collisions. Also, the fact that v_1^even differs by about one order of magnitude from $v_1\{2, |\Delta\eta| > 0.8\}$ [229, 222] and $v_1\{4\}$ [224] suggests that indeed Ψ_1, being mostly due to initial-state fluctuations, is poorly correlated with Ψ_SP.

7.2 Systematic uncertainties

The systematic uncertainties are evaluated following the procedure explained in Sec. 3.5. Possible sources of systematic uncertainties that are investigated are:

- track quality variables:
  - number of TPC space points
  - χ^2_TPC
  - χ^2_ITS
  - fraction of shared TPC space points
  - in which ITS layer hits are required
- event selection criteria:
  - pile-up cuts

  - centrality determination
  - ALICE dipole magnet polarity
- reconstructed primary vertex position
- residual differences in ZDC Q-vector components

Additional sources of systematic uncertainties that are investigated and are found to be negligible include:

- contamination from secondary particles
- uncertainties in estimating the efficiency
- variations in TPC and TOF calibration (different strategies were adopted for different parts of the dataset)
- space-charge distortions in the TPC
- variations in instantaneous luminosity
- ZDC Q-vector calibration
  - effects of one faulty tower in ZDC-A for parts of the dataset
  - sensitivity on parameter α (see Eq. 3.33)
  - differences in the response of the different ZDC towers
  - correlation between the energy deposition in the common tower and the average centroid position

The variations in track quality variables are chosen in order to reject around 10% less or more tracks, with respect to the default choice, for each variable. The number of variations tested is between 1 and 4 for each of the sources and are performed independently, i.e. possible correlations are ignored. Pile-up rejection criteria (described in Sec.2.3.1) are varied in order to require a better agreement between different multiplicity estimators from the central barrel and result in rejecting around 20% of the total data sample, with respect to the default choice.

The additional controls on the ZDC calibration are performed as follows. Concerning the effects of the faulty tower of ZDC-A (see Sec.3.4), we compare $v_1\{\Psi_{\rm SP}^{\rm A}\}$ between runs during which the tower was still functioning and runs during which it was not and we find the two to be consistent. We also apply the same correction procedure on ZDC-C, simulating one tower to be missing, and we find $v_1\{\Psi_{\rm SP}^{\rm C}\}$ to be unaffected. Concerning the parameter α, we compare $v_1\{\Psi_{\rm SP}^{\rm A,C}\}$ obtained with the default value ($\alpha = 0.395$) and with $\alpha = 0.2$ and $\alpha = 1$; no significant difference is observed, suggesting that saturation effects do not bias the Q-vector reconstruction in the centrality range analysed.

The effect of the differences in the response of the different ZDC towers is evaluated equalising the corresponding energy spectra $\mathrm{d}N/\mathrm{d}E_i$. Significant differences are in fact observe, see Fig.7.4, top panels, not only on the average (which is corrected for through the

gain equalisation procedure) but also on the shape. In order to quantify these differences, we show in the bottom panels of the same figure the ratios between the spectra of the different ZDC towers and the average. The spectra are observed to be well described by the following empirical formula

$$P(E_i) = \frac{\mathrm{A}}{E_i \sigma_1 \sqrt{2\pi}} \exp\left(-\frac{(\ln E_i - \mu_1)^2}{2\sigma^2}\right) + \frac{\mathrm{B}}{\sigma_2 \sqrt{2\pi}} \exp\left(-\frac{(E_i - \mu_2)^2}{2\sigma^2}\right), \qquad (7.11)$$

which is the sum of a log-normal and a normal distribution, with A, B, σ_1, μ_1, σ_2 and μ_2 as free parameters. The continuous lines in Fig.7.4 represent fits of $\mathrm{d}N/\mathrm{d}E_i$ with Eq. 7.11 and the dashed lines show the individual contributions of the log-normal and normal part. We note that the log-normal contribution to the spectra is dominant with respect to the normal one. Knowing that two log-normal distributions α and β can be mapped to one another with the transformation

$$E \longrightarrow \exp\left(\left(\ln E - \mu_\alpha + \mu_\beta \frac{s_\alpha}{s_\beta}\right) / \frac{s_\alpha}{s_\beta}\right)$$
$$\mu = \ln\left(\frac{\langle E\rangle^2}{\sqrt{\langle E^2\rangle}}\right)$$
$$s^2 = \ln\left(1 + \frac{\sqrt{\langle E^2\rangle - \langle E\rangle^2}}{\langle E\rangle^2}\right)$$

we apply the same transformation to the individual tower spectra in order to equalise them to the average one, separately in centrality intervals of 1%. The results are shown in Fig. 7.4, for the same run and centrality interval. We observe this empirical correction to work relatively well, within a few % for most of the energy range. When we then compare results on $v_1\{\Psi_{\mathrm{SP}}^{\mathrm{A,C}}\}$ obtained with and without this correction, after the appropriate re-centring procedure, we find the two to be consistent. We conclude that the differences in the tower responses do not bias the Q-vector reconstruction and that the equalisation of $\langle E\rangle$, explained in 3.4, is sufficient. Finally, we investigate the correlation between the energy deposition in the common tower (which is not included in the calibration procedure, if not for compensating the missing tower on ZDC-A) and the average centroid position, adding a re-centring step as a function of this variable. Again, no significant differences are observed at the level of $v_1\{\Psi_{\mathrm{SP}}^{\mathrm{A,C}}\}$.

The contributions of the aforementioned sources to the total systematic uncertainty of v_1^{odd} and v_1^{even} are reported in Tab.7.1. The uncertainties are divided in "correlated" and "uncorrelated" according to their dependence on pseudorapidity. The percentages reported are computed with respect to a reference value $v_1^{\mathrm{ref}} = 0.5 \times 10^{-3}$. The uncertainties on the charge-dependent results $v_1^{\mathrm{odd}}(\pm)$ and $v_1^{\mathrm{even}}(\pm)$ are very similar and are therefore not reported.

We observe the dominant sources of systematic uncertainty to be the ZDC calibration and the run magnet polarity. For both cases, the corresponding biases at the level of v_1 are observed to be mostly correlated in η. This is concluded to be due to residual unphysical correlations between the centroid positions of the two ZDCs, which cannot be corrected for by the calibration procedure, as discussed in Sec. 3.4. The differences between results with opposite run magnet polarities suggest that the average vertical beam crossing angle

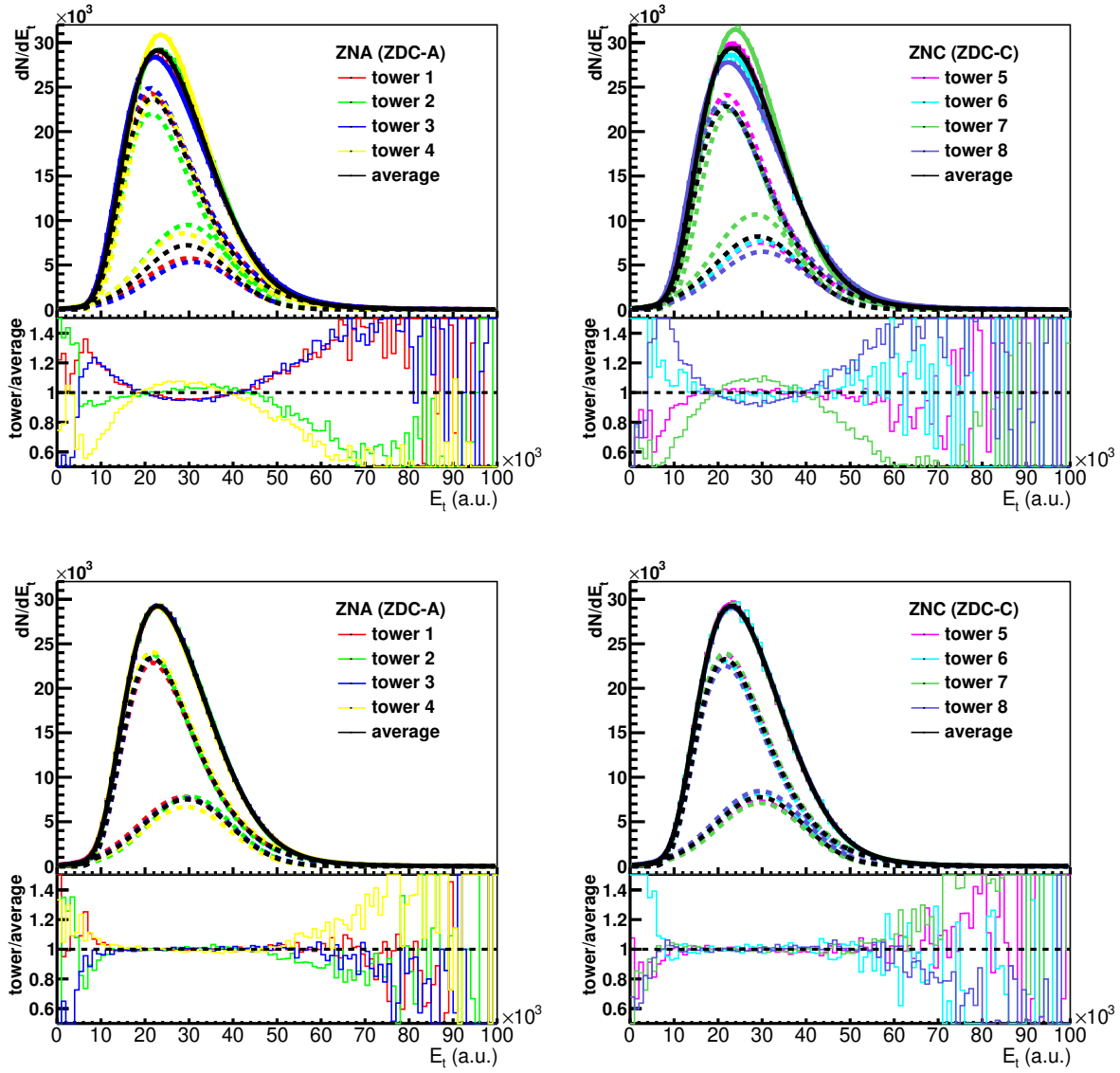

Figure 7.4: Continuous lines: energy spectra from the different ZDC towers, in ZDC-C (left) and ZDC-A (right), and their ratios with the average, before (top) and after (bottom) corrections, for centrality 30-31%. Dashed lines: contributions of the log-normal and normal distributions to the fit with Eq. 7.11.

Error source	$v_1^{\text{odd}}\{\Psi_{\text{SP}}\}$		$v_1^{\text{even}}\{\Psi_{\text{SP}}\}$	
	corr.	uncorr.	corr.	uncorr.
centrality determination	2%	n.s.	2%	n.s.
primary vertex	n.s.	3%	n.s.	3%
magnet polarity	n.s.	4%	14%	2%
pile-up	n.s.	2%	n.s.	2%
tracking	5%	4%	6%	5%
secondary contamination	1%	n.s.	1%	n.s.
space-charge distortion	n.s.	5%	n.s.	4%
ZDC Q-vectors corr.	7%	n.s.	34%	3%

Table 7.1: Maximum value of the systematic uncertainties from each source for v_1^{odd} and v_1^{even}.

Error source	Δv_1^{odd}		Δv_1^{even}	
	corr.	uncorr.	corr.	uncorr.
centrality determination	1%	n.s.	n.s.	n.s.
primary vertex	n.s.	3%	n.s.	3%
magnet polarity	n.s.	3%	n.s.	4%
pile-up	n.s.	2%	n.s.	2%
tracking	2%	3%	2%	3%
secondary contamination	n.s.	n.s.	n.s.	n.s.
space-charge distribution	n.s.	2%	n.s.	2%
ZDC Q-vectors corr.	n.s.	n.s.	n.s.	n.s.

Table 7.2: Maximum value of the systematic uncertainties from each source for Δv_1^{odd} and Δv_1^{even}.

(± 60 μrad in the y-z plane, for the dataset under consideration), which is opposite in the two cases, also plays a role.

For the charge differences Δv_1^{odd} and Δv_1^{even}, the total systematic uncertainties are reported in Tab. 7.2. We note that the biggest uncertainties on v_1^{odd} and v_1^{even}, namely magnet polarity and ZDC Q-vectors correlations, being effectively identical for positively and negatively charged particles, cancel out in the difference.

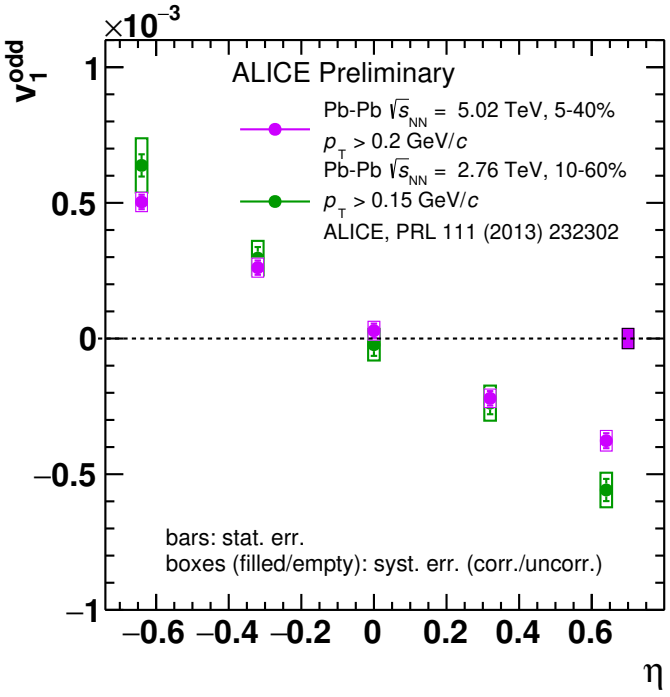

Figure 7.5: v_1^{odd} of unidentified charged particles in Pb–Pb collisions at $\sqrt{s_{\mathrm{NN}}} = 5.02$ and 2.76 TeV [218].

7.3 Results

Figure 7.5 shows v_1^{odd} of inclusive charged particles as a function of pseudorapidity and compare it with results at $\sqrt{s_{\mathrm{NN}}} = 2.76$ TeV [218]. A decrease is observed in the slope $\mathrm{d}v_1^{\mathrm{odd}}/\mathrm{d}\eta$ going from 2.76 to 5.02 TeV collision energy, which is qualitatively consistent with the energy dependence previously observed from lowest RHIC energies to LHC ones [230] and can be interpreted as a decrease in the tilt of the initial state in the x-y plane at these higher energies. To quantify this decrease, we fit data at both energies with a fit function of the form $v_1^{\mathrm{odd}}(\eta) = k \cdot \eta$ and the slope k is found to be

$$k\,[2.76\ \mathrm{TeV}] = -9.14 \pm 0.40\ (\mathrm{stat.}) \pm 1.58\ (\mathrm{syst.}) \times 10^{-4},$$
$$k\,[5.02\ \mathrm{TeV}] = -7.04 \pm 0.27\ (\mathrm{stat.}) \pm 0.35\ (\mathrm{syst.}) \times 10^{-4},$$

i.e. a difference of about 30%, with a p-value of 0.35. The significance of the difference is therefore small. However, a large part of the systematic uncertainties are known to be correlated among datasets at the two energies (especially those related to tracking, as observed for other flow coefficients, see Sec. 4.3); if this would be taken into account, the difference is expected to be significant. The difference in the centrality ranges for results at $\sqrt{s_{\mathrm{NN}}} = 2.76$ and 5.02 TeV is estimated to affect minorly the comparison, since the centrality dependence of v_1^{odd} within $|\eta| < 0.8$ is weak (Fig. 7.3, right). The same applies for the small differences in $\langle p_{\mathrm{T}} \rangle$.

The even component v_1^{even} is shown in Fig. 7.6. As for results at lower energies, we observe no significant η dependence, but with respect to those we seem to observe a

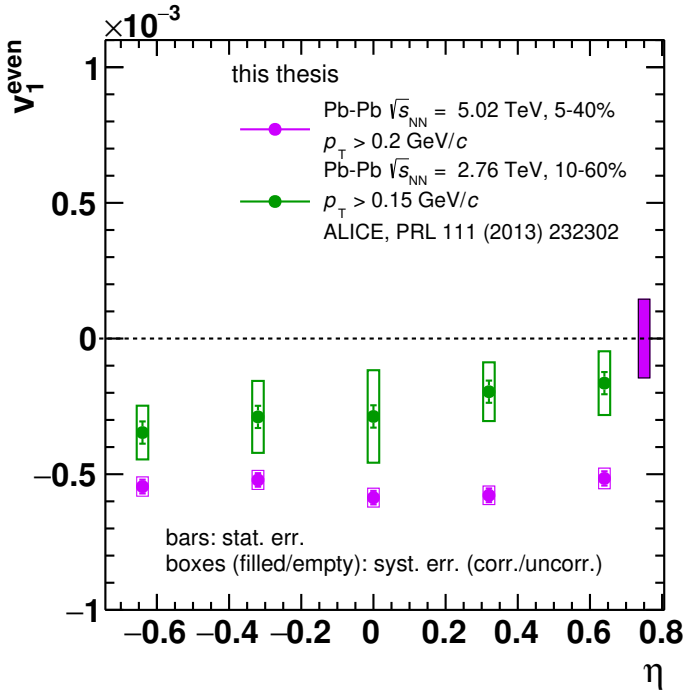

Figure 7.6: v_1^{even} of unidentified charged particles in Pb–Pb collisions at $\sqrt{s_{\text{NN}}} = 5.02$ and 2.76 TeV [218].

decrease, which could be interpreted as an increase of dipole-like fluctuations at higher energies. As for v_1^{odd}, the differences due to centrality range and $\langle p_{\text{T}} \rangle$ are expected to be negligible. In order to quantify the difference between the two energies, we fit with data with a constant function $v_1^{\text{odd}}(\eta) = a$ and the parameter a is found to be

$$a\,[2.76\ \text{TeV}] = -2.57 \pm 0.18\ (\text{stat.}) \pm 1.82\ (\text{syst.}) \times 10^{-4},$$
$$a\,[5.02\ \text{TeV}] = -5.50 \pm 0.11\ (\text{stat.}) \pm 2.04\ (\text{syst.}) \times 10^{-4}.$$

Not knowing which fraction of systematic uncertainties is correlated in η for results at $\sqrt{s_{\text{NN}}} = 2.76$ TeV, we assume it to be 50%. We then obtain a p-value of 0.18 for the difference of results at $\sqrt{s_{\text{NN}}} = 5.02$ and 2.76 TeV, which implies the difference not to be significant. Noting that the dominant source of systematic uncertainty at $\sqrt{s_{\text{NN}}} = 5.02$ TeV did not affect the data at lower energies, the significance of the difference is not expected to improve significantly if a proper evaluation of the correlation between systematic uncertainties of datasets at the two energies is performed.

Figure 7.7 shows v_1^{odd} at $\sqrt{s_{\text{NN}}} = 5.02$ TeV separately for positively and negatively charged particles (left panel), together with the charge difference $\Delta v_1^{\text{odd}} = v_1^{\text{odd+}} - v_1^{\text{odd-}}$ (right panel). To quantify a possible pseudorapidity-odd charge difference, Δv_1 is fitted using a linear function of the form $\Delta v_1^{\text{odd}}(\eta) = k \cdot \eta$ and the slope k is found to be

$$k = 1.68 \pm 0.49\,(\text{stat.}) \pm 0.41\,(\text{syst.}) \times 10^{-4}. \tag{7.12}$$

The result has a total significance of 2.6 σ, where σ is the total uncertainty, and a p-value

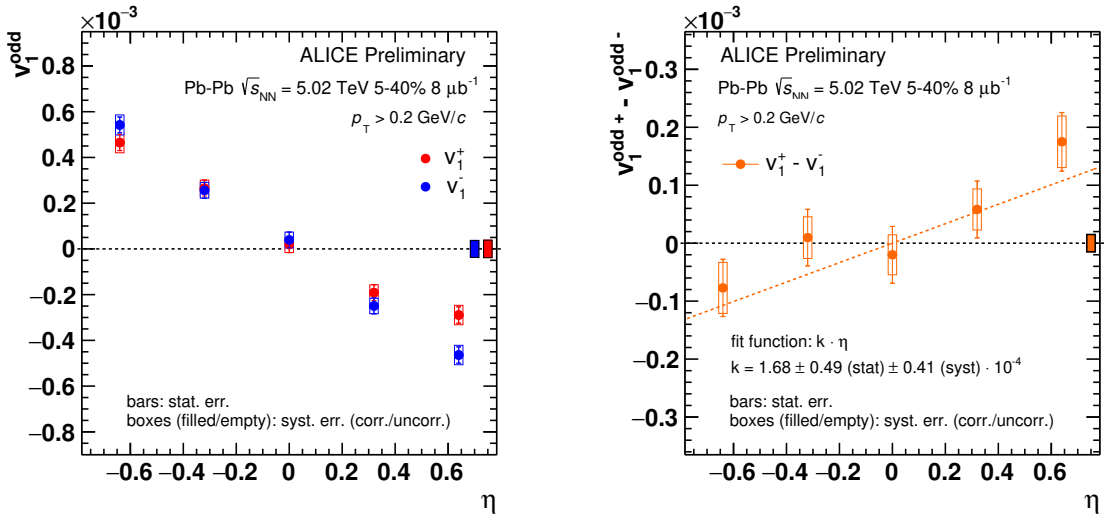

Figure 7.7: Left: v_1^{odd} of unidentified positively (red) and negatively (blue) charged particles. Right: charge difference $\Delta v_1^{\mathrm{odd}} = v_1^{\mathrm{odd}}(+) - v_1^{\mathrm{odd}}(-)$, fitted with a function of the form $\Delta v_1^{\mathrm{odd}}(\eta) = k \cdot \eta$.

of 0.03. Compared to predictions on the effect of magnetic-induced charged currents [211] for $\pi^{\pm}$ at $\sqrt{s_{\mathrm{NN}}} = 2.76$ TeV and similar $\langle p_{\mathrm{T}} \rangle$, it is around 1 order of magnitude bigger and of opposite sign. We will elaborate further on these discrepancies in Sec. 7.4. The same charge difference for v_1^{even} is shown in Fig. 7.8. Here, contrary to v_1^{odd}, we do not observe a significant difference between charges, consistently with expectations.

Finally, the centrality and p_{T} dependence of the slope $k = \mathrm{d}\Delta v_1^{\mathrm{odd}}/\mathrm{d}\eta$ are shown in Fig. 7.9, left and right panels, respectively. We observe no dependence on neither variables, within uncertainties. Regarding the centrality dependence, we can speculate that to first order the magnitude of $\Delta v_1^{\mathrm{odd}}$ should increase from central to peripheral collisions, as the strength of the magnetic field does (Fig. 6.15). The evolution with respect to p_{T}, within the low-p_{T} range accessible with the available statistics, should be determined by the relative strength of the two mechanisms at play, Faraday's law and Lorentz force. The strong p_{T} dependence that was predicted, with a sign change of thee slope between $p_{\mathrm{T}} = 0.25$ and 0.5 GeV/c (Fig. 7.2), is not observed.

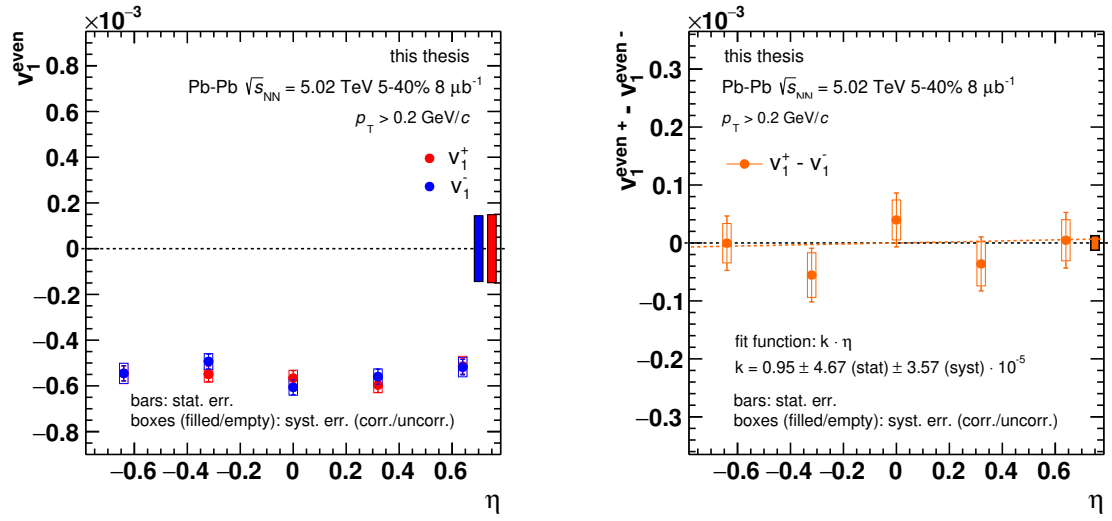

Figure 7.8: Left: v_1^{even} of unidentified positevely (red) and negatively (blue) charged particles. Right: charge difference $\Delta v_1^{\text{even}} = v_1^{\text{even}}(+) - v_1^{\text{even}}(-)$, fitted with a function of the form $\Delta v_1^{\text{even}}(\eta) = k \cdot \eta$.

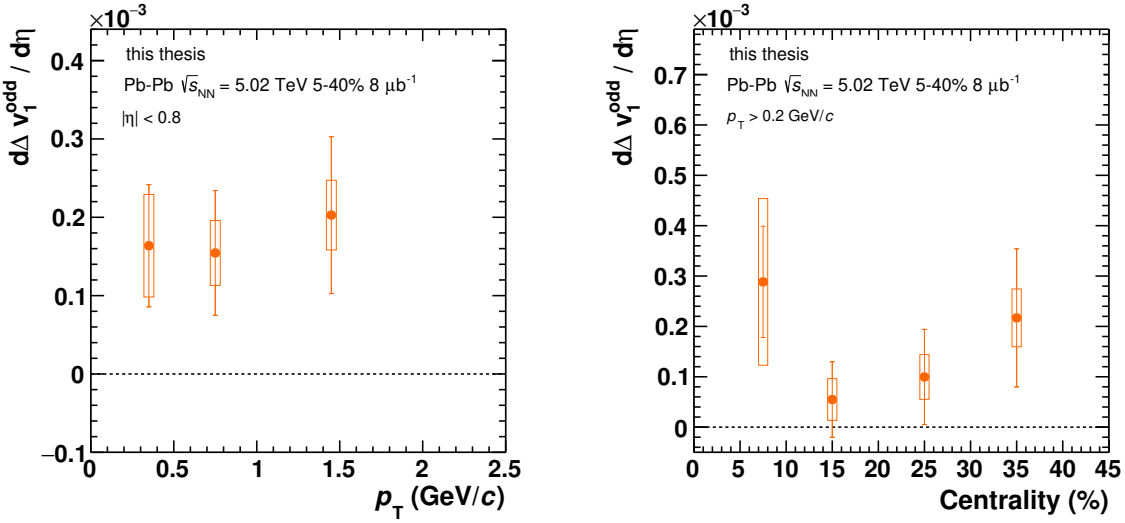

Figure 7.9: $\mathrm{d}\Delta v_1^{\text{odd}}/\mathrm{d}\eta$ as a function of p_{T} (left) and centrality (right).

7.4 Discussion

We present measurements of directed flow v_1 with respect to the spectator plane of inclusive charged particles in Pb–Pb collisions at $\sqrt{s_{\rm NN}} = 5.02$ TeV, divided into the symmetric ($v_1^{\rm even}$) and anti-symmetric ($v_1^{\rm odd}$) component with respect to pseudorapidity. While for $v_1^{\rm even}$ no charge difference is observed, a hint of a difference is observed for $v_1^{\rm odd}$, which appears to be anti-symmetric with respect to η. This difference is therefore quantified with the slope $\mathrm{d}\Delta v_1^{\rm odd}/\mathrm{d}\eta$, with $\Delta v_1^{\rm odd} = v_1^{\rm odd}(+) - v_1^{\rm odd}(-)$, and is found to be $1.68 \pm 0.49\,(\text{stat.}) \pm 0.41\,(\text{syst.}) \cdot 10^{-4}$, with a total significance of $2.6\,\sigma$, within centrality 5-40% and $p_{\rm T} > 0.2$ GeV/c, corresponding to $\langle p_{\rm T} \rangle \approx 0.76$ GeV/c (Fig. 4.13). This difference, which needs to be confirmed, could be attributed to the influence of the early-time magnetic field and in particular to charge currents in the QCD system, but both the sign and the magnitude differ from predictions, with the latter being about 1 order of magnitude bigger.

Such discrepancies are not expected to be explained by the differences in particle species in the inclusive sample, collision energy or $\langle p_{\rm T} \rangle$. At the same time, no other mechanism, as far as we know, has ever been proposed[2] to explain a possible signal with the qualitative features discussed here. We can then speculate on the possible origin of these discrepancies, assuming that indeed the observed $\Delta v_1^{\rm odd}$ originates from magnetic-induced charged currents. The sign of the effect, as discussed earlier, depends entirely on the relative strength of the two mechanisms at play, Faraday's law and Lorentz force; the results would imply the latter to be dominant, contrary to what concluded in [211]. The difference in magnitude is certainly more challenging to explain. One possibility is that the time at which the expansion of the system becomes effectively hydrodynamic-like, and therefore flow develops, is much earlier that what usually employed in hydrodynamic model calculations (and used also in [211]), as recent theoretical works suggest [12]. This, combined with the fact that the magnetic field is much stronger at these early times, would determine an increase in the predicted $\Delta v_1^{\rm odd}$. Another possibility is connected with the fact that predictions are very sensitive to the choice of some model parameters, many of which are not constrained by experimental measurements. As an example, it was found that $\Delta v_1^{\rm odd}$ is inversely proportional to the drag coefficient of quarks in the medium [231], whose precise value is currently only known from calculations for heavy quarks in $N = 4$ supersymmetric Yang-Mills theory. However, we are not in the position to estimate the uncertainty on this particular parameter and the corresponding uncertainty that this will determine on the final predictions. We conclude that more work is required on both the experimental and theoretical side to confirm this observation and its interpretation.

[2] we refer here to Pb–Pb collisions at LHC energies; lower energies, $\sqrt{s_{\rm NN}} \lesssim 100$ GeV, and/or asymmetric systems require a separate discussion, as mentioned before

Chapter 8

Outlook and Exploratory Studies

In this chapter, we will discuss the prospects for future measurements of anisotropic flow with ALICE during the next LHC Run and the results of two exploratory studies carried out during the completion of this dissertation.

8.1 Estimates for LHC Run 3

The ALICE experiment has planned an ambitious program of detector upgrades in view of the next LHC Run 3 (2021-2023), mostly driven by the necessity of increasing the readout capabilities and therefore exploit the high luminosities that the LHC will deliver. For Pb–Pb collisions, interaction rates will reach about 50 kHz, i.e. istantaneous luminosities of $\mathcal{L} = 6 \times 10^{27}$ cm^{-2}s^{-1}, about ten times larger than during previous LHC Runs. The proposed ALICE upgrade aims at recording all available collisions, which amount to an integrated luminosity of about 10 nb^{-1}; this number can be contrasted to what has been recorded so far (June 2018), about 0.3 nb^{-1} in total (for 0.6 nb^{-1} delivered). Morover, of these 0.3 nb^{-1} only about 20 μb^{-1} fulfilled trigger[1] and event selection criteria (Sec. 2.3.1); for this reason, the new read-out scheme will be mostly *trigger-less*, allowing to collect a much larger fraction of the foreseen 10 nb^{-1}. All considered, the number of recorded events should increase by a factor of 50-1000, with the lower limit estimated from past ALICE performances. Other goals of the ALICE upgrade include improve track resolution at low p_{T} and enhance particle identification capabilities; for a complete overivew, see [232].

For all measurements presented in this dissertation, most important will be the increase in available data, while other performance improvements (efficiency, event plane resolution, etc.) are quantiatively expected to play a minor role. Regarding measurements of energy dependence of anisotropic flow (Ch. 4), statistical uncertainties are already dominated by those of results at $\sqrt{s_{\mathrm{NN}}} = 2.76$ TeV, therefore there will not be a benefit. Concerning measurements at $\sqrt{s_{\mathrm{NN}}} = 5.02$ TeV, reduced statistical uncertainties will surely allow to extend the range of p_{T}-differential flow measurements up to 100 GeV/c and possibly above; however, it is unclear what additional information will this provide, as we already covered the p_{T} range separating single-track measurements from jet ones.

[1] We refer here to all triggers usable for studies presented in this dissertation, i.e. including full tracking at mid-rapidity; these changed across the years, see [105].

New observables, we argue, will be better suited to answer the remaining questions on anisotropic flow at high p_{T}, e.g. those presented in [153].

Measurements of flow fluctuations (Ch. 5) will also benefit of improved statistics, allowing to extend the study presented in this dissertation to higher harmonics (v_3, v_4, ...), identified particles and, potentially, to probe even higher moments of the flow p.d.f.s, e.g. kurtosis. It is clear that such measurements will help constrain initial-state and hydrodynamic models; what is less clear is, quantitatively, if they will have a specific advantage with respect to available measurements. The analysis of the results presented in Sec. 5.4 by phenomenologists in the near future will hopefully answer these questions; for now, we argue that there are not sufficient elements to assess the importance of extending these studies to Run 3.

Results on CME with ESE (Ch. 6) and charge-dependent directed flow (Ch. 7), on the contrary, are currently strongly limited by statistical uncertainties and contain potentially unique information, as we argue in this dissertation. Therefore, we focus on these observables in the assessment of potential advantages of Run 3. In Sec. 6.4, Fig. 6.19 we show the upper limit on the CME fraction f_{CME} (Eq. 6.33) extracted performing an ESE analysis on the charge difference of the three-particle correlator $\Delta\gamma$. We take as a representative result f_{CME} in centrality 20-30% and estimate how uncertainties will be reduced with additional data (Fig. 8.1). These estimates assumes no variations in relevant boundary conditions: charged particle multiplicities, magnitude of v_2, event-plane resolution and potential CME signal; variations of the level of a few % are expected simply by the increase in collision energy, as discussed in Sec. 4.1, but they affect minorly these estimates. In such a case, statistical uncertainties are expected to scale simply as the inverse of the number of events. Projections at $N_{\mathrm{events}} = 10^7$, 10^8 and 10^{10} in centrality 20-30% correspond to a total integrated luminosity of about 0.02, 0.1 and 10 nb^{-1}, respectively. We see that for an integrated luminosity of about 10 nb^{-1} we will be able to set upper limits of less 1 % on a potential CME signal, with progressively bigger relative uncertainties arising from differences in $p_{1,\,\mathrm{CME}}$ from different initial-state models.

Similar estimates were performed for measurements of charge-dependent directed flow. In this case, we use a dedicated Monte Carlo simulation. The simulation does not include a full description of the detector response, for reasons of limited computational power, but does contain the most important elements: limited spectator-plane resolution, tuned to the measured one, number of reconstructed tracks (assuming no changes in the corresponding efficiency), a charge-independent v_1 plus a signal: $\Delta v_1 = 5 \times 10^{-5}$, as estimated in [211]. In Fig. 8.2 we see that in Run 3, with an integrated luminosity of about 10 nb^{-1}, we will be able to discriminate a signal with excellent statistical significance. Systematic uncertainties will then dominate, most importantly those on the ZDC performance; however, having observed these to be very much dependent on beam parameters and not knowing how these will be configured during Run 3, we cannot provide a reliable estimate.

Recently, it was suggested that heavy quarks, most relevantly charm ones, having a formation time of about 0.1 fm/c, might be much more sensitive to the early-time magnetic fields [233]. Estimates of a possible magnetic-induced charge-dependent directed flow were obtained, indicating a signal several orders of magnitudes larger than for light hadrons. Since the limited heavy-flavor meson multiplicities would be compensated by a much larger signal, the masurement could be experimentally feasible. In order to test if

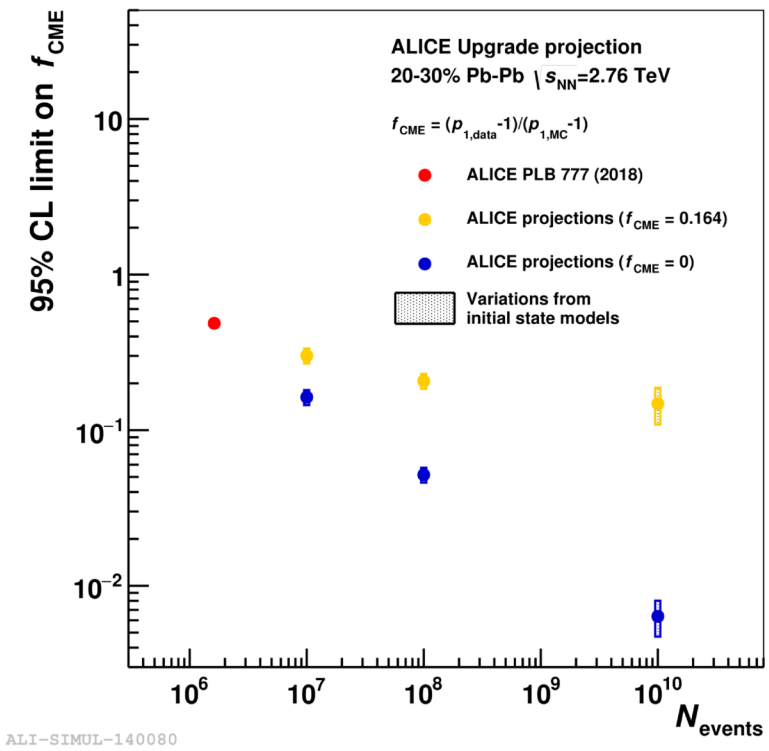

Figure 8.1: Projections on upper limits on f_{CME} (blue dots) as a function of number of events, extrapolating the upper limit in centrality 20-30% at $\sqrt{s_{\mathrm{NN}}} = 2.76$ TeV (red dot). See text for details.

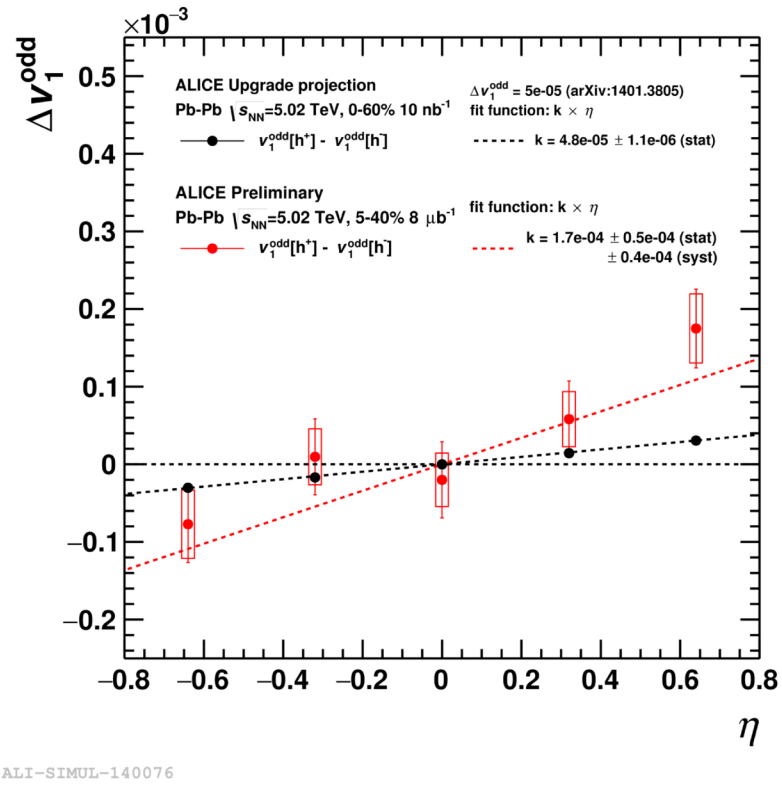

Figure 8.2: Projections on Δv_1 as a function of pseudorapidity η for inclusive charged particles. See text for details.

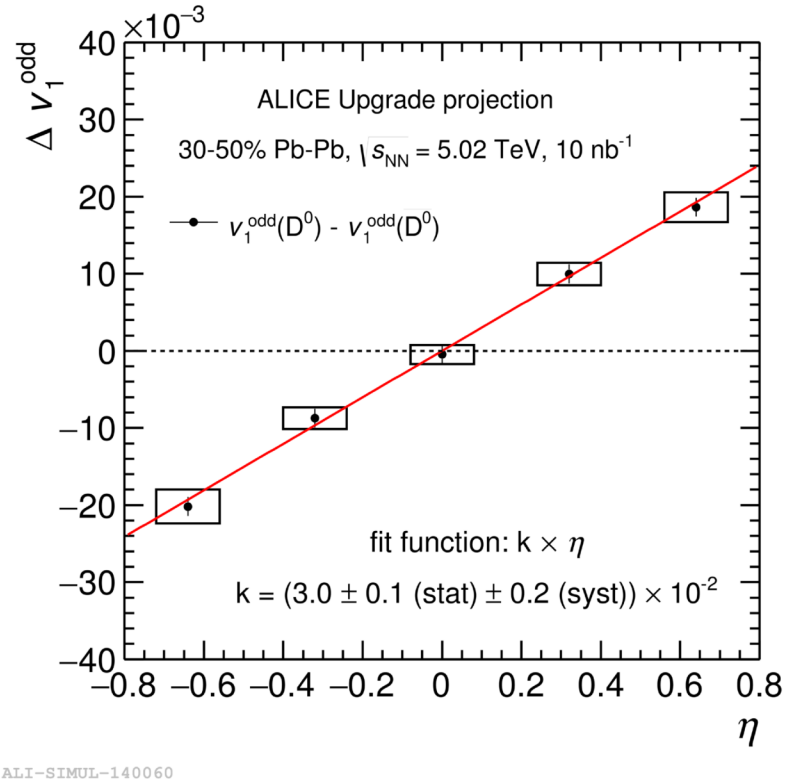

Figure 8.3: Projections on Δv_1 as a function of pseudorapidity η for D^0 mesons. Predictions from [233] are used. See text for details.

this is the case, we perform similar estimates for Run 3, assuming the signal predicted in [233] ($\Delta v_1 = 3 \times 10^{-2}$). The most abundant heavy-flavor mesons are D^0: we expect to produce 2.3 D^0 mesons per minimum bias event in Pb–Pb collisions at $\sqrt{s_{\rm NN}} = 5.02$ TeV [232]. If we factor in the branching ratio (3.8%) to the decay channel mostly used for reconstruction ($K^{\pm}\pi^{\mp}$) and the corresponding efficiency (5%) [234], we obtain about 4.4×10^{-3} reconstructed D^0 per minimum bias event. The other simulation settings are fixed as previously discussed for inclusive charged particles. Also for D^0 mesons, assuming an integrated luminosity of 10 nb^{-1}, we will be able to measure Δv_1 with high statistical significance (Fig. 8.3). The systematic uncertainties are only indicative and are assigned based on measurements of v_2 of D^0 at the same collision energy [235]. Again, systematic uncertainties on the ZDC performance are not assigned and can be dominant.

We conclude that in the years following Run 3 (2021-2023) ALICE will have the potential to perform high-precision measurements of CME observables and charge-dependent directed flow, providing strong constraints and, in practical terms, definitive answers on both subjects. We also note that the validity of these predictions rests on the capabilities of the Collaboration of reaching the goals of the upgrade program.

8.2 Spectator and participant nucleons

Introduction

The number of nucleons taking part in the collision ($N_{\rm part}$) can be estimated from the total number of spectator nucleons ($N_{\rm spec}$) as

$$N_{\rm part} = 2A - N_{\rm spec} \tag{8.1}$$

where A is the mass number of the colliding ions. $N_{\rm spec}$ can be reconstructed, in principle, from the total energy deposited in the ZDC, with the neutron calorimeter (ZN) recording spectator neutrons ($N^n_{\rm spec}$) and the proton one (ZP) recording spectator protons ($N^p_{\rm spec}$)

$$N_{\rm spec} = N^n_{\rm spec} + N^p_{\rm spec}. \tag{8.2}$$

In reality, two complications need to be taken into account. First, nuclear fragmentation mechanisms result in some spectator neutrons being bounded with spectator protons: these nuclear fragments are deflected by the magnetic field of the experiment and are subsequently lost in the beam pipe. The spectator neutrons arriving at the ZDC are therefore called *single* spectator neutrons ($N^n_{\rm spec,\ single}$) and constitute only a fraction of $N^n_{\rm spec}$. The fractional loss of spectator neutrons is grows with $N_{\rm spec}$: is almost negligible in central collisions and is dominant in peripheral ones. Nevertheless, $N^n_{\rm spec,\ single}$ and $N^n_{\rm spec}$ are monotonically correlated up to a centrality of about 50% [110]. Secondly, for single spectator protons ($N^p_{\rm spec,\ single}$), additional losses are expected due to the deflection of the magnetic field; these losses depend strongly on the LHC beam optics, irrespectively of event centralities, and on the longitudinal component of the nucleon Fermi momentum [110]. Due to these experimental complications, here we use only the neutron calorimeters to estimate $N_{\rm spec}$ and $N_{\rm part}$

$$N_{\rm spec} = \frac{A}{N} N^n_{\rm spec} \approx \frac{A}{N} \frac{E_{\rm ZNA} + E_{\rm ZNC}}{E_n}, \tag{8.3}$$

$$N_{\rm part} = 2A - N_{\rm spec}, \tag{8.4}$$

where N is the neutron number of the colliding ions, $E_{\rm ZNA}$ ($E_{\rm ZNC}$) the energy measured by the ZNA (ZNC) and E_n the beam energy per nucleon.

The estimation of $N_{\rm part}$ provides information complementary to centrality, which is based on total charged particle multiplicity (see Sec. 2.3.2). How basic bulk observables (anisotropic flow, $p_{\rm T}$ spectra), depend on $N_{\rm part}$ for a fixed multiplicity and/or impact parameter has never, to best of our knowledge, been measured.

The distribution of $E_{\rm ZN} = E_{\rm ZNA} + E_{\rm ZNC}$ as a function of centrality is shown in Fig. 8.4. For central collisions, up to a centrality of about 10%, we observe the expected proportionality: more peripheral events have lower $\langle N_{\rm part} \rangle$ and therefore higher $\langle N^n_{\rm spec} \rangle$. Brackets denote, here and in the following, an average over all events within a given centrality and/or $E_{\rm ZN}$ class. For mid-central and peripheral collisions the proportionality is progressively reduced and the correlation becomes negative above a centrality of about 50%, which indicates that nuclear fragmentation progressively becomes more important. For this study, we select events within narrow centrality intervals (1% width) and we divide them according to $E_{\rm ZN}$. For simplicity, we start by defining three classes, corresponding

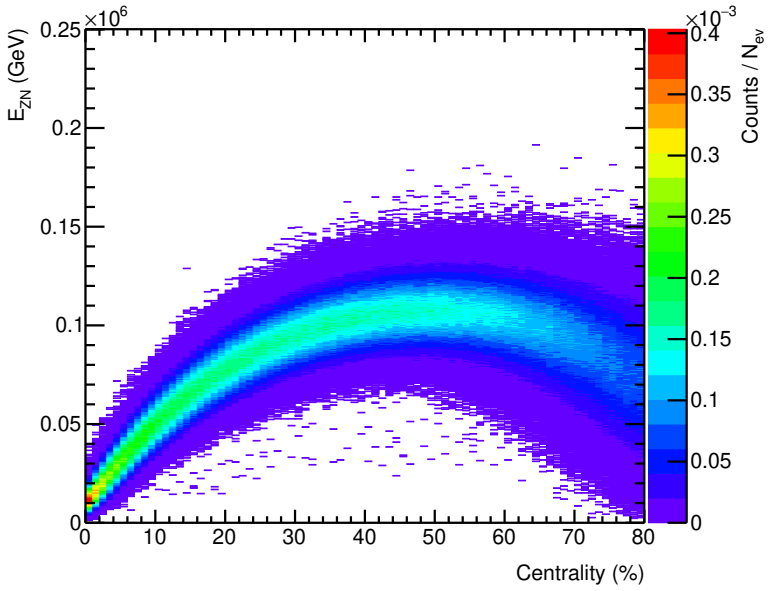

Figure 8.4: Uncorrected ZN energy spectrum $E_{\mathrm{ZN}} = E_{\mathrm{ZNA}} + E_{\mathrm{ZNC}}$ as a function of centrality in Pb–Pb collisions at $\sqrt{s_{\mathrm{NN}}} = 2.76$ TeV.

to the 33% lowest, intermediate and highest fraction of E_{ZN}. We expect a higher (lower) $\langle N_{\mathrm{part}} \rangle$ for the low (high) E_{ZN} class at a fixed centrality.

Bulk observables

We first measure how anisotropic flow and p_{T} spectra change between the low and high E_{ZN} classes, using the 2010 data set of Pb–Pb collisions at $\sqrt{s_{\mathrm{NN}}} = 2.76$ TeV (2 $\mu\mathrm{b}^{-1}$). In Fig. 8.5 we show $v_2\{4\}$, integrated in the p_{T} range $0.2 < p_{\mathrm{T}} < 5$ GeV/c, as a function of centrality (top panel), together with the ratios between low/high E_{ZN} class and the unbiased sample (bottom panel): we observe deviations of the order of 10% or less, with opposite signs in central and peripheral collisions. These deviations vanish at centrality of about 30%. No significant p_{T} dependence is observed (Fig. 8.6). Results with $v_2\{2, |\Delta\eta| > 1\}$ (not shown here) are observed to be consistent. For higher harmonics ($v_3\{2, |\Delta\eta| > 1\}$ and $v_4\{2, |\Delta\eta| > 1\}$, not shown here), deviations are barely significant (less than 2%) and apparently of similar sign. Concerning p_{T} spectra, shown in Fig. 8.7 for two extreme centrality classes, the deviations are of the order of 5% or less, with opposite signs at low p_{T} ($p_{\mathrm{T}} < 1$ GeV/c) and at higher p_{T} ($p_{\mathrm{T}} > 1$ GeV/c). Also here, the sign of these deviations is opposite between central and peripheral events and the switch happens at a centrality of about 32% (not shown here). We estimate that the variations in v_2 due to the change in $\langle p_{\mathrm{T}} \rangle$ within $0.2 < p_{\mathrm{T}} < 5$ GeV/c between the different E_{ZN} classes is of about 1% or less: the variations of v_2 and p_{T} spectra can therefore be considered mostly independent. Other event variables (average multiplicity, primary vertex position) are observed to change by less than 2% between different E_{ZN} classes.

We will now discuss possible interpretations of these observations. We assume a direct proportionality between E_{ZN}, N_{spec}^{n} and N_{spec}, or, equivalently, anti-correlation between

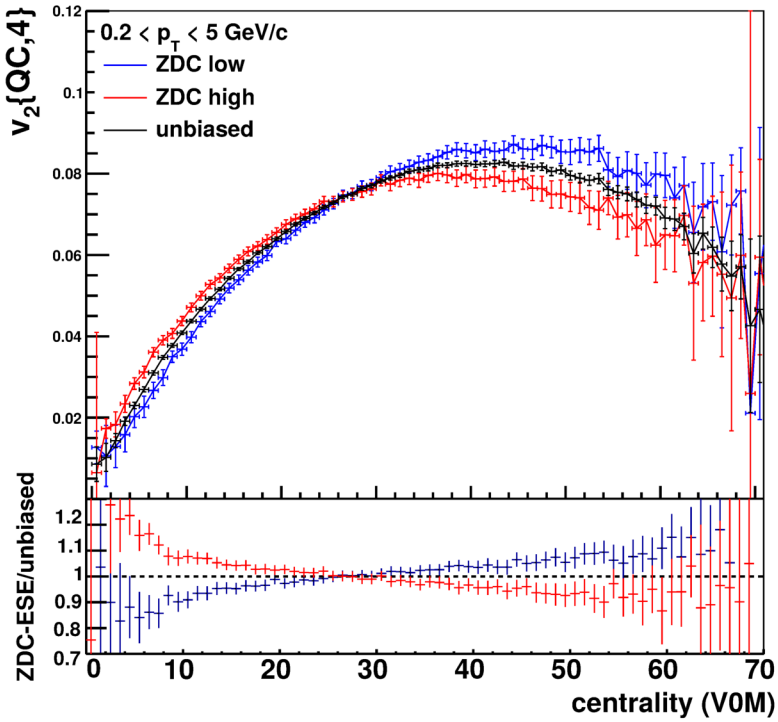

Figure 8.5: $v_2\{4\}$ as a function of centrality for different E_{ZN} classes in Pb–Pb collisions at $\sqrt{s_{\mathrm{NN}}} = 2.76$ TeV.

E_{ZN} and N_{part}. All following statements refer to events with different N_{part} but fixed final-state multiplicity, as set by the small centrality intervals, and therefore fixed total entropy. Concerning the geometry of the system and in particular ε_2, two mechanisms are at play, as already discussed: initial-state fluctuations and the geometry of the collision, which are approximately dominant in central and peripheral collisions, respectively. For central collisions, events with higher N_{part} (lower E_{ZN}) are less elliptical (lower $\langle\varepsilon_2\rangle$): the higher the number of nucleons uniformly distributed in a spherical area, the more they form an approximately spherical system. Vice-versa, the lower N_{part} (higher E_{ZN}), the higher the chances that the nucleons are distributed in a system with a non-trivial shape, therefore with higher $\langle\varepsilon_2\rangle$. For peripheral events, on the contrary, is the approximate almond-like shape of the overlapping area of the two colliding nuclei that determines ε_2; thus, the higher N_{part}, the closer the shape of the nucleon distribution will be to an almond, i.e. highly elliptical, following the same reasoning as before. Conversely, lower N_{part} results in lower $\langle\varepsilon_2\rangle$. We conclude that the centrality dependence of the variations of v_2 can be qualitatively understood from these simple geometrical arguments.

Concerning the changes in $\langle p_{\mathrm{T}}\rangle$, the interpretation is unclear. The relevant control parameters that are modified varying N_{part} for a given multiplicity are system size and energy density in the initial state, which are inversely related. Energy density is higher for lower N_{part} at any given multiplicity, the same total energy being distributed on a smaller transverse area. The $\langle p_{\mathrm{T}}\rangle$, in turn, has been observed to monotonically increase with transverse energy density from p–p to Pb–Pb collisions [236], irrespectively of event centrality. This would result in higher $\langle p_{\mathrm{T}}\rangle$ for lower N_{part} (higher E_{ZN}), as observed in central

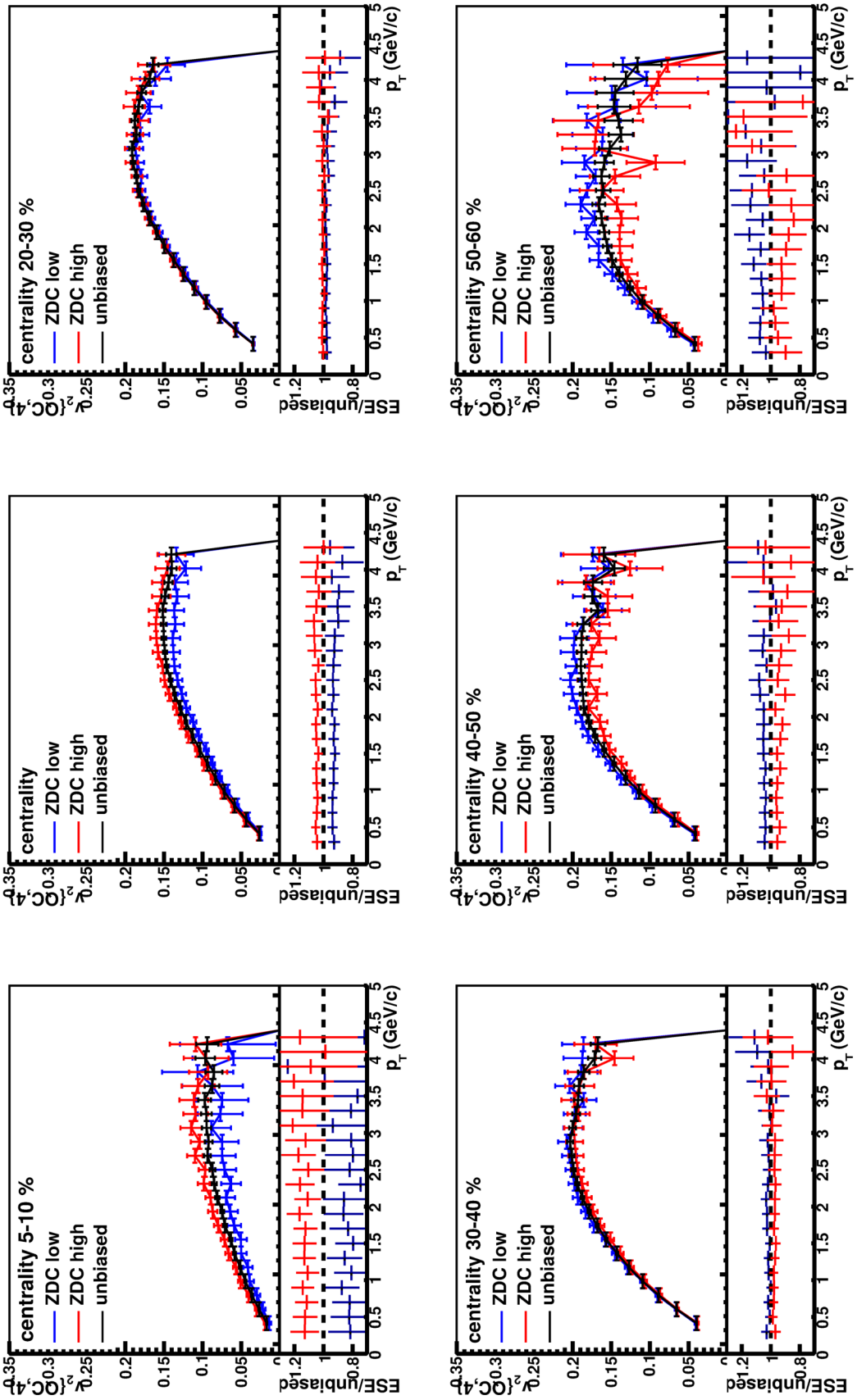

Figure 8.6: $v_2\{4\}(p_{\mathrm{T}})$ for different centralities and E_{ZN} classes in Pb–Pb collisions at $\sqrt{s_{\mathrm{NN}}} = 2.76$ TeV.

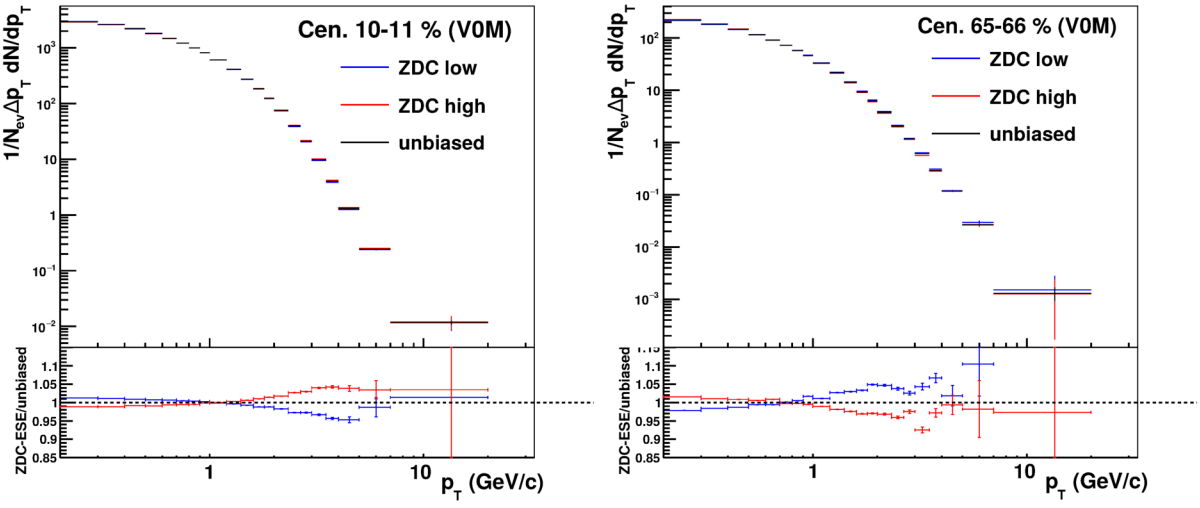

Figure 8.7: Charged particle spectra in central (left) and peripheral (right) collisions for different E_{ZN} classes in Pb–Pb collisions at $\sqrt{s_{\mathrm{NN}}} = 2.76$ TeV.

collisions. However, the opposite is observed in peripheral collisions, which is inconsistent with this general expectation. Variations in the relative contribution of soft/collective and (semi-)hard processes to final-state multiplicity as a function of event centrality can also play a role; unfortunately, their dependence on N_{part} is not well understood. Future work will hopefully expand and explain these observations.

CME observables

We also note that selecting events in classes of E_{ZN} can modify the average number of spectator protons (N^{p}_{spec}) and, therefore, the strength of the magnetic field $\vec{B}$. Unfortunately, the correlation between N^{p}_{spec} and N^{n}_{spec} at a fixed multiplicity is not clear, precisely because the exact relationship between N_{part} and multiplicity is unknown. This can be explained discussing two opposite scenarios: if we assume that the multiplicity only depends on N_{part}, fixing one equals to fixing the other. At the same time, N_{spec} is also fixed by N_{part} (Eq. 8.4). It is then clear that there would be a negative correlation between N^{p}_{spec} and N^{n}_{spec}, at fixed centrality. If, on the contrary, the multiplicity only depends on the number of binary nucleon-nucleon collisions N_{coll}, fixing the latter and selecting events with higher N^{n}_{spec}, would imply lower N_{part} (less nucleon undergoing more collisions) and, in general, higher N^{p}_{spec}. The correlation between N^{p}_{spec} and N^{n}_{spec} would then be positive. At the moment, we do not have a model-independent procedure to relate N_{part}, N_{coll} and multiplicity. The correlation between E_{ZN} and the total energy deposited in the ZP ($E_{\mathrm{ZP}} = E_{\mathrm{ZPA}} + E_{\mathrm{ZPC}}$) is positive (Fig. 8.8), but without knowing the contribution of fragmentation, which is expected to be large and of positive sign (more and/or bigger nuclear fragments being produced in one collision results in higher $N^{p}_{\mathrm{spec,\ single}}$ and $N^{n}_{\mathrm{spec,\ single}}$), is impossible to conclude much.

Notwithstanding this issue, we still expect some relationship between N^{p}_{spec} and N^{n}_{spec}, possibly dependent on centrality, and we therefore expect different E_{ZN} classes to have different $\langle\vec{B}\rangle$. We therefore perform a simple measurement of the three-particle correlator

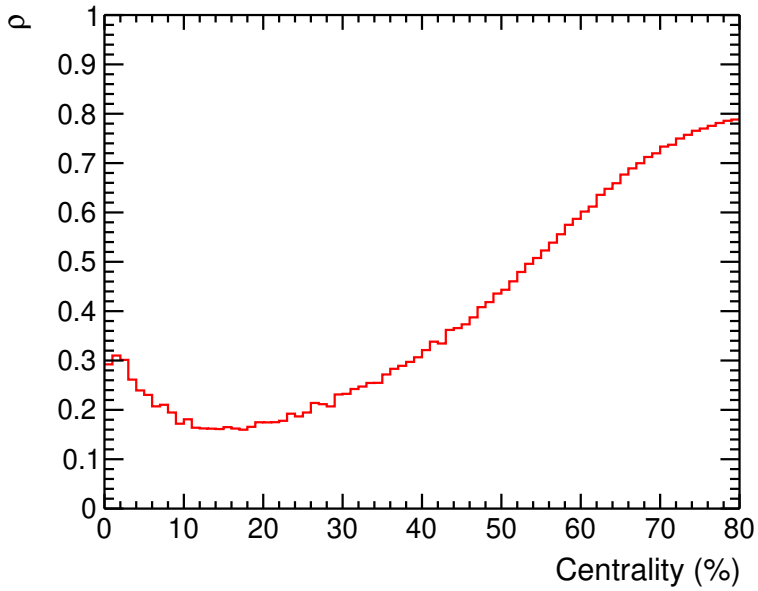

Figure 8.8: Pearson correlation coefficient between E_{ZN} and E_{ZP}, defined as $\rho = \mathrm{cov}(E_{ZN}, E_{ZP})/(\sigma_{E_{ZN}}\sigma_{E_{ZP}})$, as a function of centrality in Pb–Pb collisions at $\sqrt{s_{\mathrm{NN}}} = 2.76$ TeV.

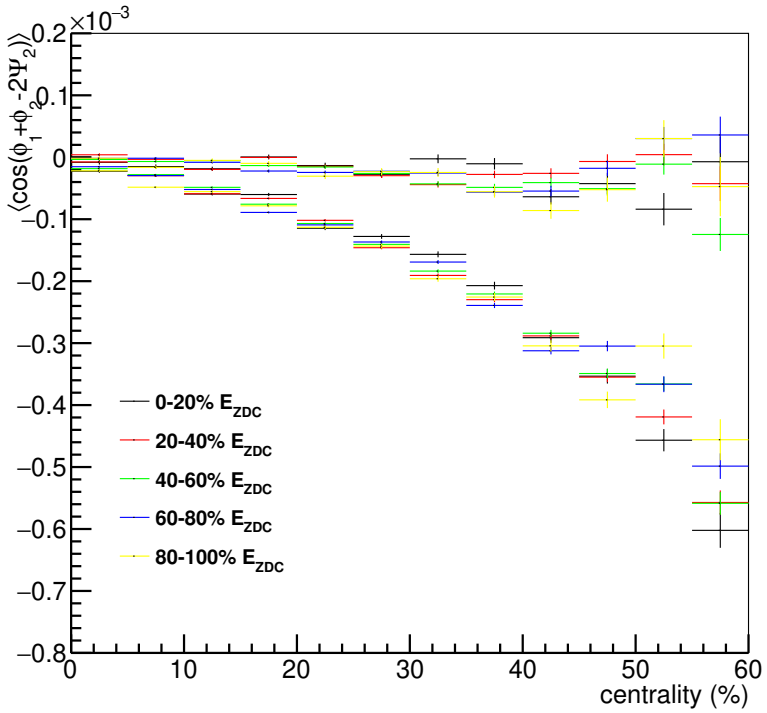

Figure 8.9: $\gamma_{\alpha\beta}$ as a function of centrality for different E_{ZN} classes in Pb–Pb collisions at $\sqrt{s_{\mathrm{NN}}} = 2.76$ TeV.

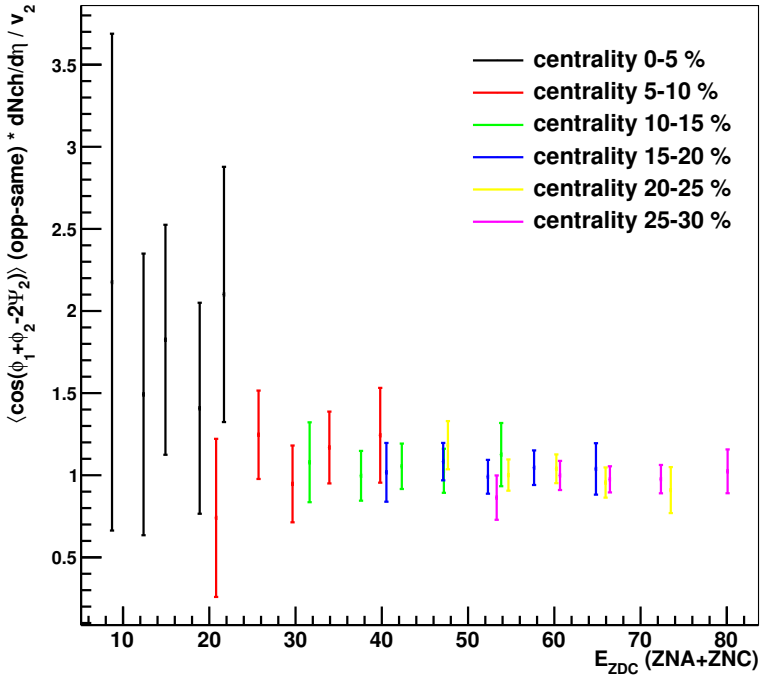

Figure 8.10: $\Delta\gamma$ scaled by average charged particle density $\langle \mathrm{d}N_{\mathrm{ch}}/\mathrm{d}\eta \rangle$ and elliptic flow $\langle v_2 \rangle$ as a function of $E_{\mathrm{ZDC}} = (E_{ZNA} + E_{ZNC})/(2E_n)$ for different centralities in Pb–Pb collisions at $\sqrt{s_{\mathrm{NN}}} = 2.76$ TeV.

$\gamma_{\alpha\beta}$ in different $E_{\rm ZN}$ classes, this time defined in intervals of 20% width (Fig. 8.9), using the 2010 data set of Pb–Pb collisions at $\sqrt{s_{\rm NN}} = 2.76$ TeV (2 μb^{-1}). In particular, we are interested in the difference between the same- and opposite-charge pair correlators $\Delta\gamma$, as explained in Sec. 6.1. $\Delta\gamma$ was observed to scale with multiplicity and to depend linearly on v_2 (Fig. 6.4). Therefore, in order to isolate the genuine dependence on $E_{\rm ZN}$, we scale $\Delta\gamma$ by the mean multiplicity and v_2 in each $E_{\rm ZN}$ class and we analyse its dependence on $E_{\rm ZN}$ (Fig. 8.10): no significant dependence is observed within statistical uncertainties.

We note that while such measurement will benefit from the larger data set currently available at $\sqrt{s_{\rm NN}} = 5.02$ TeV, its fundamental limit stands in the understanding of the correlation between $N^{p}_{\rm spec}$ and $N^{n}_{\rm spec}$ at a given centrality. Still, if this can be properly modelled, upper limits on the CME signal fraction in $\Delta\gamma$ can be extracted.

8.3 Labelled multi-particle correlators and cumulants

Algorithmic implementation

Multi-particle azimuthal cumulants [124] are a widely used experimental method to disentangle few-body correlations from many-body ones, which carry information on collective dynamics. Cumulants can be defined in terms of correlators, which can be efficiently computed from Q-vectors via the Generic Framework (GF) algorithms [122], especially when direct implementation of analytic formulae is unpractical, as discussed in Sec. 3.1.1. One limitation of the GF algorithms is that correlators must be computed from one common set of particles, whereas in some cases one would wish to correlate particles from disjoint or overlapping subsets. For some of those cases, analytic solutions have been previously derived, e.g. the so-called differential cumulants [122] and subevent cumulants [188]. A general solution to the problem was already found [241], but it is not immediately applicable to weighted Q-vectors, which is the case of interest. Here, we present a generalization of the GF algorithms which enables to automatically compute n-particle correlators between n or less sub-sets, with $n = 2, \ldots \infty$, without the need of lengthy analytic formulae, in terms of weighted Q-vectors. In particular, those sub-sets can be completely overlapping or disjoint. We call these correlators *labelled* multi-particle correlators. Following the same notation and conventions of [122], we define a labelled Q-vector as

$$Q^{s}_{n,c} = \sum_{j=1}^{M_s} w_j^c e^{in\varphi_j^s}, \tag{8.5}$$

where n is the harmonic number, c an integer exponent, s is an index indicating from which sub-set of particles the Q-vector is built (not to be confused with an exponent), M_s is the multiplicity of such sub-set and w are particle weights (generically dependent on any particle variable). We can then define a labelled multi-particle correlator $\langle m \rangle^{s_1,\ldots s_m}_{n_1,\ldots n_m}$ in harmonics $n_1, \ldots n_m$ and sub-sets $s_1, \ldots s_m$ with multiplicities $M_{s_1}, \ldots M_{s_m}$ as

$$\langle m \rangle^{s_1,\ldots s_m}_{n_1,\ldots n_m} = \langle e^{i(n_1\varphi_1^{s1} + \ldots n_m\varphi_m^{sm})} \rangle$$

$$= \frac{\sum\limits_{\substack{j_1,\ldots j_m=1 \\ j_1\neq j_2\neq\ldots j_m}}^{M_{s_1},\ldots M_{s_m}} w_{j_1}\ldots w_{j_m} e^{i(n_1\varphi_{j_1}^{s_1}+\ldots n_m\varphi_{j_m}^{s_m})}}{\sum\limits_{\substack{j_1,\ldots j_m=1 \\ j_1\neq j_2\neq\ldots j_m}}^{M_{s_1},\ldots M_{s_m}} w_{j_1}\ldots w_{j_m}}, \tag{8.6}$$

where each index j_i runs over M_{s_i} particles belonging to sub-set s_i. The expressions in the numerator $N\langle m\rangle_{n_1,\ldots n_m}^{s_1,\ldots s_m}$ and the denominator $D\langle m\rangle_{n_1,\ldots n_m}^{s_1,\ldots s_m}$ of Eq. 8.6 are trivially related: $D\langle m\rangle_{n_1,\ldots n_m}^{s_1,\ldots s_m} = N\langle m\rangle_{0,\ldots 0}^{s_1,\ldots s_m}$. Therefore, we focus only on the numerator

$$N\langle m\rangle_{n_1,\ldots n_m}^{s_1,\ldots s_m} = \sum_{\substack{j_1,\ldots j_m=1 \\ j_1\neq j_2\neq\ldots j_m}}^{M_{s_1},\ldots M_{s_m}} w_{j_1}\ldots w_{j_m} e^{i(n_1\varphi_{j_1}^{s_1}+\ldots n_m\varphi_{j_m}^{s_m})}. \tag{8.7}$$

We derive the following recursive formula to automatically calculate $N\langle m\rangle_{n_1,\ldots n_m}^{s_1,\ldots s_m}$ from labelled Q-vectors, starting from Eq. 25-26 of [122]; in pseudo-code, it reads

```
N⟨1⟩^{s1}_{n1}({c1}) : return Q^{s1}_{n1,c1}
N⟨m⟩^{s1,...sm}_{n1,...nm}({c1,...cm}) :
  C ← Q^{sm}_{nm,cm} × N⟨m−1⟩^{s1,...sm−1}_{n1,...nm−1}({c1,...cm−1})
  if cm ≤ 1 then
    for i ← 1, m−1 do
      if si ⊆ sm or si ⊇ sm then
        C ← C − ci × N⟨m−1⟩^{s1,...sm−1}_{n1,...ni+nm,...nm−1}({c1,...ci+1,...cm−1})
      end if
    end for i
  end if
  return C,
```
(8.8)

where initially all $c_i = 1$. We test the algorithm with a simple Monte Carlo simulation in which we generate two sets of particles, A and B, azimuthally distributed according to different flow coefficients (Tab. 8.1). For each event, $M_A = M_B = 500$; the total number of events is 3×10^4. We define two types of labelled multi-particle correlators

$$\langle m\rangle_n^{\rm def} = \langle e^{i(n\varphi_1^{A\cup B}+\ldots n\varphi_m^{A\cup B})}\rangle = \langle((v_{n,A}+v_{n,B})/2)^m\rangle, \tag{8.9}$$

$$\langle m\rangle_n^{\rm mix} = \langle e^{i(n\varphi_1^{B}+n\varphi_2^{A}+\ldots n\varphi_m^{A})}\rangle = \langle v_{n,B}\, v_{n,A}^{m-1}\rangle. \tag{8.10}$$

In words, $\langle m\rangle_n^{\rm def}$ is the default m-particle correlator between all particles $(A\cup B)$ and $\langle m\rangle_n^{\rm mix}$ correlates 1 particle from B with $m-1$ particles from A. In Fig. 8.11 we show that, both for $\langle m\rangle_n^{\rm def}$ (blue) and $\langle m\rangle_n^{\rm mix}$ (red), we correctly measure the expected values (dashed lines), for any order m.

We conclude that the proposed algorithm correctly and efficiently computes any m-particle correlator between m arbitrary subsets. With respect to previous approaches [188, 122], we stress that this method requires no analytic formulas, which are cumbersome

	v_2	v_3	v_4
A	0.09	0.08	0.09
B	0.11	0.10	0.07

Table 8.1: Flow coefficients for particle sets A and B.

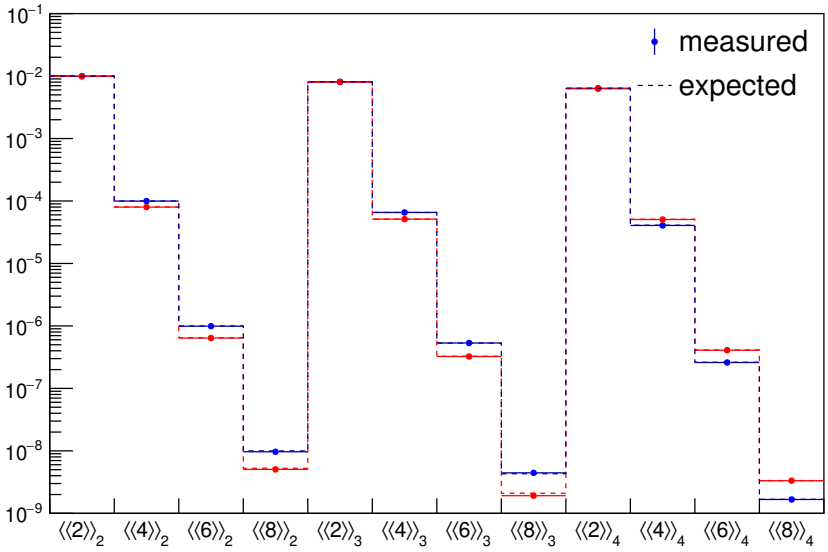

Figure 8.11: Multi-particle correlators $\langle m\rangle_n^{\mathrm{def}}$ (blue) and $\langle m\rangle_n^{\mathrm{mix}}$ (red) measured with the algorithm defined in Eq. 8.8. Dashed blue lines show expected values. See text for definitions.

already for correlators of order 4 and become unpractical for higher order ones. Moreover, equally to the GF, analytic corrections for non uniformities in detector acceptance and efficiency can be easily implemented through particle weights.

Once multi-particle correlators are computed, it is possible to isolate the corresponding multi-particle cumulants, i.e. the contribution to $\langle m\rangle_{n_1,\ldots n_m}^{s_1,\ldots s_m}$ involving all m particles. This is what effectively removes few-body correlations, which is the intrinsic advantage of using the multi-particle cumulant method. The general procedure to isolate cumulants $c\{m\}$ from correlators $\langle m\rangle$ is encoded in Kubo's formula [237]

$$c\{m\} = \sum (l-1)(-1)^{l-1} \sum_{\sum_{i=1}^{l}\{n_i\}=\{m\}} \prod_{i=1}^{l} \langle n_i\rangle. \tag{8.11}$$

Note that, with respect to the previous notation, indices referring to harmonic number and sub-set are absorbed in the index l, without any loss of generality. Bilandzic first implemented Eq. 8.11 in Mathematica [238], which can be found in Appendix J of his doctoral dissertation [239], together with a thorough explanation of its meaning. Here, we use Bilandzic's implementation to isolate the multi-particle cumulants presented in the following sections, which we will call by analogy *labelled* multi-particle cumulants.

Correlated flow fluctuations

As extensively discussed in Sec. 5.1, cumulants have different sensitivities to anisotropic flow fluctuations. In the case of differential cumulants, which involve particles from different sub-sets, the correlation between the fluctuations of anisotropic flow of those different sub-sets also plays a role. In particular, two- and four-particle differential cumulants have either positive or negative contributions due to precisely this correlation [122]. These differential cumulants, in the notation of the previous section, can be defined as

$$v_A\{2\} \equiv \frac{\langle 2\rangle^{A,B}}{\sqrt{\langle 2\rangle^{B,B}}} = \frac{\langle v_A v_B\rangle}{\sqrt{\langle v_B^2\rangle}} \tag{8.12}$$

$$v_A\{4\} \equiv \frac{-\langle 4\rangle^{A,B,B,B} + 2\langle 2\rangle^{A,B}\langle 2\rangle^{B,B}}{(-\langle 4\rangle^{B,B,B,B})^{3/4}} = \frac{-\langle v_A v_B^3\rangle + 2\langle v_A v_B\rangle\langle v_B^2\rangle}{\langle v_B^4\rangle^{3/4}}, \tag{8.13}$$

where we label the two sub-sets of interest A and B. We also omit the harmonic number at the subscript, since the following discussion applies to any harmonic. These differential cumulants can be approximated, in the limit $\sigma_v^2/\langle v^2\rangle \ll 1$, as [122]

$$v_A\{2\} \approx \langle v_A\rangle\left(1 + \rho\frac{\sigma_{v_A}\sigma_{v_B}}{\langle v_A\rangle\langle v_B\rangle} - \frac{1}{2}\frac{\sigma_{v_B}^2}{\langle v_B\rangle^2}\right), \tag{8.14}$$

$$v_A\{4\} \approx \langle v_A\rangle\left(1 - \rho\frac{\sigma_{v_A}\sigma_{v_B}}{\langle v_A\rangle\langle v_B\rangle} + \frac{1}{2}\frac{\sigma_{v_B}^2}{\langle v_B\rangle^2}\right), \tag{8.15}$$

where ρ is the Pearson correlation coefficient between v_A and v_B, which quantifies how their fluctuations are correlated. If we take the common case in which B corresponds to all charged particles, which implies σ_B and $\langle v_B\rangle$ to be known[2], while A is a sub-set of particles that we want to study, the information that we can potentially extract comparing different differential cumulants are σ_A, $\langle v_A\rangle$ and ρ. It is clear that we cannot derive all three variables only from $v_A\{2\}$ and $v_A\{4\}$. We argue that measuring other labelled multi-particle cumulants, involving different numbers of particles from A and B, can help in this regard. For instance, following the same lines of [122], we can derive what is the expected contribution of fluctuations to the cumulant

$$v_{A,A}\{4\} \equiv \frac{-\langle 4\rangle^{A,A,B,B} + 2\langle 2\rangle^{A,B}\langle 2\rangle^{A,B}}{\langle 2\rangle^{B,B}} = \frac{-\langle v_A^2 v_B^2\rangle + 2\langle v_A v_B\rangle^2}{\langle v_B^2\rangle}. \tag{8.16}$$

Assuming again $\sigma_v^2/\langle v^2\rangle \ll 1$, which implies

$$\langle f(x)\rangle \approx f(\langle x\rangle) + \frac{\sigma_x^2}{2}f''(\langle x\rangle),$$
$$\sigma_{f(x)} \approx (f'(\langle x\rangle))^2\sigma_x,$$

we see that the various terms can be approximated as

$$\begin{aligned}\langle v_A^2 v_B^2\rangle &= \langle v_A^2\rangle\langle v_B^2\rangle + \rho'\sigma_{v_A^2}\sigma_{v_B^2} \\ &= (\langle v_A\rangle^2 + \sigma_{v_A}^2)(\langle v_B\rangle^2 + \sigma_{v_B}^2) + 16\rho'\langle v_A^2\rangle\langle v_B^2\rangle\sigma_{v_A}\sigma_{v_B} \\ &\approx \langle v_A\rangle^2\langle v_B\rangle^2 + \langle v_A^2\rangle\sigma_{v_B}^2 + \langle v_B^2\rangle\sigma_{v_A}^2 + \sigma_{v_A}^2\sigma_{v_B}^2;\end{aligned}$$

[2]This is certainly true for elliptic flow; for higher harmonics, it remains to be done.

$$\langle v_A v_B \rangle = \langle v_A \rangle \langle v_B \rangle + \rho \sigma_{v_A} \sigma_{v_B}, \tag{8.17}$$

where ρ' is the correlation coefficient between v_A^2 and v_B^2. Hence, $v_{A,A}\{4\}$ reduces to

$$\begin{aligned} v_{A,A}\{4\} &= \frac{\langle v_A \rangle^2 \langle v_B \rangle^2 + 4\rho \langle v_A \rangle \langle v_B \rangle \sigma_{v_A} \sigma_{v_B} - \langle v_A \rangle^2 \sigma_{v_B}^2 - \langle v_B \rangle^2 \sigma_{v_A}^2}{\langle v_B^2 \rangle} \\ &\approx \langle v_A \rangle^2 \left(1 + 4\rho \frac{\sigma_{v_A} \sigma_{v_B}}{\sigma_{v_A} \sigma_{v_B}} - \frac{\sigma_{v_A}^2}{\langle v_A \rangle^2} - \frac{\sigma_{v_B}^2}{\langle v_B \rangle^2} \right) \left(1 - \frac{\sigma_{v_B}^2}{\langle v_B \rangle^2} \right) \\ &\approx \langle v_A \rangle^2 \left(1 + 4\rho \frac{\sigma_{v_A} \sigma_{v_B}}{\sigma_{v_A} \sigma_{v_B}} - \frac{\sigma_{v_A}^2}{\langle v_A \rangle^2} - 2\frac{\sigma_{v_B}^2}{\langle v_B \rangle^2} \right). \end{aligned} \tag{8.18}$$

Along the same lines, one can compute the contribution of flow fluctuations and their correlation in higher-order labelled multi-particle cumulants. We speculate that it is possible to extract all desired information (σ_A, $\langle v_A \rangle$ and ρ) from a combined analysis of three or more of such cumulants. Experimentally, one limitation consists in having a consistent fraction of events in which more than one particle A is detected or reconstructed, which is not always possible in practise. Another limitation - which we completely ignored for the sake of simplicity - consists in possible event plane decorrelation between A and B, whose contribution should be properly evaluated.

CME observables

Where else can labelled multi-particle cumulants find meaningful application? A case study that we propose is the CME. The potential advantages are clear: known correlators are plagued by background, specifically in the form of LCC, which is a few-particle effect (see Sec. 6.1). Higher order cumulants will be progressively less affected by such background and can reveal if a genuine, *collective* CME signal is present or not. We emphasize the use of the word collective here: as discussed in Sec. 1.5, the intrinsic multiplicity of separated charges is still unknown and can be small compared to the total one, which would make the CME a few-particle effect. Yet, the exclusion of a collective CME signal constitutes potentially interesting information.

We can define a large number of charge-dependent multi-particle cumulants sensitive to CME, involving the first harmonic and any number of other ones. However, we know that symmetry planes of harmonics $n > 2$ are determined by initial-state fluctuations and are therefore mostly uncorrelated with the direction of the magnetic field. The only ones to be partially correlated are Ψ_2, as extensively studied in Sec. 6.3, and Ψ_1, as discussed in Sec. 7.1. Thus, we limit the discussion to charge-dependent multi-particle cumulants involving the first and the second harmonic. They are defined, up to order 7, in Eq. 8.19-8.29, where the numbers at the subscript in the right-hand side of the equations are arbitrary indices associated to the charge of the particle under consideration (more in general, to the particle sub-set, irrespectively of how it is defined). Note that Eq. 8.19 and 8.20 correspond to the two- and three-particle correlators $\delta_{\alpha,\beta}$ and $\gamma_{\alpha,\beta}$, respectively. In the absence of directed flow ($v_1 = 0$, both charge-dependent and charge-independent), the CME signal a_1 can be extracted from the various cumulants as in Eq. 8.30-8.40, where we assume to correlate particles of defined charge (either positive or negative) for the first harmonic and particles of any charge (both positive and negative) for the second harmonic, e.g. $c\{3\}_{2,-1,-1} = \gamma_{\alpha,\beta} = \langle\langle \cos(2\varphi_1 - \varphi_2^+ - \varphi_3^-) \rangle\rangle$. Decorrelation between Ψ_B,

Ψ_1 and Ψ_2 will have different contributions in the different cumulants. We note that some of these cumulants can also be used to study charge-dependent directed flow with respect to the first or second order symmetry planes. Their potential and limitations will hopefully be investigated in future studies.

$$c\{2\}_{1,-1} \equiv \langle\langle\cos(\varphi_1 - \varphi_2)\rangle\rangle = \delta_{1,2}, \tag{8.19}$$

$$c\{3\}_{2,-1,-1} \equiv \langle\langle\cos(2\varphi_1 - \varphi_2 - \varphi_3)\rangle\rangle = \gamma_{2,3}, \tag{8.20}$$

$$\begin{aligned} c\{4\}_{1,1,-1,-1} \equiv{}& \langle\langle\cos(\varphi_1 + \varphi_2 - \varphi_3 - \varphi_4)\rangle\rangle \\ &- \langle\langle\cos(\varphi_1 - \varphi_3)\rangle\rangle\langle\langle\cos(\varphi_2 - \varphi_4)\rangle\rangle \\ &- \langle\langle\cos(\varphi_1 - \varphi_4)\rangle\rangle\langle\langle\cos(\varphi_2 - \varphi_3)\rangle\rangle, \end{aligned} \tag{8.21}$$

$$\begin{aligned} c\{5\}_{2,1,-1,-1,-1} \equiv{}& \langle\langle\cos(2\varphi_1 + \varphi_2 - \varphi_3 - \varphi_4 - \varphi_5)\rangle\rangle \\ &- \langle\langle\cos(2\varphi_1 - \varphi_3 - \varphi_4)\rangle\rangle\langle\langle\cos(\varphi_2 - \varphi_5)\rangle\rangle \\ &- \langle\langle\cos(2\varphi_1 - \varphi_3 - \varphi_5)\rangle\rangle\langle\langle\cos(\varphi_2 - \varphi_4)\rangle\rangle \\ &- \langle\langle\cos(2\varphi_1 - \varphi_4 - \varphi_5)\rangle\rangle\langle\langle\cos(\varphi_2 - \varphi_3)\rangle\rangle, \end{aligned} \tag{8.22}$$

$$\begin{aligned} c\{5\}_{2,2,-2,-1,-1} \equiv{}& \langle\langle\cos(2\varphi_1 + 2\varphi_2 - 2\varphi_3 - \varphi_4 - \varphi_5)\rangle\rangle \\ &- \langle\langle\cos(2\varphi_1 - \varphi_4 - \varphi_5)\rangle\rangle\langle\langle\cos(2\varphi_2 - 2\varphi_3)\rangle\rangle \\ &- \langle\langle\cos(2\varphi_2 - \varphi_4 - \varphi_5)\rangle\rangle\langle\langle\cos(2\varphi_1 - 2\varphi_3)\rangle\rangle, \end{aligned} \tag{8.23}$$

$$\begin{aligned} c\{6\}_{1,1,1,-1,-1,-1} \equiv{}& \langle\langle\cos(\varphi_1 + \varphi_2 + \varphi_3 - \varphi_4 - \varphi_5 - \varphi_6)\rangle\rangle \\ &- \langle\langle\cos(\varphi_1 + \varphi_2 - \varphi_4 - \varphi_5)\rangle\rangle\langle\langle\cos(\varphi_3 - \varphi_6)\rangle\rangle \\ &- \langle\langle\cos(\varphi_1 + \varphi_2 - \varphi_4 - \varphi_6)\rangle\rangle\langle\langle\cos(\varphi_3 - \varphi_5)\rangle\rangle \\ &- \langle\langle\cos(\varphi_1 + \varphi_2 - \varphi_5 - \varphi_6)\rangle\rangle\langle\langle\cos(\varphi_3 - \varphi_4)\rangle\rangle \\ &- \langle\langle\cos(\varphi_1 + \varphi_3 - \varphi_4 - \varphi_5)\rangle\rangle\langle\langle\cos(\varphi_2 - \varphi_6)\rangle\rangle \\ &- \langle\langle\cos(\varphi_1 + \varphi_3 - \varphi_4 - \varphi_6)\rangle\rangle\langle\langle\cos(\varphi_2 - \varphi_5)\rangle\rangle \\ &- \langle\langle\cos(\varphi_1 + \varphi_3 - \varphi_5 - \varphi_6)\rangle\rangle\langle\langle\cos(\varphi_2 - \varphi_4)\rangle\rangle \\ &- \langle\langle\cos(\varphi_2 + \varphi_3 - \varphi_4 - \varphi_5)\rangle\rangle\langle\langle\cos(\varphi_1 - \varphi_6)\rangle\rangle \\ &- \langle\langle\cos(\varphi_2 + \varphi_3 - \varphi_4 - \varphi_6)\rangle\rangle\langle\langle\cos(\varphi_1 - \varphi_5)\rangle\rangle \\ &- \langle\langle\cos(\varphi_2 + \varphi_3 - \varphi_5 - \varphi_6)\rangle\rangle\langle\langle\cos(\varphi_1 - \varphi_4)\rangle\rangle \\ &+ 2\langle\langle\cos(\varphi_1 - \varphi_4)\rangle\rangle\langle\langle\cos(\varphi_2 - \varphi_5)\rangle\rangle\langle\langle\cos(\varphi_3 - \varphi_6)\rangle\rangle \\ &+ 2\langle\langle\cos(\varphi_1 - \varphi_4)\rangle\rangle\langle\langle\cos(\varphi_2 - \varphi_6)\rangle\rangle\langle\langle\cos(\varphi_3 - \varphi_5)\rangle\rangle \\ &+ 2\langle\langle\cos(\varphi_1 - \varphi_4)\rangle\rangle\langle\langle\cos(\varphi_3 - \varphi_5)\rangle\rangle\langle\langle\cos(\varphi_2 - \varphi_6)\rangle\rangle \\ &+ 2\langle\langle\cos(\varphi_1 - \varphi_4)\rangle\rangle\langle\langle\cos(\varphi_3 - \varphi_6)\rangle\rangle\langle\langle\cos(\varphi_2 - \varphi_5)\rangle\rangle \\ &+ 2\langle\langle\cos(\varphi_1 - \varphi_5)\rangle\rangle\langle\langle\cos(\varphi_2 - \varphi_4)\rangle\rangle\langle\langle\cos(\varphi_3 - \varphi_6)\rangle\rangle \\ &+ 2\langle\langle\cos(\varphi_1 - \varphi_5)\rangle\rangle\langle\langle\cos(\varphi_2 - \varphi_6)\rangle\rangle\langle\langle\cos(\varphi_3 - \varphi_4)\rangle\rangle \\ &+ 2\langle\langle\cos(\varphi_1 - \varphi_5)\rangle\rangle\langle\langle\cos(\varphi_3 - \varphi_4)\rangle\rangle\langle\langle\cos(\varphi_2 - \varphi_6)\rangle\rangle \\ &+ 2\langle\langle\cos(\varphi_1 - \varphi_5)\rangle\rangle\langle\langle\cos(\varphi_3 - \varphi_6)\rangle\rangle\langle\langle\cos(\varphi_2 - \varphi_4)\rangle\rangle \\ &+ 2\langle\langle\cos(\varphi_1 - \varphi_6)\rangle\rangle\langle\langle\cos(\varphi_2 - \varphi_4)\rangle\rangle\langle\langle\cos(\varphi_3 - \varphi_5)\rangle\rangle \\ &+ 2\langle\langle\cos(\varphi_1 - \varphi_6)\rangle\rangle\langle\langle\cos(\varphi_2 - \varphi_5)\rangle\rangle\langle\langle\cos(\varphi_3 - \varphi_4)\rangle\rangle \\ &+ 2\langle\langle\cos(\varphi_1 - \varphi_6)\rangle\rangle\langle\langle\cos(\varphi_3 - \varphi_4)\rangle\rangle\langle\langle\cos(\varphi_2 - \varphi_5)\rangle\rangle \end{aligned}$$

$$
\begin{aligned}
&+2\langle\langle\cos(\varphi_1-\varphi_6)\rangle\rangle\langle\langle\cos(\varphi_3-\varphi_5)\rangle\rangle\langle\langle\cos(\varphi_2-\varphi_4)\rangle\rangle\\
&+2\langle\langle\cos(\varphi_2-\varphi_4)\rangle\rangle\langle\langle\cos(\varphi_1-\varphi_5)\rangle\rangle\langle\langle\cos(\varphi_3-\varphi_6)\rangle\rangle\\
&+2\langle\langle\cos(\varphi_2-\varphi_4)\rangle\rangle\langle\langle\cos(\varphi_1-\varphi_6)\rangle\rangle\langle\langle\cos(\varphi_3-\varphi_5)\rangle\rangle\\
&+2\langle\langle\cos(\varphi_2-\varphi_4)\rangle\rangle\langle\langle\cos(\varphi_3-\varphi_5)\rangle\rangle\langle\langle\cos(\varphi_1-\varphi_6)\rangle\rangle\\
&+2\langle\langle\cos(\varphi_2-\varphi_4)\rangle\rangle\langle\langle\cos(\varphi_3-\varphi_6)\rangle\rangle\langle\langle\cos(\varphi_1-\varphi_5)\rangle\rangle\\
&+2\langle\langle\cos(\varphi_2-\varphi_5)\rangle\rangle\langle\langle\cos(\varphi_1-\varphi_4)\rangle\rangle\langle\langle\cos(\varphi_3-\varphi_6)\rangle\rangle\\
&+2\langle\langle\cos(\varphi_2-\varphi_5)\rangle\rangle\langle\langle\cos(\varphi_1-\varphi_6)\rangle\rangle\langle\langle\cos(\varphi_3-\varphi_4)\rangle\rangle\\
&+2\langle\langle\cos(\varphi_2-\varphi_5)\rangle\rangle\langle\langle\cos(\varphi_3-\varphi_4)\rangle\rangle\langle\langle\cos(\varphi_1-\varphi_6)\rangle\rangle\\
&+2\langle\langle\cos(\varphi_2-\varphi_5)\rangle\rangle\langle\langle\cos(\varphi_3-\varphi_6)\rangle\rangle\langle\langle\cos(\varphi_1-\varphi_4)\rangle\rangle\\
&+2\langle\langle\cos(\varphi_2-\varphi_6)\rangle\rangle\langle\langle\cos(\varphi_1-\varphi_4)\rangle\rangle\langle\langle\cos(\varphi_3-\varphi_5)\rangle\rangle\\
&+2\langle\langle\cos(\varphi_2-\varphi_6)\rangle\rangle\langle\langle\cos(\varphi_1-\varphi_5)\rangle\rangle\langle\langle\cos(\varphi_3-\varphi_4)\rangle\rangle\\
&+2\langle\langle\cos(\varphi_2-\varphi_6)\rangle\rangle\langle\langle\cos(\varphi_3-\varphi_4)\rangle\rangle\langle\langle\cos(\varphi_1-\varphi_5)\rangle\rangle\\
&+2\langle\langle\cos(\varphi_2-\varphi_6)\rangle\rangle\langle\langle\cos(\varphi_3-\varphi_5)\rangle\rangle\langle\langle\cos(\varphi_1-\varphi_4)\rangle\rangle\\
&+2\langle\langle\cos(\varphi_3-\varphi_4)\rangle\rangle\langle\langle\cos(\varphi_1-\varphi_5)\rangle\rangle\langle\langle\cos(\varphi_2-\varphi_6)\rangle\rangle\\
&+2\langle\langle\cos(\varphi_3-\varphi_4)\rangle\rangle\langle\langle\cos(\varphi_1-\varphi_6)\rangle\rangle\langle\langle\cos(\varphi_2-\varphi_5)\rangle\rangle\\
&+2\langle\langle\cos(\varphi_3-\varphi_4)\rangle\rangle\langle\langle\cos(\varphi_2-\varphi_5)\rangle\rangle\langle\langle\cos(\varphi_1-\varphi_6)\rangle\rangle\\
&+2\langle\langle\cos(\varphi_3-\varphi_4)\rangle\rangle\langle\langle\cos(\varphi_2-\varphi_6)\rangle\rangle\langle\langle\cos(\varphi_1-\varphi_5)\rangle\rangle\\
&+2\langle\langle\cos(\varphi_3-\varphi_5)\rangle\rangle\langle\langle\cos(\varphi_1-\varphi_4)\rangle\rangle\langle\langle\cos(\varphi_2-\varphi_6)\rangle\rangle\\
&+2\langle\langle\cos(\varphi_3-\varphi_5)\rangle\rangle\langle\langle\cos(\varphi_1-\varphi_6)\rangle\rangle\langle\langle\cos(\varphi_2-\varphi_4)\rangle\rangle\\
&+2\langle\langle\cos(\varphi_3-\varphi_5)\rangle\rangle\langle\langle\cos(\varphi_2-\varphi_4)\rangle\rangle\langle\langle\cos(\varphi_1-\varphi_6)\rangle\rangle\\
&+2\langle\langle\cos(\varphi_3-\varphi_5)\rangle\rangle\langle\langle\cos(\varphi_2-\varphi_6)\rangle\rangle\langle\langle\cos(\varphi_1-\varphi_4)\rangle\rangle\\
&+2\langle\langle\cos(\varphi_3-\varphi_6)\rangle\rangle\langle\langle\cos(\varphi_1-\varphi_4)\rangle\rangle\langle\langle\cos(\varphi_2-\varphi_5)\rangle\rangle\\
&+2\langle\langle\cos(\varphi_3-\varphi_6)\rangle\rangle\langle\langle\cos(\varphi_1-\varphi_5)\rangle\rangle\langle\langle\cos(\varphi_2-\varphi_4)\rangle\rangle\\
&+2\langle\langle\cos(\varphi_3-\varphi_6)\rangle\rangle\langle\langle\cos(\varphi_2-\varphi_4)\rangle\rangle\langle\langle\cos(\varphi_1-\varphi_5)\rangle\rangle\\
&+2\langle\langle\cos(\varphi_3-\varphi_6)\rangle\rangle\langle\langle\cos(\varphi_2-\varphi_5)\rangle\rangle\langle\langle\cos(\varphi_1-\varphi_4)\rangle\rangle, \qquad (8.24)
\end{aligned}
$$

$$
\begin{aligned}
c\{6\}_{2,2,-1,-1,-1,-1} &\equiv \langle\langle\cos(2\varphi_1+2\varphi_2-\varphi_3-\varphi_4-\varphi_5-\varphi_6)\rangle\rangle\\
&-\langle\langle\cos(2\varphi_1-\varphi_3-\varphi_4)\rangle\rangle\langle\langle\cos(2\varphi_2-\varphi_5-\varphi_6)\rangle\rangle\\
&-\langle\langle\cos(2\varphi_1-\varphi_3-\varphi_5)\rangle\rangle\langle\langle\cos(2\varphi_2-\varphi_4-\varphi_6)\rangle\rangle\\
&-\langle\langle\cos(2\varphi_1-\varphi_3-\varphi_6)\rangle\rangle\langle\langle\cos(2\varphi_2-\varphi_4-\varphi_5)\rangle\rangle\\
&-\langle\langle\cos(2\varphi_1-\varphi_4-\varphi_5)\rangle\rangle\langle\langle\cos(2\varphi_2-\varphi_3-\varphi_6)\rangle\rangle\\
&-\langle\langle\cos(2\varphi_1-\varphi_4-\varphi_6)\rangle\rangle\langle\langle\cos(2\varphi_2-\varphi_3-\varphi_5)\rangle\rangle\\
&-\langle\langle\cos(2\varphi_1-\varphi_5-\varphi_6)\rangle\rangle\langle\langle\cos(2\varphi_2-\varphi_3-\varphi_4)\rangle\rangle, \qquad (8.25)
\end{aligned}
$$

$$
\begin{aligned}
c\{6\}_{2,1,1,-2,-1,-1} &\equiv \langle\langle\cos(2\varphi_1+\varphi_2+\varphi_3-2\varphi_4-\varphi_5-\varphi_6)\rangle\rangle\\
&-\langle\langle\cos(\varphi_2+\varphi_3-\varphi_5-\varphi_6)\rangle\rangle\langle\langle\cos(2\varphi_1-2\varphi_4)\rangle\rangle\\
&-\langle\langle\cos(2\varphi_1+\varphi_2-2\varphi_4-\varphi_5)\rangle\rangle\langle\langle\cos(\varphi_3-\varphi_6)\rangle\rangle\\
&-\langle\langle\cos(2\varphi_1+\varphi_3-2\varphi_4-\varphi_5)\rangle\rangle\langle\langle\cos(\varphi_2-\varphi_6)\rangle\rangle\\
&-\langle\langle\cos(2\varphi_1+\varphi_2-2\varphi_4-\varphi_6)\rangle\rangle\langle\langle\cos(\varphi_3-\varphi_5)\rangle\rangle\\
&-\langle\langle\cos(2\varphi_1+\varphi_3-2\varphi_4-\varphi_6)\rangle\rangle\langle\langle\cos(\varphi_2-\varphi_5)\rangle\rangle
\end{aligned}
$$

$$
\begin{aligned}
&- \langle\langle\cos(2\varphi_1 - \varphi_5 - \varphi_6)\rangle\rangle\langle\langle\cos(2\varphi_4 - \varphi_2 - \varphi_3)\rangle\rangle \\
&+ 2\langle\langle\cos(\varphi_2 - \varphi_6)\rangle\rangle\langle\langle\cos(\varphi_2 - \varphi_6)\rangle\rangle\langle\langle\cos(\varphi_2 - \varphi_6)\rangle\rangle \\
&+ 2\langle\langle\cos(\varphi_2 - \varphi_6)\rangle\rangle\langle\langle\cos(\varphi_2 - \varphi_6)\rangle\rangle\langle\langle\cos(\varphi_2 - \varphi_6)\rangle\rangle, \qquad (8.26)
\end{aligned}
$$

$$
\begin{aligned}
c\{7\}_{2,1,1,-1,-1,-1,-1} &\equiv \langle\langle\cos(2\varphi_1 + \varphi_2 + \varphi_3 - \varphi_4 - \varphi_5 - \varphi_6 - \varphi_7)\rangle\rangle \\
&- \langle\langle\cos(2\varphi_1 + \varphi_2 - \varphi_4 - \varphi_5 - \varphi_6)\rangle\rangle\langle\langle\cos(\varphi_3 - \varphi_7)\rangle\rangle \\
&- \langle\langle\cos(2\varphi_1 + \varphi_2 - \varphi_4 - \varphi_5 - \varphi_7)\rangle\rangle\langle\langle\cos(\varphi_3 - \varphi_6)\rangle\rangle \\
&- \langle\langle\cos(2\varphi_1 + \varphi_2 - \varphi_4 - \varphi_6 - \varphi_7)\rangle\rangle\langle\langle\cos(\varphi_3 - \varphi_5)\rangle\rangle \\
&- \langle\langle\cos(2\varphi_1 + \varphi_2 - \varphi_5 - \varphi_6 - \varphi_7)\rangle\rangle\langle\langle\cos(\varphi_3 - \varphi_4)\rangle\rangle \\
&- \langle\langle\cos(2\varphi_1 + \varphi_3 - \varphi_4 - \varphi_5 - \varphi_6)\rangle\rangle\langle\langle\cos(\varphi_2 - \varphi_7)\rangle\rangle \\
&- \langle\langle\cos(2\varphi_1 + \varphi_3 - \varphi_4 - \varphi_5 - \varphi_7)\rangle\rangle\langle\langle\cos(\varphi_2 - \varphi_6)\rangle\rangle \\
&- \langle\langle\cos(2\varphi_1 + \varphi_3 - \varphi_4 - \varphi_6 - \varphi_7)\rangle\rangle\langle\langle\cos(\varphi_2 - \varphi_5)\rangle\rangle \\
&- \langle\langle\cos(2\varphi_1 + \varphi_3 - \varphi_5 - \varphi_6 - \varphi_7)\rangle\rangle\langle\langle\cos(\varphi_2 - \varphi_4)\rangle\rangle \\
&- \langle\langle\cos(\varphi_2 + \varphi_3 - \varphi_4 - \varphi_5)\rangle\rangle\langle\langle\cos(2\varphi_1 - \varphi_6 - \varphi_7)\rangle\rangle \\
&- \langle\langle\cos(\varphi_2 + \varphi_3 - \varphi_4 - \varphi_6)\rangle\rangle\langle\langle\cos(2\varphi_1 - \varphi_5 - \varphi_7)\rangle\rangle \\
&- \langle\langle\cos(\varphi_2 + \varphi_3 - \varphi_4 - \varphi_7)\rangle\rangle\langle\langle\cos(2\varphi_1 - \varphi_5 - \varphi_6)\rangle\rangle \\
&- \langle\langle\cos(\varphi_2 + \varphi_3 - \varphi_5 - \varphi_6)\rangle\rangle\langle\langle\cos(2\varphi_1 - \varphi_4 - \varphi_7)\rangle\rangle \\
&- \langle\langle\cos(\varphi_2 + \varphi_3 - \varphi_5 - \varphi_7)\rangle\rangle\langle\langle\cos(2\varphi_1 - \varphi_4 - \varphi_6)\rangle\rangle \\
&- \langle\langle\cos(\varphi_2 + \varphi_3 - \varphi_6 - \varphi_7)\rangle\rangle\langle\langle\cos(2\varphi_1 - \varphi_4 - \varphi_5)\rangle\rangle \\
&+ 2\langle\langle\cos(2\varphi_1 - \varphi_4 - \varphi_5)\rangle\rangle\langle\langle\cos(\varphi_2 - \varphi_6)\rangle\rangle\langle\langle\cos(\varphi_3 - \varphi_7)\rangle\rangle \\
&+ 2\langle\langle\cos(2\varphi_1 - \varphi_4 - \varphi_5)\rangle\rangle\langle\langle\cos(\varphi_2 - \varphi_7)\rangle\rangle\langle\langle\cos(\varphi_3 - \varphi_6)\rangle\rangle \\
&+ 2\langle\langle\cos(2\varphi_1 - \varphi_4 - \varphi_5)\rangle\rangle\langle\langle\cos(\varphi_3 - \varphi_6)\rangle\rangle\langle\langle\cos(\varphi_2 - \varphi_7)\rangle\rangle \\
&+ 2\langle\langle\cos(2\varphi_1 - \varphi_4 - \varphi_5)\rangle\rangle\langle\langle\cos(\varphi_3 - \varphi_7)\rangle\rangle\langle\langle\cos(\varphi_2 - \varphi_6)\rangle\rangle \\
&+ 2\langle\langle\cos(2\varphi_1 - \varphi_4 - \varphi_6)\rangle\rangle\langle\langle\cos(\varphi_2 - \varphi_5)\rangle\rangle\langle\langle\cos(\varphi_3 - \varphi_7)\rangle\rangle \\
&+ 2\langle\langle\cos(2\varphi_1 - \varphi_4 - \varphi_6)\rangle\rangle\langle\langle\cos(\varphi_2 - \varphi_7)\rangle\rangle\langle\langle\cos(\varphi_3 - \varphi_5)\rangle\rangle \\
&+ 2\langle\langle\cos(2\varphi_1 - \varphi_4 - \varphi_6)\rangle\rangle\langle\langle\cos(\varphi_3 - \varphi_5)\rangle\rangle\langle\langle\cos(\varphi_2 - \varphi_7)\rangle\rangle \\
&+ 2\langle\langle\cos(2\varphi_1 - \varphi_4 - \varphi_6)\rangle\rangle\langle\langle\cos(\varphi_3 - \varphi_7)\rangle\rangle\langle\langle\cos(\varphi_2 - \varphi_5)\rangle\rangle \\
&+ 2\langle\langle\cos(2\varphi_1 - \varphi_4 - \varphi_7)\rangle\rangle\langle\langle\cos(\varphi_2 - \varphi_5)\rangle\rangle\langle\langle\cos(\varphi_3 - \varphi_6)\rangle\rangle \\
&+ 2\langle\langle\cos(2\varphi_1 - \varphi_4 - \varphi_7)\rangle\rangle\langle\langle\cos(\varphi_2 - \varphi_6)\rangle\rangle\langle\langle\cos(\varphi_3 - \varphi_5)\rangle\rangle \\
&+ 2\langle\langle\cos(2\varphi_1 - \varphi_4 - \varphi_7)\rangle\rangle\langle\langle\cos(\varphi_3 - \varphi_5)\rangle\rangle\langle\langle\cos(\varphi_2 - \varphi_6)\rangle\rangle \\
&+ 2\langle\langle\cos(2\varphi_1 - \varphi_4 - \varphi_7)\rangle\rangle\langle\langle\cos(\varphi_3 - \varphi_6)\rangle\rangle\langle\langle\cos(\varphi_2 - \varphi_5)\rangle\rangle \\
&+ 2\langle\langle\cos(2\varphi_1 - \varphi_5 - \varphi_6)\rangle\rangle\langle\langle\cos(\varphi_2 - \varphi_4)\rangle\rangle\langle\langle\cos(\varphi_3 - \varphi_7)\rangle\rangle \\
&+ 2\langle\langle\cos(2\varphi_1 - \varphi_5 - \varphi_6)\rangle\rangle\langle\langle\cos(\varphi_2 - \varphi_7)\rangle\rangle\langle\langle\cos(\varphi_3 - \varphi_4)\rangle\rangle \\
&+ 2\langle\langle\cos(2\varphi_1 - \varphi_5 - \varphi_6)\rangle\rangle\langle\langle\cos(\varphi_3 - \varphi_4)\rangle\rangle\langle\langle\cos(\varphi_2 - \varphi_7)\rangle\rangle \\
&+ 2\langle\langle\cos(2\varphi_1 - \varphi_5 - \varphi_6)\rangle\rangle\langle\langle\cos(\varphi_3 - \varphi_7)\rangle\rangle\langle\langle\cos(\varphi_2 - \varphi_4)\rangle\rangle \\
&+ 2\langle\langle\cos(2\varphi_1 - \varphi_5 - \varphi_7)\rangle\rangle\langle\langle\cos(\varphi_2 - \varphi_4)\rangle\rangle\langle\langle\cos(\varphi_3 - \varphi_6)\rangle\rangle \\
&+ 2\langle\langle\cos(2\varphi_1 - \varphi_5 - \varphi_7)\rangle\rangle\langle\langle\cos(\varphi_2 - \varphi_6)\rangle\rangle\langle\langle\cos(\varphi_3 - \varphi_4)\rangle\rangle \\
&+ 2\langle\langle\cos(2\varphi_1 - \varphi_5 - \varphi_7)\rangle\rangle\langle\langle\cos(\varphi_3 - \varphi_4)\rangle\rangle\langle\langle\cos(\varphi_2 - \varphi_6)\rangle\rangle \\
&+ 2\langle\langle\cos(2\varphi_1 - \varphi_5 - \varphi_7)\rangle\rangle\langle\langle\cos(\varphi_3 - \varphi_6)\rangle\rangle\langle\langle\cos(\varphi_2 - \varphi_4)\rangle\rangle
\end{aligned}
$$

$$
\begin{aligned}
&+2\langle\langle\cos(2\varphi_1-\varphi_6-\varphi_7)\rangle\rangle\langle\langle\cos(\varphi_2-\varphi_4)\rangle\rangle\langle\langle\cos(\varphi_3-\varphi_5)\rangle\rangle\\
&+2\langle\langle\cos(2\varphi_1-\varphi_6-\varphi_7)\rangle\rangle\langle\langle\cos(\varphi_2-\varphi_5)\rangle\rangle\langle\langle\cos(\varphi_3-\varphi_4)\rangle\rangle\\
&+2\langle\langle\cos(2\varphi_1-\varphi_6-\varphi_7)\rangle\rangle\langle\langle\cos(\varphi_3-\varphi_4)\rangle\rangle\langle\langle\cos(\varphi_2-\varphi_5)\rangle\rangle\\
&+2\langle\langle\cos(2\varphi_1-\varphi_6-\varphi_7)\rangle\rangle\langle\langle\cos(\varphi_3-\varphi_5)\rangle\rangle\langle\langle\cos(\varphi_2-\varphi_4)\rangle\rangle, \qquad (8.27)
\end{aligned}
$$

$$
\begin{aligned}
c\{7\}_{2,2,1,-2,-1,-1,-1} &\equiv \langle\langle\cos(2\varphi_1+2\varphi_2+\varphi_3-2\varphi_4-\varphi_5-\varphi_6-\varphi_7)\rangle\rangle\\
&-\langle\langle\cos(2\varphi_1+2\varphi_2-2\varphi_4-\varphi_5-\varphi_6)\rangle\rangle\langle\langle\cos(\varphi_3-\varphi_7)\rangle\rangle\\
&-\langle\langle\cos(2\varphi_1+2\varphi_2-2\varphi_4-\varphi_5-\varphi_7)\rangle\rangle\langle\langle\cos(\varphi_3-\varphi_6)\rangle\rangle\\
&-\langle\langle\cos(2\varphi_1+2\varphi_2-2\varphi_4-\varphi_6-\varphi_7)\rangle\rangle\langle\langle\cos(\varphi_3-\varphi_5)\rangle\rangle\\
&-\langle\langle\cos(2\varphi_1+\varphi_3-\varphi_5-\varphi_6-\varphi_7)\rangle\rangle\langle\langle\cos(2\varphi_2-2\varphi_4)\rangle\rangle\\
&-\langle\langle\cos(2\varphi_2+\varphi_3-\varphi_5-\varphi_6-\varphi_7)\rangle\rangle\langle\langle\cos(2\varphi_1-2\varphi_4)\rangle\rangle\\
&-\langle\langle\cos(2\varphi_1+\varphi_3-2\varphi_4-\varphi_5)\rangle\rangle\langle\langle\cos(2\varphi_2-\varphi_6-\varphi_7)\rangle\rangle\\
&-\langle\langle\cos(2\varphi_1+\varphi_3-2\varphi_4-\varphi_6)\rangle\rangle\langle\langle\cos(2\varphi_2-\varphi_5-\varphi_7)\rangle\rangle\\
&-\langle\langle\cos(2\varphi_1+\varphi_3-2\varphi_4-\varphi_7)\rangle\rangle\langle\langle\cos(2\varphi_2-\varphi_5-\varphi_6)\rangle\rangle\\
&-\langle\langle\cos(2\varphi_2+\varphi_3-2\varphi_4-\varphi_5)\rangle\rangle\langle\langle\cos(2\varphi_1-\varphi_6-\varphi_7)\rangle\rangle\\
&-\langle\langle\cos(2\varphi_2+\varphi_3-2\varphi_4-\varphi_6)\rangle\rangle\langle\langle\cos(2\varphi_1-\varphi_5-\varphi_7)\rangle\rangle\\
&-\langle\langle\cos(2\varphi_2+\varphi_3-2\varphi_4-\varphi_7)\rangle\rangle\langle\langle\cos(2\varphi_1-\varphi_5-\varphi_6)\rangle\rangle\\
&+2\langle\langle\cos(2\varphi_1-\varphi_5-\varphi_6)\rangle\rangle\langle\langle\cos(2\varphi_2-2\varphi_4)\rangle\rangle\langle\langle\cos(\varphi_3-\varphi_7)\rangle\rangle\\
&+2\langle\langle\cos(2\varphi_1-\varphi_5-\varphi_6)\rangle\rangle\langle\langle\cos(\varphi_3-\varphi_7)\rangle\rangle\langle\langle\cos(2\varphi_2-2\varphi_4)\rangle\rangle\\
&+2\langle\langle\cos(2\varphi_1-\varphi_5-\varphi_7)\rangle\rangle\langle\langle\cos(2\varphi_2-2\varphi_4)\rangle\rangle\langle\langle\cos(\varphi_3-\varphi_6)\rangle\rangle\\
&+2\langle\langle\cos(2\varphi_1-\varphi_5-\varphi_7)\rangle\rangle\langle\langle\cos(\varphi_3-\varphi_6)\rangle\rangle\langle\langle\cos(2\varphi_2-2\varphi_4)\rangle\rangle\\
&+2\langle\langle\cos(2\varphi_1-\varphi_6-\varphi_7)\rangle\rangle\langle\langle\cos(2\varphi_2-2\varphi_4)\rangle\rangle\langle\langle\cos(\varphi_3-\varphi_5)\rangle\rangle\\
&+2\langle\langle\cos(2\varphi_1-\varphi_6-\varphi_7)\rangle\rangle\langle\langle\cos(\varphi_3-\varphi_5)\rangle\rangle\langle\langle\cos(2\varphi_2-2\varphi_4)\rangle\rangle\\
&+2\langle\langle\cos(2\varphi_2-\varphi_5-\varphi_6)\rangle\rangle\langle\langle\cos(2\varphi_1-2\varphi_4)\rangle\rangle\langle\langle\cos(\varphi_3-\varphi_7)\rangle\rangle\\
&+2\langle\langle\cos(2\varphi_2-\varphi_5-\varphi_6)\rangle\rangle\langle\langle\cos(\varphi_3-\varphi_7)\rangle\rangle\langle\langle\cos(2\varphi_1-2\varphi_4)\rangle\rangle\\
&+2\langle\langle\cos(2\varphi_2-\varphi_5-\varphi_7)\rangle\rangle\langle\langle\cos(2\varphi_1-2\varphi_4)\rangle\rangle\langle\langle\cos(\varphi_3-\varphi_6)\rangle\rangle\\
&+2\langle\langle\cos(2\varphi_2-\varphi_5-\varphi_7)\rangle\rangle\langle\langle\cos(\varphi_3-\varphi_6)\rangle\rangle\langle\langle\cos(2\varphi_1-2\varphi_4)\rangle\rangle\\
&+2\langle\langle\cos(2\varphi_2-\varphi_6-\varphi_7)\rangle\rangle\langle\langle\cos(2\varphi_1-2\varphi_4)\rangle\rangle\langle\langle\cos(\varphi_3-\varphi_5)\rangle\rangle\\
&+2\langle\langle\cos(2\varphi_2-\varphi_6-\varphi_7)\rangle\rangle\langle\langle\cos(\varphi_3-\varphi_5)\rangle\rangle\langle\langle\cos(2\varphi_1-2\varphi_4)\rangle\rangle, \qquad (8.28)
\end{aligned}
$$

$$
\begin{aligned}
c\{7\}_{2,2,2,-2,-2,-1,-1} &\equiv \langle\langle\cos(2\varphi_1+2\varphi_2+2\varphi_3-2\varphi_4-2\varphi_5-\varphi_6-\varphi_7)\rangle\rangle\\
&-\langle\langle\cos(2\varphi_1+2\varphi_2-2\varphi_4-\varphi_6-\varphi_7)\rangle\rangle\langle\langle\cos(2\varphi_3-2\varphi_5)\rangle\rangle\\
&-\langle\langle\cos(2\varphi_1+2\varphi_2-2\varphi_5-\varphi_6-\varphi_7)\rangle\rangle\langle\langle\cos(2\varphi_3-2\varphi_4)\rangle\rangle\\
&-\langle\langle\cos(2\varphi_1+2\varphi_3-2\varphi_4-\varphi_6-\varphi_7)\rangle\rangle\langle\langle\cos(2\varphi_2-2\varphi_5)\rangle\rangle\\
&-\langle\langle\cos(2\varphi_1+2\varphi_3-2\varphi_5-\varphi_6-\varphi_7)\rangle\rangle\langle\langle\cos(2\varphi_2-2\varphi_4)\rangle\rangle\\
&-\langle\langle\cos(2\varphi_2+2\varphi_3-2\varphi_4-\varphi_6-\varphi_7)\rangle\rangle\langle\langle\cos(2\varphi_1-2\varphi_5)\rangle\rangle\\
&-\langle\langle\cos(2\varphi_2+2\varphi_3-2\varphi_5-\varphi_6-\varphi_7)\rangle\rangle\langle\langle\cos(2\varphi_1-2\varphi_4)\rangle\rangle\\
&-\langle\langle\cos(2\varphi_1+2\varphi_2-2\varphi_4-2\varphi_5)\rangle\rangle\langle\langle\cos(2\varphi_3-\varphi_6-\varphi_7)\rangle\rangle\\
&-\langle\langle\cos(2\varphi_1+2\varphi_3-2\varphi_4-2\varphi_5)\rangle\rangle\langle\langle\cos(2\varphi_2-\varphi_6-\varphi_7)\rangle\rangle\\
&-\langle\langle\cos(2\varphi_2+2\varphi_3-2\varphi_4-2\varphi_5)\rangle\rangle\langle\langle\cos(2\varphi_1-\varphi_6-\varphi_7)\rangle\rangle
\end{aligned}
$$

$$
\begin{aligned}
&+2\langle\langle\cos(2\varphi_1-\varphi_6-\varphi_7)\rangle\rangle\langle\langle\cos(2\varphi_2-2\varphi_4)\rangle\rangle\langle\langle\cos(2\varphi_3-2\varphi_5)\rangle\rangle\\
&+2\langle\langle\cos(2\varphi_1-\varphi_6-\varphi_7)\rangle\rangle\langle\langle\cos(2\varphi_2-2\varphi_5)\rangle\rangle\langle\langle\cos(2\varphi_3-2\varphi_4)\rangle\rangle\\
&+2\langle\langle\cos(2\varphi_1-\varphi_6-\varphi_7)\rangle\rangle\langle\langle\cos(2\varphi_3-2\varphi_4)\rangle\rangle\langle\langle\cos(2\varphi_2-2\varphi_5)\rangle\rangle\\
&+2\langle\langle\cos(2\varphi_1-\varphi_6-\varphi_7)\rangle\rangle\langle\langle\cos(2\varphi_3-2\varphi_5)\rangle\rangle\langle\langle\cos(2\varphi_2-2\varphi_4)\rangle\rangle\\
&+2\langle\langle\cos(2\varphi_2-\varphi_6-\varphi_7)\rangle\rangle\langle\langle\cos(2\varphi_1-2\varphi_4)\rangle\rangle\langle\langle\cos(2\varphi_3-2\varphi_5)\rangle\rangle\\
&+2\langle\langle\cos(2\varphi_2-\varphi_6-\varphi_7)\rangle\rangle\langle\langle\cos(2\varphi_1-2\varphi_5)\rangle\rangle\langle\langle\cos(2\varphi_3-2\varphi_4)\rangle\rangle\\
&+2\langle\langle\cos(2\varphi_2-\varphi_6-\varphi_7)\rangle\rangle\langle\langle\cos(2\varphi_3-2\varphi_4)\rangle\rangle\langle\langle\cos(2\varphi_1-2\varphi_5)\rangle\rangle\\
&+2\langle\langle\cos(2\varphi_2-\varphi_6-\varphi_7)\rangle\rangle\langle\langle\cos(2\varphi_3-2\varphi_5)\rangle\rangle\langle\langle\cos(2\varphi_1-2\varphi_4)\rangle\rangle\\
&+2\langle\langle\cos(2\varphi_3-\varphi_6-\varphi_7)\rangle\rangle\langle\langle\cos(2\varphi_1-2\varphi_4)\rangle\rangle\langle\langle\cos(2\varphi_2-2\varphi_5)\rangle\rangle\\
&+2\langle\langle\cos(2\varphi_3-\varphi_6-\varphi_7)\rangle\rangle\langle\langle\cos(2\varphi_1-2\varphi_5)\rangle\rangle\langle\langle\cos(2\varphi_2-2\varphi_4)\rangle\rangle\\
&+2\langle\langle\cos(2\varphi_3-\varphi_6-\varphi_7)\rangle\rangle\langle\langle\cos(2\varphi_2-2\varphi_4)\rangle\rangle\langle\langle\cos(2\varphi_1-2\varphi_5)\rangle\rangle\\
&+2\langle\langle\cos(2\varphi_3-\varphi_6-\varphi_7)\rangle\rangle\langle\langle\cos(2\varphi_2-2\varphi_5)\rangle\rangle\langle\langle\cos(2\varphi_1-2\varphi_4)\rangle\rangle,
\end{aligned}
\tag{8.29}
$$

$$a_1\{2\} \equiv \sqrt[2]{|c\{2\}_{1,-1}|}, \tag{8.30}$$

$$a_1\{3\} \equiv \sqrt[2]{\left|\frac{c\{3\}_{2,-1,-1}}{\langle v_2\rangle}\right|}, \tag{8.31}$$

$$a_1\{4\} \equiv \sqrt[4]{|c\{4\}_{1,1,-1,-1}|}, \tag{8.32}$$

$$a_1\{5\} \equiv \sqrt[4]{\left|\frac{1}{2}\frac{c\{5\}_{2,1,-1,-1,-1}}{\langle v_2\rangle}\right|}, \tag{8.33}$$

$$a_1\{5\}' \equiv \sqrt[2]{\left|\frac{c\{5\}_{2,2,-2,-1,-1}}{\langle v_2^3\rangle}\right|}, \tag{8.34}$$

$$a_1\{6\} \equiv \sqrt[6]{|c\{6\}_{1,1,1,-1,-1,-1}|}, \tag{8.35}$$

$$a_1\{6\}' \equiv \sqrt[4]{\left|\frac{1}{5}\frac{c\{6\}_{2,2,-1,-1,-1,-1}}{\langle v_2^2\rangle}\right|}, \tag{8.36}$$

$$a_1\{6\}'' \equiv \sqrt[4]{\left|\frac{c\{6\}_{2,1,1,-2,-1,-1}}{\langle v_2^2\rangle}\right|}, \tag{8.37}$$

$$a_1\{7\} \equiv \sqrt[6]{\left|\frac{1}{11}\frac{c\{7\}_{2,1,1,-1,-1,-1,-1}}{\langle v_2\rangle}\right|}, \tag{8.38}$$

$$a_1\{7\}' \equiv \sqrt[4]{\left|\frac{1}{2}\frac{c\{7\}_{2,2,1,-2,-1,-1,-1}}{\langle v_2^3\rangle}\right|}, \tag{8.39}$$

$$a_1\{7\}'' \equiv \sqrt[2]{\left|\frac{1}{4}\frac{c\{7\}_{2,2,2,-2,-2,-1,-1}}{\langle v_2^5\rangle}\right|}. \tag{8.40}$$

Bibliography

[1] F. Halzen and A. D. Martin, "Quarks And Leptons: An Introductory Course In Modern Particle Physics," New York, Usa: Wiley (1984) 396p

[2] D. J. Gross and F. Wilczek, "Asymptotically Free Gauge Theories - I," Phys. Rev. D **8** (1973) 3633. doi:10.1103/PhysRevD.8.3633

[3] G. Martinez, "Advances in Quark Gluon Plasma," arXiv:1304.1452 [nucl-ex].

[4] C. Patrignani *et al.* [Particle Data Group], "Review of Particle Physics," Chin. Phys. C **40** (2016) no.10, 100001. doi:10.1088/1674-1137/40/10/100001

[5] Callaway, David J. E. and Rahman, Aneesur, "Lattice gauge theory in the microcanonical ensemble," Phys. Rev. D **28** (1983) 1506. doi:10.1103/PhysRevD.28.1506

[6] C. Ratti, "Lattice QCD and heavy ion collisions: a review of recent progress," arXiv:1804.07810 [hep-lat].

[7] M. G. Alford, A. Schmitt, K. Rajagopal and T. Schäfer, "Color superconductivity in dense quark matter," Rev. Mod. Phys. **80** (2008) 1455 doi:10.1103/RevModPhys.80.1455 [arXiv:0709.4635 [hep-ph]].

[8] S. Borsanyi, "Thermodynamics of the QCD transition from lattice," Nucl. Phys. A **904-905** (2013) 270c doi:10.1016/j.nuclphysa.2013.01.072 [arXiv:1210.6901 [hep-lat]].

[9] F. M. Steffens, "The Temperature dependence of the QCD running coupling," Braz. J. Phys. **36** (2006) 582 doi:10.1590/S0103-97332006000400020 [hep-ph/0409329].

[10] U. W. Heinz, "The Strongly coupled quark-gluon plasma created at RHIC," J. Phys. A **42** (2009) 214003 doi:10.1088/1751-8113/42/21/214003 [arXiv:0810.5529 [nucl-th]].

[11] C. Shen and U. Heinz, "The road to precision: Extraction of the specific shear viscosity of the quark-gluon plasma," Nucl. Phys. News **25** (2015) no.2, 6 doi:10.1080/10619127.2015.1006502 [arXiv:1507.01558 [nucl-th]].

[12] W. Busza, K. Rajagopal and W. van der Schee, "Heavy Ion Collisions: The Big Picture, and the Big Questions," arXiv:1802.04801 [hep-ph].

[13] L. D. McLerran and R. Venugopalan, "Computing quark and gluon distribution functions for very large nuclei," Phys. Rev. D **49** (1994) 2233 doi:10.1103/PhysRevD.49.2233 [hep-ph/9309289].

[14] K. J. Eskola, K. Kajantie, P. V. Ruuskanen and K. Tuominen, "Scaling of transverse energies and multiplicities with atomic number and energy in ultrarelativistic nuclear collisions," Nucl. Phys. B **570** (2000) 379 doi:10.1016/S0550-3213(99)00720-8 [hep-ph/9909456].

[15] J. Bartels, K. J. Golec-Biernat and H. Kowalski, "A modification of the saturation model: DGLAP evolution," Phys. Rev. D **66** (2002) 014001 doi:10.1103/PhysRevD.66.014001 [hep-ph/0203258].

[16] K. J. Eskola, H. Niemi, R. Paatelainen and K. Tuominen, "Latest results from the EbyE NLO EKRT model," Nucl. Phys. A **967** (2017) 313 doi:10.1016/j.nuclphysa.2017.04.038 [arXiv:1704.04060 [hep-ph]].

[17] C. Gale, S. Jeon, B. Schenke, P. Tribedy and R. Venugopalan, "Event-by-event anisotropic flow in heavy-ion collisions from combined Yang-Mills and viscous fluid dynamics," Phys. Rev. Lett. **110** (2013) no.1, 012302 doi:10.1103/PhysRevLett.110.012302 [arXiv:1209.6330 [nucl-th]].

[18] J. E. Bernhard, J. S. Moreland, S. A. Bass, J. Liu and U. Heinz, "Applying Bayesian parameter estimation to relativistic heavy-ion collisions: simultaneous characterization of the initial state and quark-gluon plasma medium," Phys. Rev. C **94** (2016) no.2, 024907 doi:10.1103/PhysRevC.94.024907 [arXiv:1605.03954 [nucl-th]].

[19] B. Alver, M. Baker, C. Loizides and P. Steinberg, "The PHOBOS Glauber Monte Carlo," arXiv:0805.4411 [nucl-ex].

[20] M. L. Miller, K. Reygers, S. J. Sanders and P. Steinberg, "Glauber modeling in high energy nuclear collisions," Ann. Rev. Nucl. Part. Sci. **57** (2007) 205 doi:10.1146/annurev.nucl.57.090506.123020 [nucl-ex/0701025].

[21] J. S. Moreland, J. E. Bernhard, W. Ke and S. A. Bass, "Flow in small and large quark-gluon plasma droplets: the role of nucleon substructure," Nucl. Phys. A **967** (2017) 361 doi:10.1016/j.nuclphysa.2017.05.054 [arXiv:1704.04486 [nucl-th]].

[22] J. L. Albacete, H. Petersen and A. Soto-Ontoso, "Symmetric cumulants as a probe of the proton substructure at LHC energies," Phys. Lett. B **778** (2018) 128 doi:10.1016/j.physletb.2018.01.011 [arXiv:1707.05592 [hep-ph]].

[23] W. Broniowski, P. Bozek and M. Rybczynski, "Wounded quarks at the LHC," Acta Phys. Polon. Supp. **10** (2017) 513 doi:10.5506/APhysPolBSupp.10.513 [arXiv:1611.00250 [nucl-th]].

[24] S. Acharya *et al.* [ALICE Collaboration], "Anisotropic flow in Xe-Xe collisions at $\sqrt{s_{\rm NN}} = \mathbf{5.44}$ TeV," arXiv:1805.01832 [nucl-ex].

[25] R. Baier, A. H. Mueller, D. Schiff and D. T. Son, "'Bottom up' thermalization in heavy ion collisions," Phys. Lett. B **502** (2001) 51 doi:10.1016/S0370-2693(01)00191-5 [hep-ph/0009237].

[26] A. Kurkela, A. Mazeliauskas, J. F. Paquet, S. Schlichting and D. Teaney, "Matching the non-equilibrium initial stage of heavy ion collisions to hydrodynamics with QCD kinetic theory," arXiv:1805.01604 [hep-ph].

[27] A. Kurkela, A. Mazeliauskas, J. F. Paquet, S. Schlichting and D. Teaney, arXiv:1805.00961 [hep-ph].

[28] A. Behtash, C. N. Cruz-Camacho and M. Martinez, "Far-from-equilibrium attractors and nonlinear dynamical systems approach to the Gubser flow," Phys. Rev. D **97** (2018) no.4, 044041 doi:10.1103/PhysRevD.97.044041 [arXiv:1711.01745 [hep-th]].

[29] P. B. Arnold, G. D. Moore and L. G. Yaffe, "Effective kinetic theory for high temperature gauge theories," JHEP **0301** (2003) 030 doi:10.1088/1126-6708/2003/01/030 [hep-ph/0209353].

[30] U. Heinz and R. Snellings, "Collective flow and viscosity in relativistic heavy-ion collisions," Ann. Rev. Nucl. Part. Sci. **63** (2013) 123 doi:10.1146/annurev-nucl-102212-170540 [arXiv:1301.2826 [nucl-th]].

[31] P. M. Jacobs and M. van Leeuwen, "High p(T) in nuclear collisions at SPS, RHIC, and LHC," Nucl. Phys. A **774** (2006) 237 doi:10.1016/j.nuclphysa.2006.06.044 [nucl-ex/0511013].

[32] R. Baier, D. Schiff and B. G. Zakharov, "Energy loss in perturbative QCD," Ann. Rev. Nucl. Part. Sci. **50** (2000) 37 doi:10.1146/annurev.nucl.50.1.37 [hep-ph/0002198].

[33] C. Gale, "Photon Production in Hot and Dense Strongly Interacting Matter," Landolt-Bornstein **23** (2010) 445 doi:10.1007/978-3-642-01539-7_15 [arXiv:0904.2184 [hep-ph]].

[34] K. C. Han, R. J. Fries and C. M. Ko, "Jet Fragmentation via Recombination of Parton Showers," Phys. Rev. C **93** (2016) no.4, 045207 doi:10.1103/PhysRevC.93.045207 [arXiv:1601.00708 [nucl-th]].

[35] F. Cooper and G. Frye, "Single-particle distribution in the hydrodynamic and statistical thermodynamic models of multiparticle production," Phys. Rev. D **10** (1974) no.1, 186 doi:10.1103/PhysRevD.10.186

[36] A. L. S. Angelis *et al.* [BCMOR Collaboration], "Large Transverse Momentum π^0 Production in $\alpha\alpha dd$ and pp Collisions at the CERN ISR," Phys. Lett. B **185** (1987) 213. doi:10.1016/0370-2693(87)91557-7

[37] M. M. Aggarwal *et al.* [WA98 Collaboration], "Transverse mass distributions of neutral pions from Pb-208 induced reactions at 158-A-GeV," Eur. Phys. J. C **23** (2002) 225 doi:10.1007/s100520100886 [nucl-ex/0108006].

[38] R. Hanbury Brown and R. Q. Twiss, "A Test of a New Type of Stellar Interferometer on Sirius," Nature **178** (1956) 1046. doi:10.1038/1781046a0

[39] M. A. Lisa, S. Pratt, R. Soltz and U. Wiedemann, "Femtoscopy in relativistic heavy ion collisions," Ann. Rev. Nucl. Part. Sci. **55** (2005) 357 doi:10.1146/annurev.nucl.55.090704.151533 [nucl-ex/0505014].

[40] R. Pasechnik and M. Šumbera, "Phenomenological Review on Quark–Gluon Plasma: Concepts vs. Observations," Universe **3** (2017) no.1, 7 doi:10.3390/universe3010007 [arXiv:1611.01533 [hep-ph]].

[41] J. Y. Ollitrault, "Anisotropy as a signature of transverse collective flow," Phys. Rev. D **46** (1992) 229. doi:10.1103/PhysRevD.46.229

[42] S. Voloshin and Y. Zhang, "Flow study in relativistic nuclear collisions by Fourier expansion of Azimuthal particle distributions," Z. Phys. C **70** (1996) 665 doi:10.1007/s002880050141 [hep-ph/9407282].

[43] K. Aamodt *et al.* [ALICE Collaboration], "Higher harmonic anisotropic flow measurements of charged particles in Pb-Pb collisions at $\sqrt{s_{NN}}$=2.76 TeV," Phys. Rev. Lett. **107** (2011) 032301 doi:10.1103/PhysRevLett.107.032301 [arXiv:1105.3865 [nucl-ex]].

[44] R. Snellings, "Collective Expansion at the LHC: selected ALICE anisotropic flow measurements," J. Phys. G **41** (2014) no.12, 124007 doi:10.1088/0954-3899/41/12/124007 [arXiv:1408.2532 [nucl-ex]].

[45] S. A. Voloshin and A. M. Poskanzer, "The Physics of the centrality dependence of elliptic flow," Phys. Lett. B **474** (2000) 27 doi:10.1016/S0370-2693(00)00017-4 [nucl-th/9906075].

[46] D. Teaney and L. Yan, "Triangularity and Dipole Asymmetry in Heavy Ion Collisions," Phys. Rev. C **83** (2011) 064904 doi:10.1103/PhysRevC.83.064904 [arXiv:1010.1876 [nucl-th]].

[47] V. Khachatryan *et al.* [CMS Collaboration], "Evidence for transverse momentum and pseudorapidity dependent event plane fluctuations in PbPb and pPb collisions," Phys. Rev. C **92** (2015) no.3, 034911 doi:10.1103/PhysRevC.92.034911 [arXiv:1503.01692 [nucl-ex]].

[48] M. Aaboud *et al.* [ATLAS Collaboration], "Measurement of longitudinal flow decorrelations in Pb+Pb collisions at $\sqrt{s_{\rm NN}}$ = 2.76 and 5.02 TeV with the ATLAS detector," Eur. Phys. J. C **78** (2018) no.2, 142 doi:10.1140/epjc/s10052-018-5605-7 [arXiv:1709.02301 [nucl-ex]].

[49] T. Hirano, U. W. Heinz, D. Kharzeev, R. Lacey and Y. Nara, "Hadronic dissipative effects on elliptic flow in ultrarelativistic heavy-ion collisions," Phys. Lett. B **636** (2006) 299 doi:10.1016/j.physletb.2006.03.060 [arXiv:nucl-th/0511046].

[50] R. Snellings, "How much does the hadronic phase contribute to the observed anisotropic flow at the LHC?," EPJ Web Conf. **97** (2015) 00025 doi:10.1051/epjconf/20159700025 [arXiv:1411.7690 [nucl-ex]].

[51] P. Romatschke, "New Developments in Relativistic Viscous Hydrodynamics," Int. J. Mod. Phys. E **19** (2010) 1 doi:10.1142/S0218301310014613 [arXiv:0902.3663 [hep-ph]].

[52] C. Shen, U. Heinz, P. Huovinen and H. Song, "Systematic parameter study of hadron spectra and elliptic flow from viscous hydrodynamic simulations of Au+Au collisions at $\sqrt{s_{NN}}$ = 200 GeV," Phys. Rev. C **82** (2010) 054904 doi:10.1103/PhysRevC.82.054904 [arXiv:1010.1856 [nucl-th]].

[53] S. Ryu, J.-F. Paquet, C. Shen, G. S. Denicol, B. Schenke, S. Jeon and C. Gale, "Importance of the Bulk Viscosity of QCD in Ultrarelativistic Heavy-Ion Collisions," Phys. Rev. Lett. **115** (2015) no.13, 132301 doi:10.1103/PhysRevLett.115.132301 [arXiv:1502.01675 [nucl-th]].

[54] S. Pratt, E. Sangaline, P. Sorensen and H. Wang, "Constraining the Eq. of State of Super-Hadronic Matter from Heavy-Ion Collisions," Phys. Rev. Lett. **114**, 202301 (2015) doi:10.1103/PhysRevLett.114.202301 [arXiv:1501.04042 [nucl-th]].

[55] J. Auvinen, I. Karpenko, J. E. Bernhard and S. A. Bass, "Investigating the collision energy dependence of η/s in RHIC beam energy scan using Bayesian statistics," [arXiv:1706.03666 [hep-ph]].

[56] M. Gyulassy, I. Vitev and X. N. Wang, "High p(T) azimuthal asymmetry in noncentral A+A at RHIC," Phys. Rev. Lett. **86** (2001) 2537 doi:10.1103/PhysRevLett.86.2537 [arXiv:nucl-th/0012092].

[57] X. N. Wang, "Jet quenching and azimuthal anisotropy of large p(T) spectra in noncentral high-energy heavy ion collisions," Phys. Rev. C **63** (2001) 054902 doi:10.1103/PhysRevC.63.054902 [arXiv:nucl-th/0009019].

[58] E. V. Shuryak, "The Azimuthal asymmetry at large p(t) seem to be too large for a 'jet quenching'," Phys. Rev. C **66** (2002) 027902 doi:10.1103/PhysRevC.66.027902 [arXiv:nucl-th/0112042].

[59] G. Aad *et al.* [ATLAS Collaboration], "Measurement of the Azimuthal Angle Dependence of Inclusive Jet Yields in Pb+Pb Collisions at $\sqrt{s_{NN}}$ = 2.76 TeV with the ATLAS detector," Phys. Rev. Lett. **111** (2013) no.15, 152301 doi:10.1103/PhysRevLett.111.152301 [arXiv:1306.6469 [hep-ex]].

[60] J. Adam *et al.* [ALICE Collaboration], "Azimuthal anisotropy of charged jet production in $\sqrt{s_{NN}}$ = 2.76 TeV Pb-Pb collisions," Phys. Lett. B **753** (2016) 511 doi:10.1016/j.physletb.2015.12.047 [arXiv:1509.07334 [nucl-ex]].

[61] A. M. Sirunyan *et al.* [CMS Collaboration], "Azimuthal anisotropy of charged particles with transverse momentum up to 100 GeV in PbPb collisions at $\sqrt{s_{NN}}$ = 5.02 TeV," arXiv:1702.00630 [hep-ex].

[62] R. Baier, Y. L. Dokshitzer, A. H. Mueller, S. Peigne and D. Schiff, "Radiative energy loss and p(T) broadening of high-energy partons in nuclei," Nucl. Phys. B **484** (1997) 265 doi:10.1016/S0550-3213(96)00581-0 [hep-ph/9608322].

[63] A. Majumder, B. Muller and X. N. Wang, "Small shear viscosity of a quark-gluon plasma implies strong jet quenching," Phys. Rev. Lett. **99** (2007) 192301 doi:10.1103/PhysRevLett.99.192301 [hep-ph/0703082].

[64] H. Song, S. A. Bass and U. Heinz, "Elliptic flow in 200 A GeV Au+Au collisions and 2.76 A TeV Pb+Pb collisions: insights from viscous hydrodynamics + hadron cascade hybrid model," Phys. Rev. C **83** (2011) 054912 Erratum: [Phys. Rev. C **87** (2013) no.1, 019902] doi:10.1103/PhysRevC.83.054912, 10.1103/PhysRevC.87.019902 [arXiv:1103.2380 [nucl-th]].

[65] K. M. Burke *et al.* [JET Collaboration], "Extracting the jet transport coefficient from jet quenching in high-energy heavy-ion collisions," Phys. Rev. C **90** (2014) no.1, 014909 doi:10.1103/PhysRevC.90.014909 [arXiv:1312.5003 [nucl-th]].

[66] K. Tuchin, "Particle production in strong electromagnetic fields in relativistic heavy-ion collisions," Adv. High Energy Phys. **2013** (2013) 490495 doi:10.1155/2013/490495 [arXiv:1301.0099 [hep-ph]].

[67] V. Skokov, A. Y. Illarionov and V. Toneev, "Estimate of the magnetic field strength in heavy-ion collisions," Int. J. Mod. Phys. A **24** (2009) 5925 doi:10.1142/S0217751X09047570 [arXiv:0907.1396 [nucl-th]].

[68] V. M. Kaspi and A. Beloborodov, "Magnetars," Ann. Rev. Astron. Astrophys. **55** (2017) 261 doi:10.1146/annurev-astro-081915-023329 [arXiv:1703.00068 [astro-ph.HE]].

[69] D. E. Kharzeev, K. Landsteiner, A. Schmitt and H. U. Yee, "Strongly interacting matter in magnetic fields" Lect. Notes Phys. **871** (2013) 1 doi:10.1007/978-3-642-37305-3_1 [arXiv:1211.6245 [hep-ph]].

[70] H.-T. Ding, A. Francis, O. Kaczmarek, F. Karsch, E. Laermann and W. Soeldner, "Thermal dilepton rate and electrical conductivity: An analysis of vector current correlation functions in quenched lattice QCD," Phys. Rev. D **83** (2011) 034504 doi:10.1103/PhysRevD.83.034504 [arXiv:1012.4963 [hep-lat]].

[71] A. Francis and O. Kaczmarek, "On the temperature dependence of the electrical conductivity in hot quenched lattice QCD," Prog. Part. Nucl. Phys. **67** (2012) 212 doi:10.1016/j.ppnp.2011.12.020 [arXiv:1112.4802 [hep-lat]].

[72] A. Amato, G. Aarts, C. Allton, P. Giudice, S. Hands and J. I. Skullerud, "Electrical conductivity of the quark-gluon plasma across the deconfinement transition," Phys. Rev. Lett. **111** (2013) no.17, 172001 doi:10.1103/PhysRevLett.111.172001 [arXiv:1307.6763 [hep-lat]].

[73] O. Kaczmarek and M. Müller, "Temperature dependence of electrical conductivity and dilepton rates from hot quenched lattice QCD," PoS LATTICE **2013** (2014) 175 [arXiv:1312.5609 [hep-lat]].

[74] V. Voronyuk, V. D. Toneev, W. Cassing, E. L. Bratkovskaya, V. P. Konchakovski and S. A. Voloshin, "(Electro-)Magnetic field evolution in relativistic heavy-ion collisions," Phys. Rev. C **83** (2011) 054911 doi:10.1103/PhysRevC.83.054911 [arXiv:1103.4239 [nucl-th]].

[75] A. A. Belavin, A. M. Polyakov, A. S. Schwartz and Y. S. Tyupkin, "Pseudoparticle Solutions of the Yang-Mills Equations," Phys. Lett. B **59** (1975) 85 [Phys. Lett. **59B** (1975) 85]. doi:10.1016/0370-2693(75)90163-X

[76] F. R. Klinkhamer and N. S. Manton, "A Saddle Point Solution in the Weinberg-Salam Theory," Phys. Rev. D **30** (1984) 2212. doi:10.1103/PhysRevD.30.2212

[77] N. S. Manton, "Topology in the Weinberg-Salam Theory," Phys. Rev. D **28** (1983) 2019. doi:10.1103/PhysRevD.28.2019

[78] G. D. Moore and M. Tassler, "The Sphaleron Rate in SU(N) Gauge Theory," JHEP **1102** (2011) 105 doi:10.1007/JHEP02(2011)105 [arXiv:1011.1167 [hep-ph]].

[79] M. Mace, S. Schlichting and R. Venugopalan, "Off-equilibrium sphaleron transitions in the Glasma," Phys. Rev. D **93** (2016) no.7, 074036 doi:10.1103/PhysRevD.93.074036 [arXiv:1601.07342 [hep-ph]].

[80] T. Schäfer and E. V. Shuryak, "Instantons in QCD," Rev. Mod. Phys. **70** (1998) 323 doi:10.1103/RevModPhys.70.323 [hep-ph/9610451].

[81] D. E. Kharzeev and E. M. Levin, "Color Confinement and Screening in the θ Vacuum of QCD," Phys. Rev. Lett. **114** (2015) no.24, 242001 doi:10.1103/PhysRevLett.114.242001 [arXiv:1501.04622 [hep-ph]].

[82] L. D. McLerran, E. Mottola and M. E. Shaposhnikov, "Sphalerons and Axion Dynamics in High Temperature QCD," Phys. Rev. D **43** (1991) 2027. doi:10.1103/PhysRevD.43.2027

[83] G. 't Hooft, "Symmetry Breaking Through Bell-Jackiw Anomalies," Phys. Rev. Lett. **37** (1976) 8. doi:10.1103/PhysRevLett.37.8

[84] D. Kharzeev, "Parity violation in hot QCD: Why it can happen, and how to look for it," Phys. Lett. B **633** (2006) 260 doi:10.1016/j.physletb.2005.11.075 [hep-ph/0406125].

[85] D. E. Kharzeev, L. D. McLerran and H. J. Warringa, "The Effects of topological charge change in heavy ion collisions: 'Event by event P and CP violation'," Nucl. Phys. A **803** (2008) 227 doi:10.1016/j.nuclphysa.2008.02.298 [arXiv:0711.0950 [hep-ph]].

[86] K. Fukushima, D. E. Kharzeev and H. J. Warringa, "The Chiral Magnetic Effect," Phys. Rev. D **78** (2008) 074033 doi:10.1103/PhysRevD.78.074033 [arXiv:0808.3382 [hep-ph]].

[87] D. E. Kharzeev, J. Liao, S. A. Voloshin and G. Wang, "Chiral magnetic and vortical effects in high-energy nuclear collisions—A status report," Prog. Part. Nucl. Phys. **88** (2016) 1 doi:10.1016/j.ppnp.2016.01.001 [arXiv:1511.04050 [hep-ph]].

[88] V. Koch, S. Schlichting, V. Skokov, P. Sorensen, J. Thomas, S. Voloshin, G. Wang and H. U. Yee, "Status of the chiral magnetic effect and collisions of isobars," Chin. Phys. C **41** (2017) no.7, 072001 doi:10.1088/1674-1137/41/7/072001 [arXiv:1608.00982 [nucl-th]].

[89] V. D. Toneev and V. Voronyuk, "The Chiral Magnetic Effect: Beam-energy and system-size dependence," Phys. Atom. Nucl. **75** (2012) 607 doi:10.1134/S1063778812050274 [arXiv:1012.1508 [nucl-th]].

[90] B. Muller and A. Schafer, "Charge Fluctuations from the Chiral Magnetic Effect in Nuclear Collisions," Phys. Rev. C **82** (2010) 057902 doi:10.1103/PhysRevC.82.057902 [arXiv:1009.1053 [hep-ph]].

[91] G. L. Ma and B. Zhang, "Effects of final state interactions on charge separation in relativistic heavy ion collisions," Phys. Lett. B **700** (2011) 39 doi:10.1016/j.physletb.2011.04.057 [arXiv:1101.1701 [nucl-th]].

[92] K. Aamodt *et al.* [ALICE Collaboration], "Centrality dependence of the charged-particle multiplicity density at mid-rapidity in Pb-Pb collisions at $\sqrt{s_{NN}} = 2.76$ TeV," Phys. Rev. Lett. **106** (2011) 032301 doi:10.1103/PhysRevLett.106.032301 [arXiv:1012.1657 [nucl-ex]].

[93] S. A. Voloshin, "Parity violation in hot QCD: How to detect it," Phys. Rev. C **70** (2004) 057901 doi:10.1103/PhysRevC.70.057901 [hep-ph/0406311].

[94] S. Pratt, S. Schlichting and S. Gavin, "Effects of Momentum Conservation and Flow on Angular Correlations at RHIC," Phys. Rev. C **84** (2011) 024909 doi:10.1103/PhysRevC.84.024909 [arXiv:1011.6053 [nucl-th]].

[95] A. Bzdak, V. Koch and J. Liao, "Azimuthal correlations from transverse momentum conservation and possible local parity violation," Phys. Rev. C **83** (2011) 014905 doi:10.1103/PhysRevC.83.014905 [arXiv:1008.4919 [nucl-th]].

[96] S. Schlichting and S. Pratt, "Charge conservation at energies available at the BNL Relativistic Heavy Ion Collider and contributions to local parity violation observables," Phys. Rev. C **83** (2011) 014913 doi:10.1103/PhysRevC.83.014913 [arXiv:1009.4283 [nucl-th]].

[97] Y. Hori, T. Gunji, H. Hamagaki and S. Schlichting, "Collective flow effects on charge balance correlations and local parity-violation observables in $\sqrt{s_{NN}} = 2.76$ TeV Pb+Pb collisions at the LHC," arXiv:1208.0603 [nucl-th].

[98] G. Aad *et al.* [ATLAS Collaboration], "The ATLAS Experiment at the CERN Large Hadron Collider," JINST **3** (2008) S08003. doi:10.1088/1748-0221/3/08/S08003

[99] S. Chatrchyan *et al.* [CMS Collaboration], "The CMS Experiment at the CERN LHC," JINST **3** (2008) S08004. doi:10.1088/1748-0221/3/08/S08004

[100] A. A. Alves, Jr. *et al.* [LHCb Collaboration], "The LHCb Detector at the LHC," JINST **3** (2008) S08005. doi:10.1088/1748-0221/3/08/S08005

[101] L. Evans and P. Bryant, "LHC Machine," JINST **3** (2008) S08001. doi:10.1088/1748-0221/3/08/S08001

[102] K. Aamodt *et al.* [ALICE Collaboration], "The ALICE experiment at the CERN LHC," JINST **3** (2008) S08002. doi:10.1088/1748-0221/3/08/S08002

[103] F. Carminati *et al.* [ALICE Collaboration], "ALICE: Physics performance report, volume I," J. Phys. G **30** (2004) 1517 doi:10.1088/0954-3899/30/11/001.

[104] B. Alessandro *et al.* [ALICE Collaboration], "ALICE: Physics performance report, volume II," J. Phys. G **32** (2006) 1295. doi:10.1088/0954-3899/32/10/001

[105] B. B. Abelev *et al.* [ALICE Collaboration], "Performance of the ALICE Experiment at the CERN LHC," Int. J. Mod. Phys. A **29** (2014) 1430044 doi:10.1142/S0217751X14300440 [arXiv:1402.4476 [nucl-ex]].

[106] K. Aamodt *et al.* [ALICE Collaboration], "Alignment of the ALICE Inner Tracking System with cosmic-ray tracks," JINST **5** (2010) P03003 doi:10.1088/1748-0221/5/03/P03003 [arXiv:1001.0502 [physics.ins-det]].

[107] J. Alme *et al.*, "The ALICE TPC, a large 3-dimensional tracking device with fast readout for ultra-high multiplicity events," Nucl. Instrum. Meth. A **622** (2010) 316 doi:10.1016/j.nima.2010.04.042 [arXiv:1001.1950 [physics.ins-det]].

[108] K. Oyama [ALICE Collaboration], "Reference cross section measurements with ALICE in pp and Pb-Pb collisions at LHC," arXiv:1305.7044 [nucl-ex].

[109] E. Abbas *et al.* [ALICE Collaboration], "Performance of the ALICE VZERO system," JINST **8** (2013) P10016 doi:10.1088/1748-0221/8/10/P10016 [arXiv:1306.3130 [nucl-ex]].

[113]

[110] G. Dellacasa *et al.* [ALICE Collaboration], "ALICE technical design report of the zero degree calorimeter (ZDC)," CERN-LHCC-99-05.

[111] R. Gemme, "Study of the ALICE ZDC detector performance," Ph.D. Thesis (2006), Turin University, CERN-THESIS-2006-089.

[112] B. Abelev *et al.* [ALICE Collaboration], "Centrality determination of Pb-Pb collisions at $\sqrt{s_{NN}} = 2.76$ TeV with ALICE," Phys. Rev. C **88** (2013) no.4, 044909 doi:10.1103/PhysRevC.88.044909 [arXiv:1301.4361 [nucl-ex]].

[113] S. J. Das, G. Giacalone, P. A. Monard and J. Y. Ollitrault, "Relating centrality to impact parameter in nucleus-nucleus collisions," Phys. Rev. C **97** (2018) no.1, 014905 doi:10.1103/PhysRevC.97.014905 [arXiv:1708.00081 [nucl-th]].

[114] R. Fruhwirth, "Application of Kalman filtering to track and vertex fitting," Nucl. Instrum. Meth. A **262** (1987) 444. doi:10.1016/0168-9002(87)90887-4

[115] B. B. Abelev *et al.* [ALICE Collaboration], "The ALICE definition of primary particles," ALICE-PUBLIC-2017-005 https://cds.cern.ch/record/2270008

[116] S. Chatrchyan *et al.* [CMS Collaboration], "Multiplicity and transverse momentum dependence of two- and four-particle correlations in pPb and PbPb collisions," Phys. Lett. B **724** (2013) 213 doi:10.1016/j.physletb.2013.06.028 [arXiv:1305.0609 [nucl-ex]].

[117] A. M. Poskanzer and S. A. Voloshin, "Methods for analyzing anisotropic flow in relativistic nuclear collisions," Phys. Rev. C **58** (1998) 1671 doi:10.1103/PhysRevC.58.1671 [nucl-ex/9805001].

[118] P. Danielewicz and G. Odyniec, "Transverse Momentum Analysis of Collective Motion in Relativistic Nuclear Collisions," Phys. Lett. **157B** (1985) 146. doi:10.1016/0370-2693(85)91535-7

[119] S. A. Voloshin, A. M. Poskanzer and R. Snellings, "Collective phenomena in non-central nuclear collisions," Landolt-Bornstein **23** (2010) 293 doi:10.1007/978-3-642-01539-7_10 [arXiv:0809.2949 [nucl-ex]].

[120] A. Bilandzic, R. Snellings and S. Voloshin, "Flow analysis with cumulants: Direct calculations," Phys. Rev. C **83** (2011) 044913 doi:10.1103/PhysRevC.83.044913 [arXiv:1010.0233 [nucl-ex]].

[121] C. Adler *et al.* [STAR Collaboration], "Elliptic flow from two and four particle correlations in Au+Au collisions at s(NN)**(1/2) = 130-GeV," Phys. Rev. C **66** (2002) 034904 doi:10.1103/PhysRevC.66.034904 [nucl-ex/0206001].

[122] A. Bilandzic, C. H. Christensen, K. Gulbrandsen, A. Hansen and Y. Zhou, "Generic framework for anisotropic flow analyses with multiparticle azimuthal correlations," Phys. Rev. C **89** (2014) no.6, 064904 doi:10.1103/PhysRevC.89.064904 [arXiv:1312.3572 [nucl-ex]].

[123] J. Y. Ollitrault, A. M. Poskanzer and S. A. Voloshin, "Effect of flow fluctuations and nonflow on elliptic flow methods," Phys. Rev. C **80** (2009) 014904 doi:10.1103/PhysRevC.80.014904 [arXiv:0904.2315 [nucl-ex]].

[124] N. Borghini, P. M. Dinh and J. Y. Ollitrault, "A New method for measuring azimuthal distributions in nucleus-nucleus collisions," Phys. Rev. C **63** (2001) 054906 doi:10.1103/PhysRevC.63.054906 [nucl-th/0007063].

[125] M. Luzum and J. Y. Ollitrault, "Eliminating experimental bias in anisotropic-flow measurements of high-energy nuclear collisions," Phys. Rev. C **87** (2013) no.4, 044907 doi:10.1103/PhysRevC.87.044907 [arXiv:1209.2323 [nucl-ex]].

[126] M. Gyulassy and X. N. Wang, "HIJING 1.0: A Monte Carlo program for parton and particle production in high-energy hadronic and nuclear collisions," Comput. Phys. Commun. **83** (1994) 307 doi:10.1016/0010-4655(94)90057-4 [nucl-th/9502021].

[127] B. Andersson, G. Gustafson, G. Ingelman and T. Sjostrand, "Parton Fragmentation and String Dynamics," Phys. Rept. **97** (1983) 31. doi:10.1016/0370-1573(83)90080-7

[128] R. Brun, F. Bruyant, F. Carminati, S. Giani, M. Maire, A. McPherson, G. Patrick and L. Urban, "GEANT Detector Description and Simulation Tool," doi:10.17181/CERN.MUHF.DMJ1

[129] R. Barlow, "Systematic errors: Facts and fictions," [arXiv:hep-ex/0207026].

[130] J. Noronha-Hostler, M. Luzum and J. Y. Ollitrault, "Hydrodynamic predictions for 5.02 TeV Pb-Pb collisions," Phys. Rev. C **93** (2016) no.3, 034912 doi:10.1103/PhysRevC.93.034912 [arXiv:1511.06289 [nucl-th]].

[131] H. Niemi, K. J. Eskola, R. Paatelainen and K. Tuominen, "Predictions for 5.023 TeV Pb + Pb collisions at the CERN Large Hadron Collider," Phys. Rev. C **93** (2016) no.1, 014912 doi:10.1103/PhysRevC.93.014912 [arXiv:1511.04296 [hep-ph]].

[132] S. McDonald, C. Shen, F. Fillion-Gourdeau, S. Jeon and C. Gale, "Hydrodynamic predictions for Pb+Pb collisions at 5.02 TeV," Phys. Rev. C **95** (2017) no.6, 064913 doi:10.1103/PhysRevC.95.064913 [arXiv:1609.02958 [hep-ph]].

[133] W. Zhao, H. j. Xu and H. Song, "Collective flow in 2.76 A TeV and 5.02 A TeV Pb+Pb collisions," Eur. Phys. J. C **77** (2017) no.9, 645 doi:10.1140/epjc/s10052-017-5186-x [arXiv:1703.10792 [nucl-th]].

[134] K. Aamodt *et al.* [ALICE Collaboration], Phys. Rev. Lett. **105** (2010) 252302 doi:10.1103/PhysRevLett.105.252302 [arXiv:1011.3914 [nucl-ex]].

[135] B. I. Abelev *et al.* [STAR Collaboration], "Centrality dependence of charged hadron and strange hadron elliptic flow from s(NN)**(1/2) = 200-GeV Au + Au collisions," Phys. Rev. C **77** (2008) 054901 doi:10.1103/PhysRevC.77.054901 [arXiv:0801.3466 [nucl-ex]].

[136] C. Shen, U. Heinz, P. Huovinen and H. Song, "Radial and elliptic flow in Pb+Pb collisions at the Large Hadron Collider from viscous hydrodynamic," Phys. Rev. C **84** (2011) 044903 doi:10.1103/PhysRevC.84.044903 [arXiv:1105.3226 [nucl-th]].

[137] H. Niemi, K. J. Eskola and R. Paatelainen, "Event-by-event fluctuations in a perturbative QCD + saturation + hydrodynamics model: Determining QCD matter shear viscosity in ultrarelativistic heavy-ion collisions," Phys. Rev. C **93** (2016) no.2, 024907 doi:10.1103/PhysRevC.93.024907 [arXiv:1505.02677 [hep-ph]].

[138] J.Y. Ollitrault, "Impact parameter dependence of transverse momentum in nucleus-nucleus collisions," Phys. Lett. B **273** (1991) 1 https://doi.org/10.1016/0370-2693(91)90548-5.

[139] J. S. Moreland, J. E. Bernhard and S. A. Bass, "Alternative ansatz to wounded nucleon and binary collision scaling in high-energy nuclear collisions," Phys. Rev. C **92** (2015) no.1, 011901 doi:10.1103/PhysRevC.92.011901 [arXiv:1412.4708 [nucl-th]].

[140] H.-J. Drescher and Y. Nara, "Effects of fluctuations on the initial eccentricity from the Color Glass Condensate in heavy ion collisions," Phys. Rev. C **75** (2007) 034905 doi:10.1103/PhysRevC.75.034905 [nucl-th/0611017].

[141] J. L. ALbacete and A. Dumitru, "A model for gluon production in heavy-ion collisions at the LHC with rcBK unintegrated gluon densities," arXiv:1011.5161 [hep-ph].

[142] J. Adam *et al.* [ALICE Collaboration], "Anisotropic flow of charged particles in Pb-Pb collisions at $\sqrt{s_{\rm NN}} = 5.02$ TeV," Phys. Rev. Lett. **116** (2016) no.13, 132302 doi:10.1103/PhysRevLett.116.132302 [arXiv:1602.01119 [nucl-ex]].

[143] K. H. Ackermann *et al.* [STAR Collaboration], "Elliptic flow in Au + Au collisions at (S(NN))**(1/2) = 130 GeV," Phys. Rev. Lett. **86** (2001) 402 doi:10.1103/PhysRevLett.86.402 [nucl-ex/0009011].

[144] N. Borghini and J. Y. Ollitrault, "Momentum spectra, anisotropic flow, and ideal fluids," Phys. Lett. B **642** (2006) 227 doi:10.1016/j.physletb.2006.09.062 [nucl-th/0506045].

[145] B. H. Alver, C. Gombeaud, M. Luzum and J. Y. Ollitrault, "Triangular flow in hydrodynamics and transport theory," Phys. Rev. C **82** (2010) 034913 doi:10.1103/PhysRevC.82.034913 [arXiv:1007.5469 [nucl-th]].

[146] D. Teaney, "The Effects of viscosity on spectra, elliptic flow, and HBT radii," Phys. Rev. C **68** (2003) 034913 doi:10.1103/PhysRevC.68.034913 [nucl-th/0301099].

[147] Z. Qiu and U. W. Heinz, "Event-by-event shape and flow fluctuations of relativistic heavy-ion collision fireballs," Phys. Rev. C **84** (2011) 024911 doi:10.1103/PhysRevC.84.024911 [arXiv:1104.0650 [nucl-th]].

[148] F. G. Gardim, F. Grassi, M. Luzum and J. Y. Ollitrault, "Mapping the hydrodynamic response to the initial geometry in heavy-ion collisions," Phys. Rev. C **85** (2012) 024908 doi:10.1103/PhysRevC.85.024908 [arXiv:1111.6538 [nucl-th]].

[149] C. Andrés, M. Braun and C. Pajares, "Energy loss as the origin of a universal scaling law of the elliptic flow," Eur. Phys. J. A **53** (2017) no.3, 41 doi:10.1140/epja/i2017-12226-5 [arXiv:1609.03927 [hep-ph]].

[150] F. G. Gardim, F. Grassi, M. Luzum and J. Y. Ollitrault, "Breaking of factorization of two-particle correlations in hydrodynamics," Phys. Rev. C **87** (2013) no.3, 031901 doi:10.1103/PhysRevC.87.031901 [arXiv:1211.0989 [nucl-th]].

[151] Z. W. Lin, C. M. Ko, B. A. Li, B. Zhang and S. Pal, "A Multi-phase transport model for relativistic heavy ion collisions," Phys. Rev. C **72** (2005) 064901 doi:10.1103/PhysRevC.72.064901 [nucl-th/0411110].

[152] S. A. Bass *et al.*, "Microscopic models for ultrarelativistic heavy ion collisions," Prog. Part. Nucl. Phys. **41** (1998) 255 [Prog. Part. Nucl. Phys. **41** (1998) 225] doi:10.1016/S0146-6410(98)00058-1 [nucl-th/9803035].

[153] B. Betz, M. Gyulassy, M. Luzum, J. Noronha, J. Noronha-Hostler, I. Portillo and C. Ratti, "Cumulants and nonlinear response of high p_T harmonic flow at $\sqrt{s_{NN}} = 5.02$ TeV," Phys. Rev. C **95** (2017) no.4, 044901 doi:10.1103/PhysRevC.95.044901 [arXiv:1609.05171 [nucl-th]].

[154] J. Noronha-Hostler, G. S. Denicol, J. Noronha, R. P. G. Andrade and F. Grassi, "Bulk Viscosity Effects in Event-by-Event Relativistic Hydrodynamics," Phys. Rev. C **88** (2013) no.4, 044916 doi:10.1103/PhysRevC.88.044916 [arXiv:1305.1981 [nucl-th]].

[155] B. Betz, M. Gyulassy and G. Torrieri, "Fourier Harmonics of High-pT Particles Probing the Fluctuating Intitial Condition Geometries in Heavy-Ion Collisions," Phys. Rev. C **84** (2011) 024913 doi:10.1103/PhysRevC.84.024913 [arXiv:1102.5416 [nucl-th]].

[156] R. J. Fries, V. Greco and P. Sorensen, "Coalescence Models For Hadron Formation From Quark Gluon Plasma," Ann. Rev. Nucl. Part. Sci. **58** (2008) 177 doi:10.1146/annurev.nucl.58.110707.171134 [arXiv:0807.4939 [nucl-th]].

[157] G. Aad *et al.* [ATLAS Collaboration], "Measurement of the distributions of event-by-event flow harmonics in lead-lead collisions at = 2.76 TeV with the ATLAS detector at the LHC," JHEP **1311** (2013) 183 doi:10.1007/JHEP11(2013)183 [arXiv:1305.2942 [hep-ex]].

[158] J. Adam *et al.* [ALICE Collaboration], "Event shape engineering for inclusive spectra and elliptic flow in Pb-Pb collisions at $\sqrt{s_{\rm NN}}$ TeV," Phys. Rev. C **93** (2016) no.3, 034916 doi:10.1103/PhysRevC.93.034916 [arXiv:1507.06194 [nucl-ex]].

[159] J. Schukraft, A. Timmins and S. A. Voloshin, "Ultra-relativistic nuclear collisions: event shape engineering," Phys. Lett. B **719** (2013) 394 doi:10.1016/j.physletb.2013.01.045 [arXiv:1208.4563 [nucl-ex]].

[160] B. Abelev *et al.* [ALICE Collaboration], "Anisotropic flow of charged hadrons, pions and (anti-)protons measured at high transverse momentum in Pb-Pb collisions at $\sqrt{s_{NN}}$=2.76 TeV," Phys. Lett. B **719** (2013) 18 doi:10.1016/j.physletb.2012.12.066 [arXiv:1205.5761 [nucl-ex]].

[161] J. Adams *et al.* [STAR Collaboration], "Azimuthal anisotropy at RHIC: The First and fourth harmonics," Phys. Rev. Lett. **92** (2004) 062301 doi:10.1103/PhysRevLett.92.062301 [nucl-ex/0310029].

[162] A. Adare *et al.* [PHENIX Collaboration], "Elliptic and hexadecapole flow of charged hadrons in Au+Au collisions at $\sqrt{s_{NN}}$ = 200 GeV," Phys. Rev. Lett. **105** (2010) 062301 doi:10.1103/PhysRevLett.105.062301 [arXiv:1003.5586 [nucl-ex]].

[163] G. Aad *et al.* [ATLAS Collaboration], "Measurement of the azimuthal anisotropy for charged particle production in $\sqrt{s_{NN}}$ = 2.76 TeV lead-lead collisions with the ATLAS detector," Phys. Rev. C **86** (2012) 014907. doi:10.1103/PhysRevC.86.014907 [arXiv:1203.3087 [hep-ex]].

[164] C. Gombeaud and J. Y. Ollitrault, "Effects of flow fluctuations and partial thermalization on v(4)," Phys. Rev. C **81** (2010) 014901 doi:10.1103/PhysRevC.81.014901 [arXiv:0907.4664 [nucl-th]].

[165] P. F. Kolb, L. W. Chen, V. Greco and C. M. Ko, "Momentum anisotropies in the quark coalescence model," Phys. Rev. C **69** (2004) 051901 doi:10.1103/PhysRevC.69.051901 [nucl-th/0402049].

[166] P. Liu and R. A. Lacey, "Acoustic scaling of linear and mode-coupled anisotropic flow; implications for precision extraction of the specific shear viscosity," arXiv:1802.06595 [nucl-ex].

[167] R. A. Lacey, A. Taranenko, N. N. Ajitanand and J. M. Alexander, "Scaling of the higher-order flow harmonics: implications for initial-eccentricity models and the 'viscous horizon'," arXiv:1105.3782 [nucl-ex].

[168] B. Abelev *et al.* [ALICE Collaboration], Phys. Lett. B **720** (2013) 52 doi:10.1016/j.physletb.2013.01.051 [arXiv:1208.2711 [hep-ex]].

[169] J. Gronefeld [ALICE Collaboration], PoS LHCP **2016** (2016) 126 [arXiv:1609.07334 [nucl-ex]].

[170] J. Auvinen, I. Karpenko, J. E. Bernhard and S. A. Bass, "Revealing the collision energy dependence of η/s in RHIC-BES Au+Au collisions using Bayesian statistics," Nucl. Phys. A **967** (2017) 784 doi:10.1016/j.nuclphysa.2017.05.107 [arXiv:1704.04643 [nucl-th]].

[171] F. Retiere and M. A. Lisa, "Observable implications of geometrical and dynamical aspects of freeze out in heavy ion collisions," Phys. Rev. C **70** (2004) 044907 doi:10.1103/PhysRevC.70.044907 [nucl-th/0312024].

[172] B. B. Abelev *et al.* [ALICE Collaboration], "Production of charged pions, kaons and protons at large transverse momenta in pp and Pb–Pb collisions at $\sqrt{s_{\rm NN}}$ =2.76 TeV," Phys. Lett. B **736** (2014) 196 doi:10.1016/j.physletb.2014.07.011 [arXiv:1401.1250 [nucl-ex]].

[173] B. B. Abelev *et al.* [ALICE Collaboration], "Elliptic flow of identified hadrons in Pb-Pb collisions at $\sqrt{s_{\rm NN}}$ = 2.76 TeV," JHEP **1506** (2015) 190 doi:10.1007/JHEP06(2015)190 [arXiv:1405.4632 [nucl-ex]].

[174] M. Miller and R. Snellings, "Eccentricity fluctuations and its possible effect on elliptic flow measurements," nucl-ex/0312008.

[175] G. Agakishiev *et al.* [STAR Collaboration], "Energy and system-size dependence of two- and four-particle v_2 measurements in heavy-ion collisions at RHIC and their implications on flow fluctuations and nonflow," Phys. Rev. C **86** (2012) 014904 doi:10.1103/PhysRevC.86.014904 [arXiv:1111.5637 [nucl-ex]].

[176] B. Alver *et al.* [PHOBOS Collaboration], "Non-flow correlations and elliptic flow fluctuations in gold-gold collisions at $\sqrt{s_{NN}}$ = 200 GeV," Phys. Rev. C **81** (2010) 034915 doi:10.1103/PhysRevC.81.034915 [arXiv:1002.0534 [nucl-ex]].

[177] B. Alver *et al.* [PHOBOS Collaboration], "Event-by-Event Fluctuations of Azimuthal Particle Anisotropy in Au + Au Collisions at $\sqrt{s_{NN}}$ = 200 GeV," Phys. Rev. Lett. **104** (2010) 142301 doi:10.1103/PhysRevLett.104.142301 [nucl-ex/0702036].

[178] S. A. Voloshin, A. M. Poskanzer, A. Tang and G. Wang, "Elliptic flow in the Gaussian model of eccentricity fluctuations," Phys. Lett. B **659** (2008) 537 doi:10.1016/j.physletb.2007.11.043 [arXiv:0708.0800 [nucl-th]].

[179] L. Yan and J. Y. Ollitrault, "Universal fluctuation-driven eccentricities in proton-proton, proton-nucleus and nucleus-nucleus collisions," Phys. Rev. Lett. **112** (2014) 082301 doi:10.1103/PhysRevLett.112.082301 [arXiv:1312.6555 [nucl-th]].

[180] L. Yan, J. Y. Ollitrault and A. M. Poskanzer, "Eccentricity distributions in nucleus-nucleus collisions," Phys. Rev. C **90** (2014) no.2, 024903 doi:10.1103/PhysRevC.90.024903 [arXiv:1405.6595 [nucl-th]].

[181] H. Grönqvist, J. P. Blaizot and J. Y. Ollitrault, "Non-Gaussian eccentricity fluctuations," Phys. Rev. C **94** (2016) no.3, 034905 doi:10.1103/PhysRevC.94.034905 [arXiv:1604.07230 [nucl-th]].

[182] G. Giacalone, L. Yan, J. Noronha-Hostler and J. Y. Ollitrault, "Skewness of elliptic flow fluctuations," Phys. Rev. C **95** (2017) no.1, 014913 doi:10.1103/PhysRevC.95.014913 [arXiv:1608.01823 [nucl-th]].

[183] G. Aad *et al.* [ATLAS Collaboration], "Measurement of flow harmonics with multiparticle cumulants in Pb+Pb collisions at $\sqrt{s_{\rm NN}} = 2.76$ TeV with the ATLAS detector," Eur. Phys. J. C **74** (2014) no.11, 3157 doi:10.1140/epjc/s10052-014-3157-z [arXiv:1408.4342 [hep-ex]].

[184] L. Yan, J. Y. Ollitrault and A. M. Poskanzer, "Azimuthal Anisotropy Distributions in High-Energy Collisions," Phys. Lett. B **742** (2015) 290 doi:10.1016/j.physletb.2015.01.039 [arXiv:1408.0921 [nucl-th]].

[185] J. Noronha-Hostler, L. Yan, F. G. Gardim and J. Y. Ollitrault, "Linear and cubic response to the initial eccentricity in heavy-ion collisions," Phys. Rev. C **93** (2016) no.1, 014909 doi:10.1103/PhysRevC.93.014909 [arXiv:1511.03896 [nucl-th]].

[186] B. B. Abelev *et al.* [ALICE Collaboration], "Multiparticle azimuthal correlations in p-Pb and Pb-Pb collisions at the CERN Large Hadron Collider," Phys. Rev. C **90** (2014) no.5, 054901 doi:10.1103/PhysRevC.90.054901 [arXiv:1406.2474 [nucl-ex]].

[187] A. M. Sirunyan *et al.* [CMS Collaboration], "Non-Gaussian elliptic-flow fluctuations in PbPb collisions at $\sqrt{s_{\rm NN}} = 5.02$ TeV," [arXiv:1711.05594 [nucl-ex]].

[188] J. Jia, M. Zhou and A. Trzupek, "Revealing long-range multiparticle collectivity in small collision systems via subevent cumulants," Phys. Rev. C **96** (2017) no.3, 034906 doi:10.1103/PhysRevC.96.034906 [arXiv:1701.03830 [nucl-th]].

[189] A. Kolmogorov, "Sulla determinazione empirica di una legge di distribuzione" G. Ist. Ital. Attuari. **4** (1933) 83–91.

[190] N. Smirnov, "Table for estimating the goodness of fit of empirical distributions" Ann. of Math. Stat. **19** (1948) 279–281. doi:10.1214/aoms/1177730256

[191] B. I. Abelev *et al.* [STAR Collaboration], "Azimuthal Charged-Particle Correlations and Possible Local Strong Parity Violation," Phys. Rev. Lett. **103** (2009) 251601 doi:10.1103/PhysRevLett.103.251601 [arXiv:0909.1739 [nucl-ex]].

[192] B. I. Abelev *et al.* [STAR Collaboration], "Observation of charge-dependent azimuthal correlations and possible local strong parity violation in heavy ion collisions," Phys. Rev. C **81** (2010) 054908 doi:10.1103/PhysRevC.81.054908 [arXiv:0909.1717 [nucl-ex]].

[193] L. Adamczyk *et al.* [STAR Collaboration], "Fluctuations of charge separation perpendicular to the event plane and local parity violation in $\sqrt{s_{NN}} = 200$ GeV Au+Au collisions at the BNL Relativistic Heavy Ion Collider," Phys. Rev. C **88** (2013) no.6, 064911 doi:10.1103/PhysRevC.88.064911 [arXiv:1302.3802 [nucl-ex]].

[194] L. Adamczyk *et al.* [STAR Collaboration], "Beam-energy dependence of charge separation along the magnetic field in Au+Au collisions at RHIC," Phys. Rev. Lett. **113** (2014) 052302 doi:10.1103/PhysRevLett.113.052302 [arXiv:1404.1433 [nucl-ex]].

[195] B. Abelev *et al.* [ALICE Collaboration], "Charge separation relative to the reaction plane in Pb-Pb collisions at $\sqrt{s_{NN}} = 2.76$ TeV," Phys. Rev. Lett. **110** (2013) no.1, 012301 doi:10.1103/PhysRevLett.110.012301 [arXiv:1207.0900 [nucl-ex]].

[196] V. Khachatryan *et al.* [CMS Collaboration], "Observation of charge-dependent azimuthal correlations in p-Pb collisions and its implication for the search for the chiral magnetic effect," Phys. Rev. Lett. **118** (2017) no.12, 122301 doi:10.1103/PhysRevLett.118.122301 [arXiv:1610.00263 [nucl-ex]].

[197] R. Belmont and J. L. Nagle, "To CME or not to CME? Implications of p+Pb measurements of the chiral magnetic effect in heavy ion collisions," Phys. Rev. C **96** (2017) no.2, 024901 doi:10.1103/PhysRevC.96.024901 [arXiv:1610.07964 [nucl-th]].

[198] D. Kharzeev, Z. Tu, A. Zhang and W. Li, "Effect of the fluctuating proton size on the study of the chiral magnetic effect in proton-nucleus collisions," Phys. Rev. C **97** (2018) no.2, 024905 doi:10.1103/PhysRevC.97.024905 [arXiv:1712.02486 [nucl-th]].

[199] J. Adams *et al.* [STAR Collaboration], "Narrowing of the balance function with centrality in au + au collisions at (S(NN))**1/2 = 130-GeV," Phys. Rev. Lett. **90** (2003) 172301 doi:10.1103/PhysRevLett.90.172301 [nucl-ex/0301014].

[200] M. M. Aggarwal *et al.* [STAR Collaboration], "Balance Functions from Au+Au, d+Au, and $p+p$ Collisions at $\sqrt{s_{NN}} = 200$ GeV," Phys. Rev. C **82** (2010) 024905 doi:10.1103/PhysRevC.82.024905 [arXiv:1005.2307 [nucl-ex]].

[201] B. Abelev *et al.* [ALICE Collaboration], "Charge correlations using the balance function in Pb-Pb collisions at $\sqrt{s_{NN}} = 2.76$ TeV," Phys. Lett. B **723** (2013) 267 doi:10.1016/j.physletb.2013.05.039 [arXiv:1301.3756 [nucl-ex]].

[202] J. Adam *et al.* [ALICE Collaboration], "Multiplicity and transverse momentum evolution of charge-dependent correlations in pp, p–Pb, and Pb–Pb collisions at

the LHC," Eur. Phys. J. C **76** (2016) no.2, 86 doi:10.1140/epjc/s10052-016-3915-1 [arXiv:1509.07255 [nucl-ex]].

[203] G. Aad *et al.* [ATLAS Collaboration], "Measurement of the correlation between flow harmonics of different order in lead-lead collisions at $\sqrt{s_{\rm NN}}$=2.76 TeV with the ATLAS detector," Phys. Rev. C **92** (2015) no.3, 034903 doi:10.1103/PhysRevC.92.034903 [arXiv:1504.01289 [hep-ex]].

[204] S. Acharya *et al.* [ALICE Collaboration], "Constraining the magnitude of the Chiral Magnetic Effect with Event Shape Engineering in Pb-Pb collisions at $\sqrt{s_{\rm NN}}$ = 2.76 TeV," Phys. Lett. B **777** (2018) 151 doi:10.1016/j.physletb.2017.12.021 [arXiv:1709.04723 [nucl-ex]].

[205] Z. Wu, "Blast-Wave Model Fit for Identified Particle Spectra and Elliptic Flow," Master Thesis (2015), Utrecht University.

[206] A. M. Sirunyan *et al.* [CMS Collaboration], "Constraints on the chiral magnetic effect using charge-dependent azimuthal correlations in pPb and PbPb collisions at the LHC," arXiv:1708.01602 [nucl-ex].

[207] H. De Vries, C.W. De Jager and C. De Vries, Atomic Data and Nuclear Data Tables **36** 495-536 (1987).

[208] S. Abrahamyan *et al.*, "Measurement of the Neutron Radius of 208Pb Through Parity-Violation in Electron Scattering," Phys. Rev. Lett. **108** (2012) 112502 doi:10.1103/PhysRevLett.108.112502 [arXiv:1201.2568 [nucl-ex]].

[209] W. T. Deng and X. G. Huang, "Event-by-event generation of electromagnetic fields in heavy-ion collisions," Phys. Rev. C **85** (2012) 044907 doi:10.1103/PhysRevC.85.044907 [arXiv:1201.5108 [nucl-th]].

[210] L. McLerran and V. Skokov, "Comments About the Electromagnetic Field in Heavy-Ion Collisions," Nucl. Phys. A **929** (2014) 184 doi:10.1016/j.nuclphysa.2014.05.008 [arXiv:1305.0774 [hep-ph]].

[211] U. Gursoy, D. Kharzeev and K. Rajagopal, "Magnetohydrodynamics, charged currents and directed flow in heavy ion collisions," Phys. Rev. C **89** (2014) no.5, 054905 doi:10.1103/PhysRevC.89.054905 [arXiv:1401.3805 [hep-ph]].

[212] G. J. Feldman and R. D. Cousins, "A Unified approach to the classical statistical analysis of small signals," Phys. Rev. D **57** (1998) 3873 doi:10.1103/PhysRevD.57.3873 [physics/9711021 [physics.data-an]].

[213] S. Singha, P. Shanmuganathan and D. Keane, "The first moment of azimuthal anisotropy in nuclear collisions from AGS to LHC energies," Adv. High Energy Phys. **2016** (2016) 2836989 doi:10.1155/2016/2836989 [arXiv:1610.00646 [nucl-ex]].

[214] R. J. M. Snellings, H. Sorge, S. A. Voloshin, F. Q. Wang and N. Xu, "Novel rapidity dependence of directed flow in high-energy heavy ion collisions," Phys. Rev. Lett. **84** (2000) 2803 doi:10.1103/PhysRevLett.84.2803 [nucl-ex/9908001].

[215] P. Bozek and I. Wyskiel, "Directed flow in ultrarelativistic heavy-ion collisions," Phys. Rev. C **81** (2010) 054902 doi:10.1103/PhysRevC.81.054902 [arXiv:1002.4999 [nucl-th]].

[216] B. B. Back *et al.* [PHOBOS Collaboration], "Energy dependence of directed flow over a wide range of pseudorapidity in Au + Au collisions at RHIC," Phys. Rev. Lett. **97** (2006) 012301 doi:10.1103/PhysRevLett.97.012301 [nucl-ex/0511045].

[217] B. I. Abelev *et al.* [STAR Collaboration], "System-size independence of directed flow at the Relativistic Heavy-Ion Collider," Phys. Rev. Lett. **101** (2008) 252301 doi:10.1103/PhysRevLett.101.252301 [arXiv:0807.1518 [nucl-ex]].

[218] B. Abelev *et al.* [ALICE Collaboration], "Directed Flow of Charged Particles at Midrapidity Relative to the Spectator Plane in Pb-Pb Collisions at $\sqrt{s_{NN}}$=2.76 TeV," Phys. Rev. Lett. **111** (2013) no.23, 232302 doi:10.1103/PhysRevLett.111.232302 [arXiv:1306.4145 [nucl-ex]].

[219] J. Bleibel, G. Burau and C. Fuchs, "Anisotropic flow in Pb+Pb collisions at LHC from the quark gluon string model with parton rearrangement," Phys. Lett. B **659** (2008) 520 doi:10.1016/j.physletb.2007.11.042 [arXiv:0711.3366 [nucl-th]].

[220] L. P. Csernai, V. K. Magas, H. Stocker and D. D. Strottman, "Fluid Dynamical Prediction of Changed v1-flow at LHC," Phys. Rev. C **84** (2011) 024914 doi:10.1103/PhysRevC.84.024914 [arXiv:1101.3451 [nucl-th]].

[221] M. Luzum and J. Y. Ollitrault, "Directed flow at midrapidity in heavy-ion collisions," Phys. Rev. Lett. **106** (2011) 102301 doi:10.1103/PhysRevLett.106.102301 [arXiv:1011.6361 [nucl-ex]].

[222] E. Retinskaya, M. Luzum and J. Y. Ollitrault, "Directed flow at midrapidity in $\sqrt{s_{NN}}$ = 2.76 TeV Pb+Pb collisions," Phys. Rev. Lett. **108** (2012) 252302 doi:10.1103/PhysRevLett.108.252302 [arXiv:1203.0931 [nucl-th]].

[223] L. Adamczyk *et al.* [STAR Collaboration], "Directed Flow of Identified Particles in Au + Au Collisions at $\sqrt{s_N N}$ = 200 GeV at RHIC," Phys. Rev. Lett. **108** (2012) 202301 doi:10.1103/PhysRevLett.108.202301 [arXiv:1112.3930 [nucl-ex]].

[224] The ATLAS collaboration [ATLAS Collaboration], "Measurement of four-particle azimuthal cumulants in Pb+Pb collisions at $\sqrt{s_{NN}}$ = 5.02 TeV with the ATLAS detector," ATLAS-CONF-2017-066.

[225] A. Adare *et al.* [PHENIX Collaboration], "Measurements of directed, elliptic, and triangular flow in Cu+Au collisions at $\sqrt{s_{NN}}$ = 200 GeV," Phys. Rev. C **94** (2016) no.5, 054910 doi:10.1103/PhysRevC.94.054910 [arXiv:1509.07784 [nucl-ex]].

[226] T. Niida [STAR Collaboration], "Charge-dependent anisotropic flow in Cu + Au collisions," Nucl. Phys. A **956** (2016) 541 doi:10.1016/j.nuclphysa.2016.03.024 [arXiv:1601.01017 [nucl-ex]].

[227] S. A. Voloshin and T. Niida, "Ultrarelativistic nuclear collisions: Direction of spectator flow," Phys. Rev. C **94** (2016) no.2, 021901 doi:10.1103/PhysRevC.94.021901 [arXiv:1604.04597 [nucl-th]].

[228] L. P. Csernai, G. Eyyubova and V. K. Magas, "New method for measuring longitudinal fuctuations and directed flow in ultrarelativistic heavy ion reactions," Phys. Rev. C **86** (2012) 024912 Erratum: [Phys. Rev. C **88** (2013) 019902] doi:10.1103/PhysRevC.88.019902, 10.1103/PhysRevC.86.024912 [arXiv:1204.5885 [hep-ph]].

[229] K. Aamodt *et al.* [ALICE Collaboration], "Harmonic decomposition of two-particle angular correlations in Pb-Pb collisions at $\sqrt{s_{NN}} = 2.76$ TeV," Phys. Lett. B **708** (2012) 249 doi:10.1016/j.physletb.2012.01.060 [arXiv:1109.2501 [nucl-ex]].

[230] L. Adamczyk *et al.* [STAR Collaboration], "Beam-Energy Dependence of the Directed Flow of Protons, Antiprotons, and Pions in Au+Au Collisions," Phys. Rev. Lett. **112** (2014) no.16, 162301 doi:10.1103/PhysRevLett.112.162301(2014), 10.1103/PhysRevLett.112.162301 [arXiv:1401.3043 [nucl-ex]].

[231] E.J. Marcus, "Magnetohydrodynamics at Heavy Ion Collisions," Bachelor Thesis (2015), Utrecht University.

[232] B. Abelev *et al.* [ALICE Collaboration], "Upgrade of the ALICE Experiment: Letter Of Intent," J. Phys. G **41** (2014) 087001. doi:10.1088/0954-3899/41/8/087001

[233] S. K. Das, S. Plumari, S. Chatterjee, J. Alam, F. Scardina and V. Greco, "Directed Flow of Charm Quarks as a Witness of the Initial Strong Magnetic Field in Ultra-Relativistic Heavy Ion Collisions," Phys. Lett. B **768** (2017) 260 doi:10.1016/j.physletb.2017.02.046 [arXiv:1608.02231 [nucl-th]].

[234] B. Abelev *et al.* [ALICE Collaboration], "Technical Design Report for the Upgrade of the ALICE Inner Tracking System," J. Phys. G **41** (2014) 087002. doi:10.1088/0954-3899/41/8/087002

[235] S. Acharya *et al.* [ALICE Collaboration], "D-meson azimuthal anisotropy in mid-central Pb-Pb collisions at $\sqrt{\mathbf{s}_{\mathrm{NN}}} = \mathbf{5.02}$ TeV," Phys. Rev. Lett. **120** (2018) no.10, 102301 doi:10.1103/PhysRevLett.120.102301 [arXiv:1707.01005 [nucl-ex]].

[236] B. B. Abelev *et al.* [ALICE Collaboration], "Multiplicity dependence of the average transverse momentum in pp, p-Pb, and Pb-Pb collisions at the LHC," Phys. Lett. B **727** (2013) 371 doi:10.1016/j.physletb.2013.10.054 [arXiv:1307.1094 [nucl-ex]].

[237] R. Kubo, "Generalized Cumulant Expansion Method," J. of the Phys. Soc. of Japan, Vol. 17, No. 7 (1962) doi:10.1143/JPSJ.17.1100.

[238] Wolfram Research, Inc., "Mathematica, Version 9," Champaign, IL, 2018.

[239] A. Bilandzic, "Anisotropic flow measurements in ALICE at the large hadron collider," CERN-THESIS-2012-018.

[240] S. Acharya *et al.* [ALICE Collaboration], "Energy dependence and fluctuations of anisotropic flow in Pb-Pb collisions at $\sqrt{s_{\rm NN}}$ = **5.02** and **2.76** TeV," arXiv:1804.02944 [nucl-ex].

[241] P. Di Francesco, M. Guilbaud, M. Luzum and J. Y. Ollitrault, "Systematic procedure for analyzing cumulants at any order," Phys. Rev. C **95** (2017) no.4, 044911 doi:10.1103/PhysRevC.95.044911 [arXiv:1612.05634 [nucl-th]].

[242] J. Margutti [ALICE Collaboration], "The search for magnetic-induced charged currents in Pb–Pb collisions with ALICE," arXiv:1709.05618 [nucl-ex].

[243] R. C. Larson, N. Ghaffarzadegan and Y. Xue, "Too Many PhD Graduates or Too Few Academic Job Openings: The Basic Reproductive Number R0 in Academia," Syst. Res. **31** (2014) 745–750 doi:10.1002/sres.2210

[244] European Science Foundation, "Career Tracking of Doctorate Holders," (2015) archives.esf.org/uploads/media/Career_Tracking_01.pdf

[245] M. A. Edwards and S. Roy, "Academic Research in the 21st Century: Maintaining Scientific Integrity in a Climate of Perverse Incentives and Hypercompetition," Env. Eng. Sci. **34** (2017) 51-61 10.1089/ees.2016.0223

[246] D. R. Grimes, C. Bauch and J. P. A. Ioannidis, "Modelling science trustworthiness under publish or perish pressure," The Royal Society **5** (2018) 10.1098/rsos.171511

[247] J. J. Baumberg, "The Secret Life of Science: How It Really Works and Why It Matters" Princeton University Press (2018)

[248] C. Woolston, "Graduate survey: A love–hurt relationship," Nature **550** (2017) 549-552 doi:10.1038/nj7677-549a

[249] UC Berkeley Graduate Assembly, "Graduate Student Happiness and Well-being Report," (2014) http://ga.berkeley.edu/wellbeingreport/

[250] E. Smith, Z. Brooks, "Graduate Student Mental Health," University of Arizona (2015)

[251] T. M. Evans, L. Bira, J. B. Gastelum, L. T. Weiss and N. L. Vanderford, "Evidence for a mental health crisis in graduate education," Nature Biotechnology **36** (2018) 282–284 doi:10.1038/nbt.4089

Summary

In this dissertation, we present a set of measurements of anisotropic flow in heavy-ion collisions, aimed at investigating the properties of hot and dense QCD matter. We analyse data collected by the ALICE experiment at the LHC between 2010 and 2015, colliding lead ions (^{208}Pb) at a center-of-mass energy per nucleon of a few TeV.

Anisotropic flow quantifies the degree of anisotropy in the azimuthal distribution of momenta of particles produced in the collision and provides information on collective dynamics of the system. In particular, we study how anisotropic flow, on average, depends on the collision energy of the ions, on how much they overlap, and on particle kinematic variables (e.g. velocity). We then analyse how anisotropic flow, in particular elliptic flow, changes between different collisions, which is mostly determined by the variations in the shape of the QCD system. We found all aforementioned results to be essentially compatible with expectations, thus confirming our current understanding of heavy-ion collisions. These results also constitute a large and comprehensive data set that will hopefully help to constrain even further a few important parameters in theoretical models, such as the specific shear viscosity and its temperature dependence.

We then study the strong magnetic fields created in such collisions, which could provide information on so far unexplored features of QCD and on the electromagnetic response of the system. More precisely, we search for evidence of the Chiral Magnetic Effect, measuring again azimuthal distribution of particle momenta. We use simulations to understand the expected correlation between these magnetic fields and the shape of the QCD system. This helps us to decouple the contributions to anisotropic flow coming from magnetic fields and from other phenomena, unrelated to such fields. We conclude that no significant contribution of the Chiral Magnetic Effect is present in the azimuthal distribution of particle momenta and we quantify this statement with an upper limit. We also investigate another possible effect of the magnetic field, namely a difference in directed flow according to particle electric charge. Again, we find no significant evidence of such phenomenon, although results are suggestive; future work will provide a definitive answer.

Finally, we conclude exploring the prospects for future measurements of anisotropic flow with the ALICE experiment. We also present the results of two exploratory studies and discuss their potential and limitations.

The work presented in this dissertation can be found in [142, 240, 204, 242].

Samenvatting in het Nederlands

In deze dissertatie presenteren we een reeks metingen van de anisotrope flow in zware ionenbotsingen, gericht op het onderzoeken van de eigenschappen van hete en dichte QCD-materie. We analyseren gegevens die zijn verzameld door het ALICE-experiment in de LHC tussen 2010 en 2015, waarbij loodionen (^{208}Pb) botsten bij een centrum-van-massa-energie per nucleon van een paar TeV.

De anisotrope flow kwantificeert de mate van anisotropie in de azimutale verdeling van de momenta van de deeltjes geproduceerd in de botsing en verschaft informatie over de collectieve dynamica van het systeem. We bestuderen in het bijzonder hoe de anisotrope flow gemiddeld afhangt van de botsings energie van de ionen, van de mate waarin ze elkaar overlappen, en van kinematische variabelen (e.g. snelheid). Vervolgens analyseren we hoe de anisotrope flow, in het bijzonder elliptische flow, tussen verschillende botsingen verandert, dit wordt meestal bepaald door de variaties in de vorm van het QCD-systeem. We observeren dat alle bovengenoemde resultaten in essentie compatibel zijn met de verwachtingen, waarmee we ons huidige begrip van zware ionenbotsingen bevestigen. Deze resultaten vormen ook een grote en uitgebreide dataset die hopelijk zal helpen om nog enkele belangrijke parameters in theoretische modellen te bepalen.

Vervolgens bestuderen we de sterke magnetische velden die in dergelijke botsingen zijn gecreëerd, die informatie kunnen verschaffen over tot nu toe onontgonnen kenmerken van QCD en over de elektromagnetische respons van het systeem. Om precies te zijn, we zoeken naar bewijzen van het chirale magnetische effect, waarbij opnieuw de azimutale verdeling van deeltjesmomenta wordt gemeten. We gebruiken simulaties om de verwachte correlatie tussen deze magnetische velden en de vorm van het QCD-systeem te begrijpen. Dit helpt ons om de bijdragen aan de anisotrope stroom afkomstig van magnetische velden en andere verschijnselen die geen verband houden met dergelijke velden te ontkoppelen. We concluderen dat er geen significante bijdrage van het chirale magnetische effect aanwezig is in de azimutale verdeling van de deeltjesmomenta en we kwantificeren deze conclusie met een bovengrens. We onderzoeken ook een ander mogelijk effect van het magnetisch veld, namelijk een verschil in gerichte stroom volgens de elektrische lading van het deeltje. We vinden wederom geen significant bewijs van een dergelijk fenomeen, hoewel de resultaten een indicatie geven van het effect; toekomstig werk zal een definitief antwoord geven.

Ten slotte concluderen we met de vooruitzichten voor toekomstige metingen van de anisotrope flow met het ALICE-experiment. We presenteren ook de resultaten van twee verkennende studies en bespreken hun potentieel en beperkingen.

Het werk gepresenteerd in dit proefschrift is te vinden in [142, 240, 204, 242].

Curriculum Vitæ

Profile

Someone who loves to understand how things work and to explain it to people. Currently working as researcher and data scientist at the ALICE experiment at CERN, the largest particle physics laboratory in the world. Looking to apply my skills on interesting projects with positive impact on society.

Experience

- **PhD in Particle Physics**, Utrecht University (NL), 2014-2018
  - Data analysis for the ALICE experiment (1 PB data) via a distributed grid
  - Software development (C++, Python) and maintenance via VCS (Git)
  - Mathematical modelling of stochastic systems (Monte Carlo simulations)
  - Presentation of complex topics to large and diverse audiences
  - Experience in an international collaboration (1.8k members, 42 countries)
  - Accustomed to off-site work and web conferencing

Education

- **Research internship**, Technische Universität München (DE), 2013-2014
  Main topics: particle physics, detector R&D. Resulted in my Master's thesis.
- **Erasmus Programme**, École Polytechnique (FR), 2012-2013
  Main topics: particle physics, plasma physics, optics
- **Master in Physics**, University of Milano-Bicocca (IT), 2011-2014
  Main topics: particle physics, detector technology, programming, statistics
- **Bachelor in Physics**, University of Milano-Bicocca (IT), 2008-2011
  Main topics: mathematics, physics

Languages

- Italian (native proficiency)
- English (full professional proficiency)
- French (full professional proficiency)
- Dutch (intermediate proficiency)

Publications

with ALICE as main contributor

- Energy dependence and fluctuations of anisotropic flow in Pb-Pb collisions at $\sqrt{s_{\rm NN}}$ = 5.02 and 2.76 TeV,
  Accepted for publication on Journal of High Energy Physics,
  arXiv:1804.02944 [nucl-ex]

- Constraining the magnitude of the Chiral Magnetic Effect with Event Shape Engineering in Pb-Pb collisions at $\sqrt{s_{\rm NN}}$ = 2.76 TeV
  Phys. Lett. B **777** (2018) 151,
  doi:10.1016/j.physletb.2017.12.021,
  arXiv:1709.04723 [nucl-ex]

- Anisotropic flow of charged particles in Pb-Pb collisions at $\sqrt{s_{\rm NN}}$ =5.02 TeV
  Phys. Rev. Lett. **116** (2016) no.13, 132302,
  doi:10.1103/PhysRevLett.116.132302,
  arXiv:1602.01119 [nucl-ex]

others

- Charge density as a driving factor of discharge formation in GEM-based detectors
  Nucl. Instrum. Meth. A **870** (2017) 116,
  doi:10.1016/j.nima.2017.07.042,
  arXiv:1704.01329 [physics.ins-det]

Invited talks

- CERN LHC Seminar, Geneve (CH), November 2017
  "The search for QCD sphalerons and the CME in heay-ion collisions with ALICE"

- Secondo incontro sulla fisica con ioni pesanti a LHC, Torino (IT), October 2017
  "Correlations and fluctuations in small systems"

- Data Driven Future by Quantyca, Milano (IT), September 2017
  "Data processing and management at CERN"

- HIC for FAIR Nuclear Physics Colloquium, Frankfurt (DE), February 2017
  "Measuring and interpreting anisotropic flow"

- Nikhef workshop "Theory Meets Experiment - Sphalerons", Amsterdam (NL), October 2016
  "Search for SU(3) sphalerons in ALICE: Chiral Magnetic Effect"

- University of Houston Physics Colloquium, Houston (US), September 2016
  "Anisotropic flow in Pb-Pb collisions at $\sqrt{s_{\rm NN}}$ = 5.02 TeV with ALICE"

Contributed talks

- Quark Matter 2018, Venezia (IT), May 2018
  "Measurements of anisotropic flow and flow fluctuations in Xe-Xe and Pb-Pb collisions with ALICE"

- XII Workshop on Particle Correlations and Femtoscopy, Amsterdam (NL), June 2017
  "The search for magnetic-induced charged currents in Pb-Pb collisions with ALICE"

- 52nd Rencontres de Moriond QCD, La Thuile (IT), March 2017
  "Anisotropic flow of charged and identified particles in Pb-Pb collisions at $\sqrt{s_{\rm NN}} = 5.02$ TeV with ALICE"

- Hot Quarks 2016, South Padre Island (US), September 2016
  "Anisotropic flow in Pb-Pb collisions at $\sqrt{s_{\rm NN}} = 5.02$ TeV with ALICE"

- 38th International Conference on High Energy Physics, Chicago (US), August 2016
  "Anisotropic flow in Pb-Pb collisions at $\sqrt{s_{\rm NN}} = 5.02$ TeV with ALICE"

- 52nd International Winter Meeting on Nuclear Physics, Bormio (IT), January 2014
  "Stability studies on triple-GEM detectors for the ALICE GEM-TPC upgrade"

Acknowledgements

It is impossible to identify precisely all the people who helped me complete my PhD. It is also not clear if an acknowledgement is necessary, as the contribution of some has been entirely unintentional. Given these general considerations, it is better to interpret the following as a collection of reflections on my feelings towards the people that I have met over the years, on the influence that they had on me and on the moments that we shared. Supernatural beings and TV hosts are among them. These acknowledgements do not follow any particular order or structure other than approximate reverse chronology, as I am walking backwards through my memories, along the road that led me here.

I thank my collaborators, who directly contributed to the work presented in this dissertation. Alexandru, you showed me by example what it means to do high-quality work, more than anyone else. I wish you not only the best for your career, but happiness and fulfilment, regardless of the job. Ilya, Anthony, you have been my mentors, even though through a screen. The knowledge I gained, both technical and theoretical, comes mostly from our meetings. I wish you days of wonder and discovery. Raimond, Thomas, Marco, Sergei, Cvetan, Jürgen, thanks for the suggestions and the insightful comments that you gave me throughout the years. To all the people that I just mentioned: I think I did not always show you my appreciation (I can be impatient, opinionated and stubborn), but seeing things in perspective, you were the ones asking the right questions and getting the best results out of my efforts. Thank you.

I thank all my colleagues, old and new, with whom I had a good time: Lodato, Alberto, Redmer, Panos, Paul, Goran, Naghmeh, Rihan, Auro, Bernie, Luuk, Lennart and all the others. Special mention to Mike, Zanoli, Barbara, Cristina and Caffarri: you guys saved me during the last, toughest years of my PhD. You made me feel part of a group, something whose importance I fully realise only now. You also helped me with several technical aspects, so a piece of this thesis belongs to each of you. Thank you guys, also for the friendship that we share outside the bare walls of the office: I hope this will last much longer than my PhD.

I thank all the great people that I met over these years. The list is long and I will only talk about some. Laura, cicci. I pranzi di pasqua da te (e con te) sono fra i momenti piú dolci che ho avuto il privilegio di vivere. Grazie per tutte le risate e la patatositá. Ressa, grazie per avermi accolto con affetto. Brunetti e Patrizi, grazie per avermi insegnato, col vostro esempio, che a volte é giusto mollare e partire, e che é possibile farlo. Vangone, grazie per la felicitá che irradi e per i tanti bei momenti insieme. Ti auguro tutto il meglio per la tua nuova vita a Monaco. Bastiaan, thanks for the dinners, the parties and the chats. Not only are you a wonderful person to have fun with, but you also always shows great sensitivity and intelligence. Whatever the topic was, I always felt enriched by your

well-argued, clear and consistent views. Dell'Anna, grazie per la poesia. Balázs, thank you for the lesson you taught me on that day, walking in Városliget in Budapest. Onur, thanks for being my living encyclopedia about everything remotely related to biology. Thanks Aleksandra, Angela, Benedetta, Marko, Diana, Dora, Lucas, Júlia, Christina, Gaurav, Leandro, Matthieu, Analisa, Dražen, Doron, Luca, Lena, Luis and many others.

I thank the people who first welcomed me in Utrecht. Sandro, you are the reason why I immediately felt at home here. You found me a house, you introduced me to most of the friends I have in town, you always shared a positive attitude, at work and outside. Equally importantly, you and Dubla have been my supervisors when I most needed one, other than great friends. This work owns much to you, thank you guys. Thanks also for the great, blurry nights, occasionally crowned by carbonara at 6:00 a.m.

I thank Tania, my super-paranymph. Not only are you the best flatmate someone can wish for when moving to a new town, but you have also been, since we first met, an infinite source of energy and good mood, in defiance of any physical law. We shared most of the good times I had, from the very beginning to the very end. Moreover, you showed me that all the fun does not have to come at the expense of work, as you have always put sheer determination in whatever goal you were pursuing there. This has been hugely inspirational for my PhD, thank you.

I thank Camilo, my other super-paranymph. For me, you have been a bright example of intellectual acumen and prosocial behaviour: you always offered insightful views and warm shelter with equal generosity. Most importantly, you taught me by example the exercise of freedom, may that always guide you to new adventures. Your zest and enthusiasm were precisely the reason why many moments that we shared have been so amazing. I will always carry a piece of you in me, as you would put it. I wish you to swim forever in the ocean, stark naked, and to leave the armour ashore.

I thank Fonseca, Daniel Filipe Mesquita da Fonseca. I still remember when I met you, that night at Jan Primus. What is remarkable is that I never remember this type of episodes, but somehow for you, I do. If I can look back at these years with contentment and a pinch of *saudade*, it owns a lot to you. Talking to you has enriched me, emotionally and intellectually, like few others things ever did. You have been the best friend I had in Utrecht, a constant reference point for the good and the bad times. Words can do little to express my gratitude. I wish you happiness wherever you will be, whatever you will do.

I thank my partner in crime, Ms. Manzini, for a number of things. Per il coraggio e la determinazione di essere venuta in Olanda ed aver realizzato quello che volevi, il che ci ha permesso di essere felici, insieme. Per tutto il sostegno, specialmente le volte che ho sbroccato: sei stata la fune che mi ha tenuto a bordo, quando solo affrontavo marosi. Per essere sempre stata orgogliosa di me e per averlo saputo trasmettere, negli sguardi ridenti e negli abbracci sicuri. Per saper parlare, anche delle cose piú difficili. Per le coccole. Grazie.

I thank the Italian friends of a lifetime, those I have met at school or in smelly pubs and with which I shared my youth. The list is long, those who are in know it. You were the first to teach me how to enjoy life and laugh about it, even when it is a colossal mess. You taught me how not to take myself too seriously. These turned out to be crucial skills in order to safeguard mental health during a PhD.

I thank Piero Angela, for inspiring me since I was a kid with his TV show *SuperQuark* (fortuitous coincidence?). I thank my math and science teachers, who I haven't always loved, but likely determined, some more than others, me ending up here.

I thank my parents for all their love, their teachings and their hard work. Papá, mamma, questa tesi é anche vostra. Avete lavorato duramente fin da giovani per permettermi di scegliere cosa fare nella vita, un lusso concesso a pochi e sfruttato da ancor meno. Non meno importante é l'avermi insegnato l'affetto, il rispetto e la tolleranza: se valgo qualcosa come persona, é stato per via del vostro esempio. A mio padre, in particolare, grazie per avermi insegnato la lezione piú importante della mia vita: conosci i tuoi limiti.

I thank the unknown factors[3], presumably connected to human evolution, that made our species able to experience the beauty of ideas, which is what primarily fuelled my efforts. I thank my bicycle, Locomotief, that faithfully carried me here through storms and accidents. Finally, I thank the acknowledgements, for giving me the chance to say some things that were ought to be said.

[3]If the reader knows more, please contact me and explain.

Explicit

The quest for scientific knowledge is the most distinctive and the most important human occupation. Whatever material luxury that we enjoy today, it originates more or less directly from a scientific discovery of the past, and we have good reasons to believe that the same will apply to the times to come. Moreover, scientists have the fortune to experience through their work very fulfilling emotions, such as wonder and beauty. Yet, many young scientists (and myself), after being properly trained through a PhD, choose not to continue in this career. Part of the reason, on top of personal considerations, has little to do with Science and a lot with the way our societies organise scientific research.

I want to spend the last lines of my dissertation sharing my thoughts on this topic, in the hope that it would help initiate a debate and, more realistically, be cause for reflection for the fortuitous reader.

Over the last couple of decades, there has been a steep rise in the number of PhD positions offered, largely unmatched by the modest increase in the number of permanent or long-term faculty positions [243, 244]. The steps from graduate school to professorship are thus increasingly harder, given the higher competition, and there is a growing body of evidence that the ways in which we select the winners (number of papers and citations, mostly) make little sense and are, on the long term, harmful to Science [245, 246]. So we face fewer permanent positions (relative to the number of graduate students), which are harder to get, and questionable selection procedures, while we invite more and more people to join. Also, young scientists are required to spend a large fraction of time on activities unrelated to fundamental research: grant proposals, outreach projects, *knowledge valorisation*, i.e. make your research profitable.

The underlying strategy of the funding bodies seems to be: give a chance to many, select the few ones that bring quantifiable benefits and discard the others. Even though this approach can be intuitively appealing, some people question its real effectiveness [247]. What is certain so far is the toll that it takes on the lives of those involved.

Of course, PhD graduates leaving academia and moving to other sectors is beneficial to society, one might rightly argue, as they bring new knowledge and a healthy respect for evidence with them. Yet, little guidance is currently given by supervisors on alternative paths, although some university career services do exist, and the majority of students still hope to land academic jobs [248]. This mismatch between expectations and reality is likely to fuel anxieties and frustrations.

In fact, as most people know, graduate students struggle. The transformations that we mentioned are progressively leading towards more perceived pressure and poorer mental health among them [249, 250, 251]. Unhealthy and unfair working hours (nights,

weekends) are the unwritten norm in several laboratories and research institutes.

The situation will have repercussions also on those who succeed. The extreme competition is likely to select a generation of faculty members more self-centred and ruthless with respect to (or, at best, unaware of) basic psychological needs. The tremendous stress that they experienced while competing for their position can induce them to consider it a necessary toll to pay, thus fomenting an intergenerational vicious circle.

Much of this is public knowledge. Still, we have barely started to talk about it, among those who work in Science. Is this really the most effective way to conduct research? And even if it is, do we want it? Humans have the privilege to be able to change the way they organise themselves, as our biology leaves room for many possibilities. If we can imagine a different way to organise research, one in which the private lives and well-being of those involved are not disposable, one in which failure is an option and replication studies are encouraged, one in which one can afford to invest time in difficult, long-term projects, without worrying about producing a constant stream of papers, isn't it logical and ethical to implement it, as an experiment, and see how it works out?

Despite the overall worrying trend, the problem is being investigated and solutions are being proposed, e.g. as discussed in [247]. I have already seen concrete initiatives that go in the right direction. I hope these attempts to be the harbinger of a broader cultural change and I wish the best to those working to make such a change happen.